Aalto University
School of Engineering

Jari Lydman

Impact toughness and microstructure characterization of thermally aged Alloy 52 narrow-gap dissimilar metal weld

School of Engineering

Master's Thesis submitted in partial fulfilment of the requirements for the degree of Master of Science in Technology

Espoo, 2.11.2016

Supervisor: Professor Hannu Hänninen

Instructors: M.Sc. Tapio Planman and Research Professor Kim Wallin

Aalto University
School of Engineering

Aalto University, P.O. BOX 11000, 00076 AALTO
www.aalto.fi

Abstract of master's thesis

Author Jari Lydman

Title of thesis Impact toughness and microstructure characterization of thermally aged Alloy 52 narrow-gap dissimilar metal weld

Department Department of Mechanical Engineering

Professorship Engineering Materials **Code** Kon-67

Thesis supervisor Professor Hannu Hänninen

Thesis advisors M.Sc. Tapio Planman and Research Professor Kim Wallin

Date 2.11.2016 **Number of pages** 93 + 33 **Language** English

Abstract

Dissimilar metal welds (DMW) are used in nuclear power plants, in particular for the constitution of the primary circuit, for joining primary circuit pipes, made of austenitic stainless steel, with the nozzles of the primary component vessels made of low-alloy steel (LAS). This safe-end is a part of the primary loop of reactor pressure boundary, and it is one of the key safety related components of nuclear reactor. Ni-base alloys are typically used as a weld metal in DMW joints. Narrow-gap welding (NGW) technique is used, since the amount of weld metal is small, heat input is low and the method is more economical than conventional V-grooved weld. Thermal aging of materials used in pressurized water reactors (PWR) is a time and temperature dependent degradation mechanism that typically results in a decreased toughness of the material. In general, structures constructed from alloys that exhibit ductile-to-brittle behaviour should thus be used only at temperatures above the transition region. Accelerated thermal aging at a temperature higher than the nuclear power plant operating temperature is used to simulate the thermal aging effects during the NPPs service time. Segregation of phosphorus to grain boundaries in pressure vessel steels during service at elevated temperatures is a relatively common occurrence. The segregation of P promotes a change in the brittle fracture mode from transgranular to intergranular, and degradation in mechanical properties. This is considered as a major degradation mechanism for thermal aging.

In this work, the impact toughness of as-received and 5000 hours aged conditions of the safe-end DMW joint, and in particular the heat-affected zone (HAZ), is characterized. The used test method is the instrumented Charpy-V impact toughness test. Ductile-to-brittle transition region was characterized and crack arrest toughness estimated for the test material. Scanning electron microscopy (SEM) was used to examine fracture surfaces and electron probe microanalyzer (EPMA) was used to reveal the elemental distribution and composition evolution over the HAZ and fusion line. As a result of thermal aging, the transition temperature T_{42J} and the maximum absorbed energy increased significantly. In this work, the EPMA analyses were shown to provide a good overview of the chemical composition over the fusion line. Diffusion of elements occurred during the thermal aging is clearly visible in analysed data.

Keywords dissimilar metal weld, safe-end, thermal aging, impact toughness

Aalto-yliopisto
Insinööritieteiden
korkeakoulu

Aalto-yliopisto, PL 11000, 00076 AALTO
www.aalto.fi

Diplomityön tiivistelmä

Tekijä Jari Lydman

Työn nimi Termisesti vanhennetun Alloy 52 -kapearailo-eriparihitsin iskusitkeyden ja mikrorakenteen karakterisointi

Laitos Konetekniikan laitos

Professuuri Koneenrakennuksen materiaalitekniikka **Koodi** Kon-67

Työn valvoja Professori Hannu Hänninen

Työn ohjaajat DI Tapio Planman ja tutkimusprofessori Kim Wallin

Päivämäärä 2.11.2016 **Sivumäärä** 93 + 33 **Kieli** englanti

Tiivistelmä

Eriparihitsejä käytetään ydinvoimalaitoksissa erityisesti primääripiirin rakenteellisissa liitoksissa, joissa austeniittisesta ruostumattomasta teräksestä valmistetut primääripiirin putket on liitetty niukkaseosteisesta teräksestä (LAS) valmistettuihin yhteisiin. Tämä safe-end -liitos on osa reaktorin primääripiiriä. Liitos on reaktoriturvallisuuden kannalta yksi tärkeimmistä liitoksista ydinreaktoreissa. Eriparihitsausliitoksissa hitsimateriaalina käytetään nikkeliseoksia. Uusissa laitoksissa hitsausmenetelmänä käytetään kapearailohitsausta (NGW), koska tavalliseen V-railohitsaukseen verrattuna menetelmä on taloudellisesti kannattavampi vaihtoehto. Myös hitsiaineen määrä sekä lämmöntuonti ovat vähäisempiä. Painevesireaktoreissa (PWR) käytettävien materiaalien terminen vanheneminen on ajasta ja lämpötilasta riippuva materiaalin haurastumismekanismi, joka ilmenee ennen kaikkea materiaalin sitkeyden vähenemisenä. Sitkeä-hauras -transitiokäyttäytymiseen taipuvaisia rakennemateriaaleja tulisikin käyttää ainoastaan transitioaluetta korkeammissa lämpötiloissa. Kiihdytettyä termistä vanhennusta korkeassa lämpötilassa, tyypillisesti korkeammassa kuin asianomaisen ydinvoimalaitoksen käyttölämpötila, käytetään simuloimaan termisen vanhenemisen vaikutuksia ydinvoimalaitosten käytön aikana. Fosforin suotautuminen paineastiateräksen raerajoille käytön aikana korotetuissa lämpötiloissa on yleinen ilmiö. Fosforin suotautuminen edistää haurasmurtuman muuttumista lohkomurtumasta raerajamurtumaksi, jolloin materiaalin mekaaniset ominaisuudet heikkenevät. Tätä pidetään merkittävänä haurastumismekanismina.
Tässä työssä karakterisoidaan eriparihitsausliitoksen perustilan ja 5000 tuntia vanhennetun tilan, erityisesti lämpövyöhykkeen (HAZ), iskusitkeyttä. Testausmenetelmänä käytetään instrumentoitua Charpy-V -iskusitkeyskoetta. Työssä määritetään iskusitkeyden transitioalue ja arvioidaan särön pysähtymissitkeys testatulla materiaalilla. Murtopintoja tutkittiin pyyhkäisyelektronimikroskoopilla (SEM) ja alkuaineiden pitoisuuden sekä jakautumisen muutoksia lämpövyöhykkeessä ja sularajalla analysoitiin elektronimikroanalysaattorilla (EPMA). Termisen vanhennuksen seurauksena transitiolämpötila T_{42J} sekä absorboitunut maksimienergia kasvoivat merkittävästi. EPMA:lla tehdyt analyysit kuvaavat hyvin muutosvyöhykkeen kemiallista koostumusta. Termisestä vanhennuksesta johtuva alkuaineiden diffuusio on selvästi nähtävissä mittaustuloksissa.

Avainsanat eriparihitsi, safe-end-liitos, terminen vanheneminen, iskusitkeys

Preface

Most of the work of this thesis was carried out at VTT Technical Research Centre of Finland Ltd in the Nickel-Base Alloy Welding Forum (NIWEL) project. A part of microscopy work was carried out at Paul Scherrer Institute (PSI) in Villigen, Switzerland. This thesis was funded by VTT.

First I would like to thank the supervisor of this thesis, Professor Hannu Hänninen, from Aalto University and my instructors M.Sc. Tapio Planman and Research Professor Kim Wallin from VTT.

I want to thank Roman Mouginot and Teemu Sarikka from Aalto University for their great advices.

I am grateful for my colleagues Matias Ahonen, Ulla Ehrnstén, Caitlin Hurley, Petteri Lappalainen, and Marketta Mattila from VTT, who have helped me in many ways during this thesis. My former colleague from VTT, Matti Valo, earns many thanks as well.

I also want to thank Matthias Martin, Renato Restani and Robin Grabherr from PSI for the invaluable help with this thesis.

Espoo, 2.11.2016

Jari Lydman

Contents

List of symbols and abbreviations

A	Crack arrest load 4 kN transition temperature fitting parameter (°C)
A’	Estimate of transition temperature T_{42J} fitting parameter for 10000 hours aged condition
APT	Atom probe tomography
B	Thermal aging time in years in estimation of transition temperature T_{42J} for 10000 hours aged condition
b	Height of Charpy-V -notch specimen (mm)
BCC	Body-centered cubic
BSE	Backscattered electron
BWR	Boiling water reactor
C	Charpy transition curve slope of transition fitting parameter (°C)
CDZ	Carbon-depleted zone
COD	Crack opening displacement
D	Exponent in estimation of transition temperature T_{42J} for 10000 hours aged condition
d	Lattice spacing of the diffracting material
DMW	Dissimilar metal weld
DoDF	Distance of diffusion field
EDM	Electric discharge machine
EDS	Energy dispersive X-ray spectrometer
EPMA	Electron probe microanalyzer
EPR™	European Pressurized Water Reactor, a trademark by AREVA
EPRI	Electric Power Research Institute
FA	Fracture appearance (%)
F_a	Force at end of brittle fracture (kN)
F_{gy}	General yield force (kN)
F_m	Maximum force (kN)
F_u	Force at onset of brittle fracture (kN)
FCC	Face-centered cubic
FEG	Field emission gun
FEPA	Federation of European Producers of Abrasives
GMAW	Gas metal arc welding
GTAW	Gas tungsten arc welding
HAZ	Heat-affected zone
K_{Ia}	Crack arrest toughness (MPa√m)
K_{Jc}	Elastic-plastic fracture toughness (MPa√m)
KV_2	Absorbed energy (J)
KV_{calc}	Calculated absorbed energy (J)
l	Length of Charpy-V -notch specimen (mm)
LAS	Low-alloy steel
LE	Lateral expansion (mm)
LiF	Lithium fluoride
LTCP	Low temperature crack propagation
M	Ratio of strength mismatch

MGB	Migrated grain boundary
MHI	Mitsubishi Heavy Industries
MW_e	Megawatt electrical
n	Integer referring to the order of the reflection
NGW	Narrow-gap welding
NPP	Nuclear power plant
OL1	Olkiluoto 1 nuclear power plant unit
OL2	Olkiluoto 2 nuclear power plant unit
OL3	Olkiluoto 3 nuclear power plant unit
PET	Pentaerythritol
PMZ	Partially-melted zone
ppm	Parts per million
PSI	Paul Scherrer Institute
PWHT	Post-weld heat treatment
PWR	Pressurised water reactor
Q	Activation energy
R	Gas content
RPV	Reactor pressure vessel
SA	Fracture appearance (%)
SAW	Submerged arc welding
SCC	Stress corrosion cracking
SD	Standard deviation
SE	Secondary electron
SEM	Scanning electron microscope
SGB	Solidification grain boundary
SMAW	Shielded metal arc welding
SSGB	Solidification subgrain boundary
T	Temperature
T-L	Transversal-longitudinal orientation, ASTM E1823-13
T_0	Fracture toughness reference temperature, ASTM E1921 (°C)
$T_{0.89mm}$	0.89 mm lateral expansion transition temperature (°C)
T_1	Operation temperature of NPPs in the Arrhenius equation (K)
t_1	Operation time of NPPs in the Arrhenius equation
T_2	Thermal aging temperature in the Arrhenius equation (K)
t_2	Thermal aging time in the Arrhenius equation
T_{28J}	28 J transition temperature (°C)
T_{42J}	42 J transition temperature (°C)
T_{50}	Charpy transition curve temperature at half of the transition (°C)
$T_{50\%}$	50 % ductile fracture transition temperature (°C)
T_{Fa4kN}	Crack arrest load 4 kN transition temperature (°C)
TAP	Thallium acid phthalate
TEM	Transmission electron microscope
TVO	Teollisuuden Voima Oyj
US	Upper shelf
VTT	VTT Technical Research Centre of Finland Ltd
w	Width of Charpy-V -notch specimen
WDS	Wave length dispersive X-ray spectrometer
α’-	Alpha prime phase
γ-Fe	Austenite

δ-Fe	Delta-ferrite
θ	Angle between the X-ray and the diffractor's surface
λ	Wave length of the characteristic X-ray
σ-	Sigma phase
σ_{YB}	Yield strength of base metal
σ_{YW}	Yield strength of weld metal
χ-	Chi phase

1 Introduction

1.1 Background

Materials used in the primary circuit of nuclear power plants (NPP) are exposed to a very challenging environment, such as high temperature, stress, vibration, radiation, and corrosive water. Material degradation under such harsh conditions can lead to component failure, or at least a reduction in performance, which can create several problems. The modes of degradation phenomena are complex and vary depending on location and material. There are various types of materials that make up different components. More than 25 different metal alloys can be found within the primary and secondary systems. With the operational life of NPPs becoming increasingly longer, up to 60 or even 80 years, the issue of material degradation is expected to continue as NPPs age and operating licenses are extended. It should be considered an important factor in evaluating the safety and reliability of nuclear power plants in long-term operation. This is often done using an integrated aging management strategy based on state-of-the-art technology (NRC 2013c, NEA 2011, Yoo et al. 2015). The purpose to manage materials degradation problems proactively is not only to prevent the degradation, but also to predict future degradation (Ford et al. 2010).

The EPR™ reactor is a new Generation III+ Pressurised Water Reactor (PWR) designed and manufactured by AREVA with a power generation capacity of up to 1660 MW_e, which places it among the most powerful reactors in the world. Design studies for the EPR™ began in 1992. A direct descendant of the last models manufactured by AREVA in France (the N4 plant type) and Siemens in Germany (the Konvoi plant type), the EPR™ pressurized water reactor is based on tried-and-tested technologies and principles. This reactor design was previously called European Pressurized Water Reactor or Evolutionary Power Reactor, but now it is named EPR™, a trademark of AREVA. The design service life of the EPR™ is set at 60 years to maximize cost effectiveness for the operator. (AREVA/Framatome ANP 2005, European Nuclear Society 2016, Framatome ANP 2001)

Through improved thermal efficiency the EPR™ reactor achieves a significant reduction in uranium consumption and production of long-lived radioactive waste. From a safety point of view, the EPR™ reactor ensures a very high level of safety owing to diversified, redundant active and passive safety systems to drastically reduce the probability of severe accidents compared to existing Generation II reactors as well as to ensure that there will be no impact on the surrounding area, whatever the situation. In particular, it is highly resistant to external incidents, such as commercial airplane crash, and features like multiple protected power sources and water reserves. (European Nuclear Society 2016)

The EPR™ primary system is a 4-loop design, Figure 1. In each of the four loops, the primary coolant leaving the reactor pressure vessel (RPV) through an outlet nozzle goes to a steam generator. The steam generator transfers heat to the secondary circuit. Then the coolant goes to a reactor coolant pump before returning to the reactor pressure vessel through an inlet nozzle. Inside the reactor pressure vessel, the primary coolant is first guided downward outside the core periphery, and then it is channelled upward through the

core, where it receives heat generated by the nuclear fuel. (AREVA/Framatome ANP 2005, TVO 2010) The control rods are located above the reactor pressure vessel.

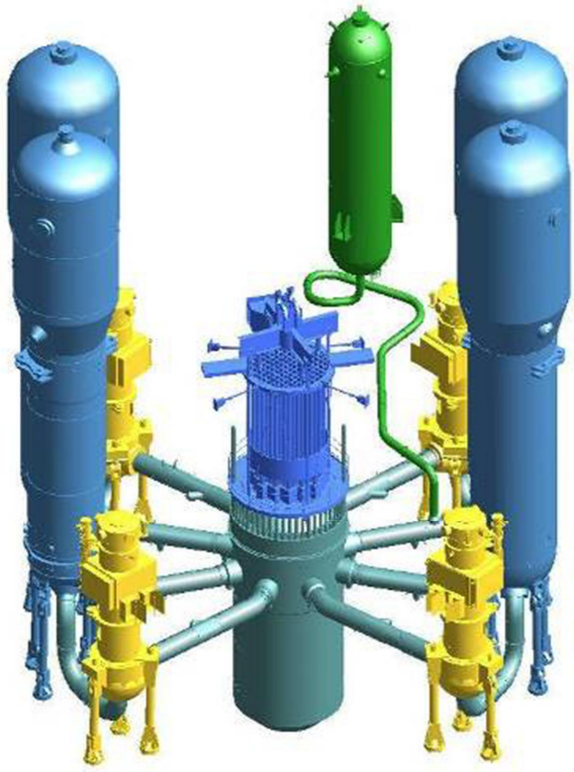

Figure 1 EPR™ primary system with a 4-loop configuration (AREVA 2011), where an RPV is in the middle, control rods are above the RPV, the yellow components are main coolant pumps, the green component is a pressurizer and the blue components are four steam generators.

A nuclear power plant has several nozzles and there are many aspects to consider when deciding on the design and materials for the joints. Weldability, coefficients of thermal expansion, stress corrosion cracking (SCC) susceptibility, manufacturing details and influence of heat treatments are important parameters to consider (Hänninen et al. 2006). The safe-end is a transition piece of pipe, generally a forging or a fitting which joins a piping system to a reactor pressure vessel nozzle. The safe-end is a part of the primary loop of reactor pressure boundary, and it is one of the key components of a nuclear reactor. The safe-end assures that the piping system can be easily joined in the field during plant construction. (EPRI 1986, Li et al. 2015)

Teollisuuden Voima Oyj (TVO) was founded in 1969 and is the developer, owner and operator of the Olkiluoto 1 (OL1) and Olkiluoto 2 (OL2) boiling water reactors (BWR) located at the Olkiluoto nuclear power plant in western Finland. TVO is currently building a third power plant unit, Olkiluoto 3 (OL3), which reactor type is EPR™. OL3's electrical output will almost double the production capacity of the two existing Olkiluoto power plants. (TVO 2010)

1.2 Scope of the work

This work is a part of Nickel-Base Alloy Welding Forum (NIWEL) joint research project that VTT and Aalto University are collaborating. NIWEL is based on the earlier Dissimilar Metal Welding (ERIPARI), Performance and Ageing of Dissimilar Metal Joints (PERDI) and Structural Integrity of Ni-base Alloy Welds (SINI) projects. The NIWEL research project is conducted in cooperation with a number of different on-going and international cooperative research projects. The content of the research includes an accelerated aging program to study the effects of thermal aging on the microstructural evolution and mechanical properties as well as fracture resistance, fracture resistance testing with small specimens including tests in PWR environment and effect of the loading rate, and determination of the residual plastic strains and residual stresses in the mock-up welds and evaluation of their effects on crack initiation and growth in various regions of the Ni-base alloy welds. The research project continues until May 2018. The project includes both mechanical testing and material characterization. (Ahonen et al. 2015a)

In Finland OL3 EPR™ plant contains a large amount of Alloy 690, 52 and 152 components, including a number of critical narrow-gap dissimilar metal welds (DMW). Improved knowledge on the long-term operation behaviour in addition to the very detailed microstructural data and the understanding of the involved mechanisms is absolutely essential. (Ahonen et al. 2015a)

This work includes a literature review of dissimilar metal welds, which consists of low-alloy steel/Ni-base alloy/austenitic stainless steel in PWR, thermal aging as well as testing and analysis methods which are used in this work. The as-received and 5000 hours aged conditions of the test material are characterized and the tests analysed. The 10000 hours aged condition is not tested, but an estimate for transition temperature is calculated based on the results from the as-received and 5000 hours aged conditions. The used test method is the instrumented Charpy-V impact toughness test. Ductile-to-brittle transition region is investigated and crack arrest toughness is estimated for the test material. Scanning electron microscopy (SEM) is used to examine crack paths and fracture surfaces and electron probe microanalyzer (EPMA) to determine the elemental distribution, possible changes in the microstructure and composition over the heat-affected zone (HAZ), fusion line and weld metal near fusion line. Charpy-V tests and EPMA analyses have not been performed earlier for this specific material. This work was carried out at VTT in Finland and PSI in Switzerland.

2 Theory and methods of research

2.1 Dissimilar metal welds

Welding is one of the most common methods in industrial practice for joining components. Its main advantages are high manufacturing speed combined with low costs and, usually, a high degree of flexibility, integrity and reliability. However, welding is a highly complex metallurgical process and, therefore, weldments are susceptible to material discontinuities, flaws and residual stresses which may lead to structural failure and life time reduction. As a consequence, weldments are an important field of application of fracture mechanics methods, although their application is more complex than for homogeneous or non-welded structures. Usually the materials involved in dissimilar metal welds show different strength and deformation properties and sometimes also different stiffness in terms of Young's modulus which causes additional stiffness mismatch. When dissimilar metal joints are made by fusion welding, some mixing of the base metal and filler metal can result around the fusion zone (ASM Handbook Volume 6 1993, Zerbst et al. 2014). A traditional dissimilar metal weld joint consists of four distinct microstructural zones which are the fusion zone, unmixed zone, heat-affected zone and base metal (Ming et al. 2016).

Dissimilar metal welds are used in nuclear power plants, in particular for the constitution of the primary circuit, for joining primary circuit pipes, made in EPR™ of austenitic stainless steel, with the nozzles of the primary component vessels made of low-alloy steel (LAS), such as the reactor pressure vessel, the steam generators, and the pressurizer. The main characteristics of dissimilar metal welds are that the weld filler metal is the corrosion resistant nickel-base alloy, the weld preparation geometry is a narrow-gap one, and welding is performed with the gas tungsten arc welding (GTAW) process (Joly et al. 2014). Nickel-base alloys are often used for dissimilar metal welds where carbon steels are joined to Ni-base alloys or stainless steels. Ni-base alloy is used as a weld metal in this type of joints for its thermal expansion coefficient (Li et al. 2015). Other common high-quality welding methods for Ni-base alloys are shielded metal arc welding (SMAW), gas metal arc welding (GMAW) and submerged arc welding (SAW) (Hänninen et al. 2006). Ni-base alloys are also used for cladding carbon steels in applications in which stainless steel cladding does not provide sufficient corrosion protection (DuPont et al. 2009, Lippold & Kotecki 2005, Takeuchi et al. 2014). Nickel Alloys 600 and 690 are widely used in PWR applications. Alloys 82 and 182 are the Alloy 600 type filler metals and Alloys 52 and 152 are the Alloy 690 type filler metals, respectively. These materials are used to weld Alloys 600 and 690 to themselves, to austenitic stainless steels, and to carbon and low-alloy steel parts. In addition, these alloys are used as buttering when welding nozzles (EPRI 2002). Despite the well acknowledged advantages of the technique, the mechanical properties of the finished welds produced by narrow-gap welding (NGW) have not yet been fully characterized (Jang et al. 2010).

The large composition differences between the nickel-base alloys and steels can result in a wide range of weld metal properties and microstructures. Dilution must be carefully controlled to prevent the formation of intermediate phases which can lead to embrittlement. In general, the dissimilar weld metals tend to be austenitic due to the strong austenite stabilizing effect of Ni. However, the solidification temperature range of the weld

metal is significantly affected from dilution by the Fe-based alloys. DMWs between nickel-base alloys and steels also exhibit a composition transition region between the diluted weld metal and the base metal. In many cases, this transition region may contain a layer of martensite (ASM Handbook Volume 6 1993, DuPont et al. 2009). The Schaeffler diagram can be used for providing a microstructure approximation of dissimilar metal welds, because stainless steels, carbon steels and low-alloy steels can be plotted on the diagram. Microstructure predictions can be made for all of these steels (Lippold & Kotecki 2005). The Schaeffler diagram with Cr- and Ni-equivalents is shown in Figure 2. The Cr-equivalent includes the most common ferrite-forming elements and the Ni-equivalent includes the austenite-forming elements (Bhadeshia & Honeycombe 2006). Predicting the transition region microstructure can be difficult, because it may change dramatically over a short distance. Within this region the microstructure can differ significantly from both the weld metal and HAZ and is subject to local compositional gradients and diffusional effects. (Lippold & Kotecki 2005)

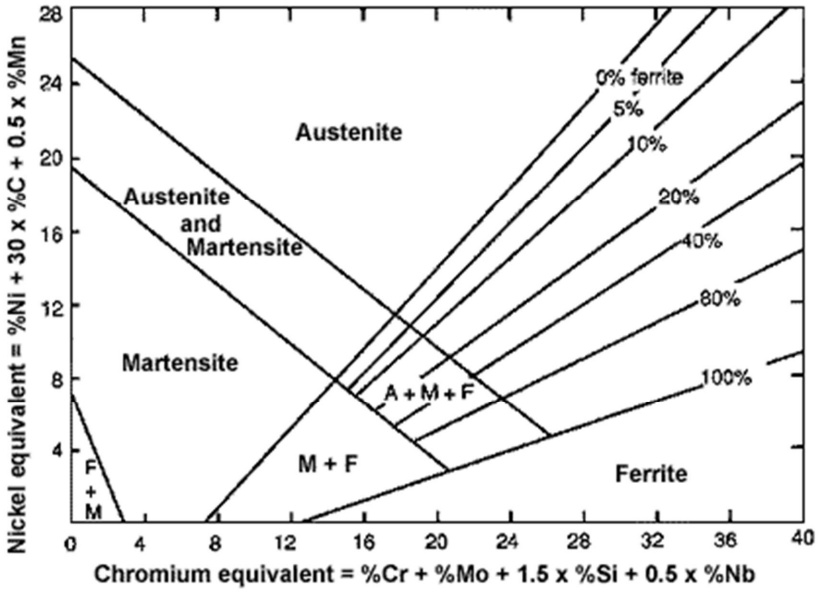

Figure 2 The Schaeffler diagram with Cr- and Ni-equivalents (Allen 2015).

In modern pressurized water reactors, the transition from filler metals Alloys 82 and 182 to Alloys 52 and 152 with higher chromium contents and the new weld design using narrow-gap welding technique are made to ensure the structural integrity of the welds. Narrow-gap welding technique is used to join together thick plate materials separated by a very narrow groove with only one pass per layer. NGW is more economical than the conventional V-grooved weld as it requires less welding consumable, shorter welding times, and reduces the volume of inspection. The reduced amount of weld metal and lower heat input lead to less shrinkage, distortion and smaller residual stresses and strains. The welding process is fully automated and thus allows a good reproducibility. The design of this type of weld, which is allowed by the modern automated technology of narrow-gap welding, was selected since it introduced a large number of improvements compared to the design of dissimilar metal welds of older plants, where the weld geometries had wide gaps, and often included a butter weld, on the low-alloy steel side, and sometimes on the stainless steel side also. NG-GTAW can be used in special applications with stainless steels and Ni-base alloys for critical structures, such as the dissimilar metal welds between the reactor pressure vessel low-alloy steel and its stainless steel safe-end in new PWR designs in

which the quality and the performance of the welded joints are key factors. The joint can be welded without any butter weld on the connected components (Hänninen et al. 2014, Joly et al. 2014, Wang et al. 2013c). Most of the dissimilar metal weld characterization studies so far have included buttering layer between low-alloy steel and weld metal.

The buttering layer in weld joints has several purposes. In dissimilar metal welds the melting temperatures of welded materials can differ. The buttering layer should serve to reduce the melting temperature differences. Buttering may also be used to provide a transition between materials with substantially different coefficients of thermal expansion, to endure cycling temperatures in service. Similarly, buttering may be used to provide a barrier layer that will slow the migration of undesirable elements, such as carbon from the base metal to the weld metal during post-weld heat treatment (PWHT) or in service at elevated temperatures (ASM Handbook Volume 6 1993, Rathod et al. 2016). Buttering is also a technique to minimize dilution (Messler, Jr. 2004). High-carbon steels can be buttered with austenitic filler metal to reduce carbon content, which lowers the risk of solidification cracking and the formation of brittle martensite (Kou 2003). A post-weld heat treatment is often required to temper the martensite (Alexandrov et al. 2013). However, solidification cracking may occur during reheating due to elemental segregation (EPRI 2013).

For an EPR™ type of reactor, the nozzles of the low-alloy steel vessels (made of RCC-M 16MND5 steel, similar to SA 508 Cl3 steel) are welded in the manufacturing shop, to stainless steel safe-ends (made of 316L type of stainless steel RCC-M Z2CND 18-12 with controlled nitrogen). The location and geometry of nozzles are shown in Figure 3. By using this manufacturing process, a weld between the safe-ends and the stainless steel pipes is carried out on site (Joly et al. 2014). Different zones of the dissimilar metal weld mock-up (low-alloy steel nozzle, stainless steel safe-end, Ni-base alloy weld metal and stainless steel cladding) are presented in Figure 4.

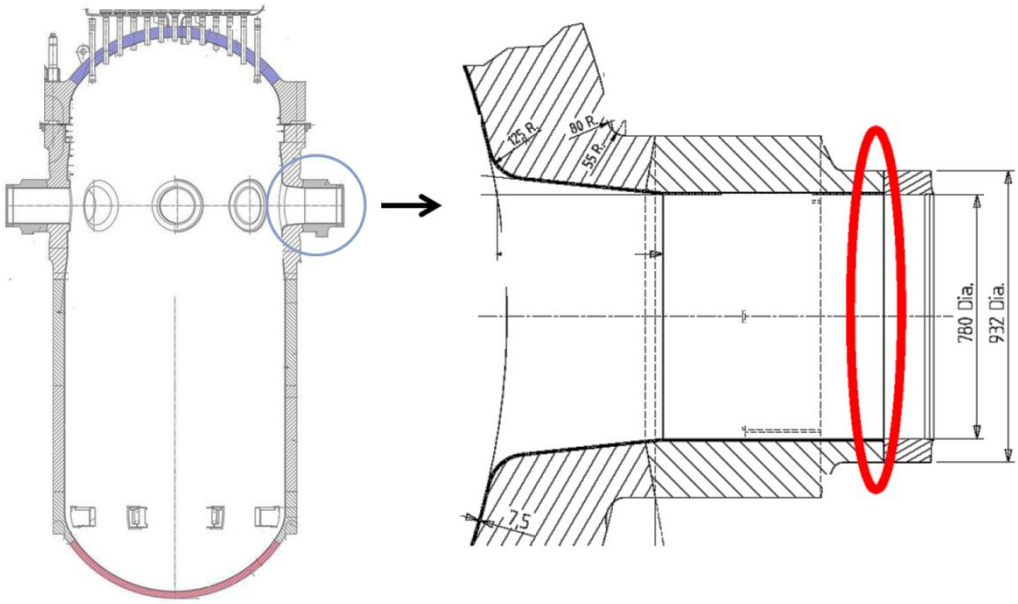

Figure 3 Location of the EPR™ RPV Alloy 52 dissimilar metal welds (IRNS 2015 (modified), Wells et al. 2009).

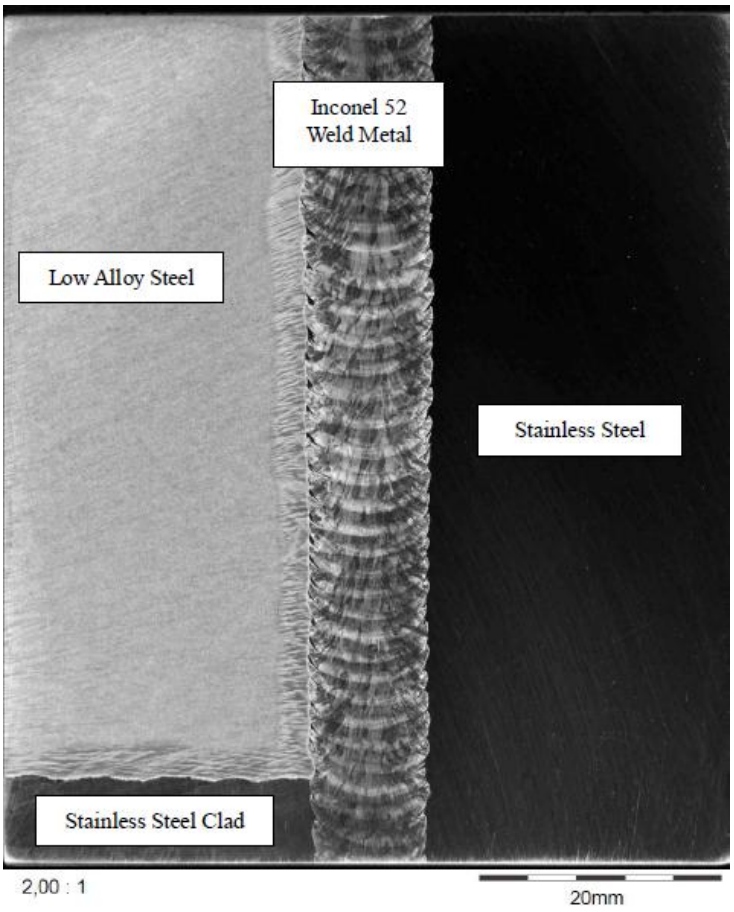

Figure 4 Macrograph of a section of the narrow-gap GTAW Alloy 52 DMW (Joly et al. 2014).

Nickel-base Inconel Alloy 82 and 182 were found to be susceptible to stress corrosion cracking in the primary water environment, and therefore, Inconel Alloy 52 and 152 with high resistance to SCC have been used to replace the Alloy 82 and 182 in new PWRs. Alloy 690 and its compatible weld metals, Alloys 52 and 152, have been in PWR primary water service for more than 20 years without any SCC identified. Furthermore, an excellent SCC resistance is indicated by laboratory testing (EPRI 2013). Alloys 52, 82, 182 and 690 are susceptible to low temperature crack propagation (LTCP) as a result of hydrogen induced cracking when exposed to hydrogenated water at low temperature, while Alloy 600 is not susceptible to this type of cracking. LTCP requires, however, pre-existing cracks produced by another mechanism, residual and applied stresses, and high hydrogen content in the water (NEI 2004). High chromium nickel-base weld filler metal Alloy 52 (ERNiCrFe-7) and Alloy 52M (ERNiCrFe-7A) have been widely used as filler metals for repair applications and fabrications for new nuclear power plants (EPRI 2002, Wang et al. 2013a, Wang et al. 2013b). Alloy 52 has also higher Al and Ti contents to improve the hot cracking resistance during welding (Buisine et al. 1997). Clarifying the fracture mechanics of the dissimilar metal welds made from new materials is critical for integrity assessment and design of the DMW joint structures (Wang et al. 2013b).

Stainless steels have proved relatively trouble free in PWR piping applications. Carbon and low-alloy steels with internal stainless steel cladding have also performed well without significant problems (EPRI 2002). However, the weld joints are widely recognized as

being susceptible to thermal aging embrittlement at PWR operating temperatures (EPRI 2008).

In this work the impact toughness of a dissimilar metal weld joint, and in particular the heat-affected zone, is characterized. Because of their microstructures, the austenitic base metal and the nickel-base alloy weld metal cannot undergo brittle fracture. Their unit cell is face-centered cubic (FCC). Almost all nickel-base alloys are tough even at -196 °C and, therefore, a ductile-to-brittle transition does not occur. Ferritic pressure vessel steel's unit cell is body-centered cubic (BCC) (Blouin et al. 2014, Hertzberg et al. 2013, Hurlich 1969). Charpy tests have been performed on samples aged during 20000 to 30000 hours at 400 °C and 5000 to 30000 hours at 450 °C. Globally, the main tendency was a slight increase of strength and a decrease in ductility with time in temperature. In addition, the ductile-to-brittle transition temperature increases and the absorbed energy (KV_2) of upper shelf (US) decreases. (Boursier et al. 2005, EPRI 2013)

Chemical compositions of the most interesting materials in this work, the pressure vessel steel SA 508 and the weld metal Alloy 52, are presented in Table 1.

Table 1 Chemical compositions of pressure vessel steel SA 508 and weld metal Alloy 52 (Hänninen et al. 2014).

Material	C	Si	Mn	P	S	Cr	Ni	Mo	Nb	N	Ti	Fe	Al	Co	Cu
SA 508	0.21	0.17	0.78	0.002	0.009	0.45	0.85	0.62	-	0.014	0.002	base	0.016	<0.003	0.06
Alloy 52	0.03	0.13	0.24	<0.001	<0.001	29.2	59.28	0.03	Nb+Ta <0.02	-	0.51	9.8	0.72	0.009	0.04

2.1.1 Strength mismatch in welds

Any kind of mismatch is an important feature of weldments. Experimental evaluation of the weld toughness is generally conducted using crack opening displacement tests (COD) and/or J-integral tests. These tests were developed under the assumption that the specimens have homogeneous mechanical properties, contrary to the welded joints that show strong mechanical heterogeneity. This heterogeneity is usually characterized through mismatching factor which is the ratio of the yield strengths of weld metal and base metal as

$$M = \sigma_{YW} / \sigma_{YB} \quad (1)$$

where M is a ratio of strength mismatch, σ_Y is yield strength and W and B refer to weld metal and base metal, respectively. Overmatching means that $\sigma_{YW} > \sigma_{YB}$ or $M > 1$, whereas undermatching refers to $\sigma_{YW} < \sigma_{YB}$ or $M < 1$. However, besides the yield strengths also the work hardening, i.e., the plastic regions of the stress-strain curves beyond yielding can show a mismatch effect. The latter is not considered in conventional assessment but plays a role in the determination of the fracture mechanics crack driving force. The mismatch definition of Equation 1 refers to what was designated as global strength mismatch above since it only considers weld metal and base metal properties. In strain-based design a more useful definition of M would be the ratio of the tensile strengths of the weld metal and base metal. (Neves & Loureiro 2004, Zerbst et al. 2014)

The implication of any kind of strength mismatch is that the resulting deformation pattern is inhomogeneous across the weld when the applied stress exceeds the lower strength of the material being joined. If the weld metal, the base metal and the heat-affected zone show different yield strengths and if the loading on the joint is sufficiently high and a flaw is present, the consequence is plastic strain concentration between the flaw tip and free surface. The driving force of a crack tip, which is located in the vicinity of such a plastic zone, will be notably affected and may be higher than it would be in a non-welded structure or a strength evenmatched weld (Zerbst et al. 2014). Blouin et al. (2014) have studied brittle fracture properties of dissimilar metal welds with different crack locations, where Alloy 52 was used as weld material and no buttering was used. Their study shows that ferritic low-alloy steel outside the HAZ is more sensitive to brittle fracture than the ferritic HAZ of the weld joint. The reason for this kind of behaviour is the presence of the nickel-base alloy close to the HAZ which has lower material yield stress than that of the ferritic low-alloy steel (Blouin et al. 2014). For inhomogeneous materials, i.e. dissimilar metal welds, the mismatch effect plays an important role in the crack growth resistance and crack growth path, particularly when cracks are lying at the interfaces of dissimilar metal weld joints. If the base and weld materials are similar (low inhomogeneity), the mismatch effects are small. The crack growth resistance will be similar to that in the homogeneous material where the initial crack lies (Wang et al. 2011). If the mechanical properties of the base metals are homogenous, the strength mismatch effect does not exist. Then the crack growth paths are approximate straight. (Wang et al. 2013b)

When a crack is located in the centre of the weld, the plastic zone is confined within the weld metal for extreme undermatching and in the base metal for extreme overmatching. As a consequence, overmatching is beneficial for the structural integrity if the crack is in the centre of the (higher strength) weld, if the weld strip is wide and if the crack is large, because this way the crack tip is shielded. In contrast, undermatching is detrimental for this configuration because the local strain in the lower strength weld metal enclosing the crack, which controls the crack driving force, is significantly higher than in a configuration without strength mismatch (Zerbst et al. 2014). The welded joints in steel structures are commonly designed to have a weld metal with a higher strength than the base metal, to prevent the failure in welds resulting from strain localization. According to Chiba et al. (2010), a strength mismatch effect was only recognized within the higher temperature range (T > X) in the Charpy test. At lower temperature, the strength mismatch effect was not significant. (Chiba et al. 2010)

When a crack is located at the fusion line or in the heat-affected zone, the plastic zone spreads into the lower strength base metal for overmatching or into the lower strength weld metal for undermatching. In the case of overmatching the strain concentration zone is in the base metal enclosing the crack tip, with the consequence of the crack driving force magnified compared to a non-mismatch configuration. Overmatching is detrimental in the case of an HAZ crack. In contrast, undermatching is beneficial because the higher strength base metal shields the crack tip such that the plastic zone is first spread into the lower strength weld metal away from the crack tip. (Zerbst et al. 2014)

2.1.2 Solidification of welds

2.1.2.1 Epitaxial grain growth

Epitaxial grain growth occurs during autogenous welding when filler metal is not used. The existing base-metal grains at the fusion line act as the substrate for nucleation. Since the liquid metal of the weld pool is in immediate contact with these substrate grains and wets them completely and crystals nucleate from the liquid metal upon the substrate grains without difficulties. Nucleation occurs from the liquid metal in the existing crystallographic orientation. For metals with a FCC and BCC crystal structure the growth direction is <100>. (Kou 2003, Messler, Jr. 2004)

2.1.2.2 Non-epitaxial grain growth

When welding with a filler metal or joining two different materials, the weld metal composition differs from the base metal composition, and the weld metal crystal structure can differ from the base metal crystal structure. When this occurs, epitaxial growth is no longer possible and new grains have to nucleate at the fusion boundary. When the base metal and the weld metal exhibit two different crystal structures at the solidification temperature, nucleation of solid weld metal occurs on heterogeneous sites on the partially melted base metal at the fusion boundary. The fusion boundary exhibits random misorientations between base metal grains and weld metal grains as a result of heterogeneous nucleation at the pool boundary. The weld metal grains may or may not follow special orientation relationships with the base metal grains they are in contact with, and they orient themselves so that certain atomic planes are parallel to specific planes and directions in the base-metal grains. (Kou 2003)

2.1.2.3 Competitive growth

Away from the fusion line the grain structure is dominated by competitive growth, Figure 5. During weld metal solidification grains tend to grow in the direction perpendicular to pool boundary because this is the direction of the maximum temperature gradient and hence maximum heat extraction. However, columnar dendrites or cells within each grain tend to grow in the easy-growth direction. During solidification grains with their easy-growth direction essentially perpendicular to the pool boundary will grow more easily and crowd out those less favourably oriented grains. This mechanism of competitive growth dominates the grain structure of the bulk weld metal. (Kou 2003)

Competitive growth in the weld fusion zone is the predominant mechanism of solidification in welds, but there are other reasons that can interrupt and/or dominate the solidification structure. These possible mechanisms of grain formation include dendrite fragmentation, grain detachment, heterogeneous nucleation and surface nucleation. (Nelson et al. 1999)

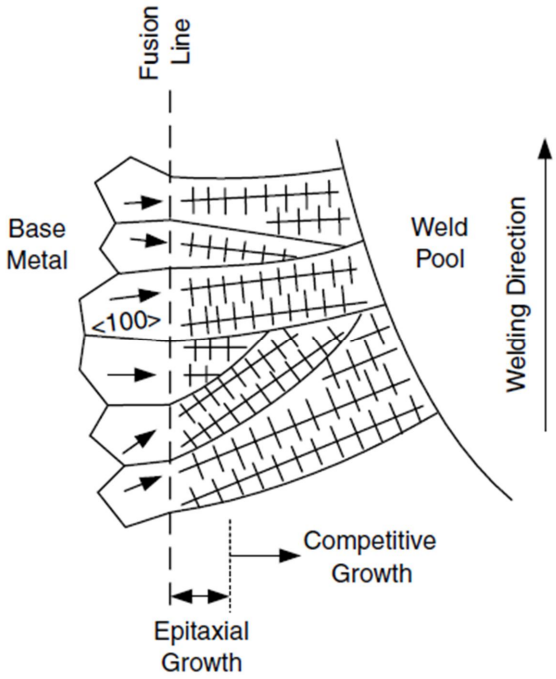

Figure 5 Competitive grain growth (Kou 2003).

2.1.2.4 Solidification boundaries and interfaces

Various boundaries or interfaces, such as solidification subgrain boundaries (SSGB), solidification grain boundaries (SGB) and migrated grain boundaries (MGB), are present in nickel-base weld metal, Figure 6. Many of the defects associated with the fusion zone during fabrication and service are associated with these boundaries. These boundaries are especially evident in nickel-base alloy weld metals because the austenite solidification structure is clearly visible after polishing and etching. (DuPont et al. 2009, Lippold & Kotecki 2005)

Solidification subgrains are normally present as cells or dendrites and the boundary separating adjacent subgrains is known as a solidification subgrain boundary. The boundaries are evident in the microstructure since their composition is different from that of the bulk microstructure. There is virtually no crystallographic misorientation across the SSGB and these boundaries are crystallographically characterized as low angle boundaries. The low misorientation results from the fact that subgrain growth during solidification occurs along preferred crystallographic directions or easy growth directions. The dislocation density along the SSGB is generally low since there is not a large structural misorientation to accommodate. (DuPont et al. 2009, Lippold & Kotecki 2005)

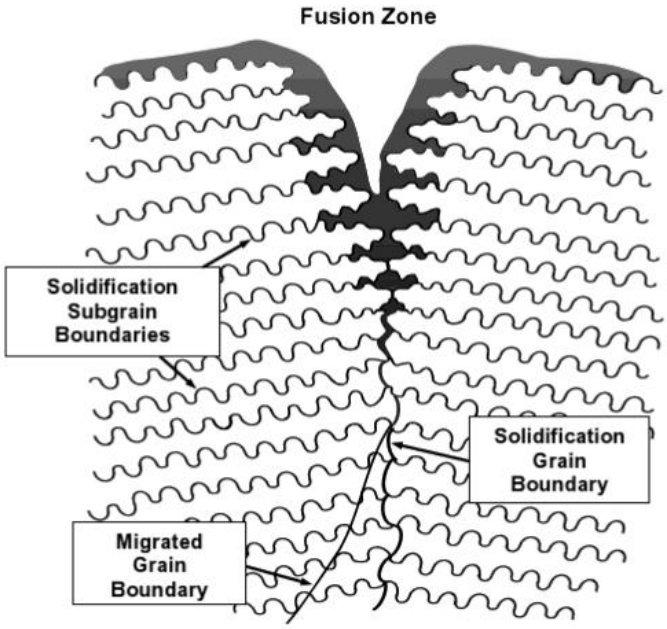

Figure 6 Schematic of different boundaries observed in weld metals which solidify as austenite (Lippold & Kotecki 2005).

The solidification grain boundary results from the intersection of groups of subgrains. SGBs are the direct result of competitive growth that occurs along the trailing edge of the weld pool. Each of these groups of subgrains has a different growth direction and orientation. Their intersection results in a boundary with high angular misorientation. The misorientation results in the development of a dislocation network along the SGB. (DuPont et al. 2009, Lippold & Kotecki 2005)

The solidification grain boundary that forms at the end of solidification has both a compositional and crystallographic component. In some situations it is possible for the crystallographic component of the SGB to migrate away from the compositional component. This new boundary carries with it the high angle misorientation of the original SGB and is called a migrated grain boundary. The driving force for the migration is the same as for simple grain growth in base metals, a lowering of boundary energy. The original SGB is quite tortuous because it forms from the intersection of opposing cells and dendrites. The composition of the MGB varies locally, depending on the composition of the microstructure where it has migrated. (DuPont et al. 2009, Lippold & Kotecki 2005)

2.1.2.5 Type II boundaries

Microstructure evolution along the fusion boundary in dissimilar metal welds can be complex. In situations where the base metal is ferritic at temperatures near the melting point and the weld metal is austenitic, normal epitaxial growth can be surpassed. This is the case when base metal and weld metal have different crystal structures. This can result in the formation of Type II boundaries, which run roughly parallel to the fusion line, typically less than 100 µm away in the weld metal. Type II boundaries are grain boundaries that are in contrast to the Type I boundaries, which result from columnar growth from base metal grains into the weld metal and are oriented roughly perpendicular to the fusion line (Lippold & Kotecki 2005, Nelson et al. 1999, Nelson et al. 2000).

The formation of the Type II boundaries is dependent on the solidification behaviour of the weld metal and the nature of solid-state transformations in the base metal substrate (Nelson et al. 2000). Type II boundaries form in the solid state during weld cooling when both the weld metal and heat-affected zone are austenitic, which allows for austenite grain growth across the fusion line. In a case of low-alloy steels, which crystal structure is BCC, this is possible due to the high welding temperature when the base metal undergoes an allotropic delta-ferrite (δ-Fe) to austenite (γ-Fe) transformation. Then the fusion line becomes an austenite (FCC) boundary between the base metal (FCC) and the weld metal (FCC) in the austenitic temperature range (Mouginot & Hänninen 2013). Type II boundaries may be sites for carbide precipitation, particularly if significant carbon migration from the base metal has occurred. The migration can result in local microstructural changes in both the HAZ and transition region. As a result, a carbon-depleted zone (CDZ) is affected by these carbides and may occur in the HAZ (Lippold & Kotecki 2005). Changing base metal dilution, which affects the composition gradient in the weld metal at the fusion line, supports the existence of this transition region (Nelson et al. 2000). Type II boundaries have generally lower Ni and Cr contents due to dilution from the base metal to the weld metal (Chung et al. 2011, Mouginot & Hänninen 2013). Yoo et al. (2015) show in their study that Type II boundaries shift away from the fusion line during thermal aging. In their study the thermal aging temperature was 450 °C. (Yoo et al. 2015)

Because of the transition in composition between base metal and diluted filler metal, a narrow region of martensite can exist along the fusion line. Type II boundaries are important because a number of instances of in-service cracking has been associated with them. The martensite layer together with a local mismatch and approximately planar interface makes the structure weak and a preferential cracking site. (Lippold & Kotecki 2005, Nelson et al. 2000)

2.2 Thermal aging

Irradiation embrittlement and thermal aging are major aging mechanisms in nuclear power plants (Nhili 2015). Thermal aging of materials used in PWRs is a time and temperature dependent degradation mechanism that typically results in a decreased toughness of the material. The hardness of many of these materials increases, and their stress corrosion cracking resistance decreases over time (EPRI 2003). The effects of elevated temperature service in metal alloys have been examined for many years. Possible effects include phase transformations that can adversely affect mechanical properties. Extended time at elevated temperature, even at service temperature, may permit even very slow phase transformations to occur. This is of particular concern for cast stainless steel components where the formation of a brittle alpha prime (α') phase can result in a loss of fracture toughness and lead to brittle failure. The effects of aging on other components are also of concern (NRC 2013c). The generally accepted temper embrittlement temperature range of low-alloy steels is between 375 °C and 560 °C (EPRI 2003). A sample aged at 450 °C exhibits slightly more severe effects of thermal aging than a sample aged at 400 °C. However, the trends for these thermal aging effects are similar (Choi et al. 2015).

Accelerated thermal aging, at a temperature higher than PWR nuclear power plant operating temperature, about 320 °C, is used to simulate the thermal aging effects during

the NPPs service time. Accelerated aging is required to investigate the thermal aging effects like degradation and cracking behaviours on the fusion line region. (Choi et al. 2015, Choi et al. 2016) However, substantial increases in temperature may promote microstructural changes affecting the thermodynamic conditions controlling segregation which might not occur at lower temperatures (Druce et al. 1986).

Heavy components of PWRs are made of low-alloy steels and selected because they demonstrated an excellent compromise between strength, toughness and weldability. They also exhibit a relative sensitivity to thermal aging, which corresponds to a shift of the ductile-to-brittle transition temperature after long-term exposure at high temperature (Andrieu et al. 2014). Thermal aging embrittlement of low-alloy steels is often caused by the diffusion and segregation of impurity elements, such as phosphorus, into the grain boundaries after prolonged exposure to temperatures in the range 350 °C to 575 °C. At temperatures below this range, very long exposure times are necessary for the impurities to diffuse to, and segregate in the grain boundaries. The presence of carbon tends to accelerate the embrittlement process, due to preferential segregation of the impurities at the interface between grain boundary carbides and ferrite grains (NEI 2004). It has been also stated that phosphorus decreases the cohesion of grain boundaries, while carbon reinforces them, which decreases the effect of P segregation (Andrieu et al. 2014) and carbon atoms desegregate during aging while phosphorus concentration is increasing (Andrieu et al. 2013). Thermal aging of reactor pressure vessel steels is not generally considered as significant issue for 40 or 60 years of operation. While as-received conditions may not cause serious cracking issues, thermal aging may change the local microstructure and decrease cracking resistance. The fusion boundary region is expected to be more susceptible to thermal aging effects because of the chemical gradient formed in the welding process (Choi et al. 2015, NRC 2013c). It is known that grain refinement increases material's strength and toughness and decreases the transition temperature (Hertzberg et al. 2013). If the grain size grows for instance during thermal aging, the results are opposite. In addition, growth of inclusions, which act as nucleation sites for fracture and widening of carbon-depleted zone may lead to embrittlement.

It has been observed that the heat-affected zones of higher-temperature low-alloy steel components are prone to thermal aging, with the pressurizer experiencing the highest temperature. The pressurizer may exhibit a significant shift in HAZ's ductile-to-brittle transition temperature. This shift increases the reactor pressure vessel irradiation embrittlement shift. For that reason, the pressurizer, if fabricated from low-alloy steel, and portions of the RPV, that operate at high temperature, could be prone to thermal aging and have significant stresses. The RPV components that reach higher temperatures (315 °C) consist of the RPV flange, the nozzle shell ring, and the outlet nozzles of all plants as well as the vessel heads of some reactors. The components like nozzle shell ring and outlet nozzles receive a low neutron dose rate exposure, which combined with thermal aging can potentially create greater-than-expected embrittlement. Some internal parts, such as RPV heads, can be replaced which will reset the thermal aging (NRC 2013b, NRC 2013c). In practice the only component that cannot be replaced is the reactor pressure vessel.

As nickel-base alloys containing about 30 % chromium (such as alloys 690, 152 and 52) have a chemical composition close to the stoichiometry Ni_2Cr, a long-term ordering transformation of the initial solid solution can occur during holding in temperature. This microstructural transformation induces hardening and embrittlement, which are important

for the operating properties. This transformation is strongly reduced by adding other elements like iron and it becomes unlikely for iron content > 8 %. However, thermal aging tests have been performed to verify that the transformation did not occur in these weld metals. (Boursier et al. 2005, Buisine et al. 1997, EPRI 2013)

Alloys 600 and 690 and their weld metals Alloy 82, 182, 52 and 152 possess very high ductility. According to Electric Power Research Institute (EPRI), no embrittling intermetallic phases such as sigma- (σ), chi- (χ), or α'-phase precipitations responsible for thermal aging embrittlement of austenitic stainless steel welds and castings have been identified from extensive investigations related to stress corrosion cracking. It can be concluded that thermal aging embrittlement is not a concern for Alloys 600, 690, the weld metals Alloy 82, 182, 52 and 152 or the heat-affected zone at elevated temperatures in PWRs. Therefore, it can be concluded that these materials will not become thermally embrittled due to long-term exposure at PWR temperatures (EPRI 2003). Long-term performance to date has been excellent, with no service induced degradation identified. However, metallurgical changes still occur at the interface and transition region, especially due to post-weld heat treatment, leading to concerns about the long-time behaviour of the welds. Long-term mechanical behaviour of narrow-gap welds and their susceptibility to aging mechanisms have not been fully characterized yet. (EPRI 2008, Hänninen et al. 2014)

Effective aging management can be jeopardised by several factors that may lead to either unexpected or premature aging degradation. These factors or weaknesses need to be identified and addressed if the proactive approach to aging management for safe long-term operation is to be successful. The most frequently encountered weaknesses of aging management are an insufficient understanding or predictability of aging, a lack of data for aging management, error-induced aging and an insufficient capability for dealing with unforeseen aging phenomena. (NEA 2011)

2.2.1 Phosphorus segregation

Segregation of phosphorus to grain boundaries in pressure vessel steels during service at elevated temperatures is a known phenomenon and has been observed in base material, weld metal and different zones of HAZ. Such segregation can occur during fabrication, especially during the slow cooling stage of a post-weld heat treatment, and as a result of in-service exposure to high operating temperature and irradiation. Extensive observations of P segregation under thermal aging, together with determination of the relevant activation energies, have enabled segregation at grain boundaries to be well-characterized for grain-coarsened heat-affected zone material. The segregation of phosphorus to grain boundaries promotes a change in the brittle fracture mode from transgranular to intergranular, and degradation in mechanical properties (EPRI 2000). This is considered as a major degradation mechanism.

The presence of P in grain boundaries can lower the grain boundary cohesion. Macroscopically, as the grain boundary P level increases, this can appear as an increase in the ductile-to-brittle transition temperature measured in Charpy impact tests, or a decrease in the lower shelf toughness (EPRI 2000).

P peak height ratio as a function of aging time in the grain-coarsened HAZ of the A533B steel with P content 0.005 % is shown in Figure 7. At the temperature of 300 °C there is barely any P segregation. At 500 °C and 550 °C the P segregation obtains an equilibrium level. Instead, a thermal treatment at 400 °C and 450 °C increases P content at grain boundaries. Saturation is reached at 450 °C, 500 °C and 550 °C. 0.008 % is the maximum phosphorus content presently allowed by the RCC-M code for the forgings used for nozzles of the primary component vessels (Joly et al. 2014).

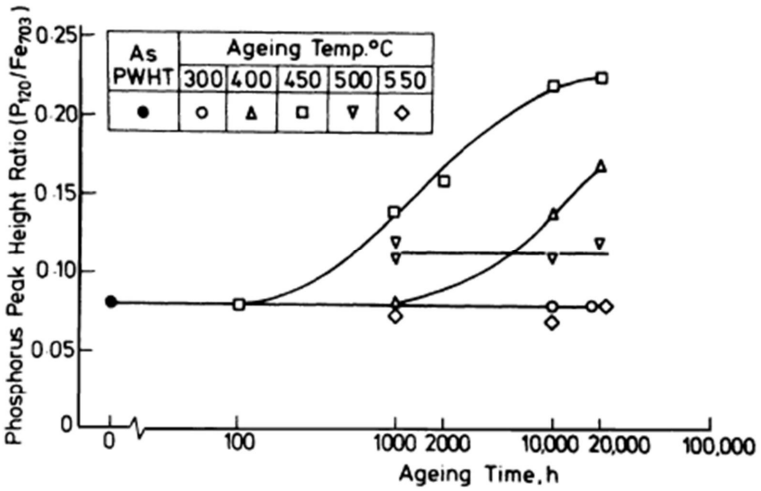

Figure 7 Effect of aging time and temperature on the grain boundary segregation of P in the grain-coarsened HAZ of the A533B steel, P content 0.005 % (Druce et al. 1986).

2.2.2 Effects of thermal aging on precipitates

For precipitate growth and coarsening to occur, there needs to be a solute. Solutes for precipitate growth are supplied by the surrounding matrix, whereas for the coarsening of larger precipitates, solutes are released by the dissolving smaller particles. However, in reality, the two sources, the surrounding matrix and the dissolving particles, usually operate simultaneously, regardless of the ongoing process being growth or coarsening. During precipitate growth, when transition phases are formed prior to the formation of a stable precipitate, the size of the stable phase increases at the expense of the transition particles. During particle coarsening, solute concentration in the surroundings of a smaller precipitate is expected to be higher than of particles of bigger size. From the view of the precipitate that grows or coarsens, the solutes are from both its surroundings and dissolved precipitates. A typical one-peak precipitation-strengthening curve is shown in Figure 8. The driving force for coarsening always consists of two parts - the difference in solute concentration and the decrease of interfacial free energy. So the diffusion processes involved in precipitate growth and coarsening have no essential difference. The difference is only in the distance of diffusion field (DoDF). The DoDF during precipitate growth decreases slightly with time if nucleation sites saturate at the beginning, and increases if more nucleation sites form during aging. Coarsening, featured with a decrease in the number of precipitates, is always accompanied with an increase in the average distance of diffusion field. Therefore, size increment during precipitate coarsening always proceeds at a slower rate than during particle growth. (Guo & Sha 2002)

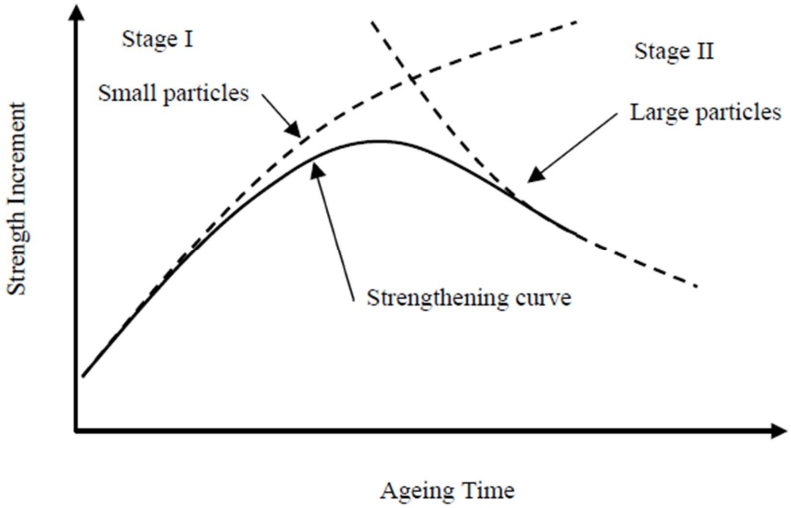

Figure 8 A typical one-peak precipitation-strengthening curve with two stages (Guo & Sha 2002).

Choi et al. (2016) have studied the effect of long-term thermal aging on the fusion boundary region between low-alloy steel and Alloy 152 weld metal with atom probe tomography (APT), which offers measurements at the atom scale. In their study the heat treatment in 400 °C and 450 °C simulated 15 and 30 years lifespan of a power plant system. The effects were an increase in the ratio of Cr constituents and Cr-rich precipitates and the formation and growth of $Cr_{23}C_6$. The mechanical properties of the fusion boundary region changed based on the distribution of Cr-rich precipitates. The material initially hardened with the formation of Cr-rich precipitates and then softened because of the reduction of residual strain or coarsening of Cr-rich precipitates. Hardening was equivalent to 15 years of service time and softening 30 years of service time. Hardening was explained by the coherent precipitates which resist the movement of dislocations in the material and are cut by dislocations. When softening, dislocations cannot cut sufficiently grown incoherent precipitates. Instead, they pass around the precipitate and leave dislocation loops around it. Thus, the strengthening effect becomes weaker than before. The Cr content of the fusion boundary tended to increase when the aging heat treatment time increased. This increase can be explained by the fact that thermal aging and a chemical gradient can provide a thermodynamic driving force and thus enhance the thermally activated diffusion of alloy constituents. The inward diffusion of alloy constituents such as Ni and Cr from Alloy 152 weld metal to low-alloy steel was thus increased (Guo & Sha 2002, Choi et al. 2016).

The formation and growth of precipitates occurs as a result of Cr being concentrated by the diffusion of Cr from the weld metal during heat treatment. The elemental change or diffusion within the weld metal is significant because of the relatively long diffusion length of Cr in the nickel-base alloy, which creates the uniform gradient within the weld metal. With the thermal aging treatment, the concentration of Cr is increased in both the weld metal near the fusion boundary and the fusion boundary region itself (Choi et al. 2015). Comparing the as-welded and aged conditions, the contribution of Cr in the precipitates is greater in the aged dissimilar metal weld, as compared to the as-welded, while Fe decreases in the HAZ of the aged dissimilar metal weld (Choi et al. 2013). In this work an

electron probe microanalyzer is used to study possible changes in the material's microstructure at the fusion boundary region due to thermal aging.

It is expected that the corrosion potential becomes larger in the fusion boundary region due to formation and growth of Cr precipitations in Fe-based matrix during thermal aging. This can increase galvanic corrosion by enlarging the difference between the corrosion potentials in the weld metal and fusion boundary region and within the fusion boundary region. The fusion boundary region initially has a lower corrosion resistance because the corrosion potential for the LAS is lower than the potential for the weld metal. In general, dissimilar metals have different corrosion potentials, and when two or more come into contact in an electrolyte, one metal acts as the anode and the other acts as the cathode. The electrochemical difference between dissimilar metals is the driving force for an accelerated attack on the anode metal of the galvanic couple. The anode metal dissolves into the electrolyte, and deposits collect on the cathodic metal. It appears that compared with the as-welded state, corrosion resistance in the fusion boundary region weakens. In the region containing the fusion boundary, the thermal treatment makes the elemental gradient sharper and induces the formation and growth of Cr precipitates in the fusion boundary region. The weakened corrosion resistance in the fusion boundary region can affect SCC (Choi et al. 2015).

2.3 Charpy-V test introduction

The Charpy-V impact test is still one of the most commonly used standard tests to evaluate fracture properties of materials. The test is quick and simple to perform. The test method is more than 100 years old (Wallin 2011). Originally, the Charpy-V test was used mainly as a quality control test. After World War II the analysis of the failures in welded merchant ships changed the nature of the Charpy-V test to more of a design tool, which led to the introduction of the transition temperature concept (Wallin et al. 2002). A typical Charpy-V test device and the equation for fracture energy, where W is the mass of pendulum, y_1 is the height at start and y_2 is the height at end, are presented in Figure 9.

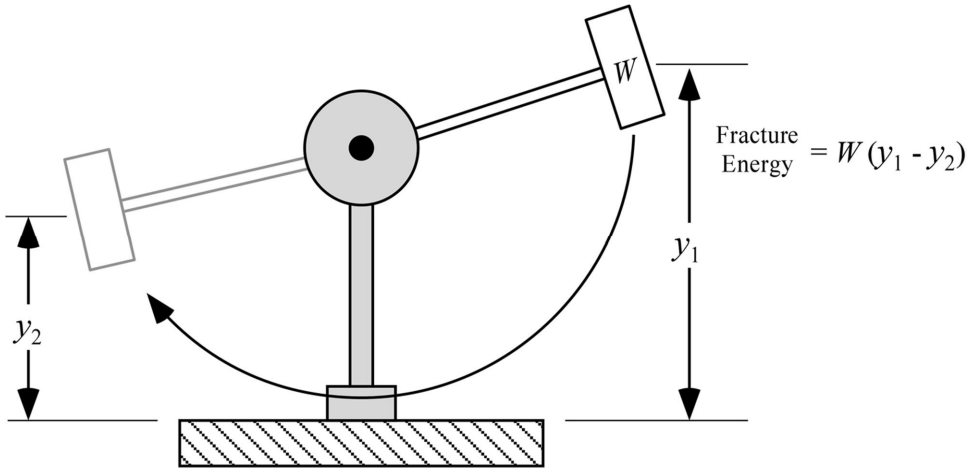

Figure 9 A typical pendulum device for Charpy-V testing and the equation for fracture energy (Anderson 1995).

The Charpy specimen is a notched beam that is impacted in three-point bending. The specimens are relatively small, and thus do not consume much material. The standard cross-section of specimens is 10 mm x 10 mm, and the length is 55 mm (Anderson 1995). The test procedure provides a relatively severe test of material toughness. The notched specimen is loaded at very high strain rates because the material must absorb the impact of falling pendulum (Hertzberg et al. 2013). The notch configuration is usually connected to material type. The V-notch is a typical choice for structural ferritic steels, which have a ductile-to-brittle transition behaviour, and the U-notch or keyhole are normally used for brittle materials such as cast irons, or tough materials such as austenitic stainless steels. (Wallin 2011)

Ductile behaviour indicates that crack propagation through the material consumes large amounts of energy and is characterized by plastic deformation. Brittle behaviour implies rapid crack propagation with low energy absorption and little plastic deformation. (EPRI 2002)

2.3.1 Impact energy

The main parameter determined in the impact test is the absorbed energy required to fracture the specimen. In the test, a certain potential energy, defined by mass of striker and height of fall, is effectively transformed into kinetic energy, part of which is used to fracture the test specimen with the remaining kinetic energy being transformed back to potential energy, defined by mass of striker and height of rise. The height difference of the striker between start and end of test gives the energy used to break the specimen. The only instrumentation needed is an angle transducer dial to give the beginning and the end test angles, from which the spent energy can be calculated when the length of arm and striker mass are known. (Wallin 2011)

For metals with body-centered cubic lattice structures the materials' toughness experiences a transition from brittle to ductile behaviour with increasing temperature. The temperature range, where this transition occurs, is called the ductile-to-brittle transition region (Wallin 2011). The lower the transition temperature is, the greater the fracture toughness of the material (François et al. 2013). Ductile-to-brittle transition curve behaviour for BCC, FCC and high-strength materials is shown in Figure 10. For many alloys there is a range of temperatures over which the ductile-to-brittle transition occurs. The range presents some difficulty in specifying a single ductile-to-brittle transition temperature. No explicit criterion has been established, and this temperature is often defined as a temperature at which the Charpy-V energy assumes a defined value. Structures constructed from alloys that exhibit this ductile-to-brittle behaviour should be used only at temperatures above the transition temperature to avoid brittle and possibly catastrophic failure (Callister & Rethwisch 2011). Absorbed energies 20/21 J and 27/28 J are common transition criteria (Wallin et al. 2002). The original values are for 20/21 J 15 ft-lb and for 27/28 J 20 ft-lb (Wallin 2011). Different countries use different values depending on if they round the value up or down. However, these values are quite low, and therefore, more suitable value is 41/42 J. In this work the applied value is 42 J.

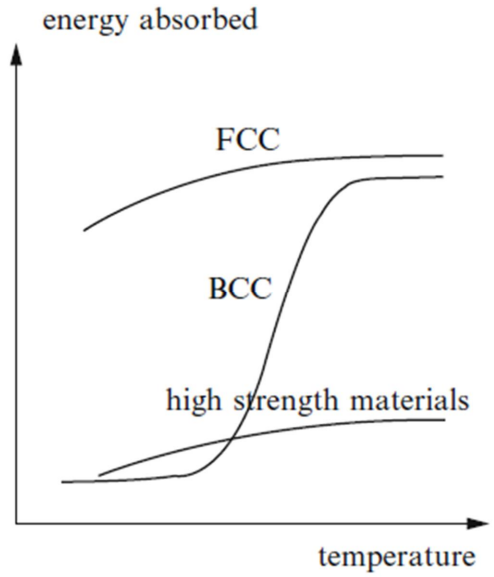

Figure 10 Ductile-to-brittle transition type curve behaviour for BCC, FCC and high-strength materials (François et al. 2013).

2.3.2 Fracture appearance

The fracture appearance (FA or SA) in a Charpy test is determined based on the proportional amount of ductile crack growth and shear fracture areas on the fracture surface. The FA is a sensible parameter only for metals that undergo a transition from cleavage fracture to ductile fracture with increasing temperature. It is thus mainly used for ferritic structural steels. The FA gives information as to where in the ductile-to-brittle transition region the test result is situated. A value close to 100 % indicates that the impact energy relates nearly to the upper shelf and an increase in temperature will not significantly change the test result. Fracture appearance values in the range 30 % to 60 % indicate that the test temperature is in the midrange of the transition region and the impact energy may be strongly dependent on even small temperature changes. In this work, the test temperature location with respect to the ductile-to-brittle transition region is 50 % which is a typical criterion (Wallin 2011, Wallin et al. 2002). The traditional way to determine the fracture appearance from the fracture surface is presented in EN ISO 148-1:2009 (2009) standard. This standard method is only used to roughly estimate the fracture appearance value.

2.3.3 Lateral expansion

Another Charpy parameter recognized in the test standards is the lateral expansion (LE). As the specimen is loaded in bending, the bottom part will be in compression and plastic deformation will cause the base of the specimen to widen. At the same time as the specimen expands laterally at the base, it also contracts laterally at the notch root. The LE gives a measure of the materials capacity to sustain deformation. Because lateral expansion is a result of plastic deformation, it depends on the strength of the material. The parameter shows similar transition behaviour as impact energy and fracture appearance for ferritic structural steels (Wallin 2011, Wallin et al. 2002). In this work, the lateral expansion

criterion used for specimen deformation with respect to the ductile-to-brittle transition region is 0.89 mm.

2.3.4 Physical aspects

One deficiency with the standard Charpy impact test is that it does not distinguish between different events related to the fracture process. Part of the absorbed energy goes into the initiation of fracture from the notch, part of the energy goes into the propagation of the crack, and part goes into the plastic deformation of the specimen. The part of the energy going into crack propagation is exceptionally complex since the propagation of the crack can occur either with a ductile or brittle micro-mechanism or a combination of both. (Wallin 2011)

The shear angle for ductile and brittle fracture differs from each other. For ductile fractures the angle is close to 45° and for brittle fractures 90°, respectively. In the combinations of brittle and ductile fractures the shear angle is between 45° and 90°.

2.3.5 Instrumented impact pendulum

When the impact pendulum is instrumented with strain gauges, it is possible to record the force vs. time signal during the test. By knowing the impact velocity and initially available energy, the time signal can be transformed into an estimate of the specimen displacement. The instrumentation allows the test to be analysed in much more detail. On the force-displacement curve (also load-deflection curve), four different force parameters can be identified. Figure 11 represents a schematic output of an instrumented impact test. The general yield force, F_{gy}, indicates the force at the beginning of general yield and it can be used to estimate the material's dynamic yield strength. The maximum force F_m corresponds to the maximum force. This value is partly descriptive of the material's dynamic flow stress, but it is also affected by the material's ductile tearing properties, because at this point some ductile crack growth has occurred. The force at onset of brittle fracture, F_u, indicates the moment of onset of brittle fracture and F_a indicates the force at end of brittle fracture or arrest properties. Based on these parameters it is possible to divide the impact energy into different regions. One can, e.g., only consider the energy up to F_u, limiting thus the information to the primary ductile crack growth region or one can examine the energy absorbed after brittle crack arrest. (Wallin 2011)

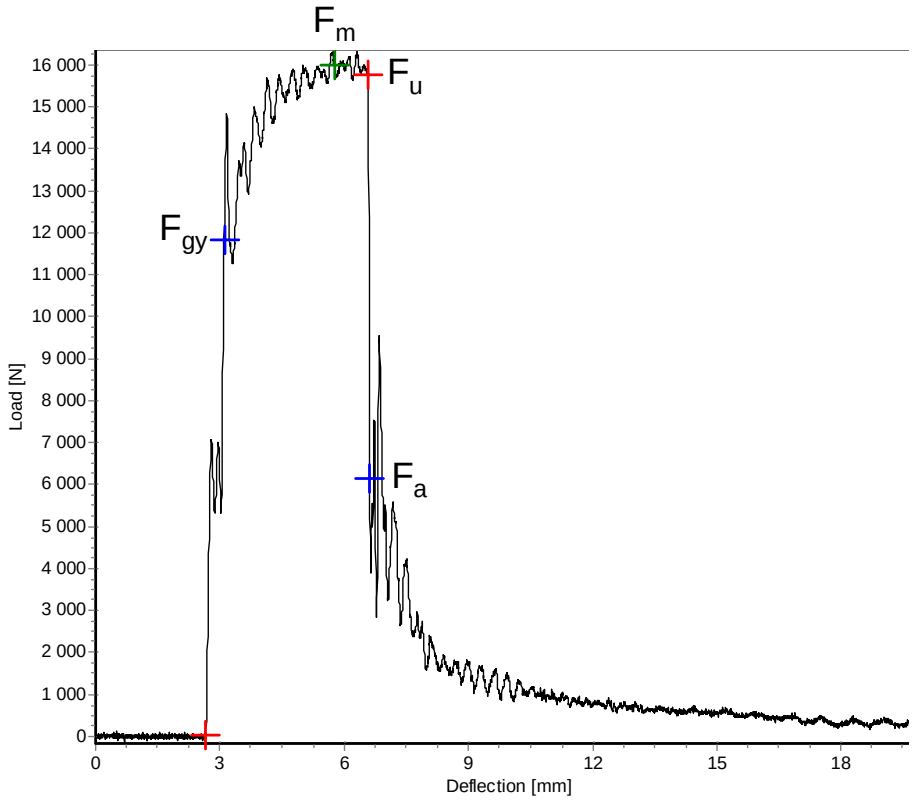

Figure 11 A load-deflection curve with basic force parameters identified in an instrumented impact test. The general yield force, F_{gy}, is marked with a blue cross, the maximum force, F_m, is marked with a green cross, the force at onset of brittle fracture, F_u, is marked with a red cross and the force at end of brittle fracture, F_a, is marked with another blue cross (Lydman 2017).

2.4 Microscopy

2.4.1 Scanning Electron Microscope introduction

Scanning electron microscopy analyses were carried out at VTT. SEM is a method for high-resolution imaging of surfaces. The SEM uses electrons for imaging. Various signals from the specimen can be collected and used to form images. Typical detection modes are Secondary Electron (SE) imaging and Backscattered Electron (BSE) imaging. Qualitative and quantitative chemical analysis information is also obtained using an energy dispersive X-ray spectrometer (EDS) with the SEM. (MEE 2016)

The SEM generates a beam of incident electrons in an electron column above the sample chamber. The electrons are produced by a thermal emission source, such as a heated tungsten filament, or by a tungsten field-emission tip or a Schottky emitter. The energy of the incident electrons can be as low as 100 eV or as high as 30 keV. The electrons are focused into a small beam by a series of electromagnetic lenses in the SEM column. Scanning coils near the end of the column direct and position the focused beam onto the sample surface. The electron beam is scanned in a raster pattern over the surface for

imaging. The beam can also be focused at a single point or scanned along a line for X-ray analysis. (Egerton 2005, MEE 2016)

To create SEM images, the incident electron beam is scanned in a raster pattern across the sample's surface. The emitted electrons are detected for each position in the scanned area by an electron detector. The intensity of the emitted electron signal is displayed as brightness on a display screen. The position in the image scan to that of the scan of the incident electron beam represents the morphology of the sample surface area scanned by the beam. Magnification of the image is the ratio of the image display size to the sample area scanned by the electron beam. The incident electrons cause electrons to be emitted from the sample due to elastic and inelastic scattering events within the sample's surface and near-surface material. High-energy electrons that are ejected by an elastic collision of an incident electron, typically with a sample atom's nucleus, are referred to as backscattered electrons. The energy of BSEs will be comparable to that of the incident electrons. Emitted lower-energy electrons resulting from inelastic scattering are called secondary electrons. SEs can be formed by collisions with the nucleus where substantial energy loss occurs or by the ejection of loosely bound electrons from the sample atoms. SEs provide higher spatial resolution images than BSEs. (Egerton 2005, MEE 2016)

2.4.2 Electron Probe Microanalyzer introduction

Electron probe microanalyzer analyses were carried out at Paul Scherrer Institute in Villigen, Switzerland (Lydman 2016). EPMA is a non-destructive method for determining the chemical composition of tiny amounts of solid materials down to concentration of a few hundreds of ppm. It measures quantitatively the elemental composition in a micro-area of a surface layer. EPMA is fundamentally the same as SEM, but EPMA is more capable when analysing chemical compositions with light elements and a big variety of elements (X-ray interferences). PSI's EPMA is half SEM and half EPMA. This means the machine is capable of taking high resolution SEM images and determining chemical compositions. The EPMA has been installed in a lead-shielded cabin of the laboratory and customized for remote control. The wave length dispersive X-ray spectrometers (WDS) have been additionally shielded against β- and γ-radiation (Restani & Wälchli 2011, Restani & Grabherr 2015). WDS is usually installed in EPMAs, not in SEMs or transmission electron microscopes (TEM) (Tanaka et al. 2008).

When the spectrometer is positioned on a peak of an element, the output pulses can be used for elemental mapping. Only one element can be mapped at a time per crystal. Using EDS, all of the energies of the characteristic X-rays incident on the detector are measured simultaneously and data acquisition is therefore very rapid across the entire spectrum. Comparing to EDS, WDS has considerably higher resolution (Oxford Instruments Analytical 2002). Elemental mapping is one of the principal advantages of X-ray analysis as it provides clear and direct information regarding the distribution of each element in the sample. (Tanaka et al. 2008).

EPMA uses a high-energy focused beam of electrons to generate X-rays characteristic of the elements within a sample from volumes as small as 0.5 to 10 μm^3 depending on the matrix and the high voltage beam. The resulting X-rays are diffracted by analysing crystals and counted using gas-flow and sealed proportional detectors. Chemical composition is

determined by comparing the intensity of X-rays from standards with those from unknown materials and correcting for the effects of X-ray generation, absorption and fluorescence in the sample (Northern Arizona University 2016, Lydman 2016). The wave length of the X-rays diffracted into the detector may be selected by varying the position of the analysing crystal with respect to the sample, according to Bragg's law:

$$n\lambda = 2d \sin\theta \qquad (2)$$

where n is an integer referring to the order of the reflection, λ is the wave length of the characteristic X-ray, d is the lattice spacing of the diffracting material, and θ is the angle between the X-ray and the diffractor's surface (Oxford Instruments Analytical 2002, Ul-Hamid et al. 2006). In WDS type of spectrometer, to maintain the correct geometrical relationship between specimen, the analysing crystal and detector for the full range of diffracted angles, it is necessary to maintain all three on the Rowland circle (Oxford Instruments Analytical 2002, Tanaka et al. 2008). There are two types of crystal geometry in use today: Johann geometry and more precise Johansson geometry which are shown in Figure 12 (Oxford Instruments Analytical 2002).

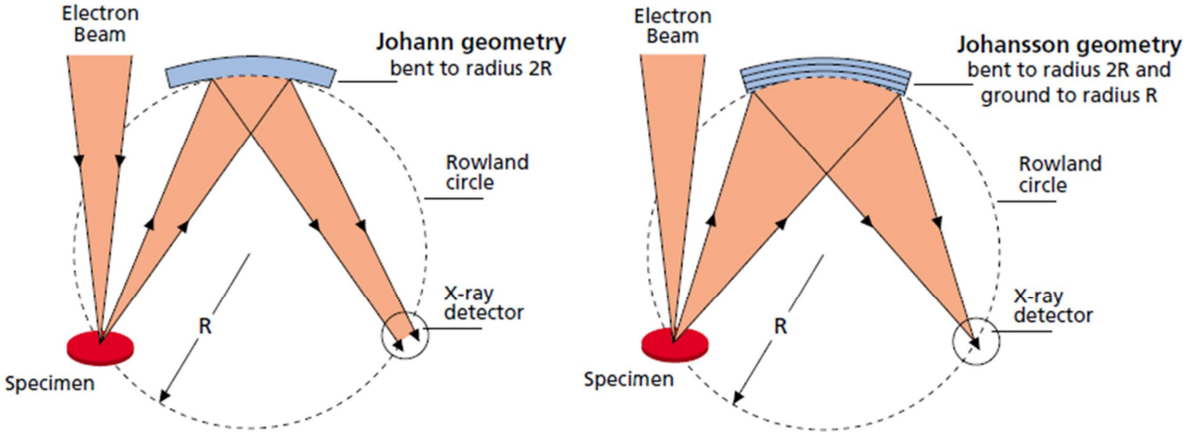

Figure 12 Johann and Johansson crystal geometries (Oxford Instruments Analytical 2002).

There are several different diffracting crystal types which all have different elemental and analysing range (Oxford Instruments Analytical 2002). The crystal types at PSI's EPMA are Thallium acid phthalate (TAP), Pentaerythritol (PET), Lithium fluoride (LiF), LD1 and LD2 (Lydman 2016).

The electron microprobe is designed specifically for detecting and measuring characteristic X-rays. It uses an electron beam current from 10 to 200 nA, roughly 1000 times greater than that in an SEM. These higher beam currents produce more X-rays from the sample and improve both the detection limits and accuracy of the resulting analysis. Analysis locations are selected using a reflected light optical microscope, which allows for accurate positioning up to about 1 µm, a feature not available with a traditional SEM. The resulting data provides quantitative chemical information in a textural context. (Northern Arizona University 2016)

3 Experimental

3.1 Test material

The test material is 1:1 scale narrow-gap weld mock-up representing the Olkiluoto 3 European Pressurized Water Reactor safe-end dissimilar metal weld. It has been manufactured by Mitsubishi Heavy Industries (MHI). Olkiluoto 3 EPR™ in Finland has a first of a kind safe-end design where the dissimilar metal joint is produced using narrow-gap welding with Alloy 52 filler metal without buttering (Ahonen et al. 2015b, Ahonen et al. 2016).

The material conditions are as-received, 5000 hours aged and 10000 hours aged and the step-cooling treatment. Each condition has been tested mechanically and fracture mechanically, including transverse tensile properties across the fusion line, Charpy-V impact toughness, fracture toughness according to ASTM E1921 (T_0), fracture resistance according to ASTM E1820 (J-R) and fatigue pre-crack located in SA 508 near the fusion boundary (Ahonen et al. 2015b). This work is focusing on Charpy-V impact toughness of as-received and 5000 hours aged conditions. Eighteen specimens for both conditions were machined.

The temperature of the thermal aging heat treatments was 400 °C. After welding, the welds were heat treated (200 °C - 310 °C / 2 hours minimum). After that a post-weld heat treatment was applied to the welds. The PWHT was performed two times: first at 550 °C for 20 hours, and then at 610 °C for 16 hours. The mock-up was thermally aged to accelerate the effects of thermal aging in a nuclear power plant operational condition (Ahonen et al. 2016, Joly et al. 2014, Yoo et al. 2015).

The section of the pipe mock-up delivered to VTT is shown in Figure 13. The inner radius of the mock-up is 920 mm, the thickness is 94 mm and the width is 65 mm. The mock-up was cut into four equal sections. Three of the sections were exposed to different environments and the fourth was characterized in the as-received condition. The treatments of the other three sections are 5000 hours aged, 10000 hours aged and the step-cooling treatment. Figure 14 shows the location of as-received condition specimens to be tested.

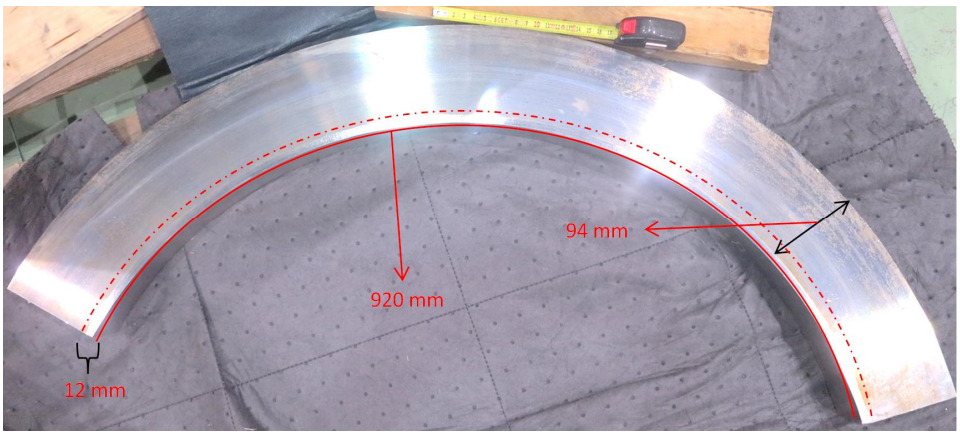

Figure 13 The section of the pipe mock-up with its dimensions, VTT.

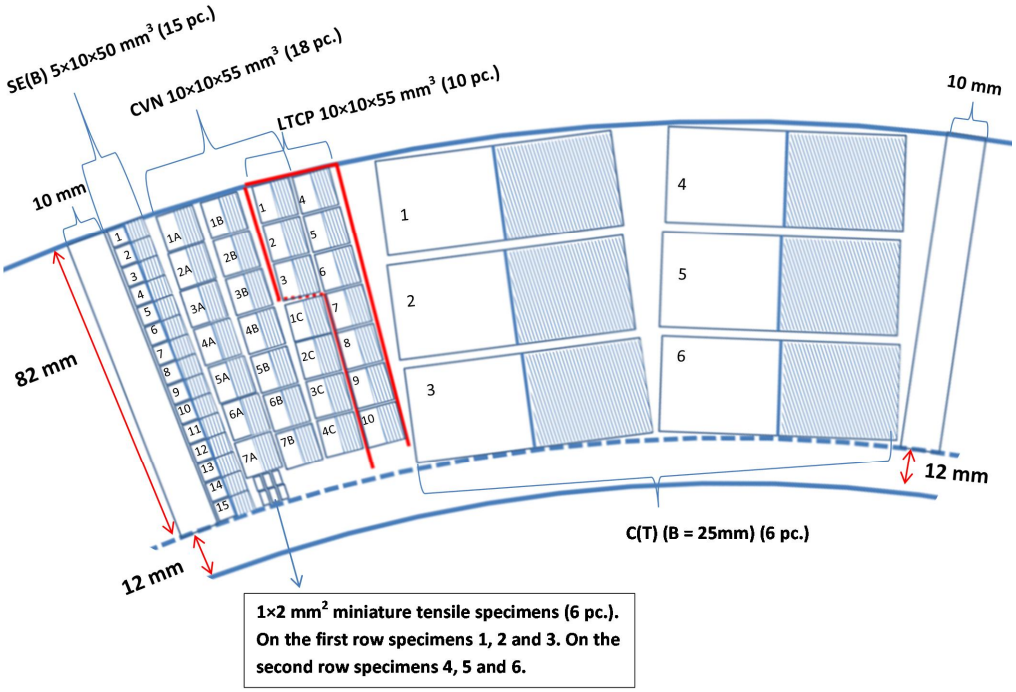

Figure 14 The location of as-received condition specimens, VTT.

Accelerated thermal aging at 400 °C was proposed, since it is based on segregation of phosphorus calculated with McLean model. The model is based on a theory of solute element segregation at grain boundaries and it predicts the quantity of solute in the grain boundary in equilibrium with the quantity of impurity in solution in the bulk of the grain. According to the model 10000 hours treatment at 400 °C covers the NPPs operation temperatures of 300 °C and 325 °C for 60 years. The P content of 0.0055 % and the grain boundary coverage of 0.065 were used in the McLean model, which is presented in the study of Druce et al. (1986) (Joly et al. 2014).

Another method to predict the NPPs service time is to use the Arrhenius equation, Equation 3 (Hertzberg et al. 2013), and calculate apparent activation energies:

$$Q = \frac{-R * \ln\left(\frac{t_1}{t_2}\right)}{\frac{1}{T_2} - \frac{1}{T_1}} \quad (3)$$

where Q is an activation energy, R is the gas constant, t_1 and t_2 are times for operation of NPPs and thermal aging and T_1 and T_2 are temperatures (K) corresponding t_1 and t_2. When placing 10000 hours aging time, 60 years operation time, 400 °C aging temperature and 325 °C operation temperature, the apparent activation energy is 177 kJ/mol. The activation energy of P diffusion in ferrite is 230 kJ/mol (temperature range 860 °C - 900 °C) (Bhadeshia & Honeycombe 2006), which means that the diffusion of P is the fastest aging controlling process in ferrite. If the activation energy of P is placed on Equation 3 instead of 177 kJ/mol, the operation time will be 198 years. The Arrhenius equation is only applicable if the same balance of reactions occurs at both the elevated accelerated aging temperatures and service temperature. If the degradation mechanisms change, the equation is not directly applicable. Also, laboratory experience over the last three decades indicates that lifetime predictions are usually not conservative, e.g. the Arrhenius approach often

over-predicts lower temperature lifetimes since the Arrhenius activation energy measured at high accelerated aging temperatures often decreases in the lower temperature extrapolation region (NRC 2013a).

3.2 Sample preparation and measurement

3.2.1 Sample preparation for Charpy-V test

Sample preparations and Charpy-V tests were performed at VTT (Lydman 2017). The specimens were machined by an electric discharge machine (EDM) at Aalto University in Espoo, Finland. The EDM, after machining, forms a thin oxide layer on the machined surface. The oxide layers were removed with hydrochloric acid solution of 50 % hydrochloric acid (HCl), 50 % water (H_2O) and hexamethylenetetramine ($C_6H_{12}N_4$). The orientation of the low-alloy steel side of specimens is transversal-longitudinal (T-L) where the crack growth is in L-direction according to ASTM E1823-13 (2013).

One side of each specimen was ground with Federation of European Producers of Abrasives (FEPA) grit 1200 (SiC) sand paper. After that the specimens were polished with DiaPro Mol 3 diamond suspension and MD-Mol polishing surface. The grinding and polishing machine was Struers™ LaboPol-21. Etax Ba technical ethanol was used to wet the polishing surface at first and to clean the specimens after polishing.

The specimens were etched with 3 % Nital which includes 3 % nitric acid (HNO_3) and 97 % Etax Ba technical ethanol. Etching time was 5 seconds per specimen. Etching with Nital reveals only the microstructure of low-alloy steel which makes it easy to identify the location of V-notches.

V-notches were photographed to see their exact location. Photographs were taken with Leica MZ12 stereo microscope and Leica DFC420 camera. Overview reprography images of the specimens were taken with Olympus E-30 camera (Appendix 1).

Before testing all the specimens were inspected visually. The following specimen dimensions (for tolerances see Appendix 2) were measured: transverse dimensions (b and w) and specimen length (l), ligament size, radius of curvature of the notch base (from photographs), the angle of V-notch (from photographs) and the distance from the notch to end piece. Dimensions were measured with Mahr MarCal 16EW caliper, Heidenhain VRZ 404 and Leica MZ12 stereo microscope and Leica DFC420 camera. The transverse dimensions were used for scaling the photographs of the fracture surfaces when measuring the percentage of ductile fracture area. The ligament size was measured from the notch bottom to the back face with a dial gauge. The notch base radius and angle of each specimen were measured optically with a mock-up, Figure 15. According to the measurements all dimensions are not within the tolerances specified in EN ISO 148-3:2009 (2009) standard. Five specimens from 5000 hours aged condition did not meet the standard's tolerances. Notches in these specimens were not exactly in the middle of the specimen and, therefore the distance from the notch to end piece was out of tolerance. This was considered when testing these specimens and they have been tested at low temperatures to avoid premature release of contact of the shorter specimen half in the support anvil. No defects were observed in the specimens.

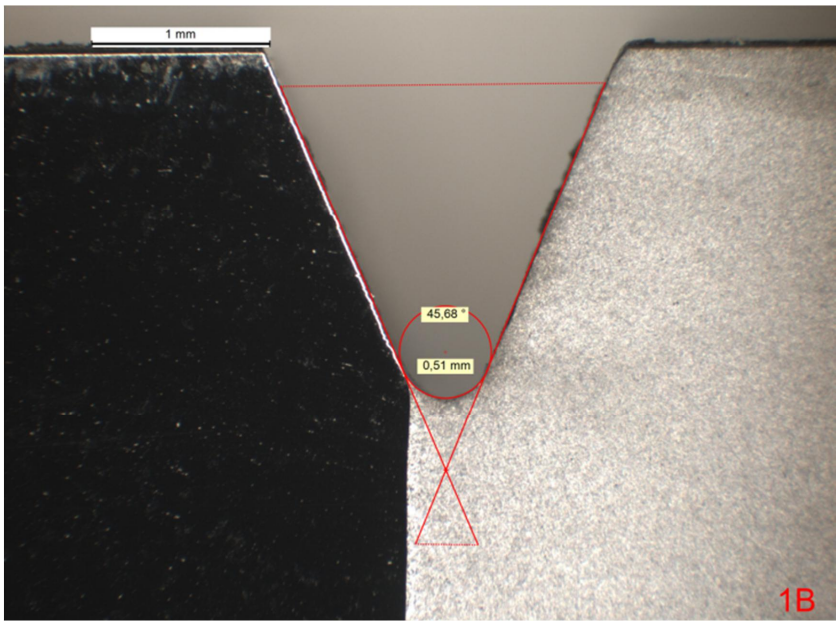

Figure 15 Measurement of notch root radius, which is a diameter divided by 2, and angle. Ni-base alloy is on the left and LAS on the right (Lydman 2017).

3.2.2 Sample preparation for EPMA

The as-received sample was prepared and analysed at PSI. The tested specimen 5A was cut in smaller piece longitudinally with a Buehler's IsoMet® diamond blade cutter. Longitudinal cut makes it possible to examine elemental distribution and composition over the heat-affected zone, fusion line and weld metal near fusion line. The thickness of the cut slice was around 2 mm. The slice was embedded in a Struers™ epoxy resin and after that it was ready for grinding and polishing. A tested Charpy-V specimen half is presented in Figure 16. The specimen's length, l, is 27.5 mm, width, w, and height, b, are 10 mm. The red line shows where the cut was made.

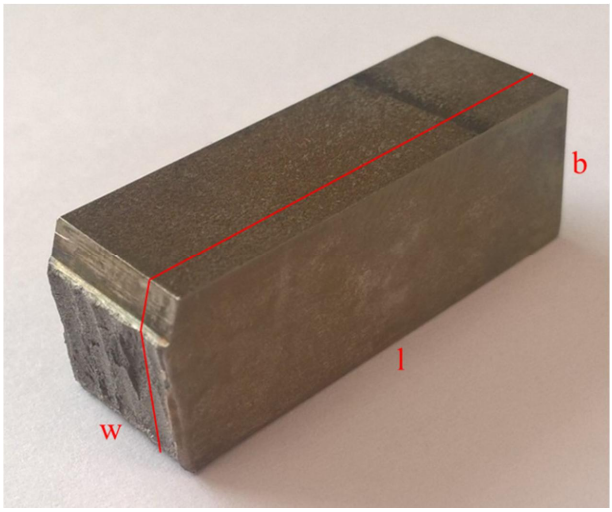

Figure 16 A tested Charpy-V specimen half, the red line shows the location of the cut.

EPMA analyses require a high quality surface finish. The sample was first ground to FEPA grit 4000 (SiC) sand paper and then polished manually with a Struers™ DiaPro Nap B 1 micron diamond suspension and MD-Nap polishing surface. The embedded sample was coated with carbon to make it electrically conductive, Figure 17. The diameter of the embedded sample is 2.54 cm.

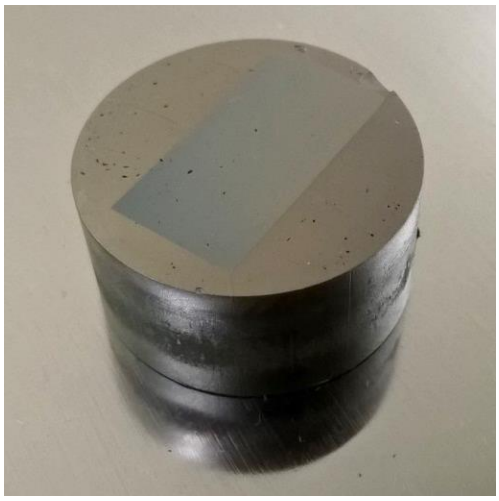

Figure 17 The carbon-coated sample (Lydman 2016).

The 5000 hours aged sample was prepared at VTT and analysed at PSI. The sample was taken from a part which was between two Charpy-V specimens. After embedding a basic grinding and polishing procedure, similar to that described above, was used. The final polishing was carried out manually with a Struers™ DiaPro Nap ¼ micron diamond suspension and MD-Nap polishing surface.

3.2.3 Sample preparation for optical microscopy

The samples, which were analysed at PSI, were also examined with optical microscopy at VTT's metallography laboratory afterwards. The samples were re-polished manually to remove the carbon coating using a Struers™ DiaPro Nap ¼ micron diamond suspension and MD-Nap polishing surface.

Nickel-base alloy side of the samples was etched with Aqua regia which is a mixture of 60 % glycerol $C_3H_5(OH)_3$, 20 % HNO_3 and 20 % HCl. Etching time was approximately 15 seconds.

The samples, which were examined at Aalto University, followed the same grinding, polishing and etching procedure.

Cross-section samples of the tested specimens, which were examined at VTT's optical microscope and SEM, were prepared with the same procedure.

3.3 Testing and analysis methods

The instrumented impact pendulum is PSW300 with the nominal impact energy of 300 J and the impact velocity of 5.43 m/s according to EN ISO 148-1:2009 (2009), ASTM E2298-13a (2013) and VTT Work instruction (2015). The pendulum is equipped with a digital angle encoder having the angle counting resolution of 160 000 pulses / 360 degrees. An ISO/DIN geometry impact striker (2 mm striker) was used in the pendulum and a static load calibration of the striker was performed before testing, following the yearly calibration programme of the striker. The loss of free swing is 0.7 J and it remains stable. This value is not subtracted from the measured pendulum energy values. The software is Charpy test program, Version 1.0.17, 27.09.2012. The pictures of fracture surfaces were taken with Nikon Digital Sight DS-Fi1 camera. Fracture appearances were measured with Crack front measurement software, Version 2.1.19, 1.10.2008. Lateral expansions were measured with Heidenhain VRZ 404.

The specimens were cooled or heated in a well-agitated liquid bath using the normal installation for instrumented Charpy testing. Depending on the test temperature either petrol ether ($T < -80$ °C), ethanol (-80 °C $< T < +70$ °C) or silicon oil ($T > +70$ °C) is used as the heating or cooling medium. The bath temperature is measured with a calibrated thermocouple and adjusted with a PDI-controller. The bath is heated electrically or cooled by circulating liquid nitrogen through a coil installed in the bath. The bath temperature is continuously monitored and recorded during the cooling and heating phases. The minimum specimen hold time at a stable temperature in a liquid bath is 5 minutes, according to EN ISO 148-1:2009 (2009). Temperatures were measured with a Fluke 52 II thermometer and K type SAB thermocouple.

The specimen was then transferred from the tempering bath into the pendulum anvil using a pneumatic equipment. This equipment grips the specimen from the V-notch and guides the notch to the correct position from the anvil support. The proper location of the impact is checked after each test from the specimen halves by setting the V-notch surfaces side by side and by checking the equality of the anvil marks on the specimen's front surfaces.

3.3.1 Determination of KV_2, LE and FA

Absorbed energy is calculated from the initial and final pendulum angles measured by the angle encoder and from the pendulum parameters. Lateral expansion is measured in a stand, where the broken specimen halves are pressed against a common support surface on a position outside the lateral expansion area of the specimen. Special care is taken to ensure that no specimen damage (collision marks etc.) is disturbing the measurement. The percentage of fracture appearance is measured from the image of fracture surface. Specimen transverse dimensions (b and w) are used for scaling the fracture appearance measurements. The difference between the shear (ductile) and brittle type fracture cannot always be differentiated clearly by visual observation. In such cases the measured load-deflection curves may be used for guidance.

3.3.2 Analysis of data for transition temperatures

Impact toughness is characterized in terms of the mean KV_2, LE and FA vs. temperature curves estimated from the test data. The curves, X = f(T), were determined by fitting the least squares function of the form:

$$X = 0.5 * X_{US} * (1 + \tanh\left(\frac{T-T_{50}}{C}\right)) \quad (4)$$

where X_{US} is the upper shelf value for X (KV_2, LE or FA), T is temperature and T_{50} and C are fitting parameters.

The upper shelf value (Equation 4) used in data analyses (X vs. T -curves) is normally fixed to the average of values showing fully ductile fracture appearance (FA = 100 %). For the test series analysed here the upper shelf energy is fixed based on only one or an evaluated upper shelf value. The lower shelf value is assumed to be zero. Load as a function of time is measured by the instrumented striker and the load as a function of deflection is calculated from this data.

Load measurement is triggered much before the striker contacts the specimen and measuring continues far beyond specimen fracture. Hence, a zero level of load is measured both before and after the impact. Integration in the above equations is continued up to a deflection value of 30 mm. The load level returns after the fracture quite well to the zero level and hence the impact energy calculated from the load deflection graphs does not depend on the end point of the integration.

The characteristic load points, i.e. the general yield load F_{gy}, the maximum load F_m, the onset of unstable crack propagation F_u and the crack arrest load F_a are determined from the load-deflection curves. The load signal consists of a quasi-static load signal and a signal due to combined vibration of the striker and the specimen. In addition to the characteristic load signals also the respective deflection value is determined.

3.3.3 Analysis of data for temperature T_{Fa4kN}

The transition criteria based on absorbed energy characterize both crack initiation and propagation, their relative proportion depending on temperature, i.e. the position in the transition range. In the instrumented Charpy-V test, the load vs. time response is recorded during the test, which produces information not only on the general yielding and initiation of brittle fracture, but also on crack arrest after the brittle fracture initiation. The portion of the load vs. time (or deflection) record, indicating brittle fracture initiation and arrest, can easily be located on the graph and is indicated by a rapid load drop, during the test, before the final (ductile) fracture. This is shown in Figure 11 where F_u represents brittle initiation and F_a represents brittle arrest. Utilising this information from tests made at various temperatures it is often possible to construct the mean crack arrest load vs. temperature curve for the material. (Wallin 2011)

To compare the crack initiation and arrest properties in terms of the fracture toughness transition temperature, T_0, the Charpy transition temperature based on a suitable criterion shall first be converted to the consistent value of T_0 using a correlation, which for the 28 J Charpy -transition temperature, T_{28J}, is as follows (ASTM E1921-13a 2013):

$$T_0 = T_{28J} - 18℃ \quad (5)$$

where T_0 (°C) is the temperature corresponding to K_{Jc} (MPa√m) equal to 100 MPa√m.

The comparable crack arrest transition temperature T_{KIa} (100 MPa√m) can be estimated from a correlation found to exist between this temperature and that corresponding to the 4 kN crack arrest load determined by instrumented Charpy tests. Crack arrest toughness, in the case of structural metals, is in practise limited to ferritic structural steels. If only a qualitative structural toughness is required, then the simple transition temperature tests may be sufficient, but for a real structural integrity assessment, a quantitative estimate of the crack arrest toughness is needed (Wallin 2011). Mechanically, arrest occurs when the local crack driving force at the crack tip decreases below the local arrest toughness over a sufficiently large portion of the crack front (Wallin et al. 2002). The original data base, including irradiated and un-irradiated steels, shows the following correspondence:

$$T_{KIa} = T_{Fa4kN} + 11.4℃ \quad (6)$$

where T_{Fa4kN} is the temperature corresponding to the mean crack arrest load of 4 kN. Transition temperature T_{Fa4kN} is determined from the least squares fit by Equation 7 (Wallin 2011):

$$F_a = 4kN * \exp\left(\frac{T - T_{Fa4kN}}{A}\right) \quad (7)$$

where F_a (kN) is crack arrest load, T is temperature and T_{Fa4kN} and A are fitting parameters. For structural steels, the maximum force in a Charpy-V test is usually in the range 13 - 20 kN, depending on upper shelf toughness and strength of the material. Since the load bearing capacity of a bend specimen is approximately related to the square of the ligament, a crack jump through half of the ligament corresponds approximately to a drop in force to a quarter of the initial value. Thus, F_a = 4 kN corresponds roughly to a crack jump through half of the ligament (Wallin 2011). The 4 kN crack arrest load temperature is a true measure of the materials crack arrest properties (Wallin et al. 2002). If the specimen has deformed significantly between the load maximum and the onset of unstable crack extension, the load-deflection data may not be valid for crack arrest characterization. Hence, relevant data points for this purpose were limited to those where

$$\frac{F_u}{F_m} > 0.7 \quad (8)$$

where F_u is the load at the onset of unstable crack extension and F_m is the maximum load. (Wallin 2011)

The determination of T_{Fa4kN} can sometimes be difficult because of limited data. Also, if the crack arrest toughness is very far from the brittle initiation fracture toughness, the Charpy-V specimen may reach upper shelf before reaching F_a = 4 kN. (Wallin 2011)

3.3.4 Conditions for EPMA analysis

The EPMA at PSI is a shielded JEOL 8500F with field emission gun (FEG-EPMA) and four wave length dispersive spectrometers.

Conditions used for the analysis were:
Beam current for as-received condition: 280 nA (±0.5 nA, measured after each point)
Beam current for 5000 aged condition: 256 nA - 260 nA (±0.5 nA)

High voltage electron beam: 15 kV
Beam diameter for mappings: 0.2 µm
Beam diameter for line scanning: 2 µm
Measurement time: line scan per point: typically 20 s peak and 20 s background
Stage mapping: 40 ms or 45 ms per pixel (200 px x 200 px (100 µm x 100 µm) / 400 px x 400 px (200 µm x 200 µm) / 400 px x 800 px (200 µm x 400 µm)) 0.5 µm stage step size

Elements:
Spectrometer (SP)1, Crystal TAP/LD2: Al (Kα), C (Kα), Si (Kα)
SP2, Crystal LiF: Cr (Kα), Mn (Kα), Fe (Kα)
SP3, Crystal LiF: Ni (Kα), Ti (Kα), S (Kα)
SP3, Crystal PET: Mo (Lα)
SP4, Crystal TAP/LD1: O (Kα)

3.4 Aim of the study

The aim of the work is to study the effects of thermal aging on the material's impact toughness properties and microstructure. Instrumented Charpy-V testing is carried out in order to determine the impact toughness properties of the HAZ. Fractographic examinations are performed to get information on the crack paths and fracture surfaces, which support the research of the degradation mechanism and to study, which zone is the weakest and the most susceptible to brittle fracture. EPMA is used to see possible changes in the microstructure, such as diffusion of main elements of DMW, segregation and carbide growth. This study is a part of a larger project.

The evidences of degradation mechanism of thermal aging are studied, which may or may not be seen after 5000 hours aging time. It has been recognized that a number of processes can lead to the embrittlement of RPV steels subject to long-term service at elevated temperatures. Such processes are segregation of P to grain boundaries leading to a lower intergranular fracture stress, segregation of impurities to dislocations leading to strain aging, growth of inclusions and/or precipitates, which act as nucleation sites for fracture, widening of carbon-depleted zone and possible grain growth. Joly et al. (2014) proposed that in the case of AREVA's mock-up, which is of the same type as VTT's mock-up (different manufacturer), the degradation mechanism of the HAZ could be segregation of P, which was observed after 10000 hours thermal aging as an intergranular fracture. Therefore, it is predicted that segregation of P will be the degradation mechanism also in this work, which would result in an increase of the transition temperature.

4 Results

4.1 Microstructure

Optical microscopy images were taken at Aalto University using Nikon Epiphot 200 microscope. The microstructure of the tested material in the as-received and 5000 hours aged conditions was characterized. An overview of the as-received condition SA 508 low-alloy steel base metal and SA 508 heat-affected zone and magnifications of SA 508 base metal, partially grain-refined SA 508 heat-affected zone, grain-refined SA 508 heat-affected zone, grain-coarsened SA 508 heat-affected zone and carbon-depleted zone are shown in Figure 18. The heat-affected zone is approximately 2 mm wide. The uneven etching in the HAZ is obviously due to differences in the chemical composition, e.g. carbon content. The appearance is typical of low-alloy steel with segregation bands. The banded appearance is similar also in the HAZ, with the difference that the general appearance is darker.

An overview of as-received condition Alloy 52 weld metal, fusion line, martensitic layer, partially-melted zone (PMZ), a discontinuous Type II boundary in Alloy 52 weld metal and LAS swirls in the Alloy 52 weld metal are shown in Figure 19. Low-alloy steel swirls can be seen inside the weld metal at the start of weld passes. A partially-melted zone and thin martensitic layer occur at the start of weld passes. Weld metal exhibits columnar dendritic microstructure typical of Alloy 52. Some of the grains are very large and elongated having lengths of several millimetres and the largest ones extend through multiple weld beads.

An overview of the as-received condition SA 508 low-alloy steel base metal and SA 508 heat-affected zone with hardness measurement indentations and magnifications of SA 508 base metal, partially grain-refined SA 508 heat-affected zone, grain-refined SA 508 heat-affected zone, grain-coarsened SA 508 heat-affected zone and carbon-depleted zone are shown in Figure 20.

An overview of as-received condition Alloy 52 weld metal, fusion line, migrated grain boundaries, a Type II boundary in Alloy 52 weld metal and LAS swirls in the Alloy 52 weld metal are shown in Figure 21.

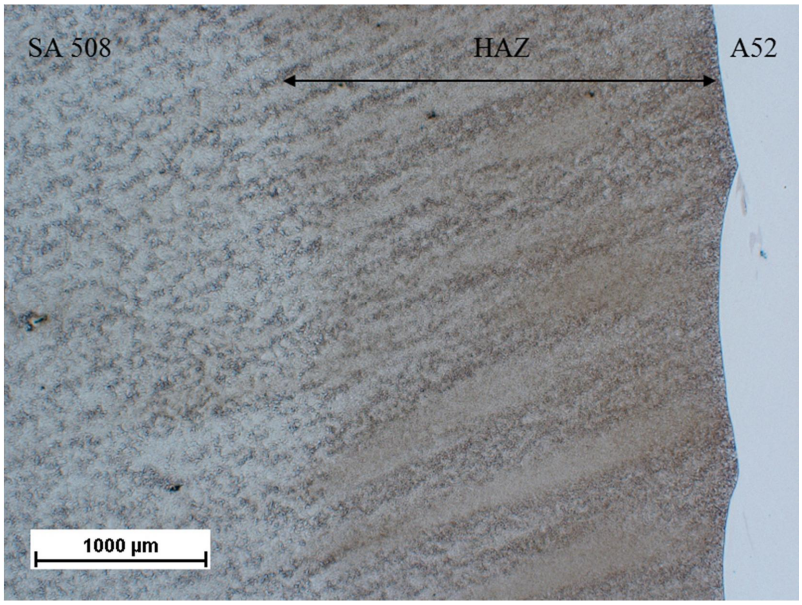

SA 508 base metal, SA 508 HAZ and Alloy 52 weld metal, 2.5x

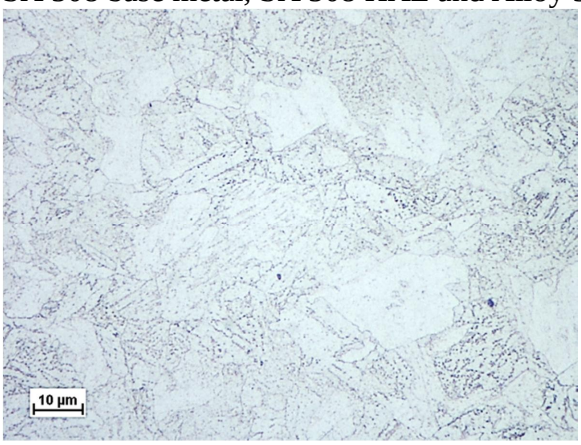

SA 508 base metal, 100x

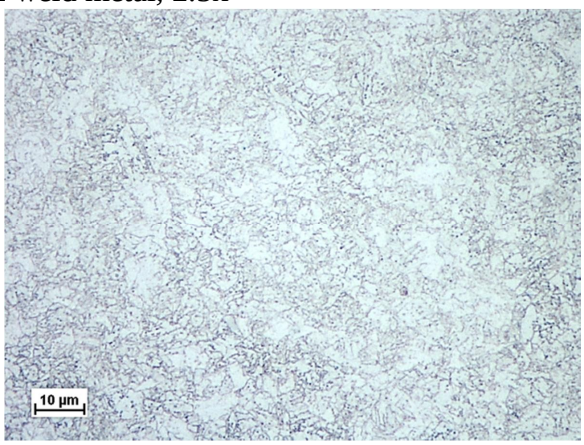

Partially grain-refined SA 508 HAZ, 100x

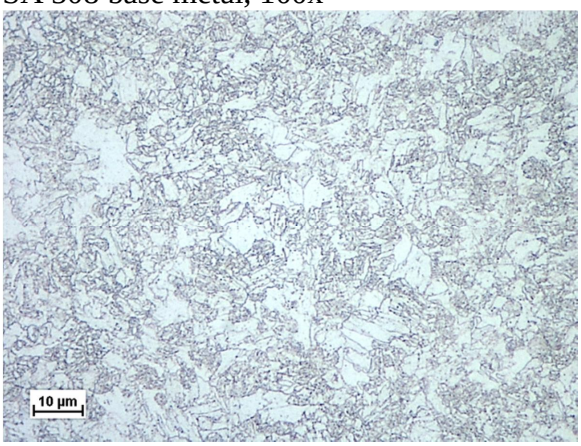

Grain-refined SA 508 HAZ, 100x

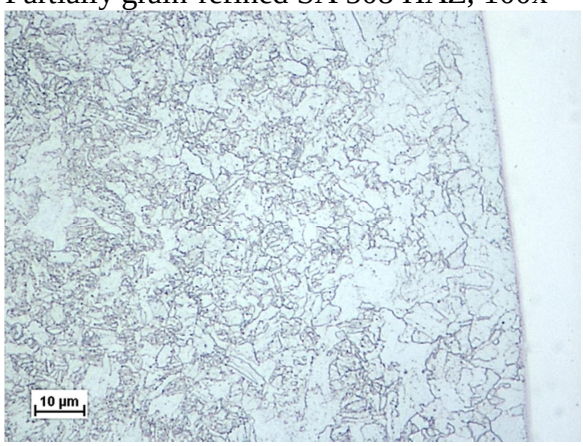

Grain-coarsened SA 508 HAZ and CDZ, 100x

Figure 18 An overview of SA 508 and SA 508 HAZ , SA 508 base metal, partially grain-refined SA 508 HAZ, grain-refined SA 508 HAZ, grain-coarsened SA 508 HAZ and CDZ, as-received condition, magnifications 2.5x and 100x. Mouginot, R., Sarikka, T., Aalto University.

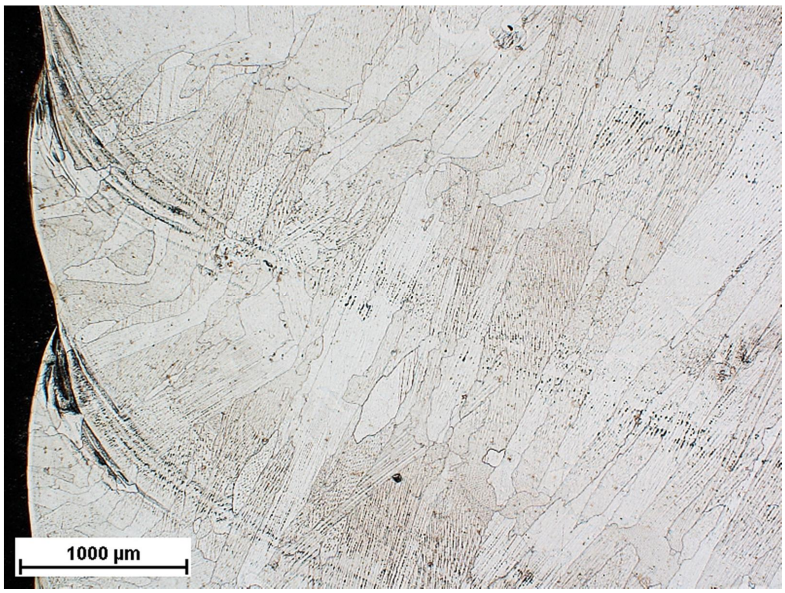

Alloy 52 weld metal, 2.5x

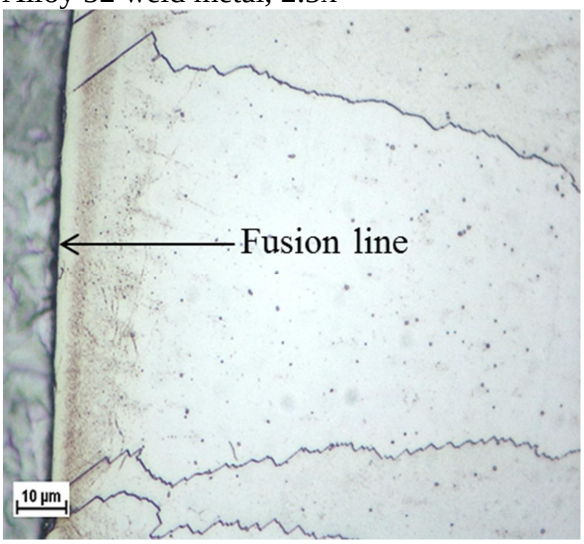

Fusion line and Alloy 52 weld metal, 100x

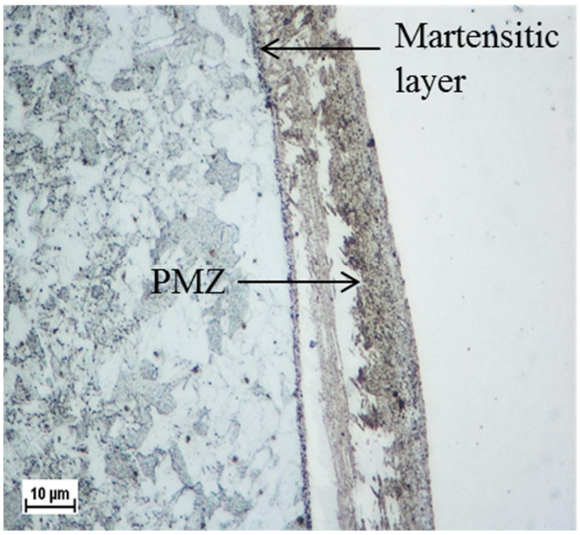

Martensitic layer and PMZ, 100x

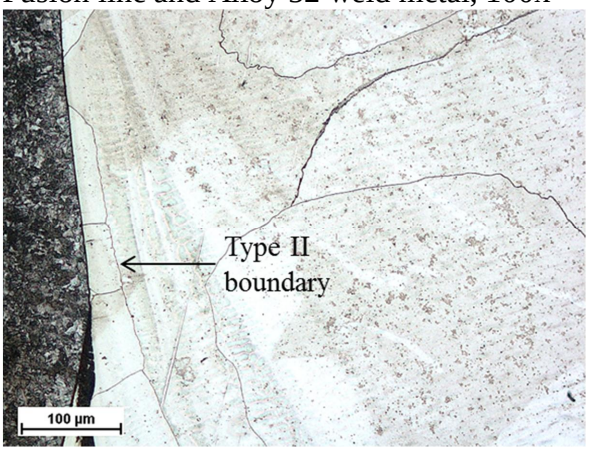

Type II boundary in A52 weld metal, 20x

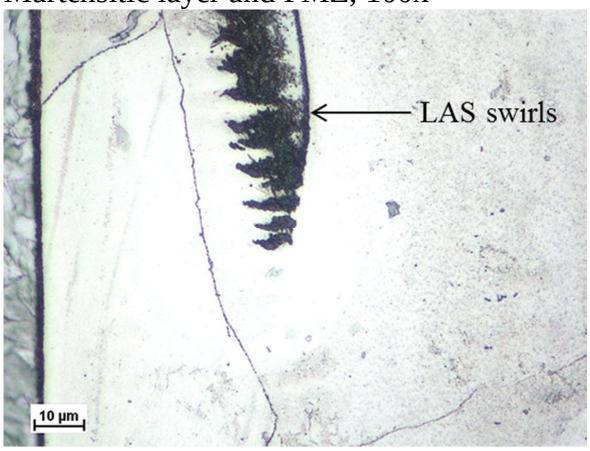

LAS swirls in Alloy 52 weld metal, 100x

Figure 19 An overview of Alloy 52 weld metal, fusion line, martensitic layer, PMZ, Type II boundary in Alloy 52 weld metal and LAS swirls in Alloy 52 weld metal, as-received condition, magnifications 2.5x, 20x and 100x. Mouginot, R., Sarikka, T., Aalto University.

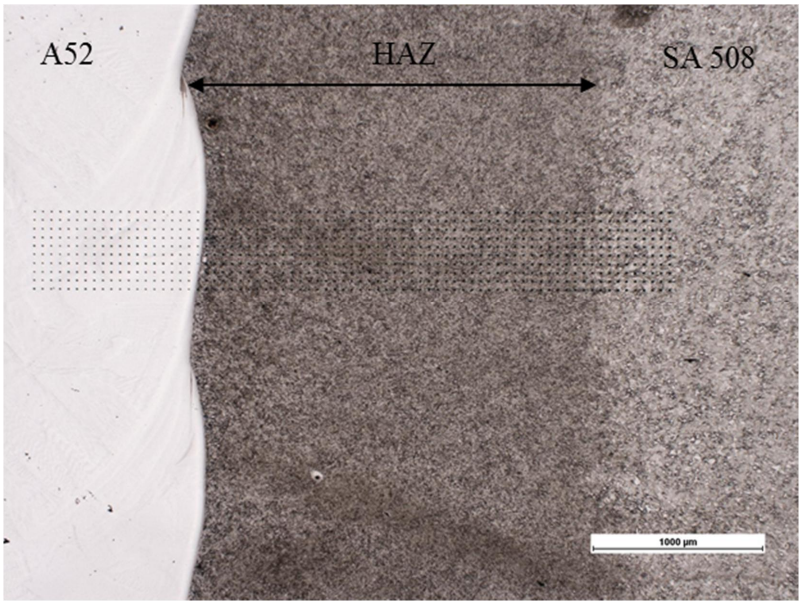

SA 508 base metal, SA 508 HAZ and Alloy 52 weld metal, 2.5x

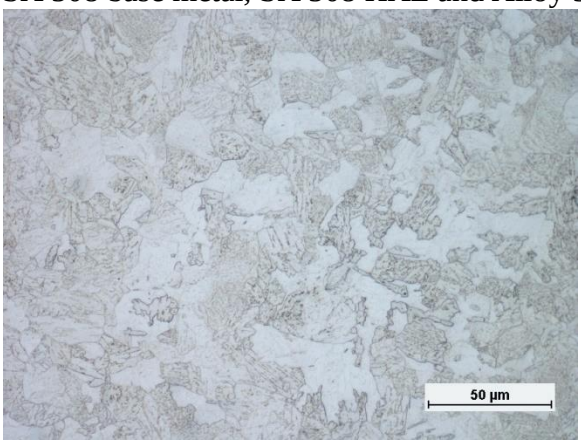

SA 508 base metal, 50x

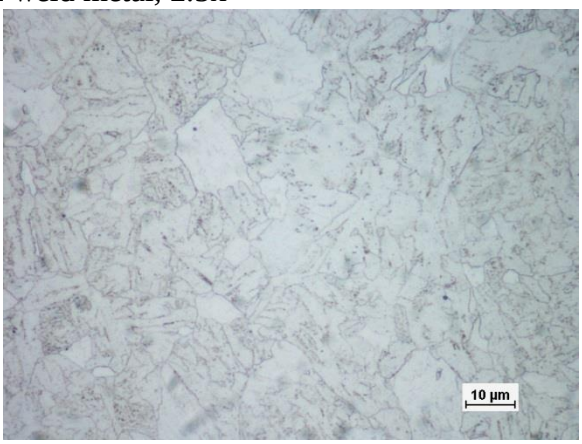

Partially grain-refined SA 508 HAZ, 100x

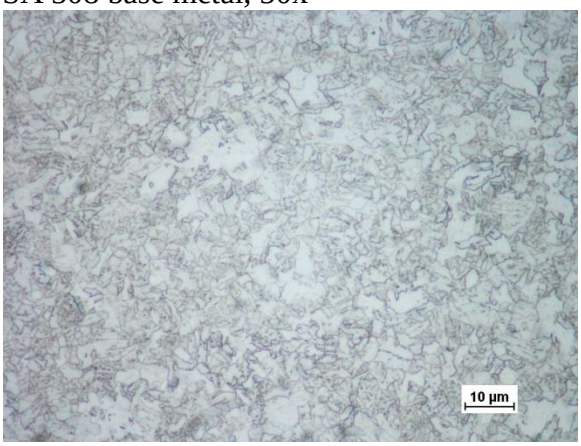

Grain-refined SA 508 HAZ, 100x

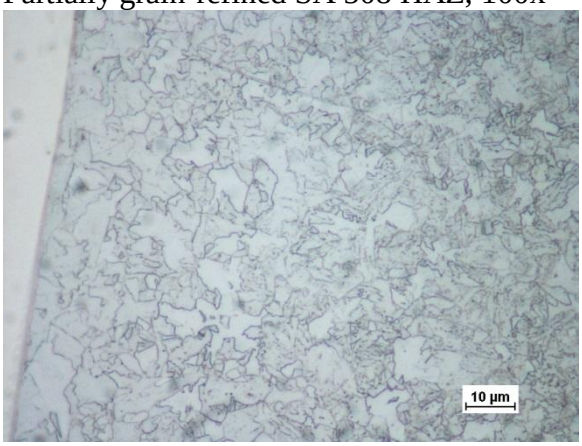

Grain-coarsened SA 508 HAZ and CDZ, 100x

Figure 20 An overview of SA 508 and SA 508 HAZ with hardness measurement indentations, SA 508 base metal, partially grain-refined SA 508 HAZ, grain-refined SA 508 HAZ, grain-coarsened SA 508 HAZ and CDZ, 5000 hours aged condition, magnifications 2.5x, 50x and 100x. Mouginot, R., Sarikka, T., Aalto University.

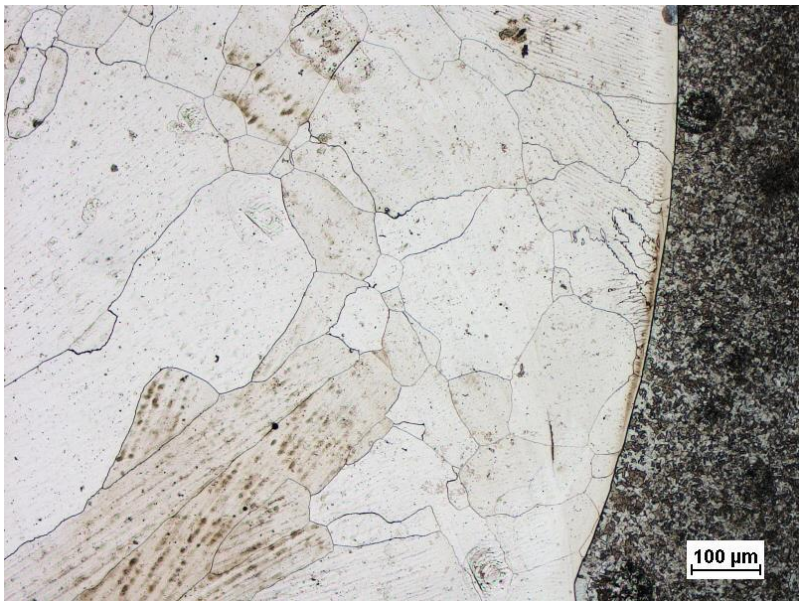

Alloy 52 weld metal, 10x

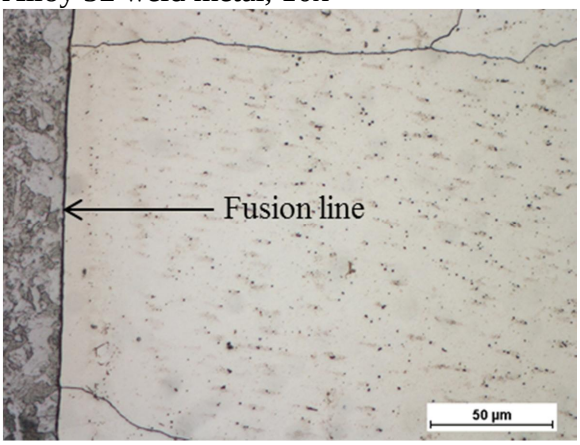

Fusion line and Alloy 52 weld metal, 50x

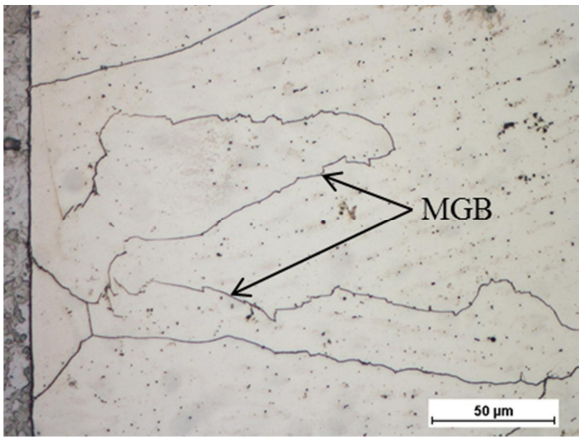

MGBs in Alloy 52 weld metal, 50x

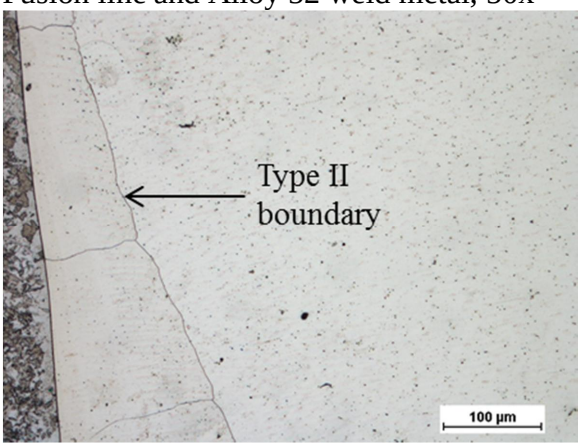

Type II boundary in Alloy 52 weld metal, 20x

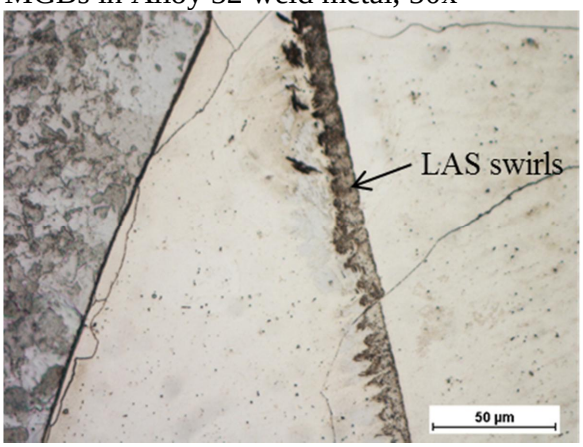

LAS swirls in Alloy 52 weld metal, 50x

Figure 21 An overview of Alloy 52 weld metal, fusion line, MGBs, Type II boundary in Alloy 52 weld metal and LAS swirls in Alloy 52 weld metal, 5000 hours aged condition, magnifications 10x, 20x and 50x. Mouginot, R., Sarikka, T., Aalto University.

4.2 Crack path examination

Several cross-section samples from tested Charpy-V specimen halves were examined with SEM and optical microscope. The SEM at VTT is a Zeiss Gemini 1 with field emission gun (FEG-SEM) and an energy dispersive X-ray spectroscopy detector. The optical microscope at VTT is Leica MEF4M. The purpose was to examine which zone of the HAZ is the weakest where the crack paths are located.

Crack paths of the specimens, which are located in transition region or lower shelf in the transition curve, follow the similar behaviour in both tested conditions. The distance of crack paths of as-received condition from the fusion line is most of the time from a few microns up to 20 µm. This is true with all brittle fracture specimens. It is possible that the crack path can propagate further away from the fusion line, up to 100 µm, but then the fracture mechanism is ductile, which can be seen in deformation of microstructure. The brittle crack paths of 5000 hours aged condition are similar to as-received condition, but can be located up to 40 µm away from fusion line. The width of carbon-depleted zone in the as-received condition is 35-40 µm and in the 5000 hours aged condition 60-70 µm. The brittle crack path is located in the carbon-depleted zone of HAZ and this zone is the weakest and the most susceptible to brittle fracture in the material. The fracture near the V-notch root showed some ductility even in brittle fractures, but the crack path propagates towards fusion line rapidly. Crack paths of the specimens, which showed more ductility, propagate most of the time close to the fusion line in the CDZ. The distances from the fusion line are almost the same as in the brittle specimens. In the case of ductile fracture, the crack path may propagate further in the HAZ, even up to 200 µm away from the fusion line. If the specimen shows significant ductility and there is a welding defect at the fusion line, the crack path can propagate locally to the weld metal. This means that the whole crack front does not propagate to the weld metal, but only a part of it.

The crack paths are presented in Appendix 6. The SEM images include six specimens from the as-received and 5000 hours aged conditions. In the images the HAZ with visible grain structure is on the top and the weld metal below.

4.3 Wave length dispersive X-ray spectroscopy examination

4.3.1 Elemental mappings of as-received condition

WDS analyses were performed on the as-received material. Since EPMA is not a very common research tool, these elemental mappings are more unique than typical EDS analyses. The heat-affected zone of pressure vessel steel side, the fusion line and the nickel-base alloy side near the fusion line were analysed - the results of these analyses can be seen in Figure 22, Figure 23 and Figure 24. In the elemental mappings of Figure 24 the lower left corner is the embedding material.

The elemental mapping locations are marked in SE and BSE images. The colours in the mappings do not show the exact content of elements. The mappings only indicate the relative content using the colour code seen below the figures. The relative content is higher

when the colour is brighter and lower when the colour is darker. Only the elements that were seen in the EDS analysis of the fracture surfaces were analysed with EPMA. The analysed elements were Fe, Cr, Ni, Mn, Mo, C, Si, Al and Ti. All the elemental mappings are stage mappings, where the sample holder is moving and the beam stays still. This enables a larger area to be analysed. For very small areas beam mapping is a better option, where the beam moves and the sample holder stays still.

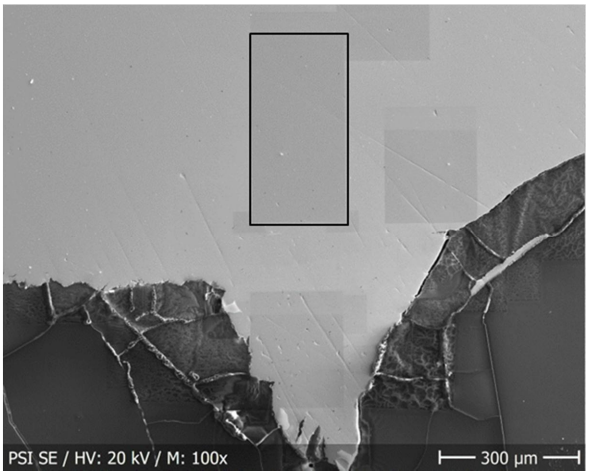

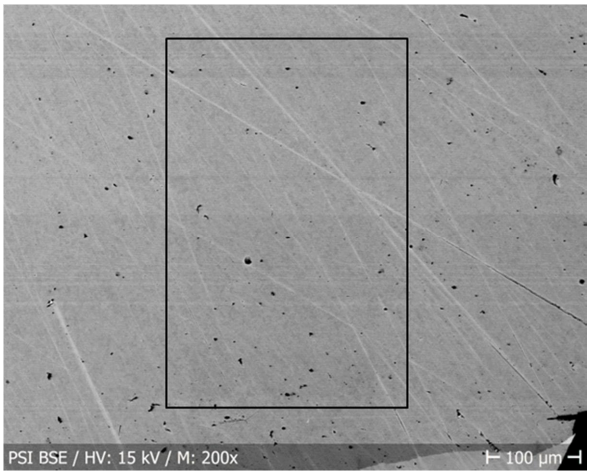

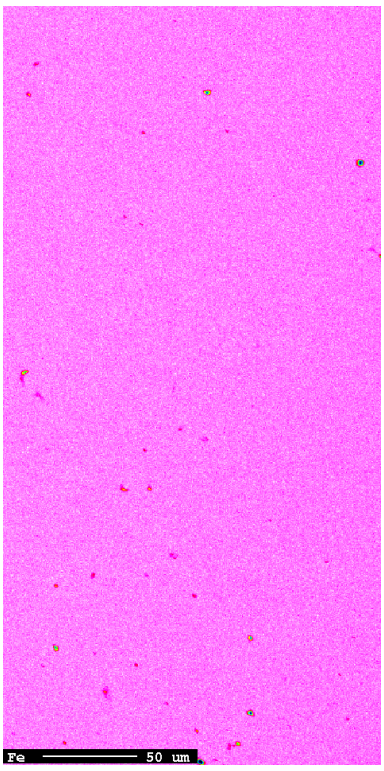

Fe

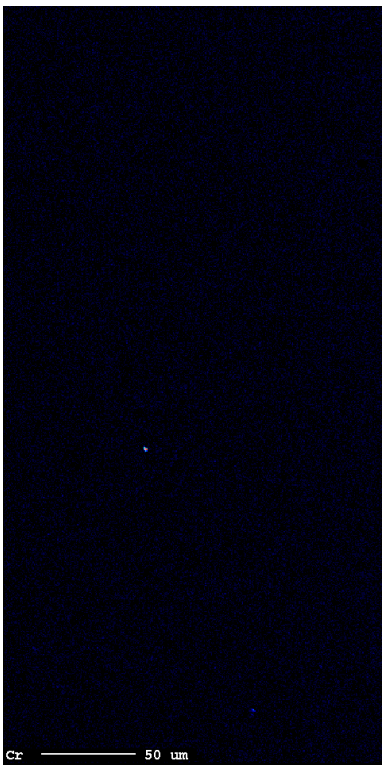

Cr

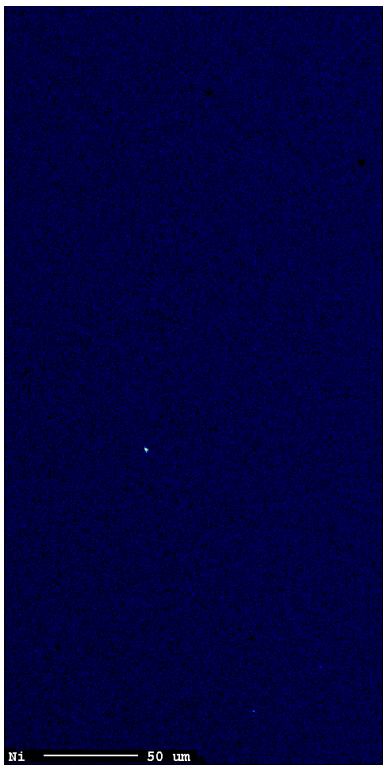

Ni

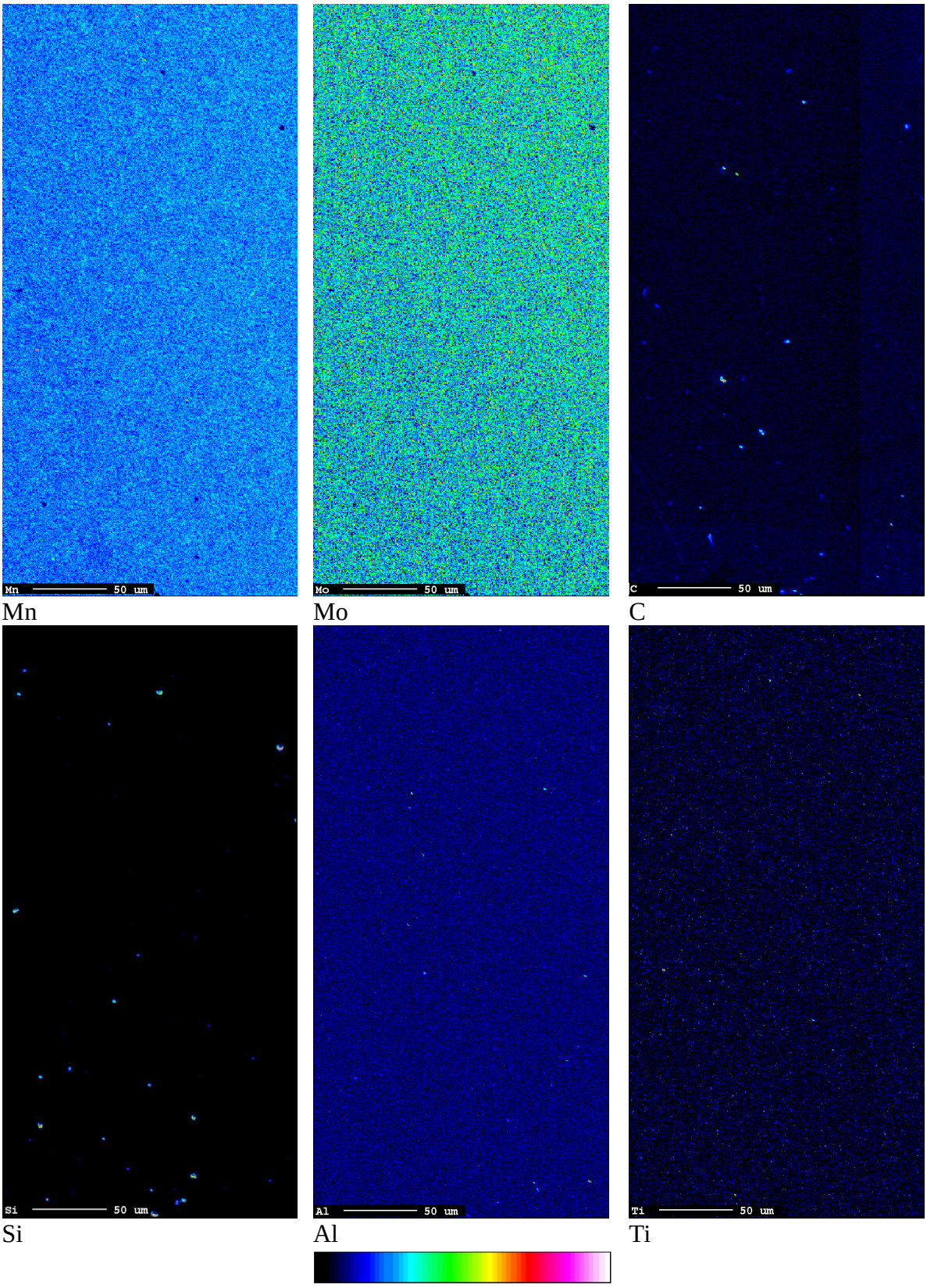

Figure 22 Elemental mappings of Fe, Cr, Ni, Mn, Mo, C, Si, Al and Ti, SE and BSE images of the EPMA mapping locations of pressure vessel steel, as-received condition.

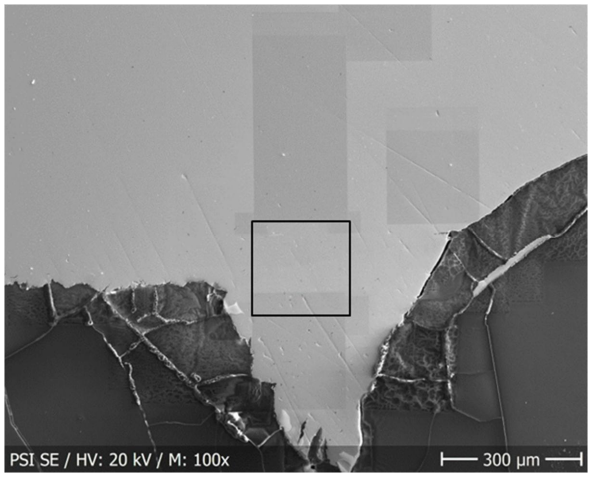

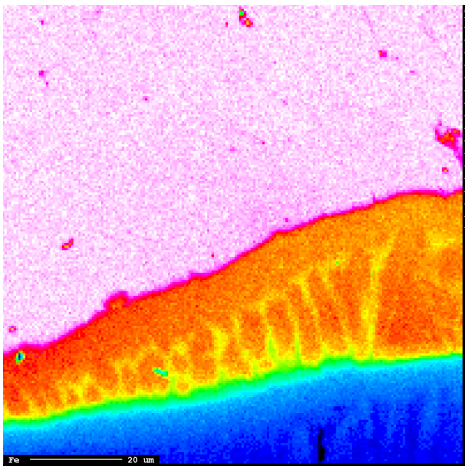

Fe

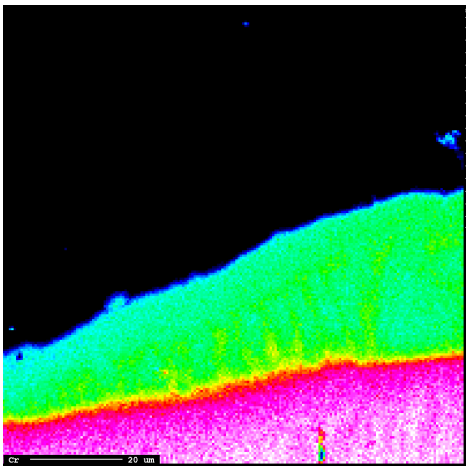

Cr

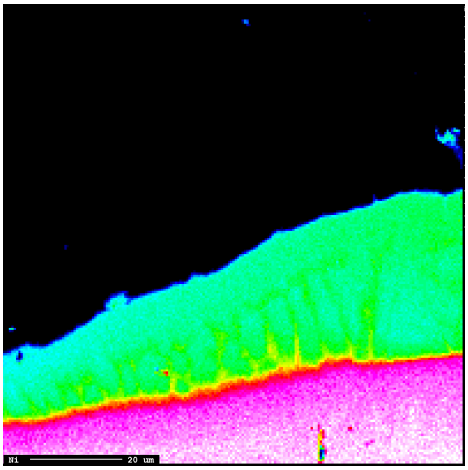

Ni

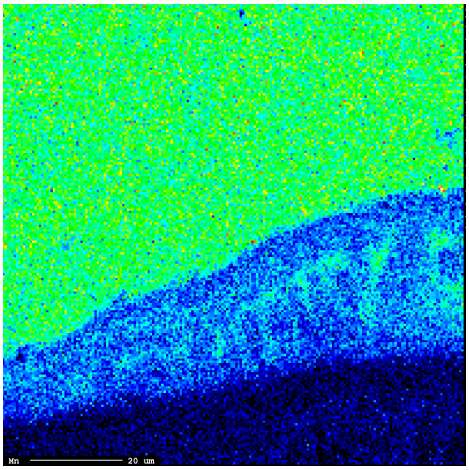

Mn

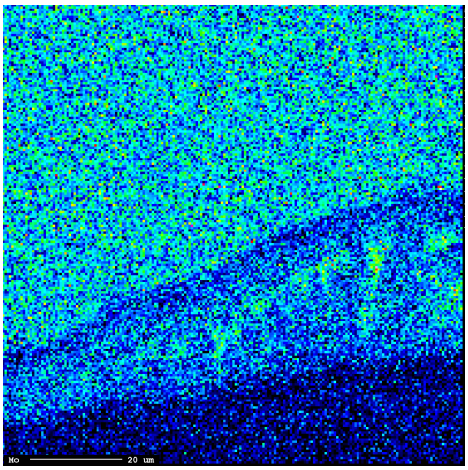

Mo

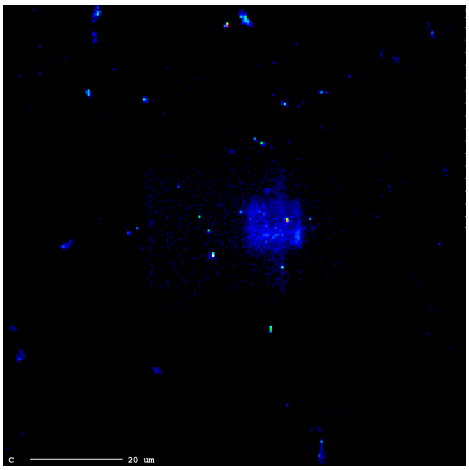

C, the square in the middle is an artefact

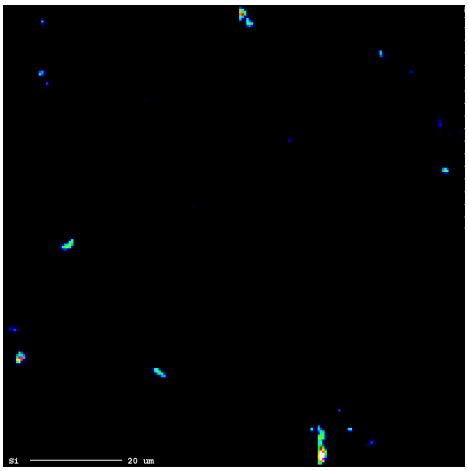

Si

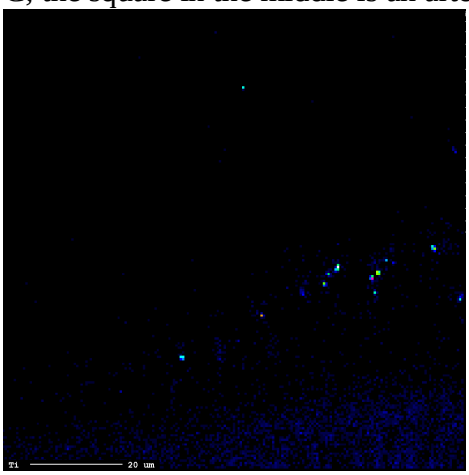

Ti

Figure 23 Elemental mappings of Fe, Cr, Ni, Mn, Mo, C, Si, and Ti, SE image of the EPMA mapping locations of fusion line, as-received condition.

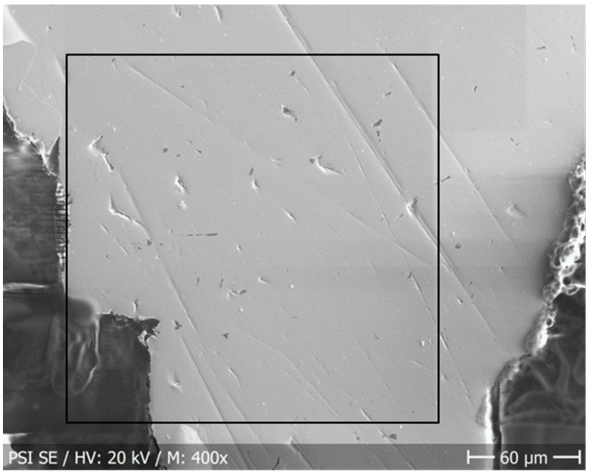
PSI SE / HV: 20 kV / M: 400x
60 µm

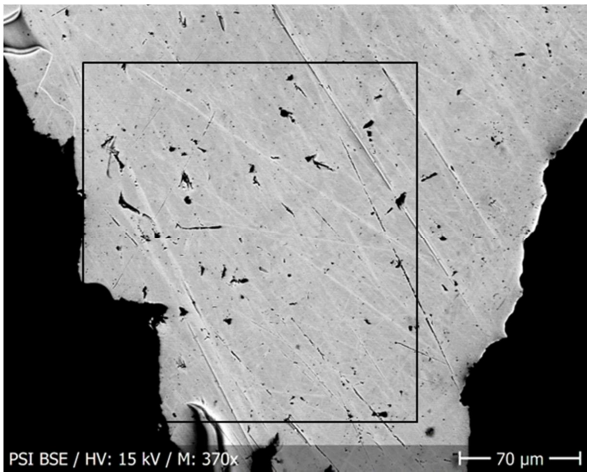
PSI BSE / HV: 15 kV / M: 370x
70 µm

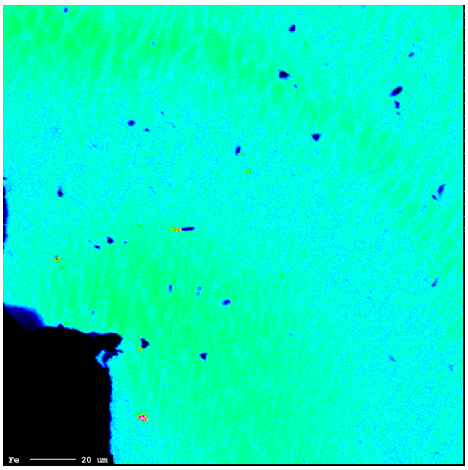
Fe
20 um

Fe

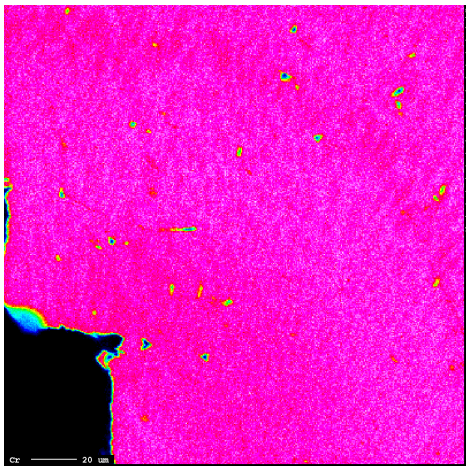
Cr
20 um

Cr

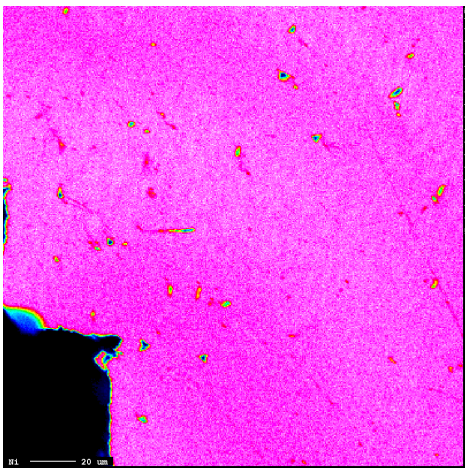
Ni
20 um

Ni

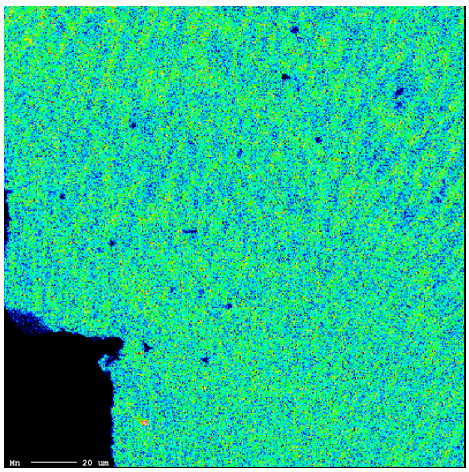
Mn
20 um

Mn

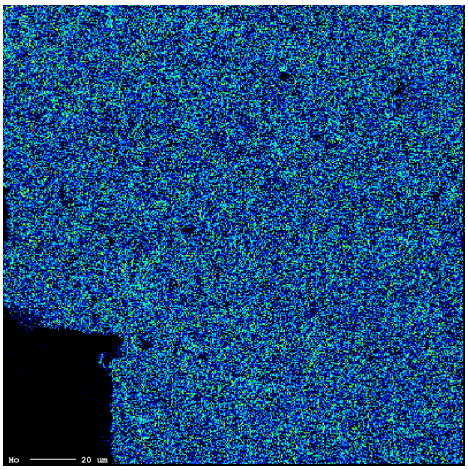

Mo

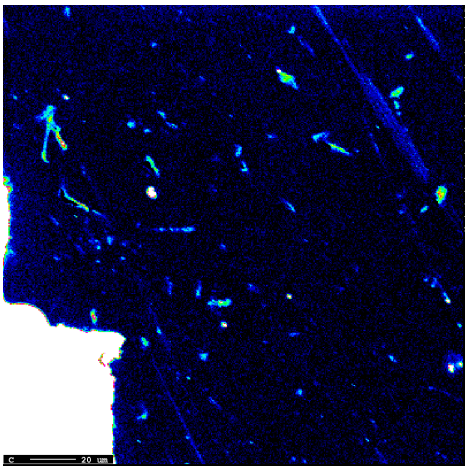

C

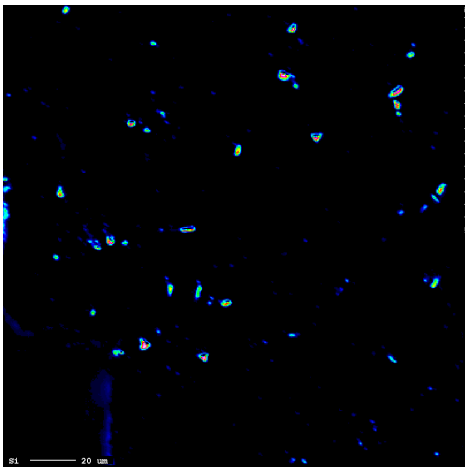

Si

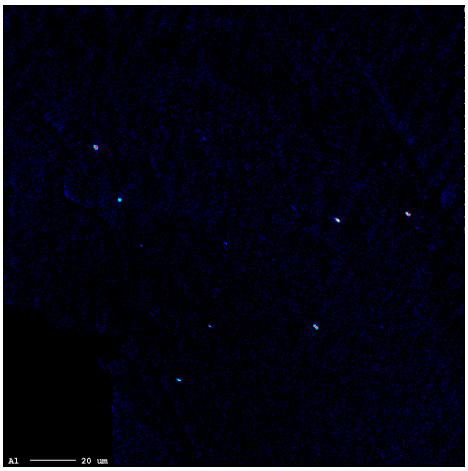

Al

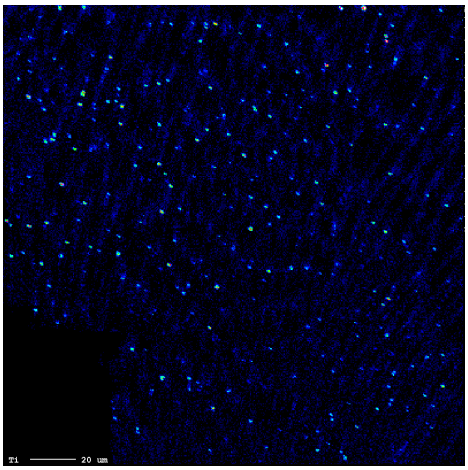

Ti

Figure 24 Elemental mappings of Fe, Cr, Ni, Mn, Mo, C, Si, Al and Ti, SE and BSE images of the EPMA mapping locations of Alloy 52, the lower left corner in the mappings is the embedding material, as-received condition.

4.3.2 Elemental mappings of 5000 hours aged condition

WDS analyses were also performed on the 5000 hours aged material. The heat-affected zone of pressure vessel steel side, the fusion line and the nickel-base alloy side were analysed and the results can be seen in Figure 25, Figure 26 and Figure 27. The elemental mapping locations are marked in SE and BSE images. The distances of pressure vessel steel side and Ni-base alloy side mappings from the fusion line are approximately 400 µm. The analysed elements were Fe, Cr, Ni, Mn, Mo, C, Si, Al and Ti.

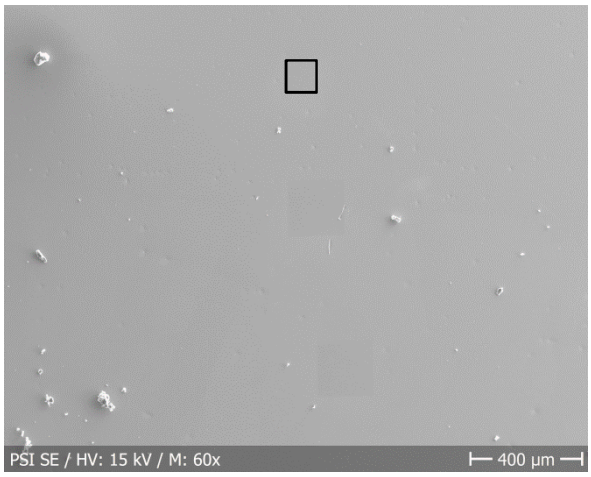

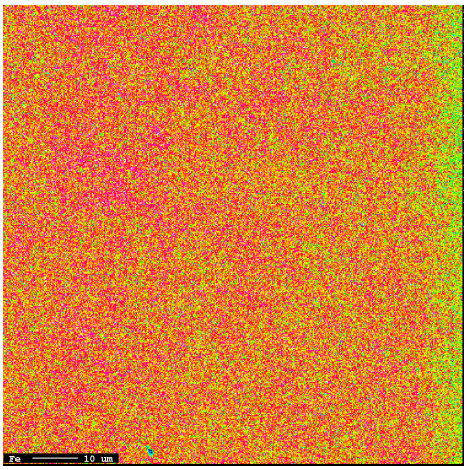

Fe

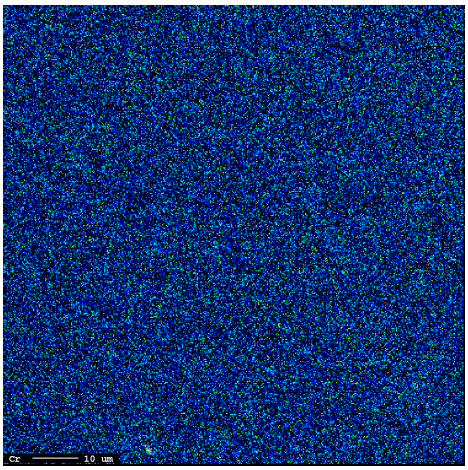

Cr

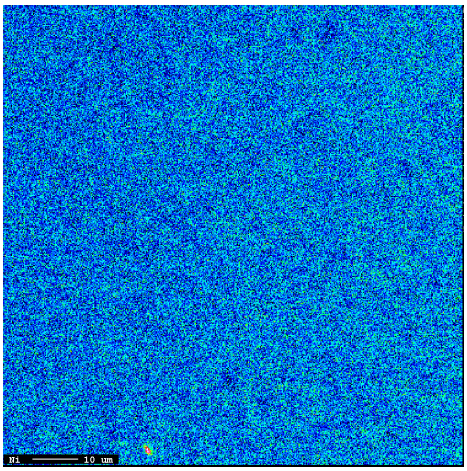

Ni

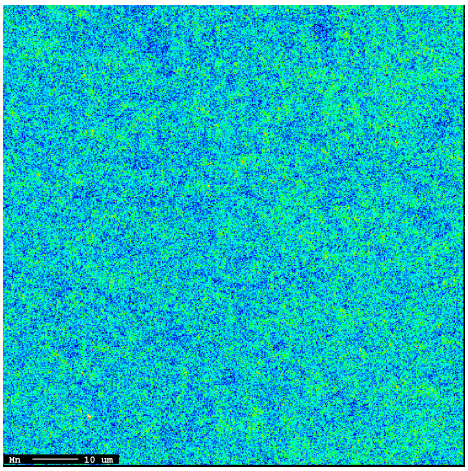

Mn

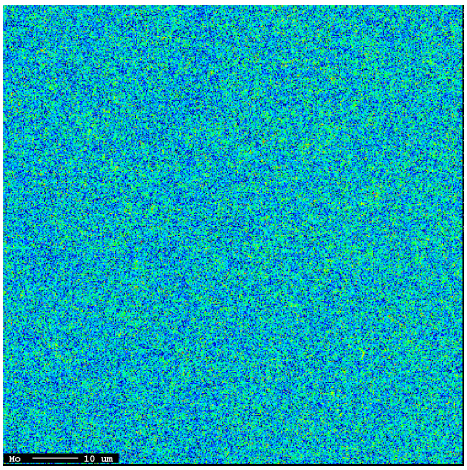

Mo

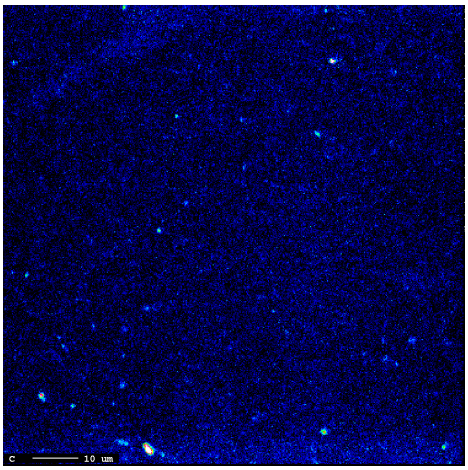

C

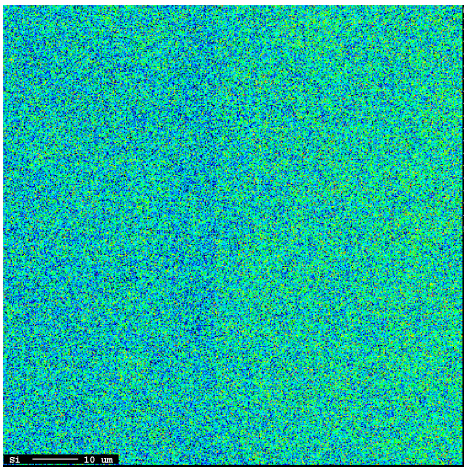

Si

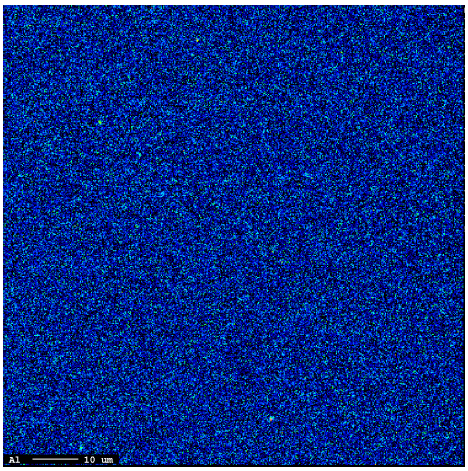

Al

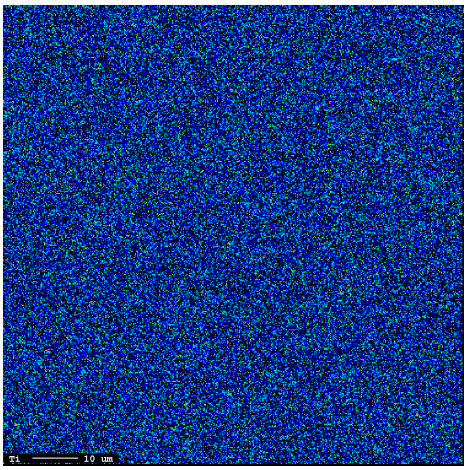

Ti

Figure 25 Elemental mappings of Fe, Cr, Ni, Mn, Mo, C, Si, Al and Ti, SE image of the EPMA mapping locations of pressure vessel steel, 5000 hours aged condition.

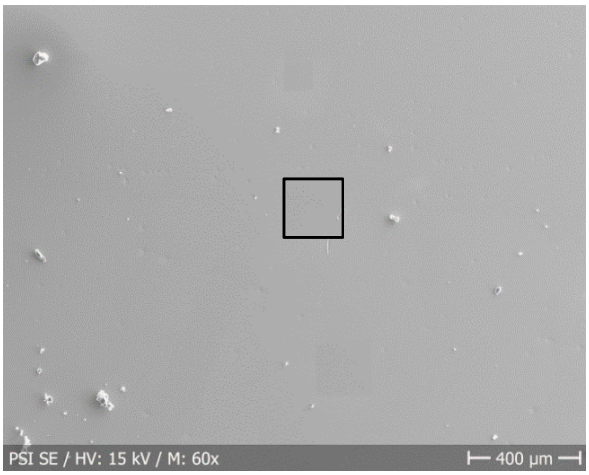
PSI SE / HV: 15 kV / M: 60x
400 µm

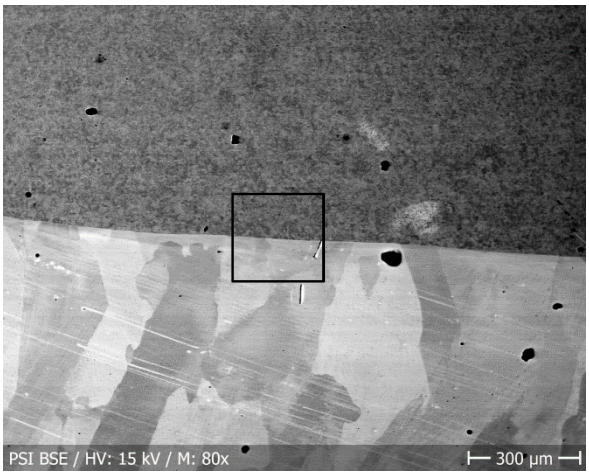
PSI BSE / HV: 15 kV / M: 80x
300 µm

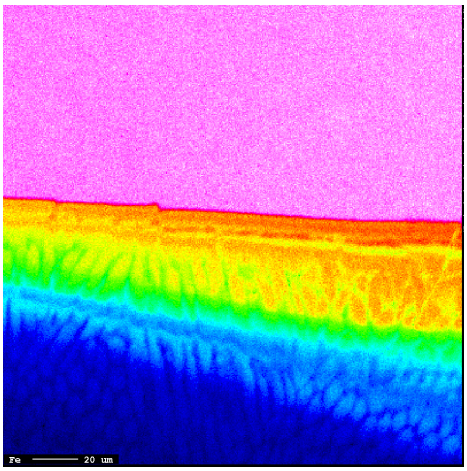
Fe
20 um

Fe

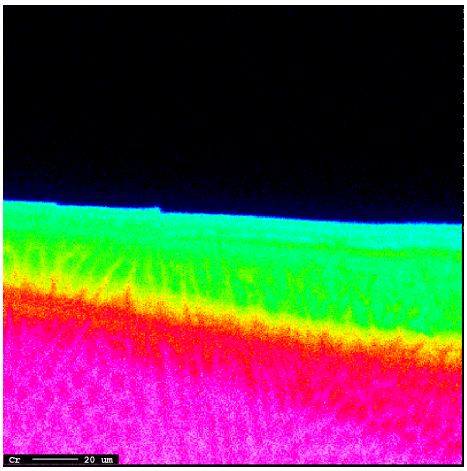
Cr
20 um

Cr

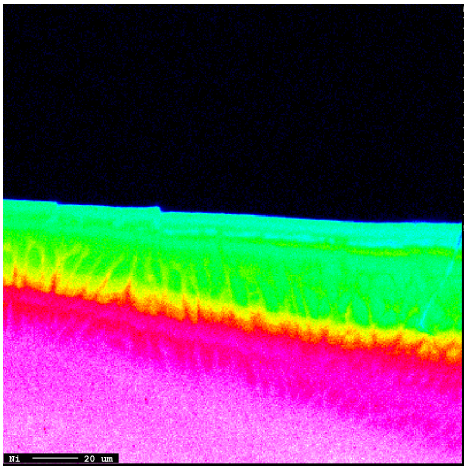
Ni
20 um

Ni

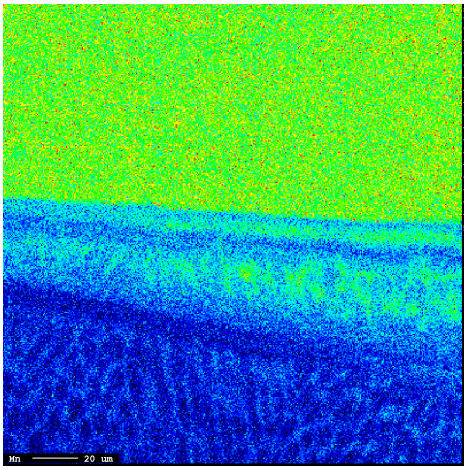
Mn
20 um

Mn

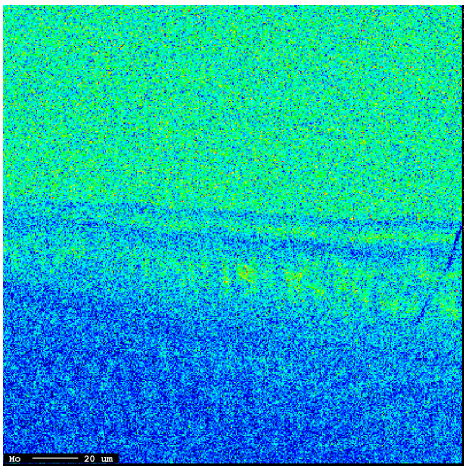

Mo

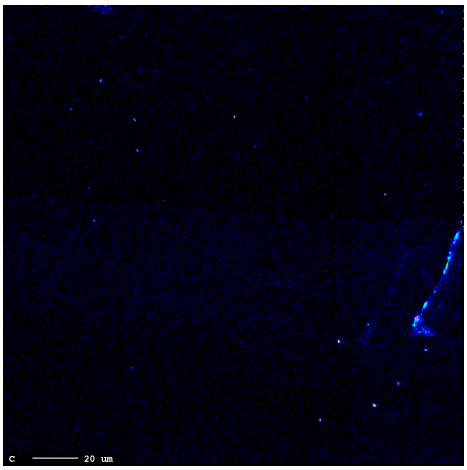

C

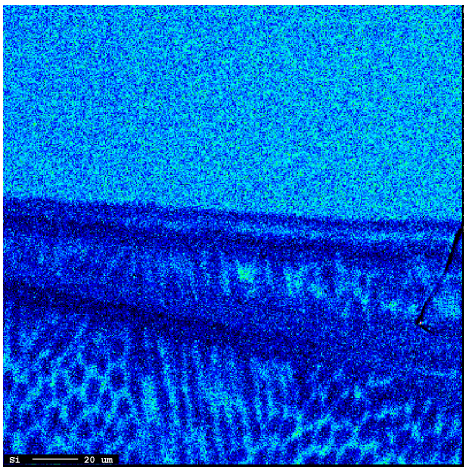

Si

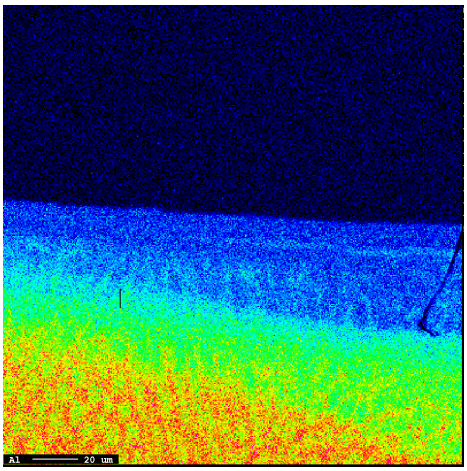

Al

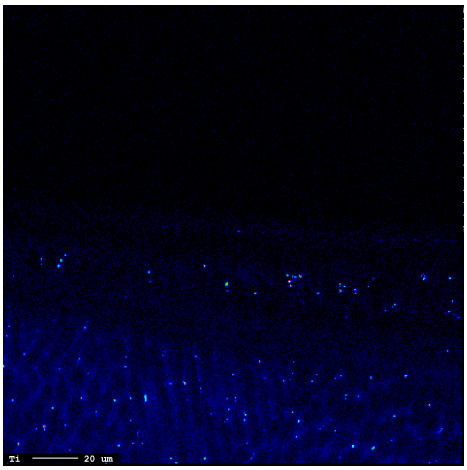

Ti

Figure 26 Elemental mappings of Fe, Cr, Ni, Mn, Mo, C, Si, Al and Ti, SE and BSE images of the EPMA mapping locations of fusion line, 5000 hours aged condition.

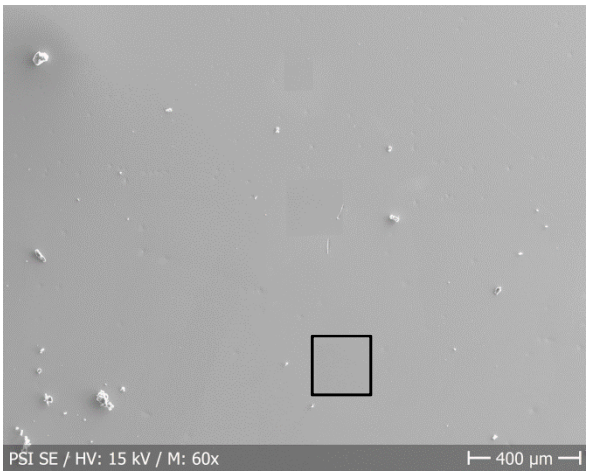

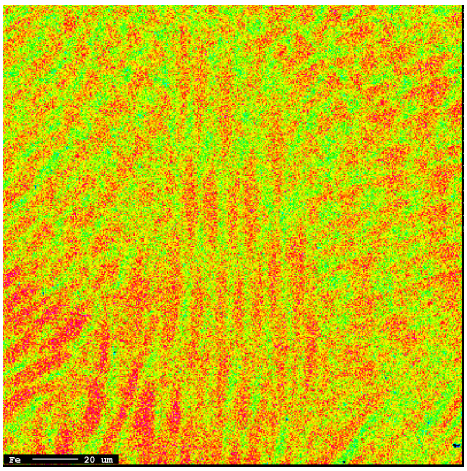

Fe

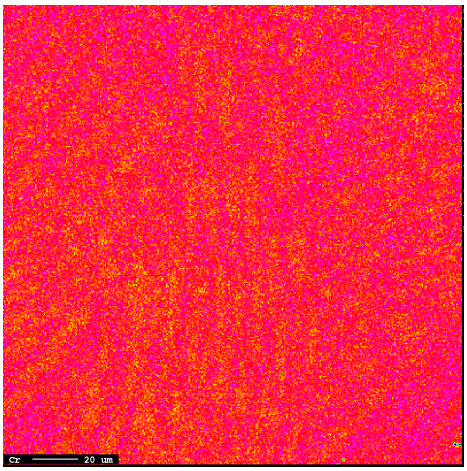

Cr

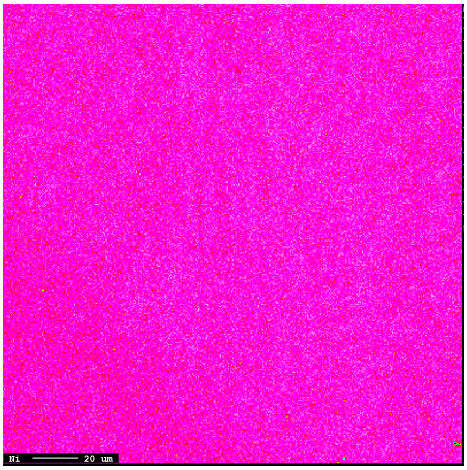

Ni

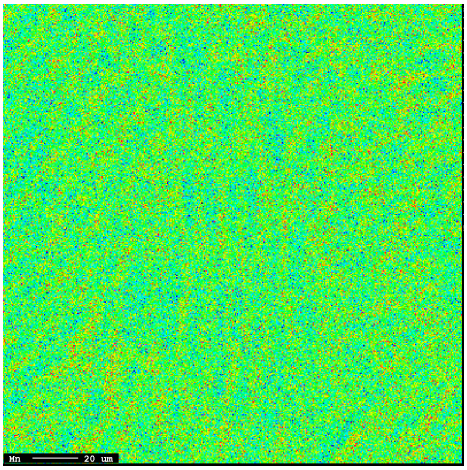

Mn

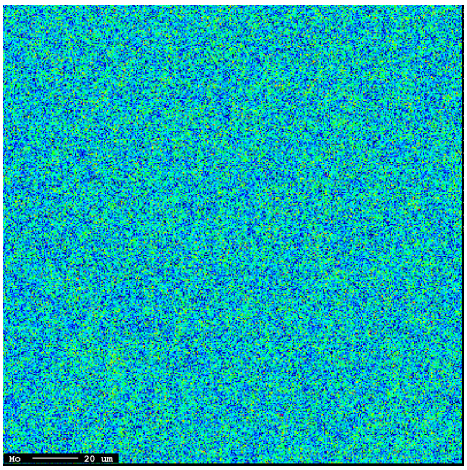

Mo

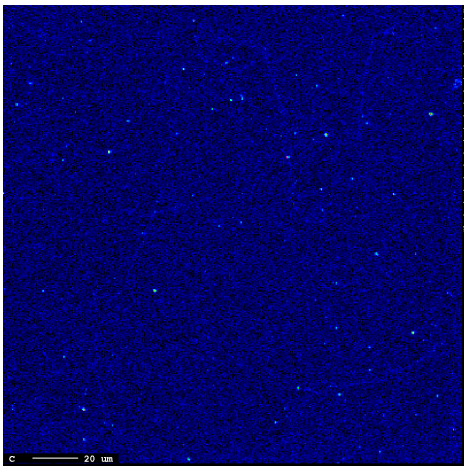

C

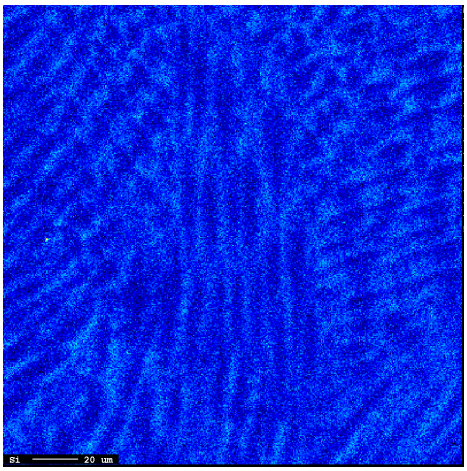

Si

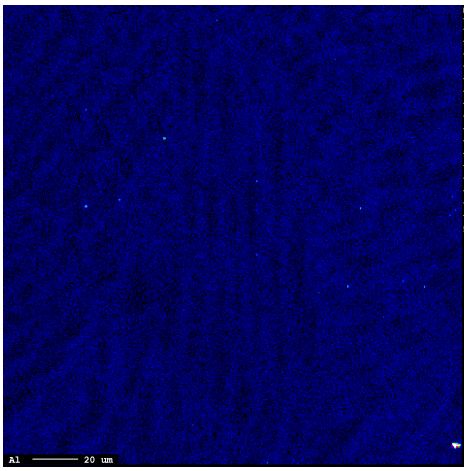

Al

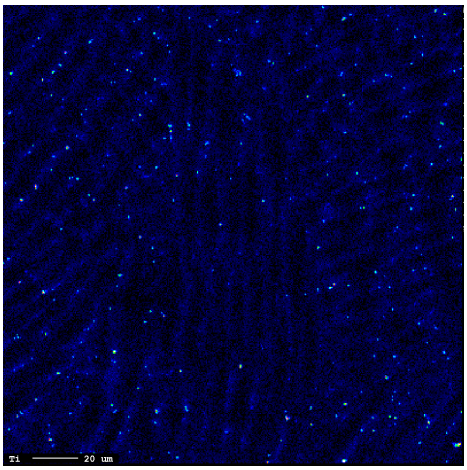

Ti

Figure 27 Elemental mappings of Fe, Cr, Ni, Mn, Mo, C, Si, Al and Ti, SE image of the EPMA mapping locations of Alloy 52, 5000 hours aged condition.

4.3.3 Line scans of as-received condition

Two quantitative line scans were carried out over the fusion line. The SE image shows the location of the scans, Figure 28. The left scan includes 40 positions with 10 µm step size, Figure 29. The right scan includes 45 positions with 1 µm step size, Figure 30. The line scans go from up to down in the SE image. Fusion line is located at 0 µm. Heat-affected zone is on the left side of the fusion line and weld metal on the right side.

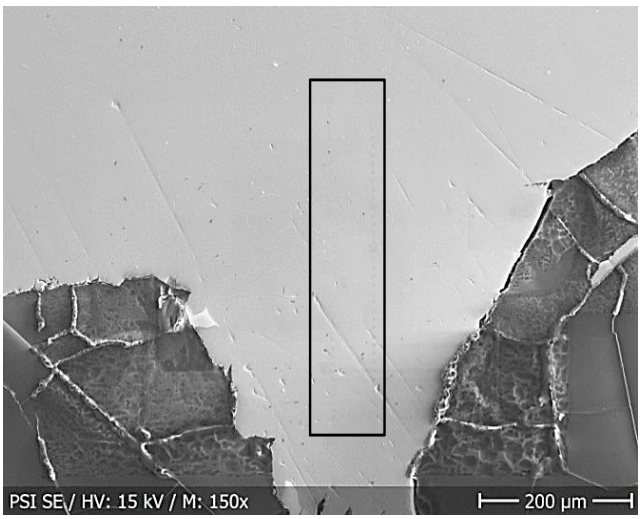

Figure 28 SE image of locations of line scans, as-received condition.

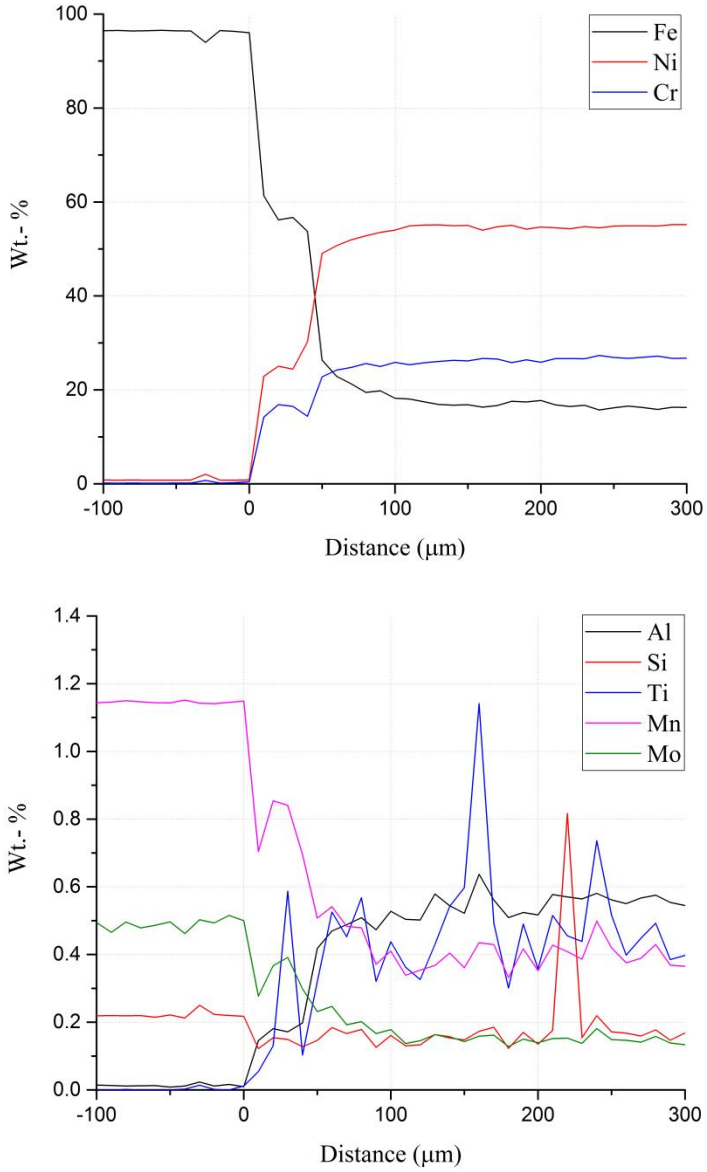

Figure 29 WDS line scans across the fusion line with 10 µm step size, fusion line is in the location of 0 µm, as-received condition.

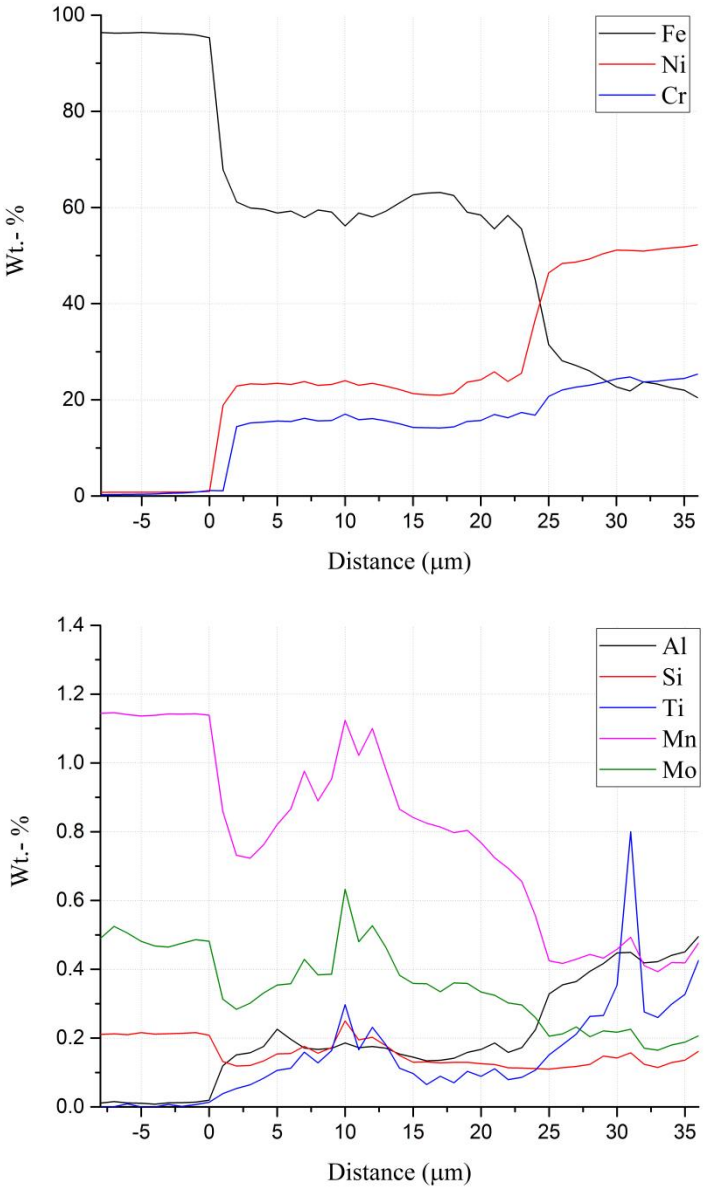

Figure 30 WDS line scans across the fusion line with 1 µm step size, fusion line is in the location of 0 µm, as-received condition.

4.3.4 Line scans of 5000 hours aged condition

Two quantitative line scans were carried out over the fusion line. The location of scans is marked in Figure 31 and the line scans are in Figure 32 and Figure 33. The line scans include 40 positions with 10 µm step size and 74 positions with 1 µm step size from -21 µm to 49 µm and 2 µm step size from 50 µm to 77 µm. The line scans go from up to down in the SE image. Fusion line is located at 0 µm. Heat-affected zone is on the left side of the fusion line and weld metal on the right side.

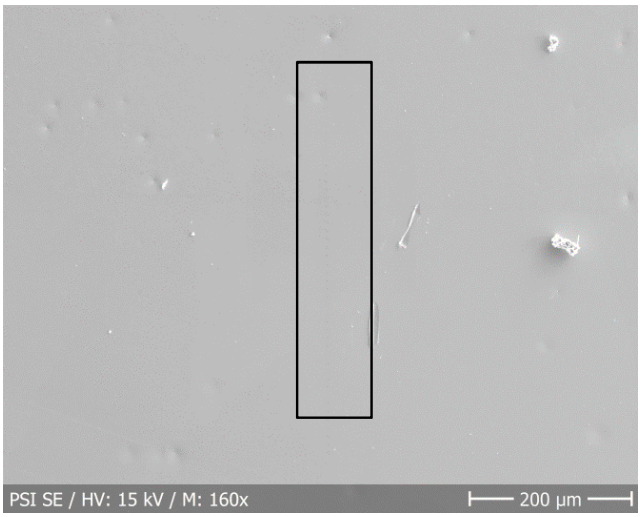

Figure 31 SE image of locations of line scans, 5000 hours aged condition.

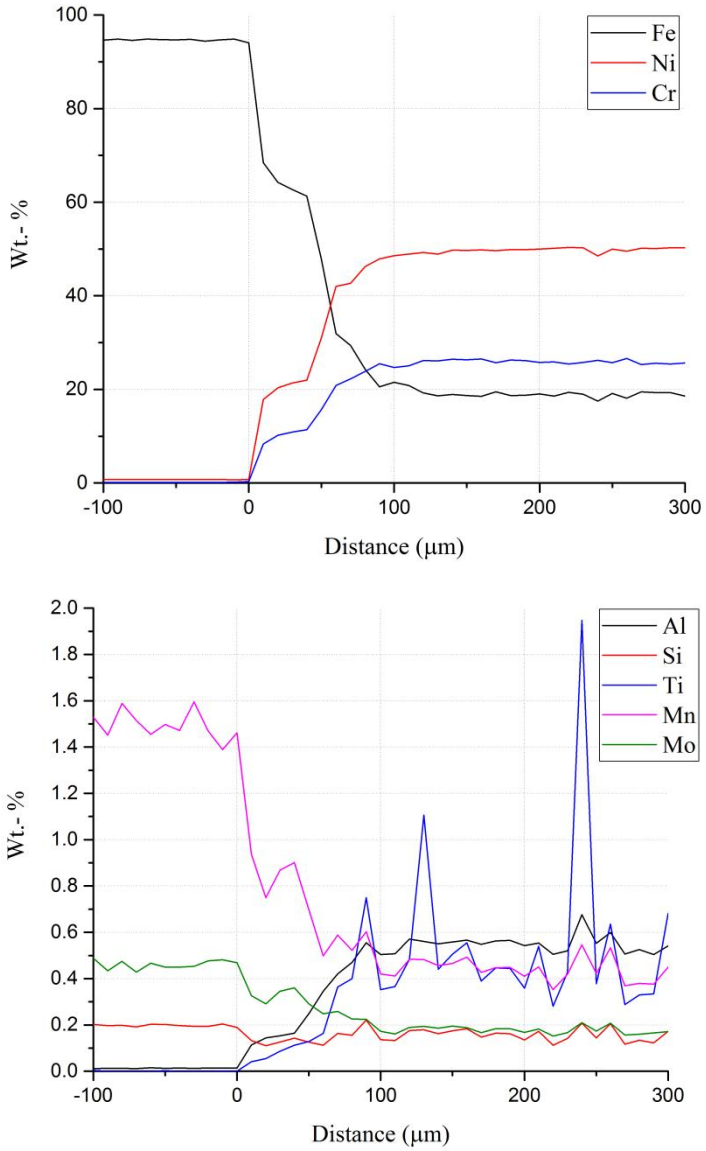

Figure 32 WDS line scans across the fusion line with 10 µm step size, fusion line is in the location of 0 µm, 5000 hours aged condition.

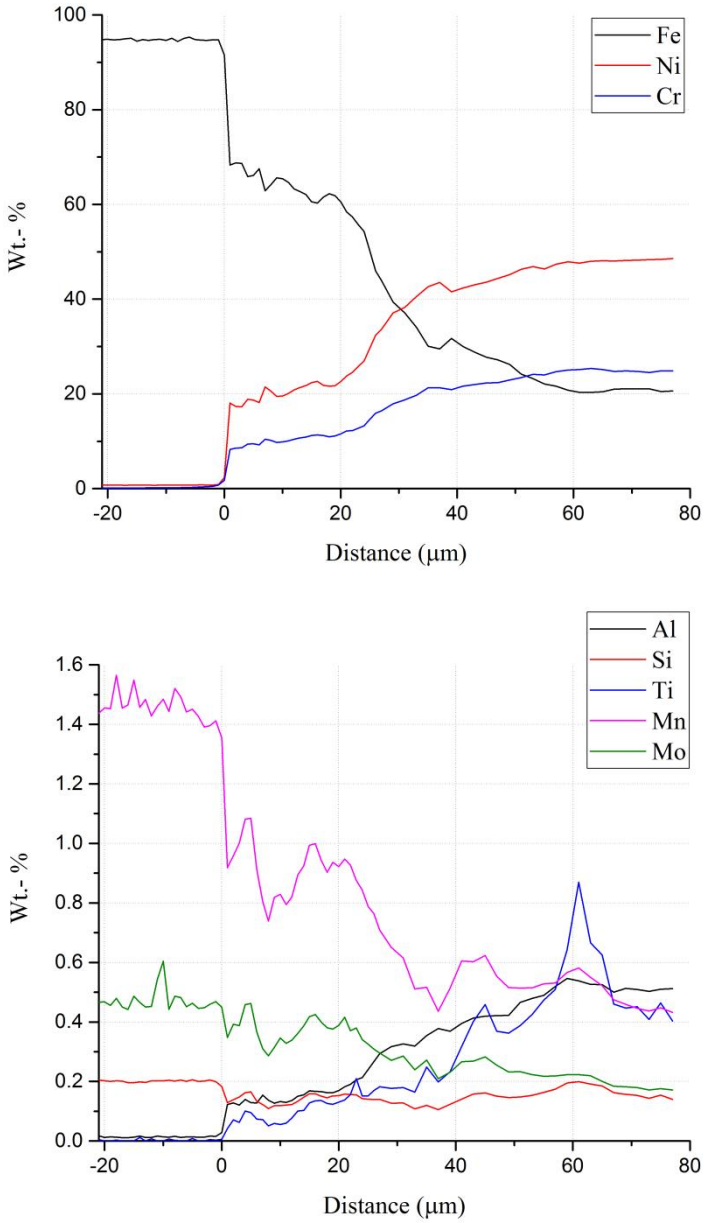

Figure 33 WDS line scans across the fusion line with 1 µm step size from -21 µm to 49 µm and 2 µm step size from 50 µm to 77 µm, fusion line is in the location of 0 µm, 5000 hours aged condition.

4.4 Optical microscopy examination

Optical microscopy observations of sample 5A were performed at VTT. Sample 5A had previously been examined by EPMA.

The examined specimen was already tested and it included a small area of nickel-base alloy, which can be seen in Figure 34. The optical microscopy image supports the WDS analyses from Ni-base alloy side. The brighter area near fusion line is a weld pass boundary where a new weld pass is welded partly onto the previous one. This zone is the same inhomogeneous zone which can be seen in elemental mappings in Figure 23 and

Figure 26. The grain boundary, approximately 200 µm away from the fusion line, is most likely a Type II boundary.

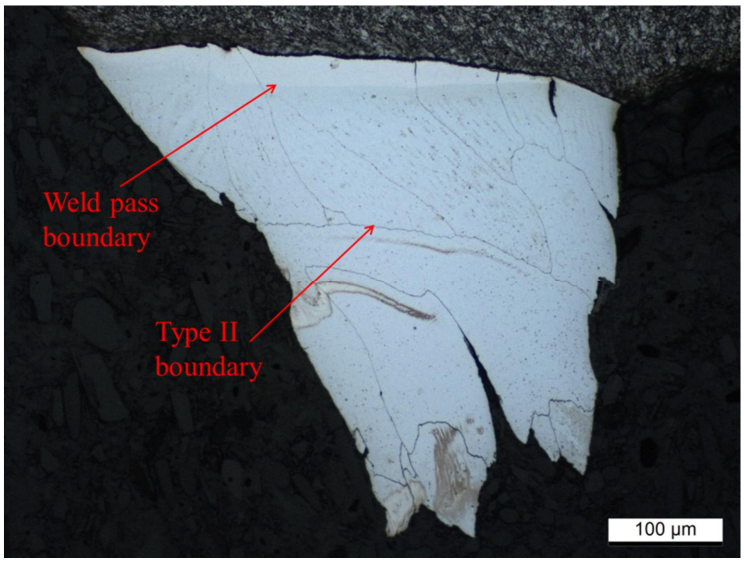

Figure 34 Optical microscopy image of Ni-base alloy of the tested specimen 5A, magnification 20x. It is very likely that the grain boundary located 200 µm away from the fusion line is a Type II boundary. A weld pass boundary is close to the fusion line.

Optical microscopy image of WDS analysed 5000 hours aged sample is presented in Figure 35. The location of elemental mappings of the fusion line is marked in the image as well as solidification grain boundaries, solidification subgrain boundaries and a weld pass boundary. The darker boundaries are SGBs and the boundaries inside SGBs are SSGBs. SSGBs inside grains are seen differently because of different grain orientation.

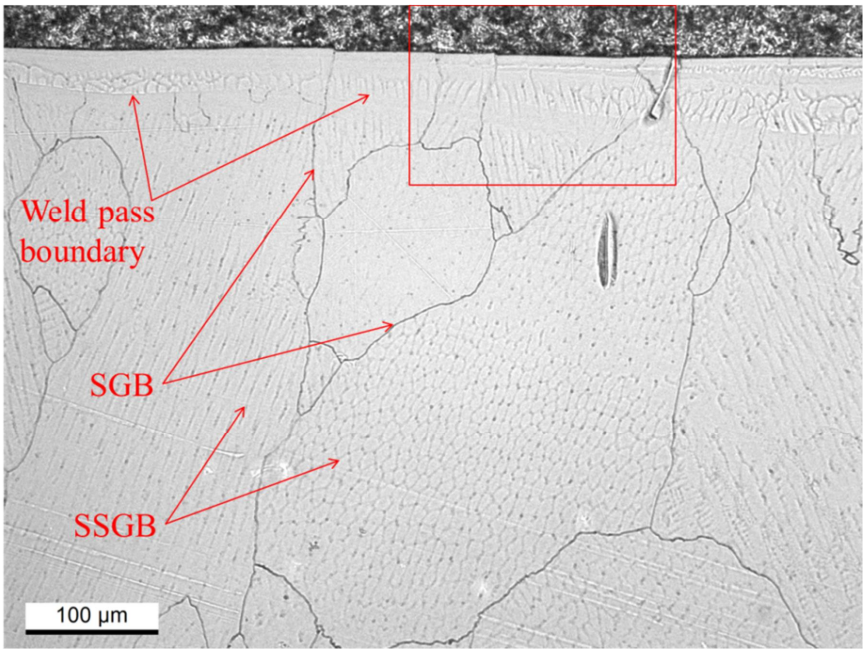

Figure 35 Optical microscopy image of fusion line, a weld pass boundary and Ni-base alloy of 5000 hours aged sample, magnification 20x. The location of elemental mappings of fusion line is marked as a red square, SGBs and SSGBs are marked with red arrows.

4.5 Non-conformances of Charpy-V impact test

Some specimens in the as-received condition were problematic because the V-notches were machined either on nickel-base alloy side of the specimen or at the fusion line of nickel-base alloy and pressure vessel steel. The V-notch should have been positioned in the heat-affected zone. The behaviour of specimens in impact testing is different depending on if the V-notch is on the nickel-base alloy side or on the pressure vessel steel side.

Figure 36 shows that the V-notch of specimen 5A is slightly on the nickel-base alloy side, Ni-base alloy is on the left side and pressure vessel steel on the right side of the notch.

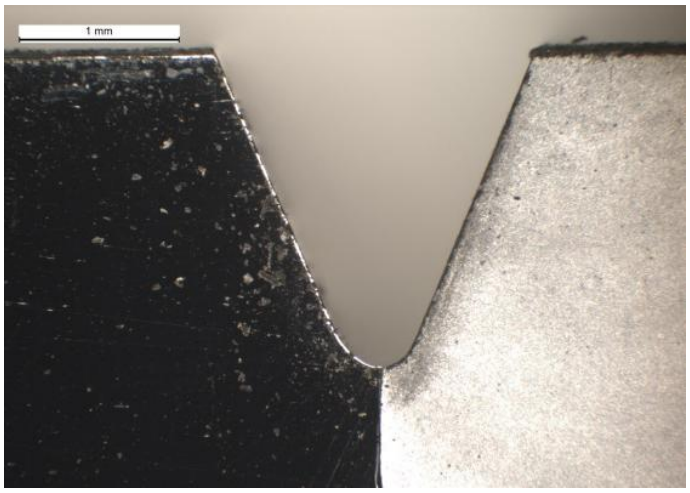

Figure 36 The incorrect V-notch location of the specimen 5A, Ni-base alloy is on the left and pressure vessel steel on the right (Lydman 2017).

In the case of specimen 5A the fracture began on the nickel-base alloy side and continued to the pressure vessel steel side, where the required energy for crack propagation is lower. This can be clearly seen from the fracture surface and SEM's EDS analysis, see Figure 37 and Figure 38. The V-notch is on the bottom of the figure. The nickel-base alloy side is still ductile and pressure vessel steel side is brittle at the testing temperature of -89.7 ˚C. As the fracture started from the nickel-base alloy side, the KV_2 is higher than expected. The correct positioning of V-notch is very important; otherwise the incorrect positioning will cause different crack growth paths which will lead to a scatter in the transition curves. According to Joly et al. (2014), incorrect notch positioning has also caused similar scatter in earlier Charpy-V tests at AREVA.

Figure 37 is an SEM micrograph indicating where elemental analysis was performed. In this figure number 1 indicates the V-notch, numbers 2 and 3 nickel-base alloy near the V-notch and numbers 4 and 5 pressure vessel steel. The EDS elemental count rates of numbers 2, 3 and 4 are shown in Figure 38. The count rates show typical behaviour for nickel-base alloy, which can be identified from the Cr, Fe and Ni peaks close to each other and for pressure vessel steel, which has two larger Fe peaks. Chemical compositions of numbers 2-4 are shown in Table 2.

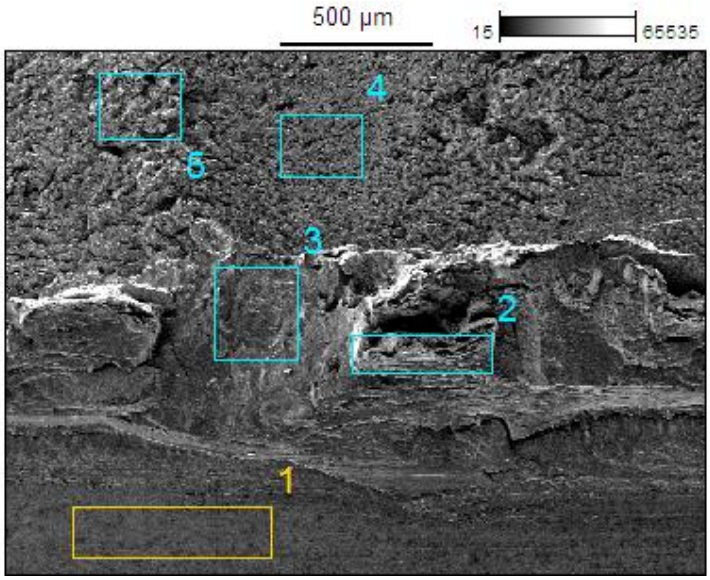

Figure 37 SEM (SE) image of specimen 5A's fracture surface, magnification 19x.

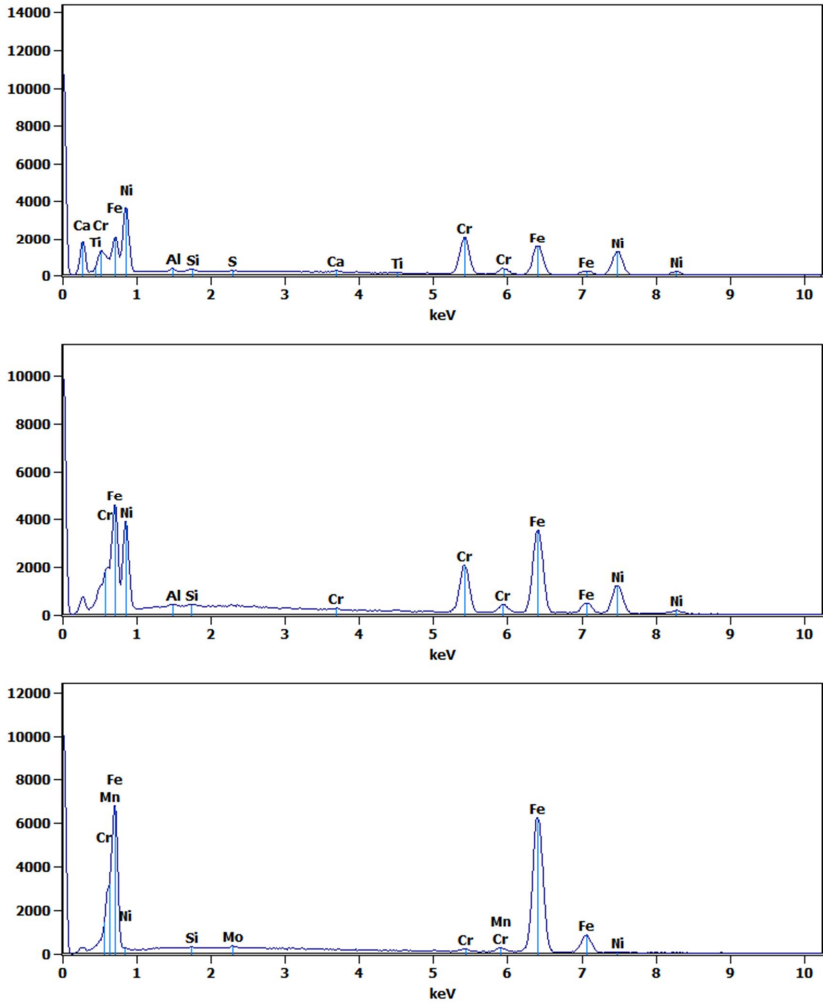

Figure 38 The EDS count rates of found elements from the specimen 5A's fracture surface, points 2, 3 and 4.

Table 2 Chemical compositions (wt.-%) of selected zones in Figure 37 determined from the elemental analyses seen in Figure 38.

Analysis number	Si	Mn	S	Cr	Ni	Mo	Ti	Fe	Al
2	0.4	-	0.3	24.3	42.6	-	0.4	30.9	0.5
3	0.2	-	-	16.7	31.0	-	-	51.7	0.3
4	0.2	2.0	-	0.7	1.4	0.6	-	95.2	-

Eighteen specimens were machined from the material aged of 5000 hours. Machining problems were also encountered with this condition. One specimen had the V-notch fully on the nickel-base alloy side, eight specimens had the other side of the notch on the Ni-base alloy side and the other on the heat-affected zone and nine specimens had the V-notch machined fully on the HAZ. The correct location for the V-notch was the heat-affected zone. This means that only nine specimens were correctly machined and thus available for the intended testing. However, the other nine specimens were also tested in parallel at the same temperatures and later examined by SEM in order to determine if any Ni-base alloy was present along the fracture surfaces.

According to standard ASTM E2298-13a (2013), for each test in which the entire force signal has been recorded, the difference between absorbed energy given by the dial and/or optical encoder KV_{calc} and the total impact energy KV_{pend} shall be within 15 % or 1 J, whichever is larger. If this requirement is not met but the difference does not exceed 25 % or 2 J, whichever is larger, force values shall be adjusted until $KV_{calc} = KV_{pend}$ within 0.01 J. If the difference exceeds 25 % or 2 J, whichever is larger, the test shall be discarded (ASTM E2298-13a 2013). If the measured energy is very high, such as with the 5000 hours aged specimens 1, 2, 8, 10 and 18, it may happen that the strain gauge does not have enough capacity and, therefore, the calculated energy value is much lower. Also, if the specimen is very tough, the load of the impact striker is executed on the side face of the striker, which loading differs much from the calibration load. Hence the load is not measured any more correctly. Based on the standard all these specimens exceed 25 %. However, this is not a reason to discard these results. Functionality of the strain gauge was noted by testing dummy specimens which showed that the strain gauge works fine. In this kind of situation the measured absorbed energy (KV_{pend} or KV_2) is always correct because it is measured from the beginning and the end test angles, and that energy matters the most.

SEM examination of the 5000 hours aged specimens showed that the fracture surfaces of specimens 5 and 6, with an incorrect V-notch position, did not include nickel-base alloy. Therefore, the results of these specimens can be added to the transition curves. EDS analysis of specimen 6 can be seen in Figure 39, where the V-notch is located at the bottom of the image. The full width of the fracture surface near the V-notch was analysed and the chemical composition of points 1, 2, 3 and 4, indicated in Figure 39, is presented in Table 3. Other specimens included areas of Ni-base alloy near the V-notch and they could not be added to the transition curves.

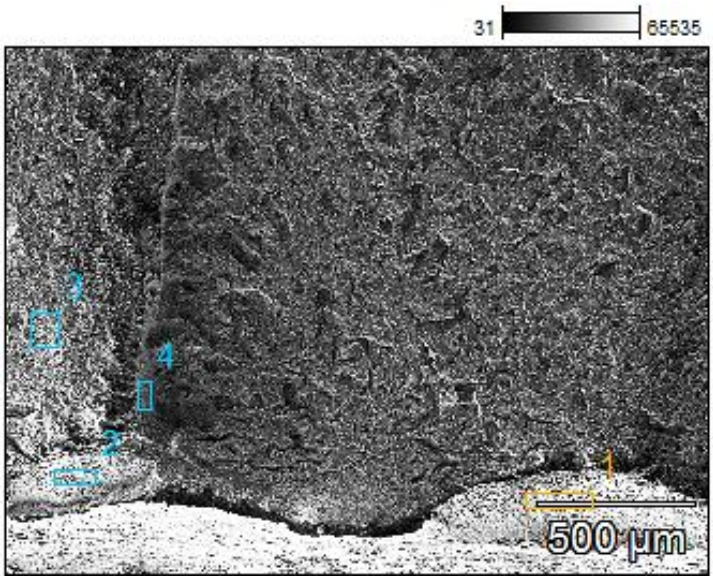

Figure 39 SEM (SE) image of specimen 6's (5000 hours aged condition) fracture surface, magnification 19x.

Table 3 Chemical composition (wt.-%) of selected zones of specimen 6 (5000 hours aged condition) indicated in Figure 39.

Analysis number	Si	Mn	Ni	Mo	Fe
1	1.0	2.1	0.9	0.5	95.5
2	0.7	1.8	-	0.5	97.1
3	0.8	1.6	-	0.5	97.2
4	0.9	1.4	-	-	97.6

4.6 Transition curves

The specimens were tested randomly. The derived energy, lateral expansion and fracture appearance based transition curves of as-received condition where specimens 1A, 2A, 4A and 5A are excluded, are shown in Figure 40, Figure 41 and Figure 42. Filled black dots in the figures indicate 100 % ductile fracture.

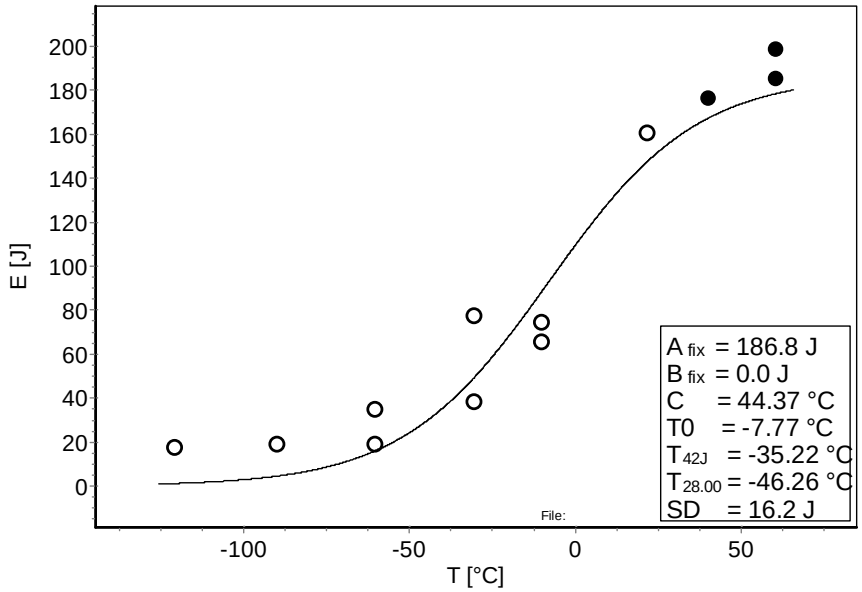

Figure 40 Transition curve for energy, filled black dots indicate 100 % ductile fracture, as-received condition.

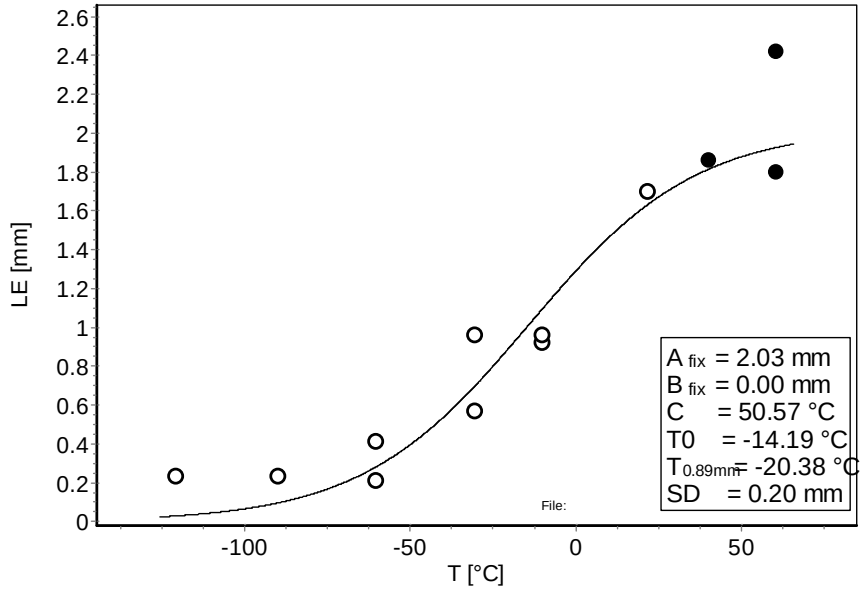

Figure 41 Transition curve for lateral expansion, filled black dots indicate 100 % ductile fracture, as-received condition.

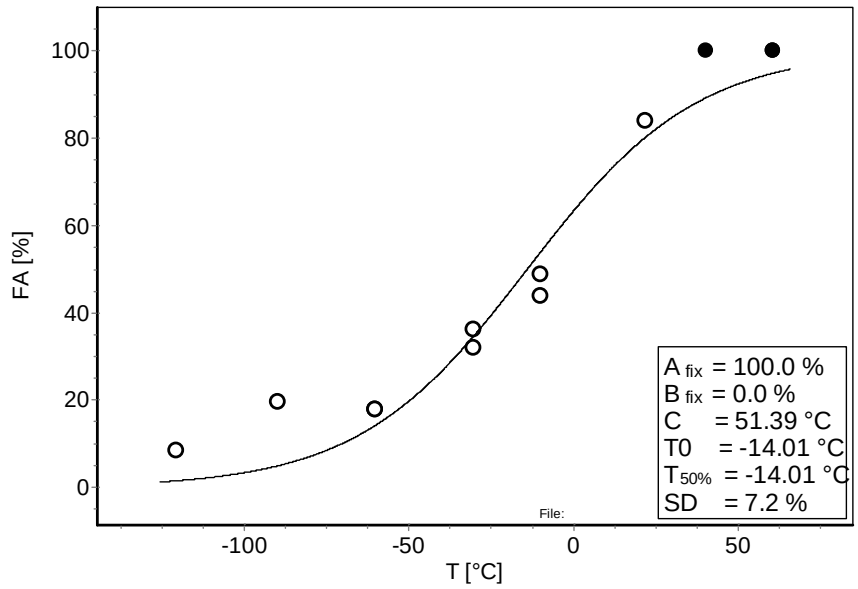

Figure 42 Transition curve for fracture appearance, filled black dots indicate 100 % ductile fracture, as-received condition.

However, if every tested specimen is included, i.e. including those in which the V-notch was incorrectly placed and therefore Ni-base alloy was exposed on the fracture surface, the transition curve changes. The derived energy based transition curve of the as-received condition is shown in Figure 43. The transition temperature T_{42J} decreases from -35.2 °C to -39.4 °C and T_0 decreases from -65.4 °C to -68.6 °C. Therefore, if all test results are included in the transition curve, it is misleading - as it indicates that the impact toughness properties of the HAZ are slightly better than what they actually are. The specimens with incorrect V-notch position cannot be accepted when analysing the results. Standard deviation (SD) is doubled due to incorrect V-notch position.

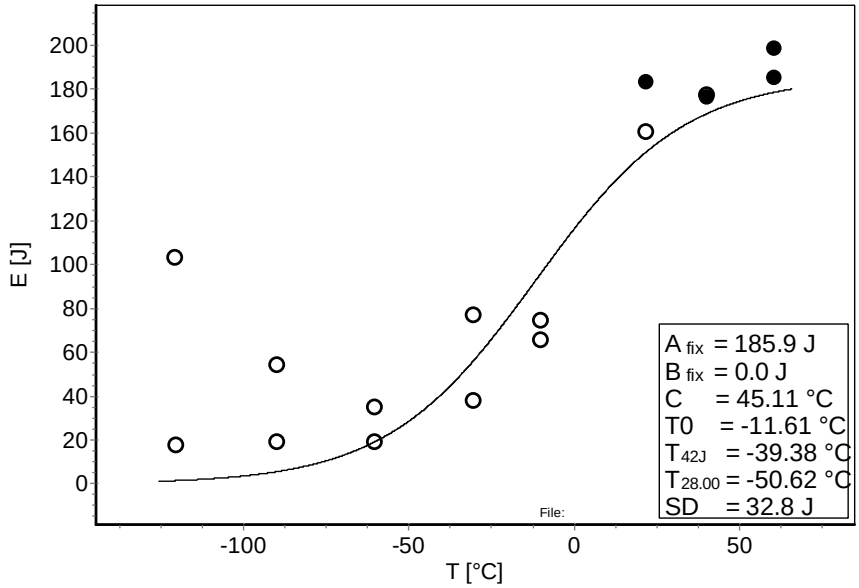

Figure 43 Transition curve for energy, filled black dots indicate 100 % ductile fracture, as-received condition, all tested specimens are included.

The derived energy, lateral expansion and fracture appearance based transition curves of 5000 hours aged condition, where specimens 1, 2, 3, 4, 9, 10 and 16 are excluded, are shown in Figure 44, Figure 45 and Figure 46. The upper shelf includes only one fully ductile result. However, the specimen tested at +60.3 °C has almost 90 % ductility and the absorbed energy is nearly the same as the upper shelf energy. Therefore, it can be concluded that the upper shelf starts at some temperature between these two specimens.

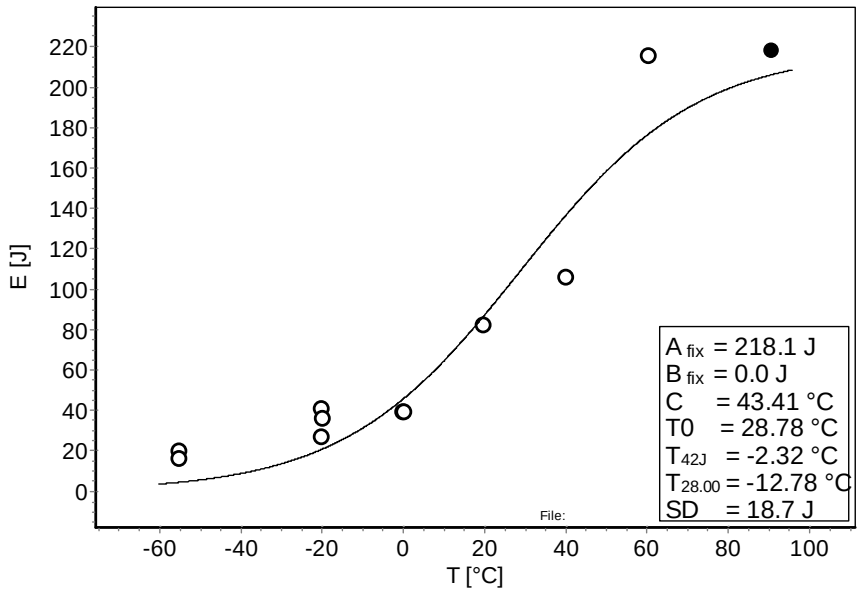

Figure 44 Transition curve for energy, the filled black dot indicates 100 % ductile fracture, 5000 hours aged condition.

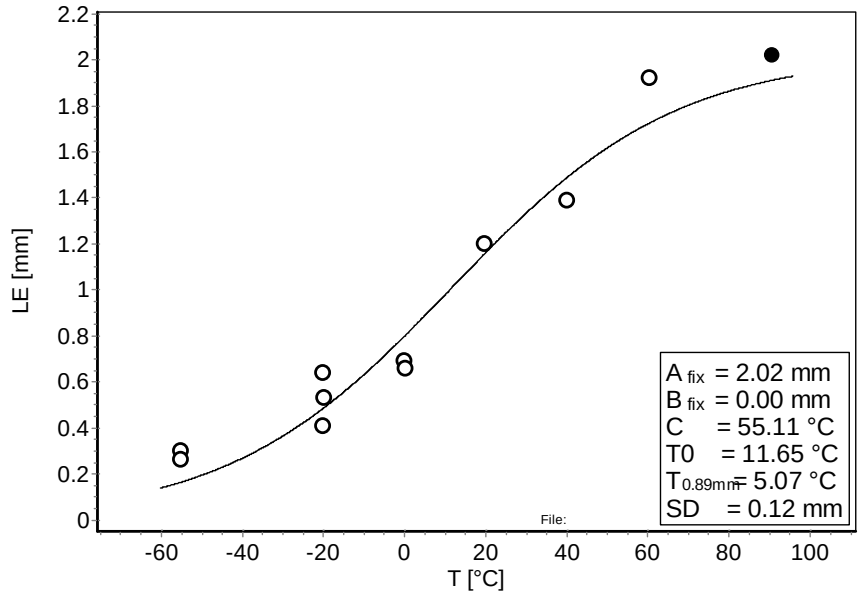

Figure 45 Transition curve for lateral expansion, the filled black dot indicates 100 % ductile fracture, 5000 hours aged condition.

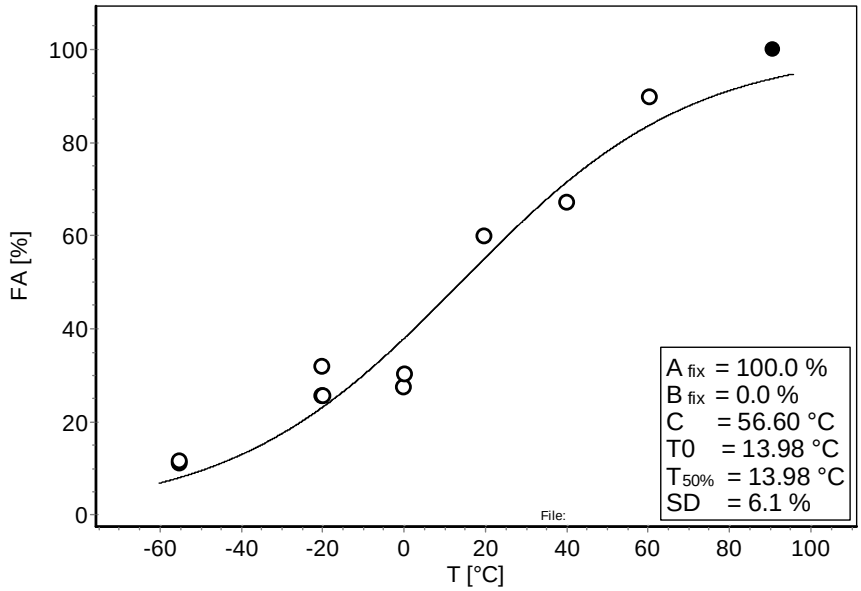

Figure 46 Transition curve for fracture appearance, the filled black dot indicates 100 % ductile fracture, 5000 hours aged condition.

At first only nine specimens of the 5000 hours aged condition were tested, because of an incorrect V-notch positioning on the remaining nine. However, the nine specimens with incorrect V-notch position were tested parallel with the specimens with correct V-notch position at the same temperatures. After testing, the fracture surfaces were examined by SEM to see if any areas of Ni-base alloy were visible near the V-notch. The examination showed that two specimens had no Ni-base alloy on the fracture surface and, therefore, these two specimens were added to the transition curves.

The derived energy based transition curve of the 5000 hours aged condition, which includes all the tested specimens (including those with incorrect V-notch placement and Ni-base alloy visible near the V-notch after fracture), is shown in Figure 47. Contrary to the as-received condition, the difference in transition temperature is almost negligible, -2.3 °C vs. -3.2 °C. The standard deviation is only slightly higher, but more scatter can be seen when comparing the transition curves of correct and incorrect V-notch positions.

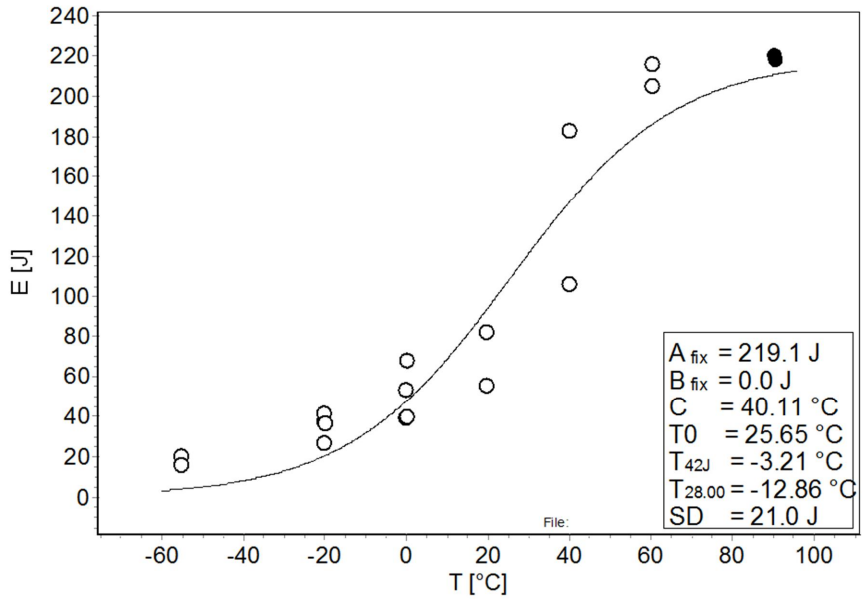

Figure 47 Transition curve for energy, filled black dots indicate 100 % ductile fracture, 5000 hours aged condition, all tested specimens are included.

Scatter of the KV_2, LE and FA is given in Table 4. The standard deviations are quite reasonable and very little scatter is seen in transition curves. Typically, scatter increases when a material's properties are weakened, i.e. irradiation promotes material inhomogeneity. Base metal always has less scatter than an inhomogeneous weld metal or heat-affected zone.

Table 4 Scatter of KV_2, LE and FA values.

Material	SD_{KV2}	SD_{LE}	SD_{FA}
	(J)	(mm)	(%)
As-received	16.2	0.20	7.2
Aging, 5000 hours	18.7	0.12	6.1

The transition temperatures are summarized in Table 5. The test data is given in Appendix 3, the load-deflection curves in Appendix 4 and the images of fracture surfaces in Appendix 5. Fracture surfaces show macroscopically a "wavy" appearance that follows the fusion line topography, i.e., the weld passes. Some fracture appearances were complex because of several crack growth and arrest areas. The same crack growth and arrest can be seen in load-deflection curves as several load drops, if it has happened. The FA values are still more exact when the area is drawn by hand than if the EN ISO 148-1:2009 (2009) standard method would have been used.

Table 5 Summary of transition temperatures and upper shelf values measured for the as-received and 5000 hours aged materials.

Material	T_{42J}	US_{KV2}	$T_{0.89mm}$	US_{LE}	$T_{FA50\%}$	US_{FA}
	(°C)	(J)	(°C)	(mm)	(°C)	(%)
As-received	-35.2	186.8	-20.38	2.03	-14.0	100
Aging, 5000 hours	-2.3	218.1	5.07	2.02	14.0	100

As a quality check of the data some correlations are presented. Energy vs. lateral expansion and energy vs. fracture appearance charts are very linear for both the as-received and 5000 hours aged conditions, see Figure 48 and Figure 49. Specimens 1A, 2A, 4A and 5A from the as-received condition and specimens 1, 2, 3, 4, 9, 10 and 16 from the 5000 hours aged condition are excluded in these correlations. If a data point is further away from the trend line, the result may not be correct and lateral expansion or fracture appearance would need to be re-measured. All the correlations are good and they confirm good quality of the measured data.

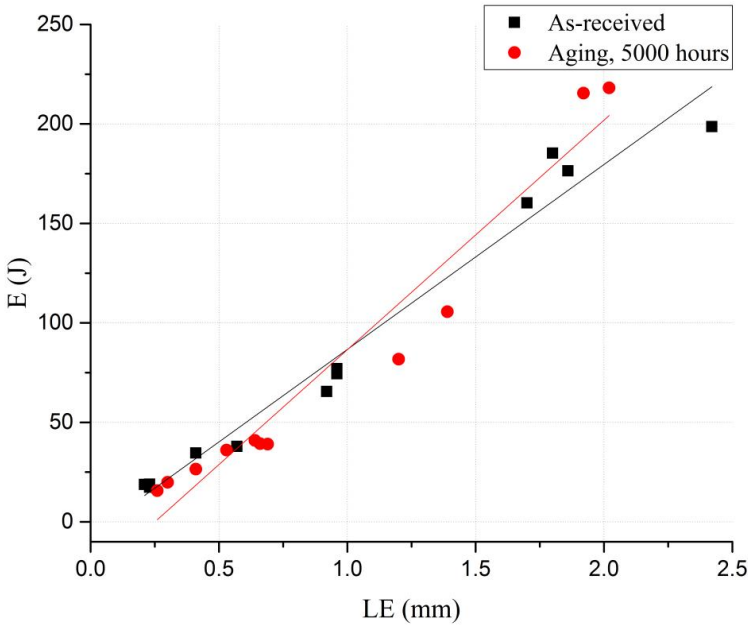

Figure 48 Absorbed energy vs. lateral expansion chart, for the as-received and 5000 hours aged conditions.

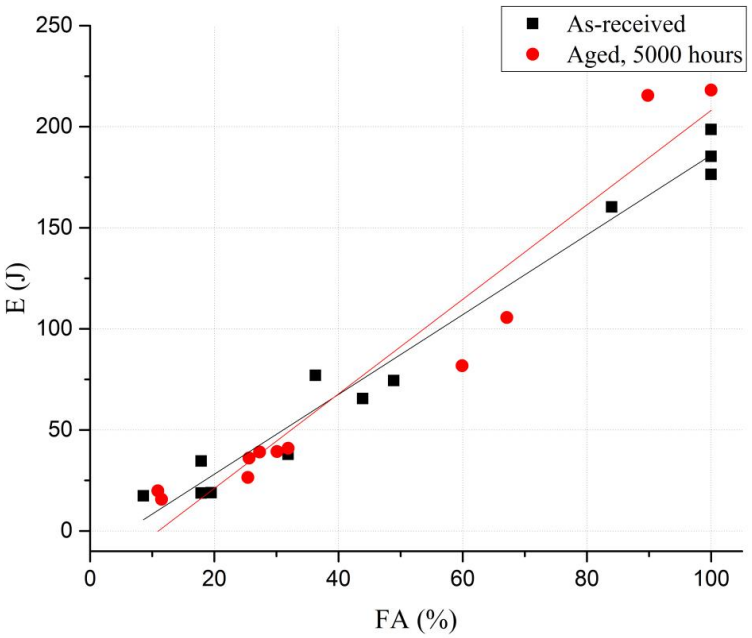

Figure 49 Absorbed energy vs. fracture appearance chart, for the as-received and 5000 hours aged conditions.

4.7 Estimation of transition temperature T_{42J} for 10000 hours aged condition

The 10000 hours aged condition was not tested within the framework of this thesis, but will be done later. An estimation of transition temperature T_{42J} can be calculated using Equation 9:

$$T_{42J} = A' * B^D \quad (9)$$

where A' is a fitting parameter, B is thermal aging time in years and D is an exponent. The exponent for the estimation is 0.5 and for lower and upper limits it is 0.3 and 0.8 (Wallin 2016). The fitting parameter A' for this estimation is 6. The estimation is presented in Figure 50. The estimation was set to start from -35.2 °C. 5000 hours of aging at 400 °C corresponds to 30 years of normal operation and 10000 hours of aging at 400 °C corresponds to 60 years of normal operation based on segregation of phosphorus calculated with McLean model, presented in the study of Druce et al. (1986). The estimation suggests that T_{42J} would be 11 °C, while lower and upper limits give a temperature range from 5 °C to 22 °C.

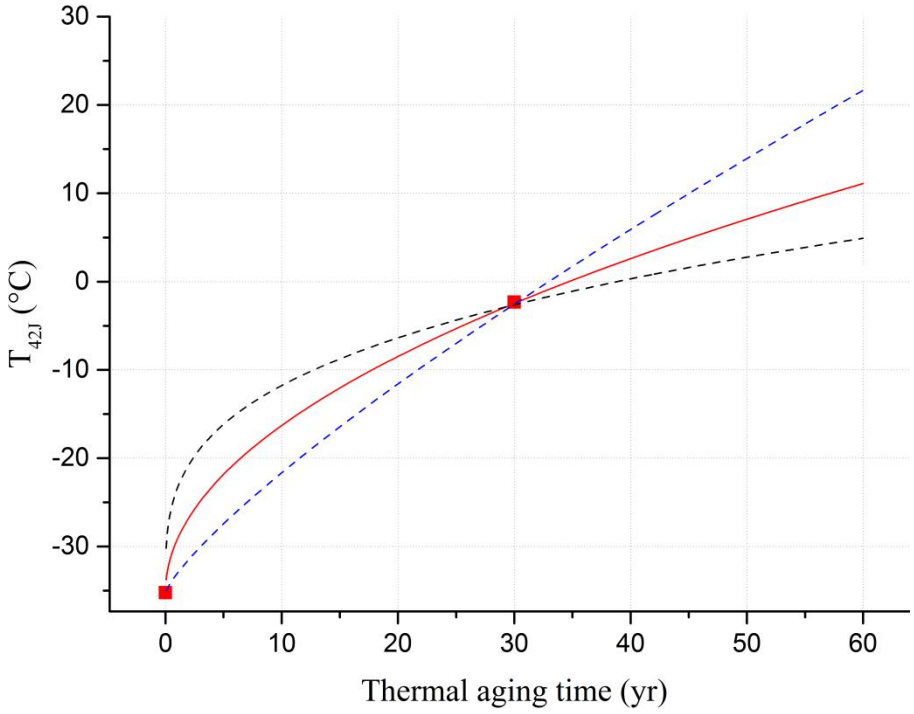

Figure 50 Estimation of the transition temperature, T_{42J}, for the 10000 hours aged condition with lower and upper limits, 5000 hours at 400 °C corresponds to 30 years and 10000 hours at 400 °C corresponds to 60 years of normal operation. The estimation suggests that T_{42J} would be 11 °C, lower and upper limits give a temperature range from 5 °C to 22 °C.

4.8 Estimation of crack arrest

The crack arrest load vs. temperature data measured for the as-received condition and 5000 hours aged condition are shown in Figure 51 and Figure 52. The scatter of data is small for the as-received condition and the data set of valid values is large enough to allow for the determination of the 4 kN crack arrest load transition temperature. The data obtained from the 5000 hours aged condition is slightly more scattered, but nonetheless here the data set of valid values is enough for estimating the 4 kN crack arrest load transition temperature.

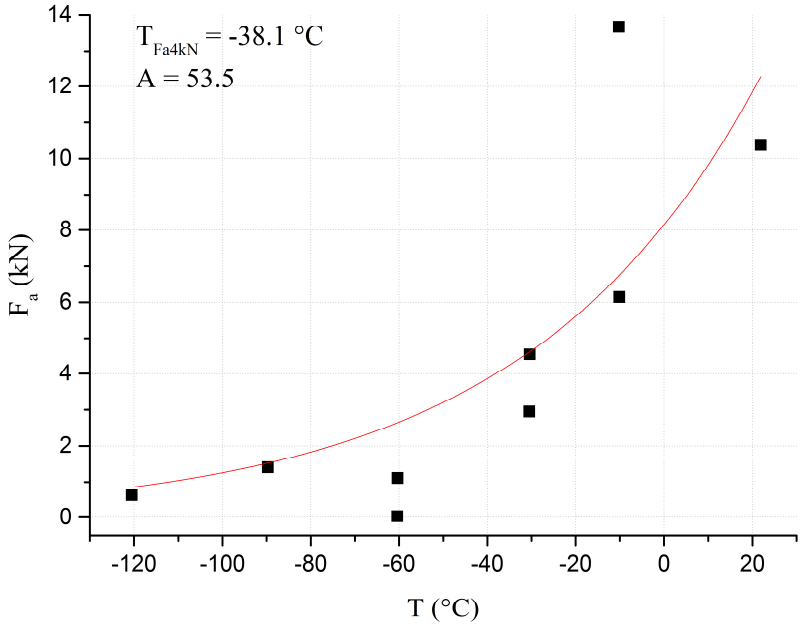

Figure 51 Crack arrest force vs. temperature on as-received condition. The fitting parameter T_{Fa4kN} is -38.1 °C and A is 53.5.

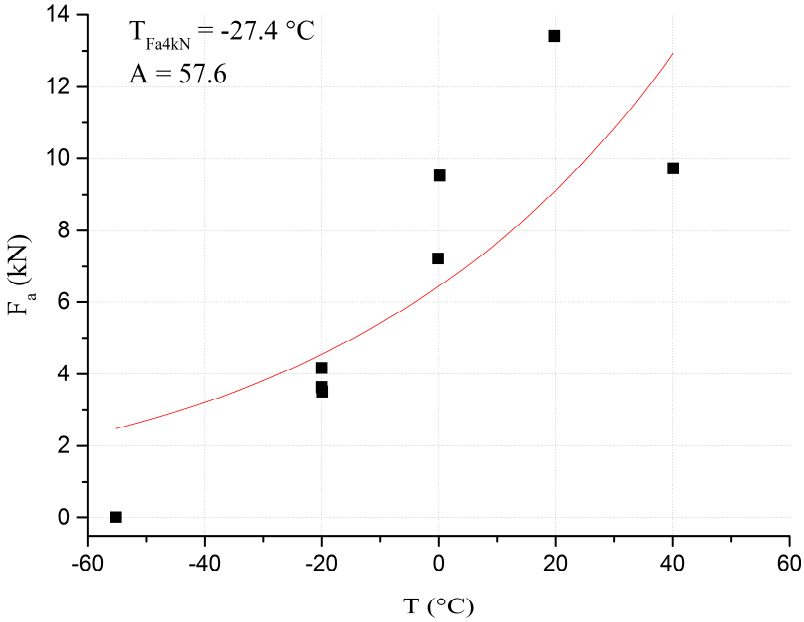

Figure 52 Crack arrest force vs. temperature on 5000 hours aged condition. The fitting parameter T_{Fa4kN} is -27.4 °C and A is 57.6.

The transition temperatures of the 4 kN crack arrest load (T_{Fa4kN}) and the consequent estimations of T_{KIa} are summarised in Table 6 together with the estimated T_0 data which are given for comparison.

Table 6 Estimates of crack arrest and initiation temperatures based on Charpy-V data.

Material	T_{FA4kN}	T_{KIa}	T_0
	(°C)	(°C)	(°C)
As-received	-38.1	-26.7	-64.3
Aging, 5000 hours	-27.4	-16.0	-30.8

4.9 Data from instrumented tests

The characteristic load values, determined from the load-deflection graphs, depend on thermal aging and test temperature. F_{gy}, which corresponds to general yielding of the specimen, with regards to testing temperature is shown in Figure 53.

The maximum load parameter F_m is determined in the same way as parameter F_{gy}. The behaviour of the test material is shown in Figure 54.

The crack arrest load was used to determine the crack arrest fracture toughness transition temperature, T_{KIa}, through its correlation with crack arrest load F_a = 4 kN. Crack initiation and crack arrest loads F_u and F_a, measured from the instrumented curves, are shown for the test material in Figure 55.

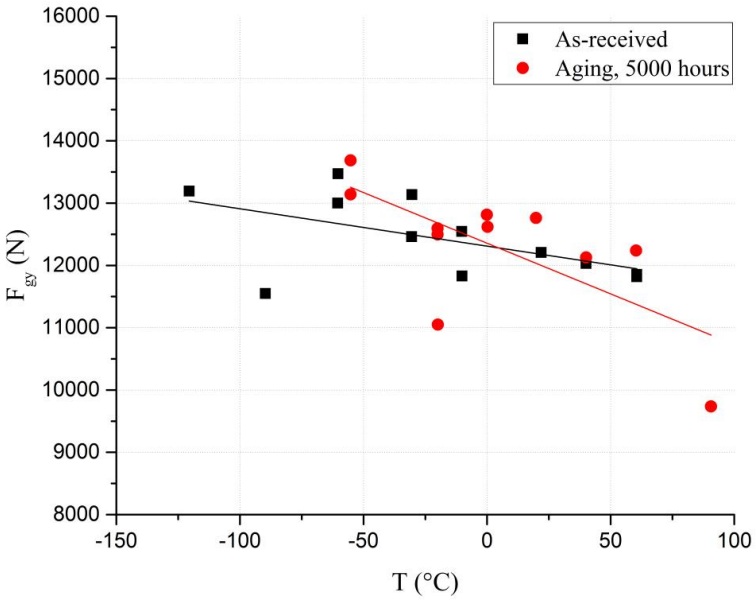

Figure 53 General yield load F_{gy} as a function of temperature for the given test material.

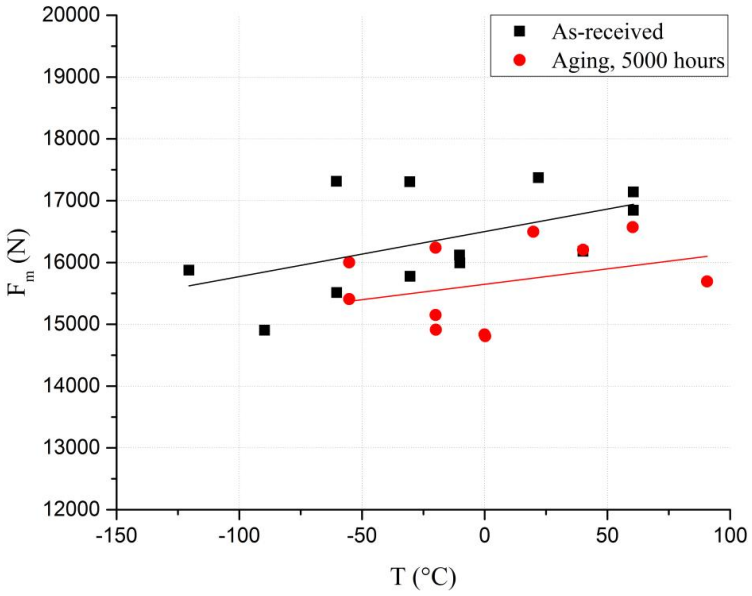

Figure 54 Maximum load F_m as a function of temperature for the given test material.

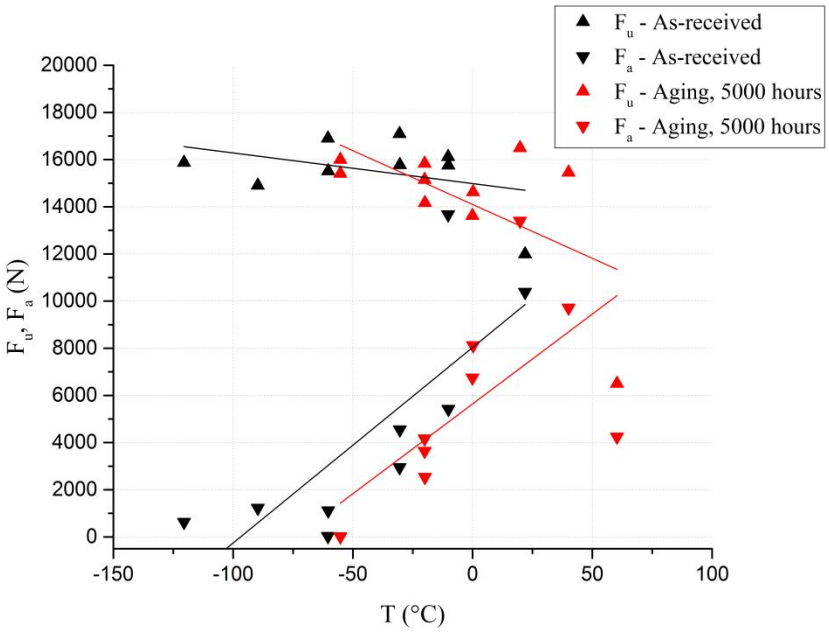

Figure 55 The onset of unstable crack propagation F_u and the crack arrest load F_a for the given test material.

4.10 Fracture surface examination

Fracture surfaces were examined by SEM at VTT. Typical brittle (cleavage) and ductile fractures of pressure vessel steel with different magnifications are shown in Figure 56 and Figure 57. The specimen in Figure 56 is the as-received specimen 2B (KV_2 = 17.4 J), the images were taken approximately 1.5 mm away from the V-notch. The specimen in Figure 57 is the as-received specimen 5B (KV_2 = 176.4 J), the images were taken approximately 1 mm away from the V-notch. On the bottom of a dimple is a round manganese sulphide inclusion, which is a nucleation site for ductile fracture, is seen in the image of 3000x magnification. As expected, the ductile structure is much more deformed than the brittle. However, fractures were not only brittle or ductile. There was also a mix of cleavage and ductile fractures seen, which is typical for fractures in the transition range.

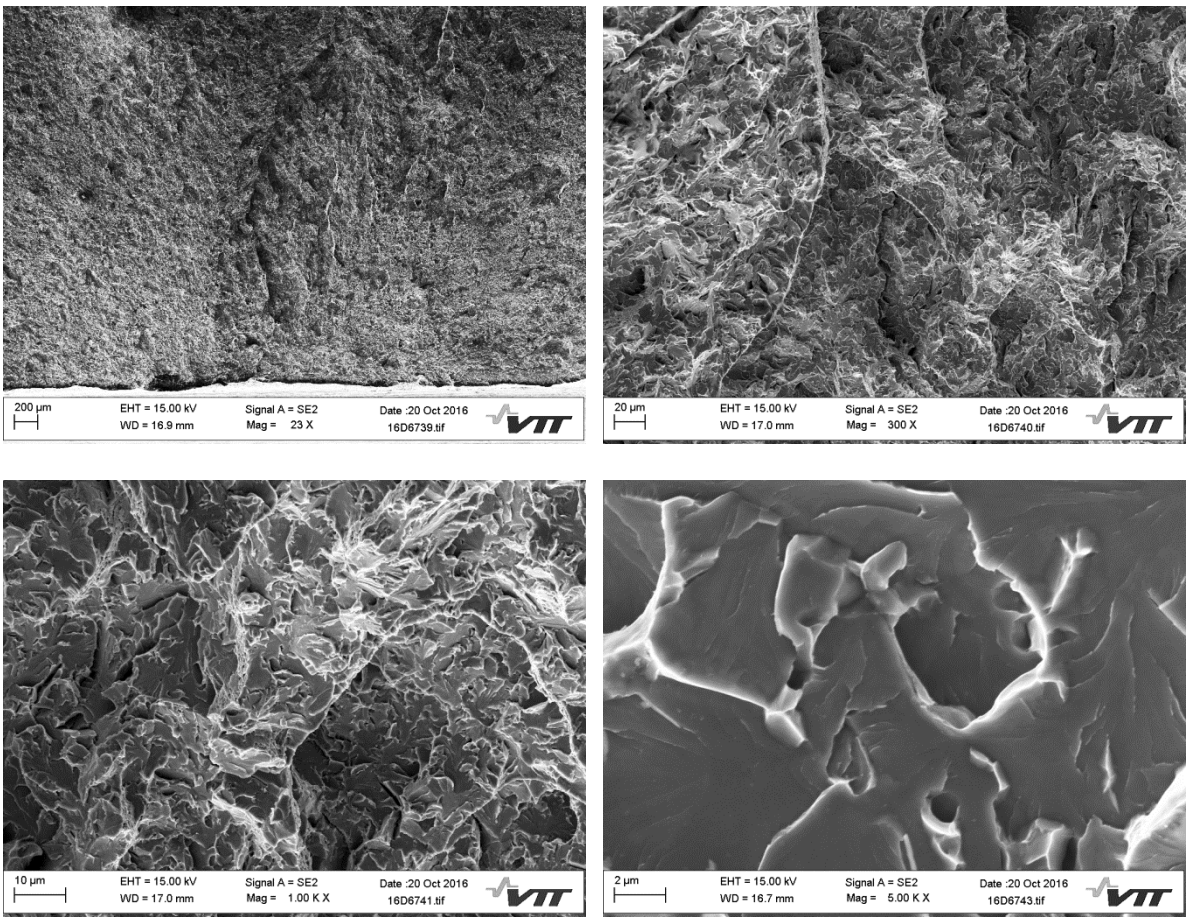

Figure 56 As-received specimen 2B, the location of SEM (SE) images approximately 1.5 mm away from the V-notch, typical cleavage fracture, magnifications 23x, 300x, 1000x and 5000x. KV_2 = 17.4 J.

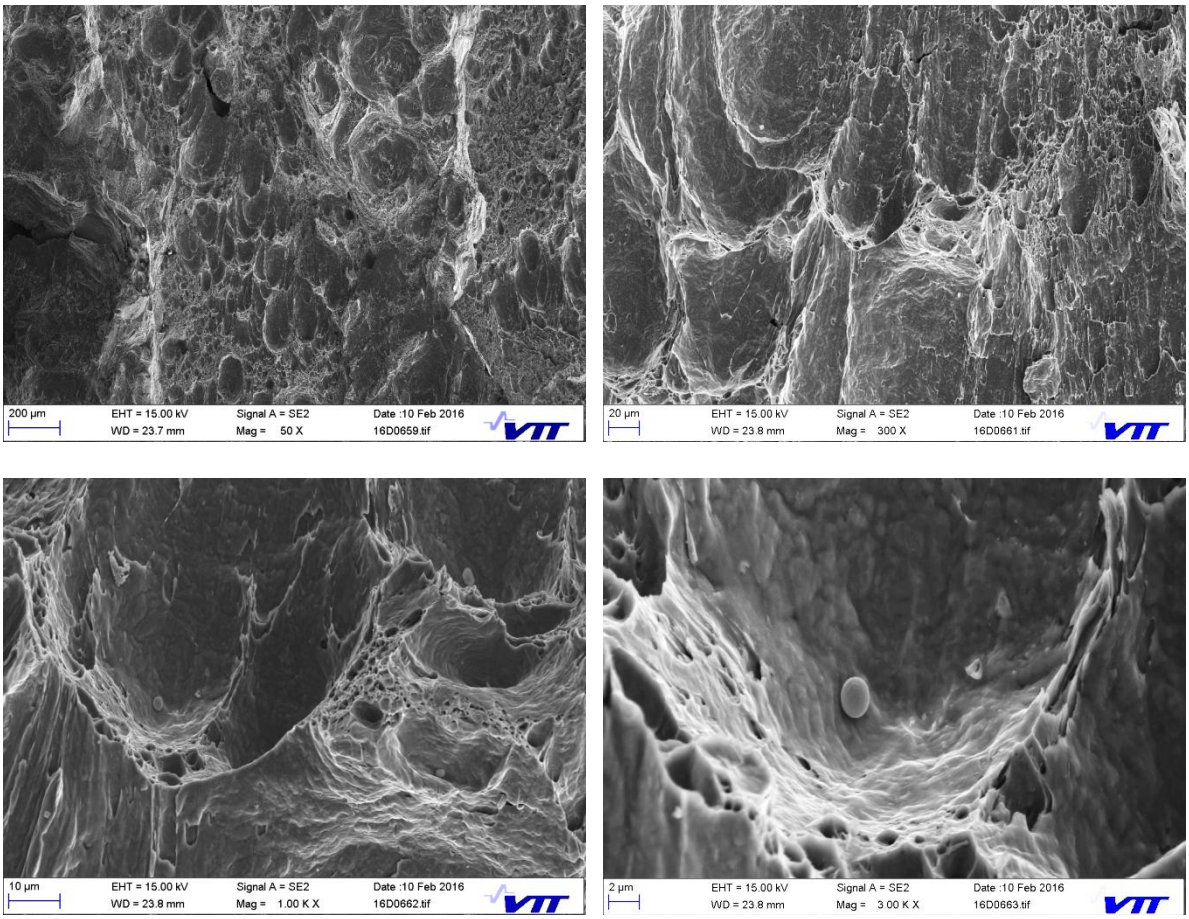

Figure 57 As-received specimen 5B, the SEM (SE) images were taken approximately 1 mm away from the V-notch, typical ductile fracture, a round MnS inclusion is seen in the image of 3000x magnification, magnifications 50x, 300x, 1000x and 3000x. KV_2 = 176.4 J.

Some brittle fracture surfaces with incorrect V-notch position included cleavage facets on the different plane as the rest of the fracture. This kind of behaviour was only seen with the as-received condition when the fracture mechanism was brittle and the V-notch was fully on the nickel-base alloy side. Figure 58 shows the cleavage facets of as-received specimen 4A. The location of the cleavage facet is close to the nickel-base alloy, where crack growth has propagated to towards the heat-affected zone. The crack nucleation site is marked with red arrows. The nucleation site is close to a Cu inclusion, which Cu composition is 25 % according to EDS analyses. The size of the inclusion is 10 µm. Another Cu inclusion is marked with a yellow arrow in the image with 3000x magnification. The cleavage facets are interesting because the fracture has propagated both downwards and forward along the main fracture surface plane.

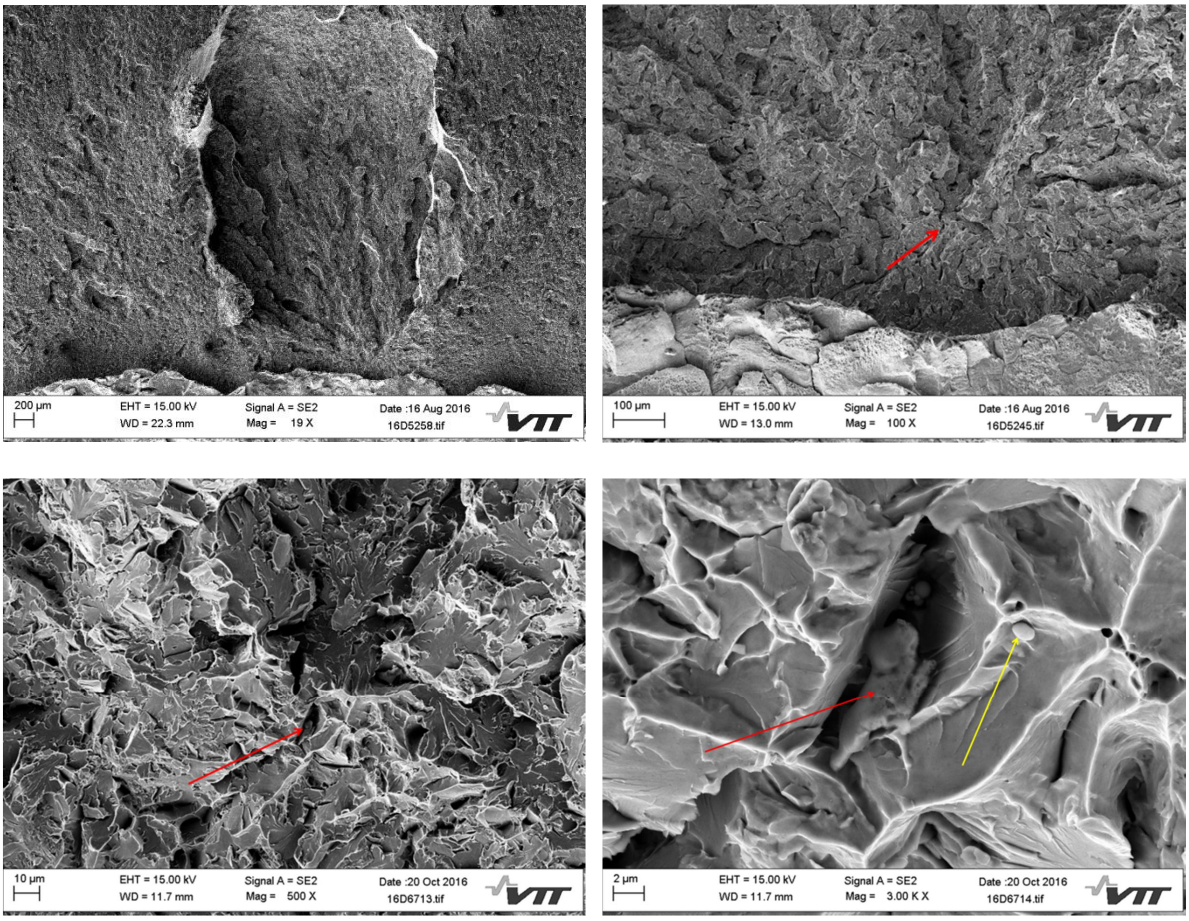

Figure 58 The as-received specimen 4A, the location of SEM (SE) images is close to the nickel-base alloy, where crack growth has propagated to HAZ, cleavage facet in a brittle fracture surface, the Cu inclusion close to the nucleation site is marked with red arrows, size of the inclusion is 10 µm. Another Cu inclusion is marked with a yellow arrow, magnifications 19x, 100x, 500x and 3000x.

Two cleavage fracture nucleation sites are presented in Figure 59. In most of the brittle fracture surfaces neither inclusions nor precipitates were seen. The distances from the V-notch are 130 µm (specimen 1B) and 200 µm (specimen 7). In Figure 59 an overview image of the area is seen as well at 5000x magnification of the nucleation sites, which are marked with red arrows.

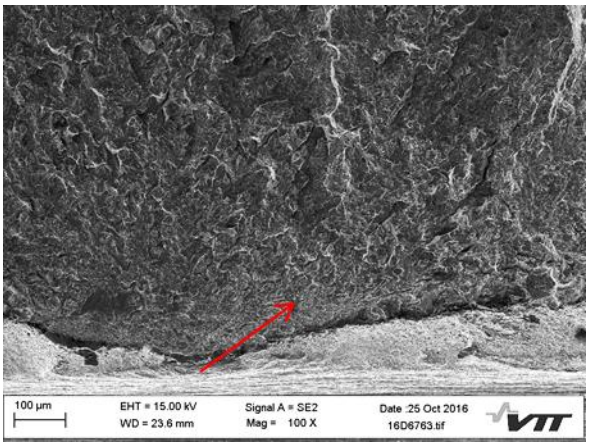

As-received specimen 1B

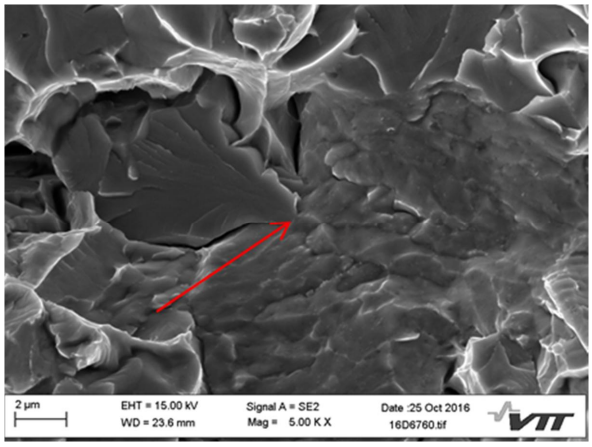

As-received specimen 1B

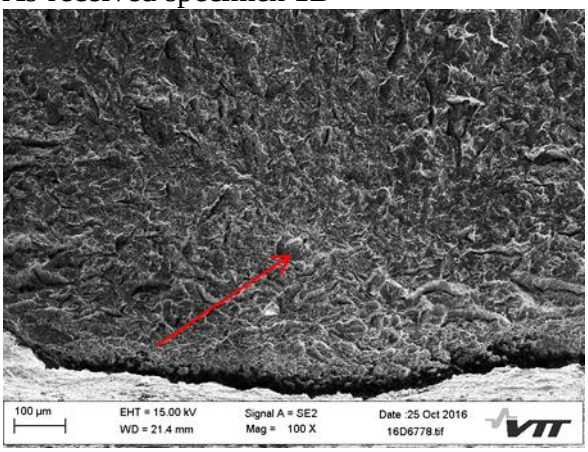

5000 hours aged specimen 7

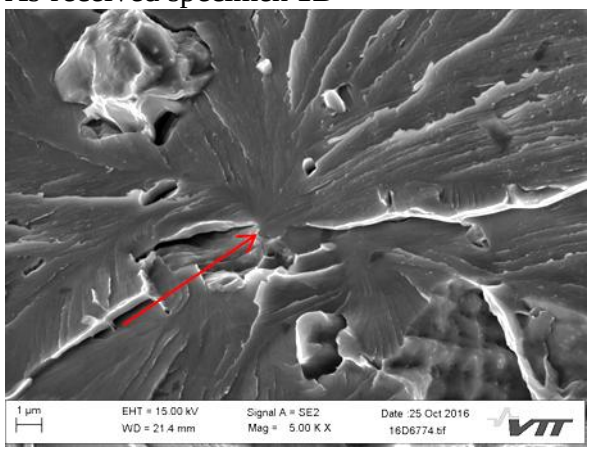

5000 hours aged specimen 7

Figure 59 Cleavage fracture nucleation sites of as-received specimen 1B and 5000 hours aged specimen 7 close to the V-notch. The nucleation sites are marked with red arrows, magnifications 100x and 5000x.

4.10.1 Welding defects

Small welding defects were seen in specimens with an incorrect V-notch location. It was typical for these defects to be located either close to the V-notch or in the area from which the crack growth propagated from the nickel-base alloy to the heat-affected zone. Small welding defects also existed in some specimens with correct V-notch locations, but where the V-notch was very close to the fusion line. In addition, these specimens showed ductility. The size of areas, where the defects located, varied from a few hundred microns up to discontinuous areas with a size of one millimetre. Areas included large areas of dendritic structure and small defects. There are several small pores, size 1-10 µm, in the weld defect area. The total amount of weld defects in fracture surfaces is very small.

Welding defects seen in fracture surfaces are shrinkage porosities. Porosities are formed during solidification and caused by gases that are trapped in the molten weld during the solidification process. Porosity is not as serious a defect as cracks primarily since shrinkage porosities usually have rounded ends and will not propagate like cracks (Cary & Helzer 2005).

The as-received specimen 2A, with a welding defect, is shown in Figure 60. The welding defect type is shrinkage porosity. Plenty of Cr-rich, based on the EDS analyses, most likely $M_{23}C_6$ carbides are seen on the dendritic surface of the defect. The specimen had incorrect V-notch location. The location of the images is approximately 1 mm from the V-notch and marked with a red circle. The carbides are marked with a red arrow.

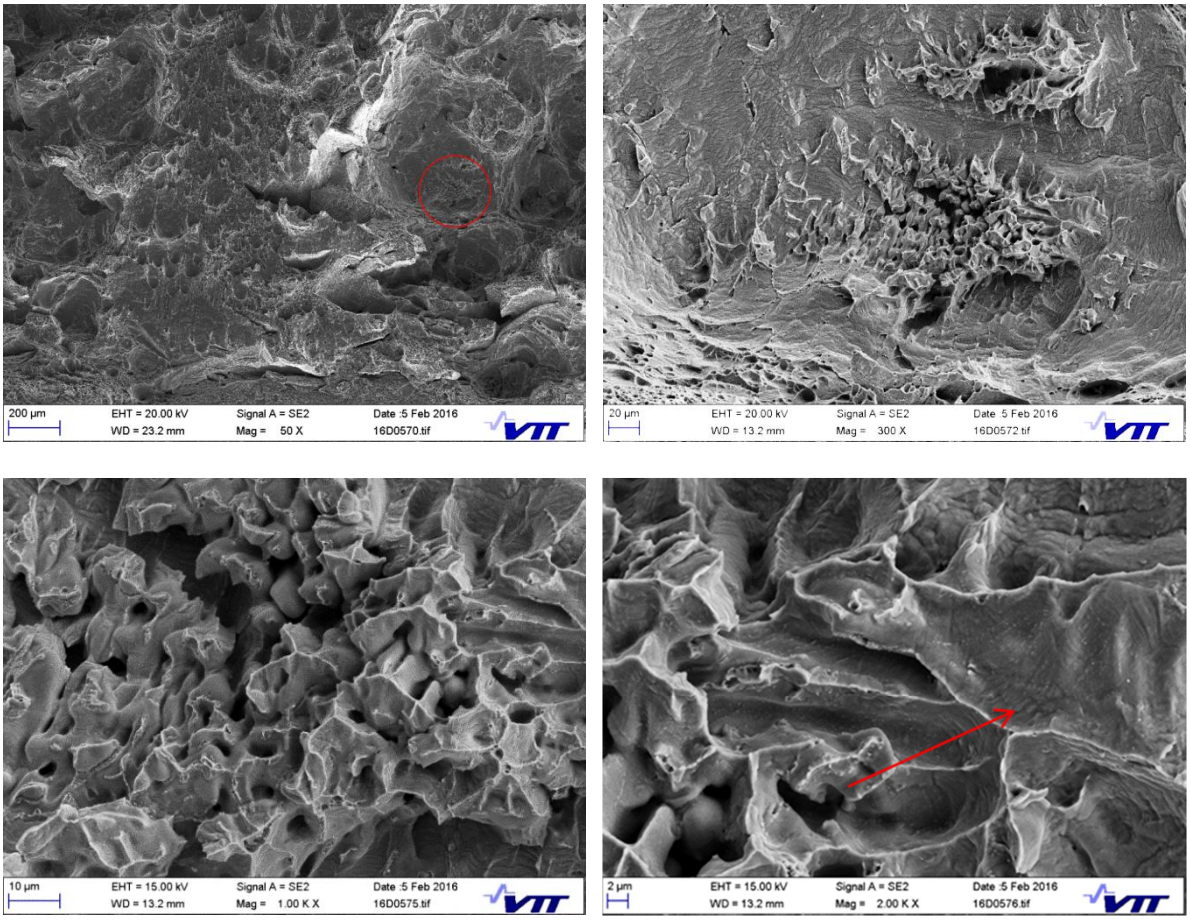

Figure 60 As-received specimen 2A with a welding defect, the location of SEM (SE) images is approximately 1 mm from the V-notch, magnifications 50x, 300x, 1000x and 2000x. The exact locations of greater magnification are marked in the image of 50x magnification with a red circle. Cr-rich $M_{23}C_6$ carbides on the surface of the defect are marked with a red arrow.

A welding defect, marked with a red circle, was seen in the 5000 hours aged specimen 2, Figure 61. The specimen had an incorrect V-notch location, and located in the weld metal. The area with shrinkage porosity defects is approximately 1 mm from the V-notch, which can be partially seen in the bottom of the image with a magnification of 21x. The carbides, which are seen on the dendritic surface of the defect, are most likely Cr-rich $M_{23}C_6$ carbides, which are seen in the InLens images. The average size of carbides is less than 0.5 µm.

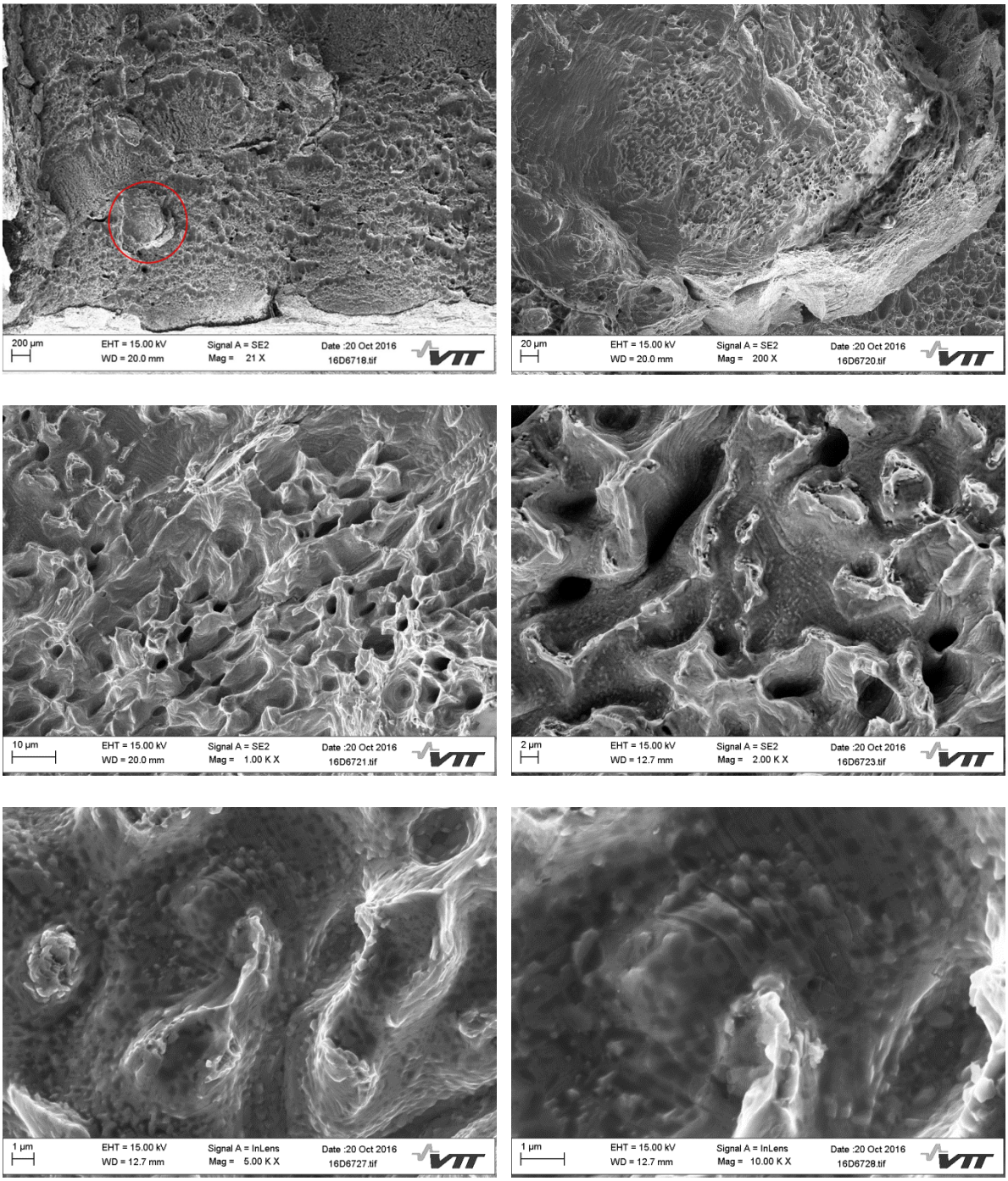

Figure 61 A welding defect seen on the fracture surface of specimen 2 approximately 1 mm from the V-notch. SEM (SE and InLens) images. It is most likely that Cr-rich $M_{23}C_6$ carbides are seen on the dendritic surface of the defect, magnifications 21x, 200x, 1000x, 2000x, 5000x and 10000x.

The 5000 hours aged specimen 8, with a welding defect is shown in Figure 62. The specimen had a correct V-notch location. The location of the welding defect is 200 µm from the V-notch and is marked with a red circle. The surface of the defect is dendritic. According to EDS analysis Ti particles, marked with red arrows, were seen on the surface of defect.

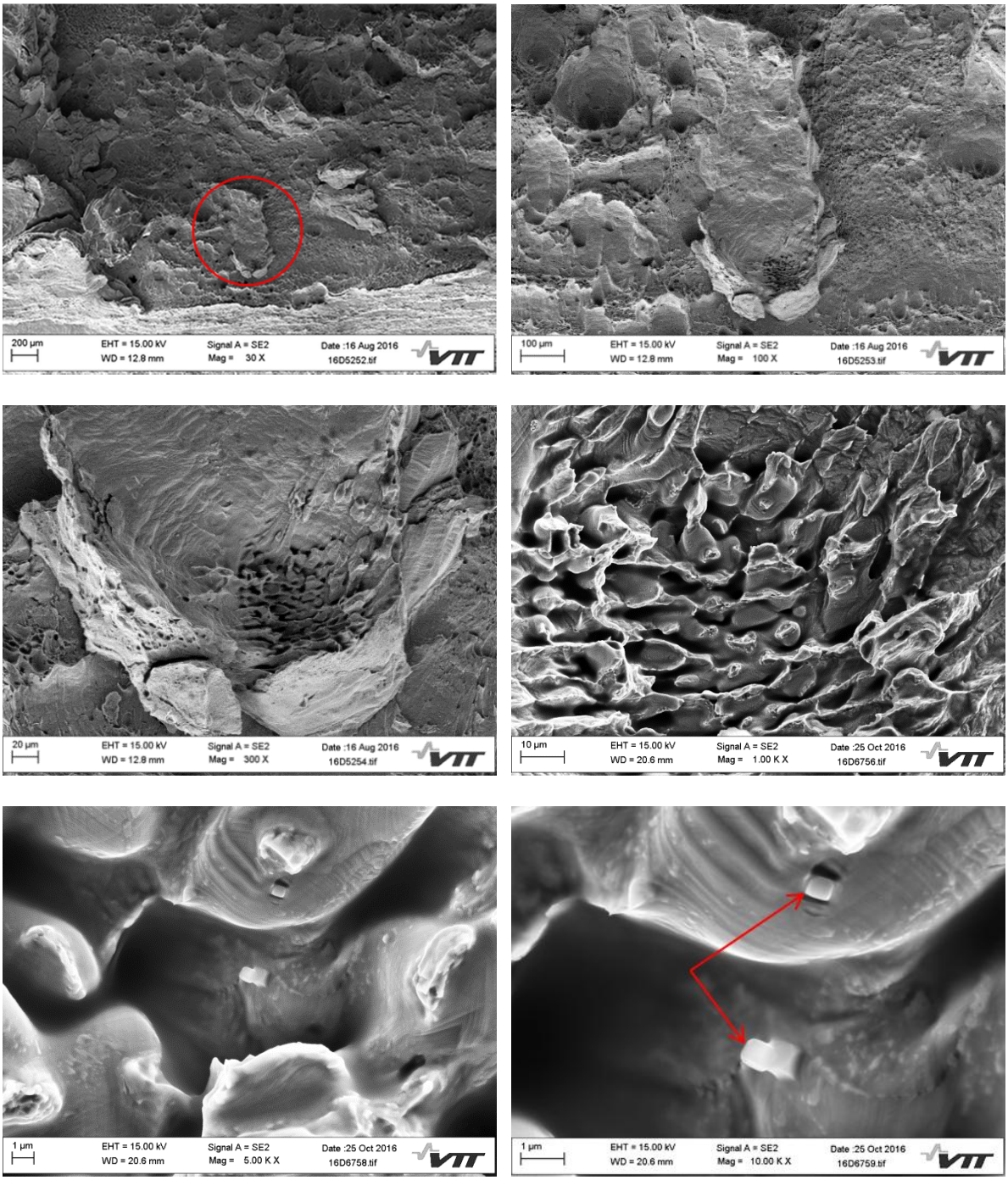

Figure 62 A welding defect, marked with a red circle, seen on the fracture surface of 5000 hours aged specimen 8 approximately 200 µm from the V-notch. Ti particles are marked with red arrows. SEM (SE) images, magnifications 30x, 100x, 300x, 1000x, 5000x and 10000x.

5 Discussion

Segregation of P to grain boundaries in pressure vessel steels during service at elevated temperatures is a recognised aging degradation mechanism in low-alloy steels. The segregation of P to grain boundaries promotes a change in the brittle fracture mode from transgranular to intergranular, and degradation in mechanical properties. Joly et al. (2014) proposed that the main degradation mechanism of the HAZ could be segregation of P, which was believed to be observed after 10000 hours thermal aging as an intergranular fracture.

In the performed investigations reported here, degradation of mechanical properties was seen in Charpy-V testing as an increase in transition temperature of 33 °C. The whole transition curve has shifted to the right after thermal aging. However, fracture surface examinations of 5000 hours aged samples at VTT showed no signs of intergranular fracture. The thermal aging times of AREVA and VTT are, however, different, being 10000 hours in the AREVA study and 5000 hours in this study. It is also possible that P has segregated to grain boundaries after 5000 hours aging time, but this would require further investigations. P segregation continues after 5000 hours with an increasing peak height ratio according to Figure 7, and signs of intergranular fracture shall be carefully investigated in the 10000 hours aged specimens after mechanical testing.

Thermal aging can affect the growth of secondary particles (inclusions and/or precipitates), which could be one reason for the observed degradation. MnS inclusion sizes, which were located at the nucleation sites of ductile fractures on the bottom of dimples, were measured with SEM from several fracture surfaces. No evidence of inclusion/precipitation growth was indicated during fractographic examinations. The average size of MnS inclusions was the same after 5000 hours aging. Several brittle fracture surfaces were examined. In most of the cases no inclusions were seen on nucleation sites, see Figure 59.

Strain aging in low-alloy steels result from interactions between dislocations and the interstitial atoms of nitrogen and carbon. Strain aging can cause an increase in yield and flow stress, a decrease in ductility, an increase in ductile-to-brittle transition temperature, and reduction in upper shelf energy. These results do not support strain aging mechanism. According to EPRI (2003) strain aging embrittlement is insignificant for carbon and low-alloy steels used in PWRs.

So far none of the degradation mechanisms support the fact that the absorbed energy of upper shelf increased after 5000 hours aging time. Higher upper shelf energy could be explained with the small number of fully ductile specimens. If more specimens would have been tested at 90 °C, the specimens should show both 100 % ductility and simultaneously relatively low absorbed energy. Only that would lower the average value of upper shelf energy. Then, that would lead to larger scatter all over the transition curve. Now there is only a little scatter in the transition curve and the shape of the curve looks very good, indicating the small number of specimens is not the reason. Druce et al. (1986) have studied impact toughness properties of A533B steel. In their study different V-notch locations in HAZ and different aging temperatures (300 °C - 550 °C) were used. It was shown that upper shelf energy increased at 450 °C when thermal aging time was increased

from 2000 hours to 10000 hours. The V-notch was located in grain-coarsened HAZ, where the grains are larger. It is known that grain refinement enhances impact toughness properties and decreases the transition temperature. If the grain size grows during thermal aging, it would increase the transition temperature. This could be an aspect for the increased upper shelf energy. On the other hand, according to global trend, the upper shelf energy decreases after 10000 hours aging time. If it really decreases, the grain growth does not explain that. Grain growth during thermal aging should be considered as an option for degradation and, therefore, it should be studied in detail. Segregation of P can be the main degradation mechanism, but there are no clear evidences of that yet. Therefore, the P segregation and other mechanisms need to be studied carefully after 10000 hours aging time. APT could be one analysis method to study the segregation, since it has been a useful tool to understand thermal aging and irradiation damage in RPV steels (Styman et al. 2013).

Cross-section examination of tested specimen halves showed that brittle fracture crack paths of the as-received and 5000 hours aged conditions showed similarities. The distances from the fusion line did not differ much. The distance of crack paths of as-received condition from the fusion line is most of the time from a few microns up to 20 µm and in the case of 5000 hours aged condition from a few microns up to 40 µm. According to microstructure images, Figure 18 and Figure 20, the carbon-depleted zone in the LAS heat-affected zone is wider after aging. The width of carbon-depleted zone in as-received condition is 35-40 µm and in 5000 hours aged condition 60-70 µm. The weakest zone of HAZ was carbon-depleted zone in both material conditions. According to Joly et al. (2014) the crack paths of AREVA's as-received condition showed similar behaviour.

The microstructure of DMW joint was examined. SA 508 heat-affected zone with microstructural zones typical of low-alloy steel was detected including partially grain-refined HAZ, grain-refined HAZ, grain-coarsened HAZ and carbon-depleted zone. Macro-segregation bands are seen in the HAZ, see the overview of SA 508 and SA 508 HAZ in Figure 18. The width of the HAZ is approximately 2 mm. The microstructure of the base metal is bainitic. The HAZ closer to the fusion line has experienced higher temperatures during welding. Thus, a higher fraction of austenite forms. After cooling, the austenite transforms into a fine distribution of ferrite grains and bainite. Along the fusion line, the temperature is at its highest. It triggers the growth of austenite grains and forms the grain-coarsening zone. The CDZ has formed as a result of carbon migration at high temperature from the base metal to the weld metal due to the composition gradients (Hänninen et al. 2014). From the Alloy 52 weld metal a martensitic layer, a partially-melted zone, migrated grain boundaries and LAS swirls were detected. The discontinuous grain boundaries seen in the microstructure images are most likely Type II boundaries. Some microstructural changes can be seen after aging heat treatment, e.g., precipitations are closer to fusion line in the weld metal. They are also larger, which can be seen if the SE images of elemental mapping locations, Figure 22 and Figure 25, are compared.

A very good elemental overview of the fusion line, including areas from the HAZ near fusion line of the pressure vessel steel and nickel-base alloy, in both its as-received and 5000 hours aged conditions, was obtained by WDS analysis. Since the mappings are qualitative the distribution of elements is fully comparable but the element content is not. On the pressure vessel steel side of the as-received condition the elemental distribution of Fe and its alloying elements is very uniform. The Mn distribution is no longer uniform

after thermal aging indicating Mn segregation. Mo is also showing signs of segregation but not to the same extent as Mn. Some Cr-rich precipitates are seen in elemental mappings of the 5000 hours aged condition in Figure 25, when comparing the small bright spots of Cr and C. A weld pass boundary can be seen in the elemental mappings in location, where a new weld pass is welded onto the previous one, close to the fusion line. The microstructure of this area is inhomogeneous. According to Wang et al. (2013c) a larger variation in the concentration of the main elements Cr, Ni and Fe within the interface regions, is caused by element migration driven by the concentration gradient during welding process. Migrations of these elements contributed to the formation of the complex microstructures. These variations can be seen in the WDS images taken from the fusion line. It is also interesting to see segregation of Ti on the fusion line in the as-received condition. These segregations can be Ti precipitates due to welding and post-weld heat treatment. Hou et al. (2010) have shown in their study that the dominant precipitates are Ti and Nb carbides. However, Nb was not analysed in this study with EPMA. SSGBs are visible in the elemental mappings of the fusion line, Figure 26. On the nickel-base alloy side of the as-received condition a well-defined dendrite structure is present especially in the elemental mappings of Fe, Cr, Ni, Mn and Ti. In the 5000 hours aged condition different orientations of SSGBs are seen because of grain structure. These boundaries are visible in the mappings due to segregation of elements.

The line scans provided a good overview of the chemical composition over the fusion line. The line scans are quantitative and, therefore, fully comparable. The concentration gradients near the fusion line of the main elements (Fe, Ni, Cr) in the as-received condition are clearly seen. The concentration of the steel alloying elements, Mn and Mo, decreases when the scan moves towards the nickel-base alloy side. The content of nickel-base alloy elements, Al and Ti, increases, respectively. The Ti peaks in weld metal, seen in Figure 29 are probably due to precipitation, which can also be seen as bright spots in the elemental mapping in Figure 24. The Si content stays almost the same. There are several peaks in the line scans, but the changes in the contents are clear. The line scans are well consistent with the elemental mappings. When the line scans are compared to the chemical contents in Table 1, it is seen that the chemical content of Fe in Alloy 52 is clearly lower than the line scan content. The Fe content in line scans is approximately 16 %, while the iron content of the weld filler metal is 10 %. The content of Cr is almost the same and the content of Ni is 4 % lower (55 % compared to 59 %). The contents of Mn and Mo are much higher in the line scans. The content of Ti is the same, but Al is lower. The content of Mn in SA 508 is lower and the content of Mo higher, respectively. These are the result of dilution.

When comparing the line scans of the two conditions, diffusion during thermal aging is clearly seen. The Fe content in heat-affected zone has decreased and in weld metal it has increased. The Mn content has increased in heat-affected zone because of thermal aging. The contents of Ni and Cr are lower in the weld metal. Also, the contents of Cr and Ni are slightly lower in heat-affected zone very close to the fusion line, Figure 63. However, only a few line scans were analysed and the contents may be slightly different in another location i.e. specimens near weld root may have a slightly different chemical composition or Cr precipitations were grown further away from the line scans. Choi et al. (2015) have discussed in their study that Cr diffusivity is low in ferrite. Their EDS analyses show that the Cr and Ni contents decrease in HAZ of A533B base metal during thermal aging. In addition, quality of preparation, accuracy of elemental reference standards, focusing of the beam or X-ray diffraction's location on the Rowland circle may cause measurement errors.

The Ti peak seen in Figure 32 is large. Al and Mo show similar behaviour as in the as-received condition. There are no Si peaks in line scans of the 5000 hours aged condition. In the as-received condition, a significantly higher Fe content, as compared to the nominal content of Alloy 52, was measured in the line scans. This is very likely explained by dilution and intermetallic diffusion. The slightly lower Ni content is probably also due to dilution. The thin martensitic layer, which can be seen in the optical microscopy image in Figure 19, is also difficult to see in the line scans. This layer should be located near the fusion line, but it is possible that it does not exist in the specific locations at which the line scans were conducted. It is advisable to carry out WDS analyses also for the 10000 hours aged condition.

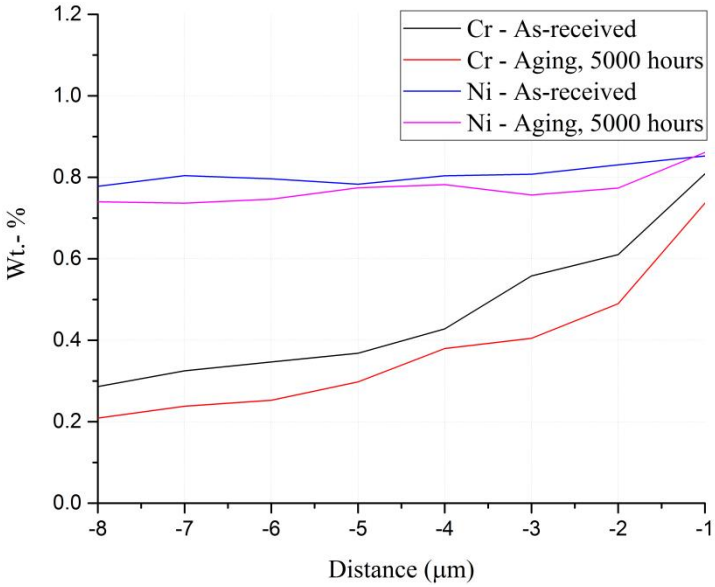

Figure 63 The contents of Cr and Ni of the as-received and the 5000 hours aged conditions in HAZ close to the fusion line, fusion line is in the location of 0 µm.

The samples, which were examined with EPMA, were also examined with optical microscopy. This examination supported the WDS analyses. It is very likely that the grain boundary seen in the optical microscopy image of the tested specimen 5A is a Type II boundary in Figure 34. Based on literature, Type II boundaries are typically located less than 100 µm away from fusion line, but as the microstructure image showed, they can be formed much further away from the fusion line. The narrow-gap welding method and different welding parameters compared to conventional V-grooved weld method may be one reason for the further distance of Type II boundaries. In the line scan, the contents of Ni and Cr are not clearly decreasing in the vicinity of a Type II boundary. According to Ahonen et al. (2016) and the optical microscopy images of Aalto University, Type II boundaries are not continuous in the MHI mock-up, but occur only close to weld bead boundaries. The SSGBs seen in Figure 35 can also be seen in the elemental mappings of the fusion line in Figure 26.

The transition temperature T_{42J} established for the as-received and 5000 hours aged conditions is based on test results in the lower transition range and is thus reliable and usable as such for further assessments of the material. In total 34 specimens were tested, while only the results of 23 specimens were acceptable. The number of acceptable

specimens may arise questions, but on the other hand the transition curves are very good and only a little scatter can be seen.

The Charpy-V test results clearly show that thermal aging has affected test material's ductility and impact toughness properties. When comparing the results obtained from the tested materials, it is clear that transition curve has shifted to the right after thermal aging. The shifting is a result of material's degradation. After thermal aging the material is still fully ductile but the initial upper shelf level is reached at a higher temperature. The degradation can also be seen as a change of the T_{42J} transition temperature from -35.2 °C to -2.3 °C. Furthermore, the $T_{0.89mm}$ increased from -20.4 °C to 5.1 °C and the $T_{FA50\%}$ increased from -14.0 °C to 14.0 °C. When comparing the transition curves, Figure 43 and Figure 47, where all the tested specimens are included, the transition temperature difference and also the scatter are lower in the thermally aged condition. This indicates that the strength mismatch effect near the fusion line is lowered due to thermal aging. The transition temperature T_{42J} for the 10000 hours aged condition was estimated. The estimation suggests that T_{42J} would be 11 °C, while lower and upper limits give a temperature range from 5 °C to 22 °C, where the transition temperature of the 10000 hours aged condition would fit.

Thermal aging can affect the Charpy-V test results in many ways. According to Boursier et al. (2005) the main tendency with thermal aging was a slight increase of strength and a decrease in ductility with increasing time and temperature, the ductile-to-brittle transition temperature increases and the upper shelf decreases. According to the estimations made using the results obtained from this thesis, the ductile-to-brittle transition temperature increases, while upper shelf does not decrease and, furthermore, the increase of strength would be more than slight. The aging times have been longer in the work of Boursier et al. (2005) and thermal aging phenomena after 5000 hours aging were not discussed. Andrieu et al. (2013) studied thermal aging embrittlement of A533B steel. Thermal aging temperature was 450 °C and time 5000 hours. As a result the transition temperature increased 39 °C from about -36 °C to 3 °C and upper shelf decreased a few joules compared to as-received condition. An EPRI Technical Report (2003) includes results for a 5000 hours aged condition, but the material, the thermal aging temperature and the welding method were different. Some comparison can be made between the as-received condition of VTT and AREVA. Joly et al. (2014) reveal only that the upper shelf energy for the as-received condition of AREVA's mock-up was 153 J, which is 32 J less than the upper shelf energy of Charpy-V test presented in this thesis. AREVA's specimen was tested at 100 °C and the specimen presented in this thesis at 60.6 °C. The Charpy-V test at VTT also shows that when the absorbed energy is 160 J at ambient temperature, the material is not fully ductile, but the ductility is 84 %. However, the chemical composition of AREVA's mock-up differs slightly from VTT's mock-up, which may explain the lower upper shelf energy.

Not much published results of DMWs or aging of 5000 hours, on a similar material to that studied in this thesis, were available. It is, therefore, difficult to say whether these results show a common trend. Choi et al. (2016) have discussed the hardening and softening phenomena during thermal aging, where hardening was equivalent to 15 years of service time and softening to 30 years of service time. In their study different activation energies were used, but it is still possible that 15 years of service time may be comparable to the 5000 hours of aging at 400 °C presented in this thesis. When the material is hardening the strength also increases. This can be seen in the results, Figure 40 and Figure 44, where the

upper shelf energy of the 5000 hours aged condition was considerably higher than the absorbed energy of as-received condition. If the study of Choi et al. (2016) is correct, the upper shelf energy should be lower after an aging for 10000 hours and the material has to become softer.

The Charpy-V test results suggest that the crack initiation fracture toughness of both the as-received condition and the 5000 hours aged condition is significantly higher than the corresponding crack arrest toughness, which can be seen at lower transition temperatures. It can be seen that the T_{KIa} value is approaching the T_0 value due to thermal aging. The temperature difference in the as-received condition is 37.6 °C and in the 5000 hours aged condition it has decreased to 14.8 °C.

When impact pendulum is instrumented with strain gauges, the instrumentation allows the test to be analysed in much more detail. According to the instrumented data the general yield load F_{gy} values decrease when test temperature is increased. The same cannot be said about the values of maximum load F_m which increases when test temperature is increased. Typically when the absorbed energy is low, the F_m values are high and when absorbed energy is high the F_m values are low. This type of behaviour was not seen for this material. The crack initiation load, F_u, and crack arrest load, F_a, approach each other at a point, where fully ductile behaviour starts. A degree of scatter is seen in the F_u and the F_a values. Several crack growth and arrest areas within a single fracture surface will cause scatter.

SEM examination of fracture surfaces of tested Charpy-V specimen halves showed typical brittle (cleavage) and ductile fracture types and also a mix of these fracture types. Cleavage facets on the fracture surfaces were seen only in two brittle specimens where the V-notch was machined completely on the nickel-base alloy side. In most cases local welding defects, shrinkage porosities, were seen in fracture surfaces of specimens with an incorrect V-notch position, but were also present in some more ductile specimens with correct V-notch positioning. This indicates that the crack path has been very close to the fusion line, in CDZ, and propagated through small welding defects where the required energy for fracture is lower. It is possible that cracks can propagate locally to the weld metal, but the whole crack front does not. The carbides, which are seen on the dendritic surface of welding defect, are most likely Cr-rich $M_{23}C_6$ carbides. To be sure, which carbide type is in question, a TEM analysis should be carried out.

When machining the specimens, care must be taken to ensure the correct location of the V-notches. This study has shown that an incorrect V-notch location, for example if it has been machined on the weld metal side and not in the HAZ, the absorbed energy is exaggerated, because of the FCC structure of the weld metal. The Ni-base alloy is ductile even at very low temperatures and it does not have a ductile-to-brittle transition region, like ferritic low-alloy steels. If the test results from the specimens with incorrect V-notch locations are included in the analysis, they cause both scatter and the results will be misleading, as the material's properties seem better than they actually are.

After testing and analysing the as-received and the 5000 hours aged conditions, only predictions can be made about how the material behaves with increasing thermal aging time. Therefore, it is essential to test the 10000 hours aged condition. In the NIWEL project the Charpy-V test results are not sufficient enough. In addition, T_0, J-R and tensile test results of all conditions must, and will be, tested and taken into account.

6 Conclusions

It is essential to understand how materials behave in long-term operation of nuclear power plants. An accelerated aging was used to simulate effects of thermal aging on DMW. The test material was 1:1 scale narrow-gap weld mock-up representing the Olkiluoto 3 EPR™ safe-end dissimilar metal weld. The material conditions were as-received and 5000 hours at 400 °C aged conditions.

Dissimilar metal welds and thermal aging were discussed in the literature review. Charpy-V impact testing and analysis methods were introduced, as well as the basics of SEM and EPMA.

It was shown that crack paths of the as-received and 5000 hours aged conditions were similar. The crack path distances were close to the fusion line and they did not differ much (a few microns to 20 µm in the as-received condition vs. a few microns to 40 µm in the 5000 hours aged condition). It can be said that 5000 hours aging did not affect the location of crack path in a case of brittle fractures. The weakest and the most susceptible zone of HAZ to brittle fracture was carbon-depleted zone. Based on literature, it was presumed that segregation of P was the main degradation mechanism, but no clear evidences of that, such as intergranular fracture, were found after 5000 hours aging time. Neither was proof of any other possible aging mechanism found. This must be studied carefully after 10000 hours aging time using versatile methods to gain understanding of aging mechanisms.

EPMA analyses were carried out. The analyses include elemental mappings and line scans which revealed the elemental distribution and composition over the HAZ, fusion line and Ni-base alloy near the fusion line. The diffusion of main elements, Fe, Ni and Cr, was observed.

Impact toughness of tested material was characterized. In total 34 specimens were tested, while only the results of 23 specimens fulfilled acceptance criteria. A significant shift in the ductile-to-brittle transition due to thermal aging was observed. Transition temperature T_{42J} increased from -35.2 °C to -2.3 °C, after 5000 hours of aging at 400 °C. The transition temperatures of $T_{0.89mm}$ and $T_{FA50\%}$ have increased as well with thermal aging. Furthermore, the T_{42J} for the 10000 hours aged condition was estimated using Equation 9. The calculated estimation, based upon the results obtained on the as-received and 5000 hours aged condition, suggests the transition temperature T_{42J} 11 °C.

Small welding defects were locally seen in fracture surfaces where the crack propagated close to the fusion line. Most of the welding defects were observed in the specimens with V-notch location in the weld metal. The defect type was shrinkage porosity, which is formed during solidification process.

It is important to test and analyse the 10000 hours aged condition to see how the material behaves when the thermal aging time is increased.

References

Ahonen, M., Sarikka, T., Hänninen, H., Ehrnstén, U. (2015a) Nickel-Base Alloy Welding Forum (NIWEL). Research Plan, 11 p.

Ahonen, M., Mouginot, R., Ehrnstén, U., Sarikka, T., Lindqvist, S., Hänninen, H. (2015b) Thermal aging of Alloy 52 narrow-gap dissimilar metal weld. EPRI Alloy 690/52/152 PWSCC Research Collaboration Meeting, Tampa, Florida, USA, 1-3 December 2015, 20 p.

Ahonen, M., Mouginot, R., Lindqvist, S., Sarikka, T., Nevasmaa, P., Ehrnstén, U., Hänninen, H. (2016) Fracture mechanical and microstructural characterization of narrow-gap safe-end dissimilar metal weld. Baltica X Conference, Life management and maintenance for power plants, Helsinki, Finland & Stockholm, Sweden, 7-9 June 2016, 15 p.

Alexandrov, B.T., Lippold, J.C., Sowards, J.W., Hope, A.T., Saltzmann, D.R. (2013) Fusion boundary microstructure evolution associated with embrittlement of Ni–base alloy overlays applied to carbon steel. Weld World, Vol. 57, 39-53.

Allen G. (2015) Good welding practice - Stainless Steels. TWI Ltd. 30 p.

Anderson, T. (1995) Fracture Mechanics Fundamentals and Applications, 2nd Edition. USA: CRC Press, Inc., 688 p. ISBN 0-8493-8974-7.

Andrieu, A., Pineau, A., Joly, P., Roch, F. (2013) On modelling of thermal embrittlement in PWR steels using the local approach to fracture. 13th International Conference on Fracture, Beijing, China, 16-21 June 2013, 10 p.

Andrieu, A., Pineau, A., Joly, P., Roch, F., Ryckelynck, D. (2014) Influence of P and C intergranular segregation during manufacturing and ageing on the fracture toughness of nuclear pressure vessel steels. Procedia Materials Science, Vol. 3, 655-660.

AREVA (2011) Design, safety technology and operability features of EPR. Interregional Workshop on Advanced Nuclear Reactor Technology for Near Term Development. Wien, Austria, 4-8 July 2011, 25 p.

AREVA/Framatome ANP (2005) EPR. 61 p.

ASM Handbook Volume 6: Welding, Brazing and Soldering. (1993) 10th Edition. USA: ASM International. 1299 p. ISBN 0-87170-382-3.

ASTM E1823-13. (2013) Standard Terminology Relating to Fatigue and Fracture Testing. West Conshohocken, Pennsylvania, USA: ASTM International. 25 p.

ASTM E1921-13a. (2013) Standard Test Method for Determination of Reference Temperature, T_0, for Ferritic Steels in the Transition Range. West Conshohocken, Pennsylvania, USA: ASTM International. 25 p.

ASTM E2298-13a. (2013) Standard Test Method for Instrumented Impact Testing of Metallic Materials. West Conshohocken, Pennsylvania, USA: ASTM International. 9 p.

Bhadeshia, H.K.D.H. & Honeycombe, R.W.K. (2006) Steels - Microstructure and Properties, 3rd Edition. USA: Elsevier Ltd. 344 p. ISBN 0-7506-8084-9.

Blouin, A., Chapuliot, S., Marie, S., Niclaeys, C., Bergheau, J.M. (2014) Brittle fracture analysis of dissimilar metal welds. Engineering Fracture Mechanics, Vol. 131, 58-73.

Boursier, J.M., Vaillant, F., Yrieix, B., Couvant, T. (2005) A review of PWSCC behavior, weldability and thermal ageing of nickel weld metals containing 15 to 30% chromium. In: Materials Reliability Program: Proceedings of the 2005 International PWSCC of Alloy 600 Conference and Exhibit Show (MRP-154), 5 Session 2A: Cracking and Reliability Studies of Alloy 600, 31-54., USA: Electric Power Research Institute (EPRI), Inc., 2106 p.

Buisine D., Milleville H., Vaillant F., Vidal P., Martinovitch M., Faure F., Dunand Roux L. (1997) Nickel base welds in nuclear components. EDF. 98NB00014. 12 p.

Callister, W.D., Rethwisch, D.G. (2011) Materials Science and Engineering, 8th Edition. Asia: John Wiley & Sons Inc., 885 p. ISBN 978-0-470-50586-1.

Cary, H.B. & Helzer, S.C. (2005) Modern Welding Technology, 6th Edition. Upper Saddle River, New Jersey, USA: Pearson Prentice Hall. 715 p. ISBN 0-13-113029-3.

Chiba, Y., Murayama, K., Satoh, S., Miyashiro, K., Ohata, M., Minami, F. (2010) Strength-mismatch effect on steel weld HAZ-toughness in CTOD and Charpy tests. Welding in the World, Vol. 54, 147-153.

Choi, K.J., Kim, J.J., Lee, B.H., Bahn, C.B., Kim, J.H. (2013) Effects of thermal aging on microstructures of low alloy steel-Ni base alloy dissimilar metal weld interfaces. Journal of Nuclear Materials, Vol. 441, 493-502.

Choi, K.J., Yoo, S.C., Kim, T., Bahn, C.B., Kim, J.H. (2015) Effects of aging temperature on microstructural evolution at dissimilar metal weld interfaces. Journal of Nuclear Materials, Vol. 462, 54-63.

Choi, K.J., Kim, T., Yoo, S.C., Kim, S., Lee, J.H., Kim, J.H. (2016) Fusion boundary precipitation in thermally aged dissimilar metal welds studied by atom probe tomography and nanoindentation. Journal of Nuclear Materials, Vol. 471, 8-16.

Chung, W.C., Huang, J.Y., Tsay, L.W., Chen, C. (2011) Microstructure and stress corrosion cracking behavior of the weld metal in Alloy 52-A508 dissimilar welds. Materials Transactions, Vol. 52, 12-19.

Druce, S.G., Gage, G., Jordan, G. (1986) Effect of ageing on properties of pressure vessel steels. Acta Metallurgica, Vol. 34, 641-652.

DuPont, J.N., Lippold, J.C., Kiser, S.D. (2009) Welding Metallurgy and Weldability of Nickel-Base Alloys. Hoboken, New Jersey, USA: John Wiley & Sons, Inc. 440 p. ISBN 987-0-470-08714-5.

Egerton, R.F. (2005) Physical Principles of Electron Microscopy - An Introduction to TEM, SEM, and AEM. USA: Springer Science+Business Media, Inc. 202 p. ISBN 0-387-25800-0

EN ISO 148-1:2009. (2009) Metallic materials - Charpy pendulum impact test - Part 1: Test method, 2nd Edition. Geneva, Switzerland: ISO. 26 p.

EPRI Final Report: Materials Reliability Program: Pressurized Water Reactor Issue Management Tables - Revision 1 (MRP-205). (2008) EPRI, Palo Alto, CA, 1018400. 542 p.

EPRI Technical Report: EPRI Materials Degradation Matrix. (2013) Revision 3, EPRI, Palo Alto, CA. 30020000628. 540 p.

EPRI Technical Report: Evaluation of Safe-end Weld Materials and Safe-end Replacement Experience. (1986) EPRI, Palo Alto, CA. NP-4443. 90 p.

EPRI Technical Report: Materials Handbook for Nuclear Plant Pressure Boundary Applications. (2002) EPRI, Palo Alto, CA. 1002792. 1017 p.

EPRI Technical Report: Materials Reliability Program: A Review of Thermal Aging Embrittlement in Pressurized Water Reactors (MRP-80). (2003) EPRI, Palo Alto, CA. 1003523. 116 p.

EPRI Technical Report: Review of Phosphorus Segregation and Intergranular Embrittlement in Reactor Pressure Vessel Steels (PWRMRP-19). (2000) EPRI, Palo Alto, CA. TR-114783. 120 p.

European Nuclear Society (2016) EPR.
https://www.euronuclear.org/info/encyclopedia/e/epr.htm (Accessed 27.6.2016).

Ford, F.P., Scott, P.M., Combrade, P. (2010) Environmentally-Assisted Degradation of Stainless Steels in LWRs. Advanced Nuclear Technology International. 49 p.

Framatome ANP (2001) The EPR. 63 p.

François, D., Pineau, A., Zaoui, A. (2013) Mechanical Behaviour of Materials, Volume II: Fracture Mechanics and Damage, 2nd Edition. Springer Springer+Business Media Dordrecht. 662 p. ISBN 978-94-007-4930-6

Guo, Z. & Sha, W. (2002) Quantification of precipitation hardening and evolution of precipitates. Materials Transactions, Vol. 43, No. 6, 1273-1282.

Hertzberg, R.W., Vinci, R.P., Hertzberg, J.L. (2013) Deformation and Fracture Mechanics of Engineering Materials, 5th Edition. USA: John Wiley & Sons, Inc., 755 p. ISBN 978-0-470-52780-1.

Hou, J., Peng, Q.J., Takeda, Y., Kuniya, J., Shoji, T., Wang, J.Q., Han, E.H., Ke, W. (2010) Microstructure and mechanical property of the fusion boundary region in an Alloy 182-low alloy steel dissimilar weld joint. Journal of Materials Science, Vol. 45, 5332-5338.

Hurlich, A. (1969) Low temperature metals, Proceedings of the 1968 Summer Study on Superconducting Devices and Accelerators Pt. 1. Brookhaven National Lab. 311-325.

Hänninen, H., Aaltonen, P., Brederholm, A., Ehrnstén, U., Gripenberg, H., Toivonen, A., Pitkänen, J., Virkkunen, I. (2006) Dissimilar metal weld joints and their performance in nuclear power plant and oil refinery conditions. Helsinki, Finland: Valopaino Oy. 208 p. ISBN 951-38-6806-0. http://www.vtt.fi/publications/index.jsp

Hänninen, H., Brederholm, A., Sarikka, T., Mouginot, R., Holmström, P., Saukkonen, T., Toivonen, A., Karjalainen-Roikonen, P., Nevasmaa, P., Keinänen, H., Leskelä, E., Ahonen, M., Ehrnstén, U., Aaltonen, P. (2014) Structural integrity of Ni-base alloy welds. Kuopio, Finland: Grano Oy. 257 p. ISBN 978-951-38-8259-4.

IRSN Report: Report to the Advisory Committee of Experts for Nuclear Pressure Equipment. (2015) IRSN Report /2015-00010, CODEP-DEP-2015-037971, Public Version, 80 p.

Jang, C., Cho, P.Y., Kim, M., Oh., S.J., Yang, J.S. (2010) Effects of microstructure and residual stress on fatigue crack growth of stainless steel narrow gap welds. Materials and Design, Vol. 31, 1862-1870.

Joly, P., Keim, E., Yescas, M. (2014) Fracture toughness in the ductile-brittle transition and thermal ageing behavior of decarburized heat affected zone of Alloy 52 dissimilar metal welds of nuclear components. PVP2014-29044. Proceedings of the ASME-2014 Pressure Vessel and Piping Conference, Anaheim, California, USA, 20-24 July 2014, 13 p.

Kou, S. (2003) Welding Metallurgy, 2nd Edition. Hoboken, New Jersey, USA: John Wiley & Sons, Inc. 461 p. ISBN 0-471-43491-4.

Li, J., Cui, P., Zhang, G.D., Xue, F., Zhou, C.Y. (2015) Study on limit loads for safe end of nuclear pressure vessel with local wall thinning. Procedia Engineering, Vol. 130, 1535-1543.

Lippold, J.C. & Kotecki, D.J. (2005) Welding Metallurgy and Weldability of Stainless Steels. Hoboken, New Jersey, USA: John Wiley & Sons, Inc. 357 p. ISBN 0-471-47379-0.

Lydman, J. (2016) A three month visit at PSI. Research Report VTT-R-03046-16, VTT, Espoo, Finland, 16 p.

Lydman, J. (2017) As-received, 5000 hours and 10000 hours thermally aged conditions of dissimilar metal weld - Instrumented Charpy-V impact toughness. Research Report VTT-R-03534-16, VTT, Espoo, Finland.

MEE Handbook: Handbook of Analytical Methods for Materials. (2016) Materials Evaluation and Engineering, Inc. 54 p. http://www.mee-inc.com/hamm/

Messler, Jr., R.W. (2004) Principles of Welding - Processes, Physics, Chemistry, and Metallurgy. Singapore: Markono Print Media Pte Ltd. 662 p. ISBN 0-471-25376-6.

Ming, H., Zhu, R., Zhang, Z., Wang, J., Han, E.H., Ke, W., Su, M. (2016) Microstructure, local mechanical properties and stress corrosion cracking susceptibility of an SA508-52M-316LN safe-end dissimilar metal weld joint by GTAW. Materials Science & Engineering A, Vol. 669, 279-290.

Mouginot, R. & Hänninen, H. (2013) Microstructures of nickel-base alloy dissimilar metal welds. Helsinki, Finland: Unigrafia Oy. 178 p. ISBN 978-952-60-5066-9 (pdf).

NEA Final Report: Technical basis for commendable practices on ageing management. (2011) NEA/CSNI/R(2010)15, Nuclear Energy Agency, Committee on the Safety of Nuclear Installations, SCC and Cable Ageing Project (SCAP). 132 p.

NEI Report: Material Degradation Matrix. (2004) NEI, ML043220014, NEI 03-08. 100 p.

Nelson, T.W., Lippold, J.C., Mills, M.J. (1999) Nature and evolution of the fusion boundary in ferritic-austenitic dissimilar weld metals, Part 1 - Nucleation and growth. Welding Journal, Vol. 78, 329-337.

Nelson, T.W., Lippold, J.C., Mills, M.J. (2000) Nature and evolution of the fusion boundary in ferritic-austenitic dissimilar metal welds, Part 2: On-cooling transformations. Welding Journal, Vol. 79, 267-277.

Neves, J. & Loureiro, A. (2004) Fracture toughness of welds - effect of brittle zones and strength mismatch. Journal of Materials Processing Technology, Vol 153-154, 537-543.

Nhili, R. (2015) Life extension and long term operation strategies EDF approach, Materials Degradation Course for Engineers in the Nuclear Industry, Materials Ageing Institute, EDF Lab Les Renardières, Moret-sur-Loing, France, 22-25 September 2015, 33 p.

Northern Arizona University (2016) Electron Microprobe Laboratory, http://nau.edu/cefns/labs/electron-microprobe/ (Accessed 12.6.2016).

NRC Report: Aging of Cables and Cable Systems. (2013a) NRC, NUREG/CR-7153, Vol. 5, ORNL/TM-2013/532. 125 p.

NRC Report: Aging of Reactor Pressure Vessels. (2013b) NRC, NUREG/CR-7153, Vol. 3, ORNL/TM-2013/532. 243 p.

NRC Report: Executive Summary of EMDA Process and Results. (2013c) NRC, NUREG/CR-7153, Vol. 1, ORNL/TM-2013/532. 55 p.

Oxford Instruments Analytical Technical Briefing: Wavelength Dispersive X-ray Microanalysis. (2002) Oxford Instruments Analytical. 12 p. https://www.oxford-instruments.com/OxfordInstruments/media/nanoanalysis/brochures%20and%20thumbs/OI_AppNote_WDS_Explained.pdf

Rathod, D.W., Dingh, P.K., Pandey, S., Aravindan, S. (2016) Effect of buffer-layered buttering on microstructure and mechanical properties of dissimilar metal weld joints for nuclear plant application. Materials Science & Engineering A, Vol. 666, 100-113.

Restani, R. & Wälchli, A. (2011) Shielded field emission EPMA for microanalysis of radioactive materials. EMAS 2011: 12th European Workshop on Modern Developments in Microbeam Analysis, Angers, France, 15-19 May 2011, 12 p.

Restani, R. & Grabherr, R. (2015) Shielded field emission EPMA for the examination of nuclear materials on sections with polished and fractured surfaces. Hotlab conference 2015 52nd annual meeting, Leuven, Belgium, 27 September - 1 October 2015, 8 p.

Styman, P.D., Hyde, J.M., Wilford, K., Smith, G.D.W. (2013) Quantitative methods for the APT analysis of thermally aged RPV steels. Ultramicroscopy, Vol. 132, 258-264.

Takeuchi, T., Kakubo, Y., Matsukawa, Y., Nozawa, Y., Toyama, T., Nagai, Y., Nishiyama, Y., Katsuyama, J., Yamaguchi, Y., Onizawa, K., Suzuki, M. (2014) Effects of thermal aging on microstructure and hardness of stainless steel weld-overlay claddings of nuclear reactor pressure vessels. Journal of Nuclear Materials, Vol. 452, 235-240.

Tanaka, M., Takeguchi, M., Furuya, K. (2008) X-ray analysis and mapping by wavelength dispersive X-ray spectroscopy in an electron microscope. Ultramicroscopy, Vol. 108, 1427-1431.

TVO (2010) Nuclear Power Plant Unit Olkiluoto 3. Teolliuuden Voima Oyj, 62 p.

Ul-Hamid, A., Tawancy, H.M., Mohammed, A.R.I., Al-Jaroudi, S.S., Abbas, N.M. (2006) Quantitative WDS analysis using electron probe microanalyzer. Materials Characterization, Vol. 56, 192-199.

VTT Work instruction: Instrumented Charpy-V impact test of irradiated material. (2015) VTT/MMC29/WI-001 Issue 2. 13 p.

Wallin, K., Nevasmaa, P., Planman, T., Valo, M. (2002) Evolution of the Charpy-V test from a quality control test to a materials evaluation tool for structural integrity assessment. European Structural Integrity Society, Vol. 30, 57-68.

Wallin, K. (2011) Fracture Toughness of Engineering Materials - Estimation and Application. Croydon: EMAS Publishing. 543 p. ISBN 0-9552994-6-2.

Wallin, K. (2016) Research Professor, VTT, Espoo, Finland, Personal conversation 17.8.2016.

Wang, H.T., Wang, G.Z., Xuan, F.Z., Tu, S.T. (2011) Numerical investigation of ductile crack growth behavior in a dissimilar metal welded joint. Nuclear Engineering and Design, Vol. 241, 3234-3243.

Wang, H.T., Wang, G.Z., Xuan, F.Z., Tu, S.T. (2013a) An experimental investigation of local fracture resistance and crack growth paths in a dissimilar metal welded joint. Materials and Design, Vol. 44, 179-189.

Wang, H.T., Wang, G.Z., Xuan, F.Z., Tu, S.T. (2013b) Fracture mechanism of a dissimilar metal welded joint in nuclear power plant. Engineering Failure Analysis, Vol. 28, 134-148.

Wang, H.T., Wang, G.Z., Xuan, F.Z., Liu, C.J., Tu, S.T. (2013c) Local mechanical properties of a dissimilar metal welded joint in nuclear power systems. Materials Science & Engineering A, Vol. 568, 108-117.

Wells, R., Joly, P., Peigney, A. (2009) Dissimilar Metal Weld (DMW) NRC Audit RAI 88, Supplement 1 (Q 05.02.03-10), AREVA NP Inc. and the NRC, 46 p.

Yoo, S.C., Choi, K.J., Bahn, C.B., Kim, S.H., Kim, J.Y., Kim, J.H. (2015) Effects of thermal aging on the microstructure of Type-II boundaries in dissimilar metal weld joints. Journal of Nuclear Materials, Vol. 459, 5-12.

Zerbst, U., Ainsworth, R.A., Beier, H.T., Pisarski, H., Zhang, Z.L., Nikbin, K., Nitsche-Pagel, T., Münstermann, S., Kucharczyk, P., Klingbeil, D. (2014) Review on fracture and crack propagation in weldments - A fracture mechanics perspective. Engineering Fracture Mechanics, Vol. 132, 200-276.

Appendices

Appendix 1 Reprography images

Appendix 2 Specimen dimensions

Appendix 3 Test results

Appendix 4 Load-deflection curves

Appendix 5 Fracture surfaces

Appendix 6 Crack paths

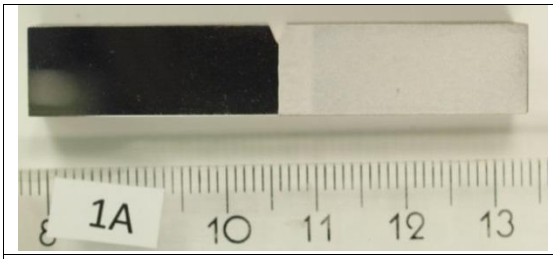

Figure 1 Specimen 1A, as-received

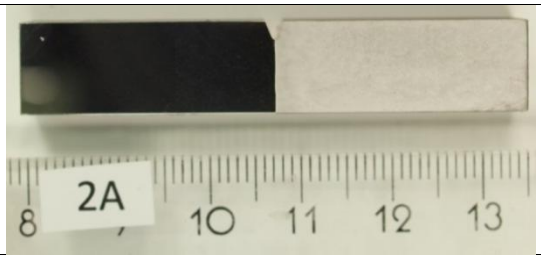

Figure 2 Specimen 2A, as-received

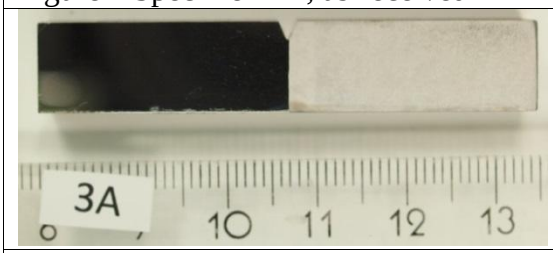

Figure 3 Specimen 3A, as-received

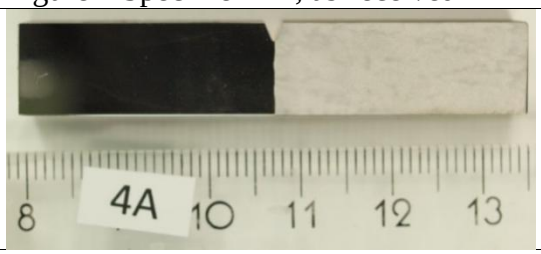

Figure 4 Specimen 4A, as-received

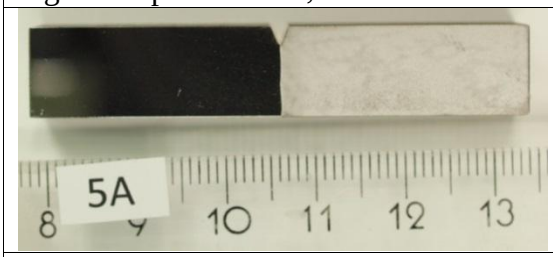

Figure 5 Specimen 5A, as-received

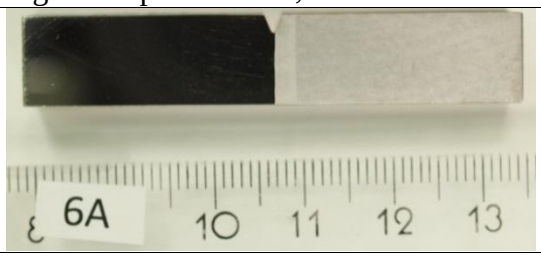

Figure 6 Specimen 6A, as-received

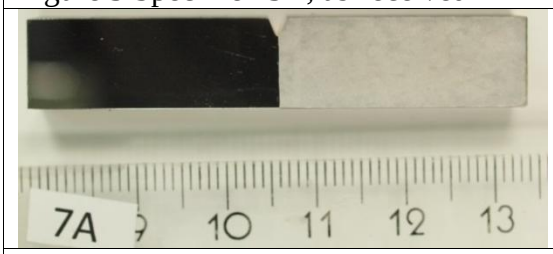

Figure 7 Specimen 7A, as-received

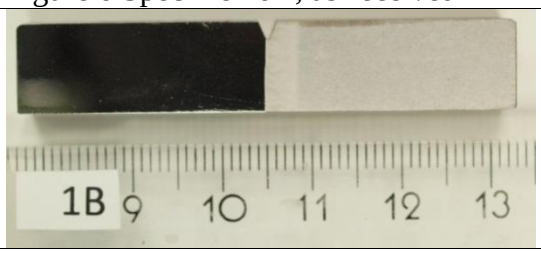

Figure 8 Specimen 1B, as-received

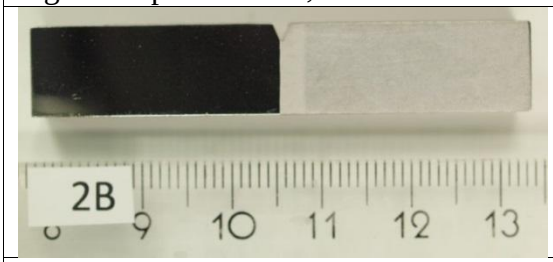

Figure 9 Specimen 2B, as-received

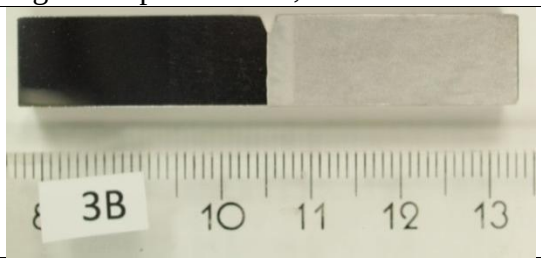

Figure 10 Specimen 3B, as-received

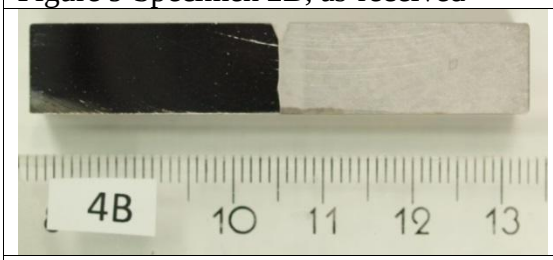

Figure 11 Specimen 4B, as-received

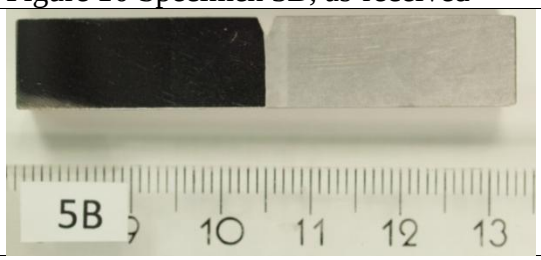

Figure 12 Specimen 5B, as-received

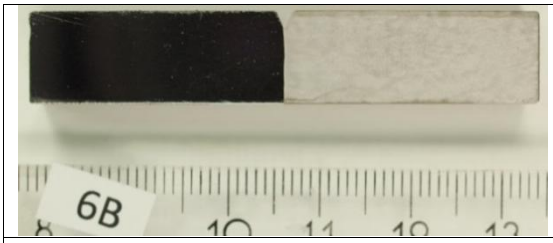

Figure 13 Specimen 6B, as-received

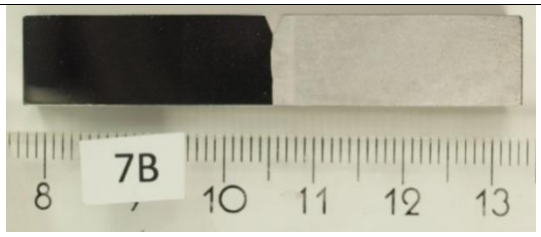

Figure 14 Specimen 7B, as-received

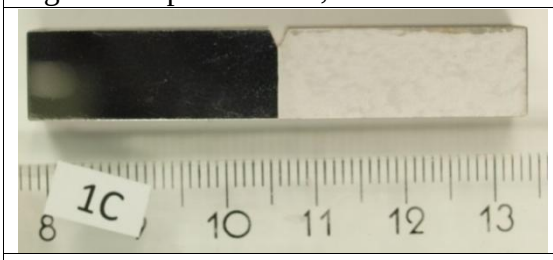

Figure 15 Specimen 1C, as-received

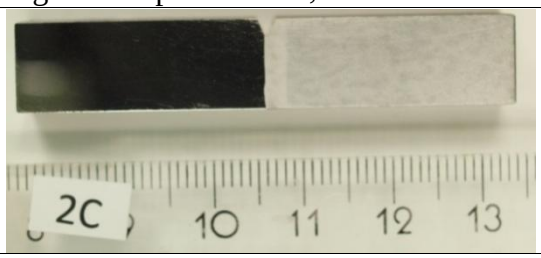

Figure 16 Specimen 2C, as-received

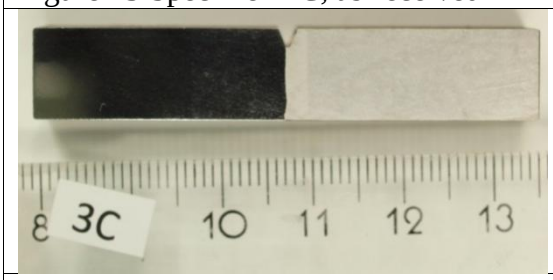

Figure 17 Specimen 3C, as-received

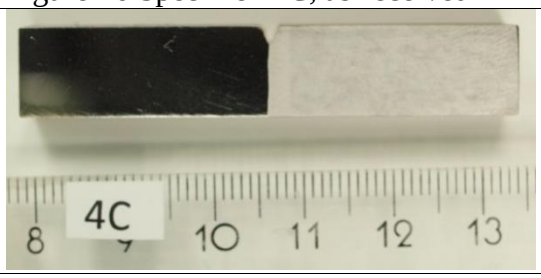

Figure 18 Specimen 4C, as-received

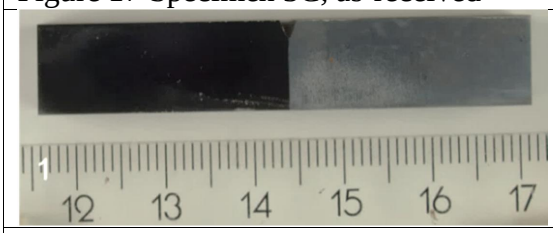

Figure 19 Specimen 1, aging, 5000 hours

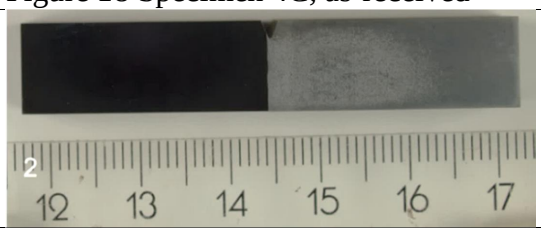

Figure 20 Specimen 2, aging, 5000 hours

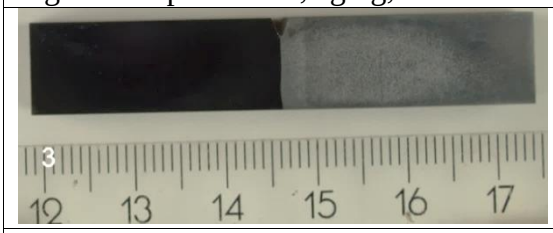

Figure 21 Specimen 3, aging, 5000 hours

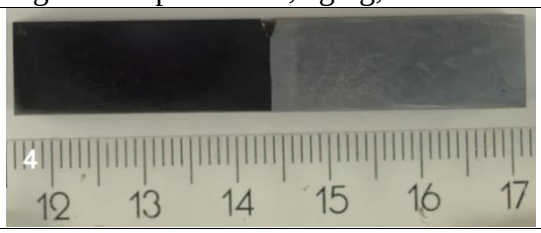

Figure 22 Specimen 4, aging, 5000 hours

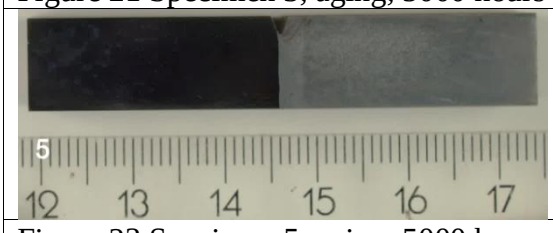

Figure 23 Specimen 5, aging, 5000 hours

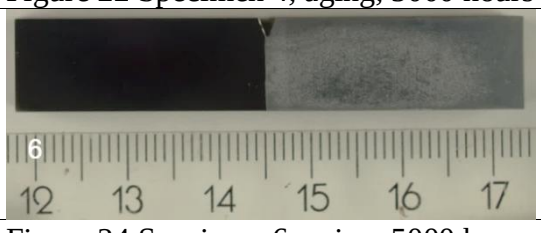

Figure 24 Specimen 6, aging, 5000 hours

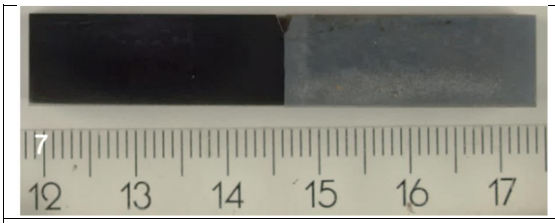

Figure 25 Specimen 7, aging, 5000 hours

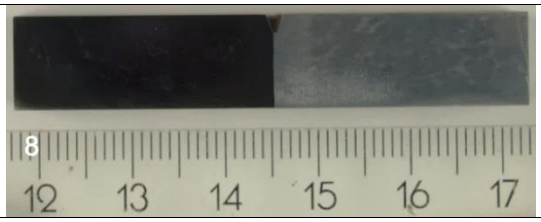

Figure 28 Specimen 8, aging, 5000 hours

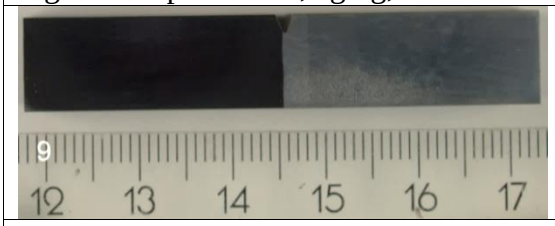

Figure 27 Specimen 9, aging, 5000 hours

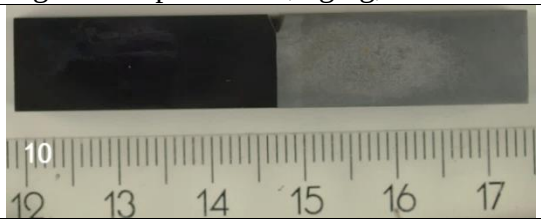

Figure 28 Specimen 10, aging, 5000 hours

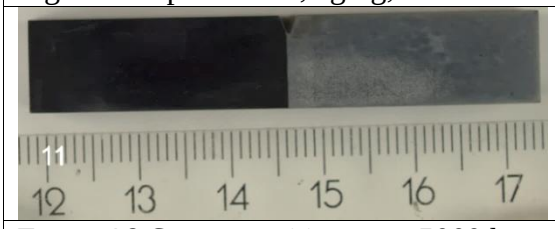

Figure 29 Specimen 11, aging, 5000 hours

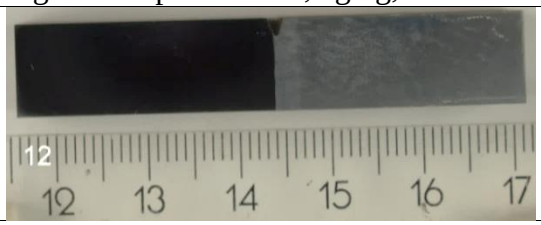

Figure 30 Specimen 12, aging, 5000 hours

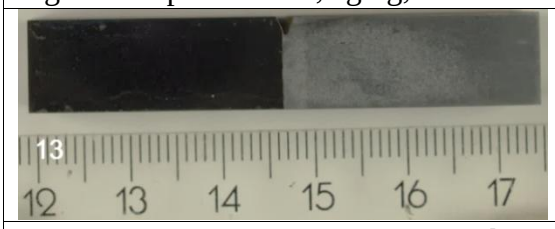

Figure 31 Specimen 13, aging, 5000 hours

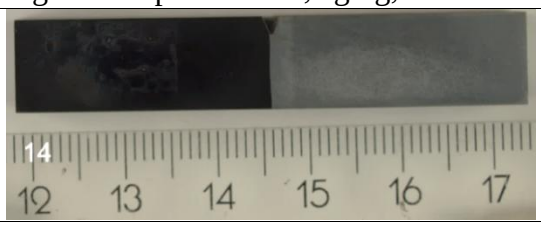

Figure 32 Specimen 14, aging, 5000 hours

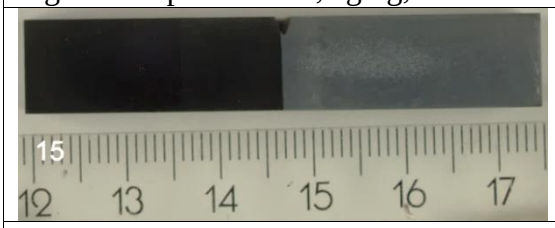

Figure 33 Specimen 15, aging, 5000 hours

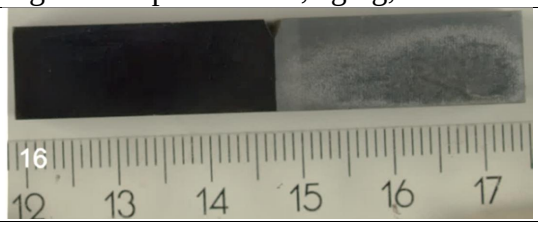

Figure 34 Specimen 16, aging, 5000 hours

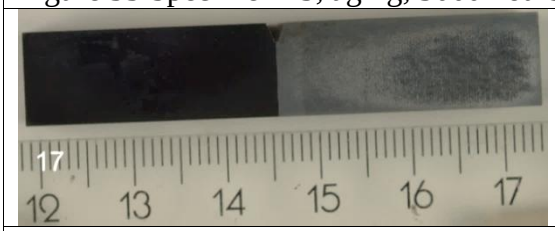

Figure 35 Specimen 17, aging, 5000 hours

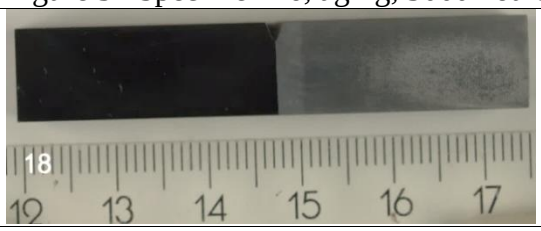

Figure 36 Specimen 18, aging, 5000 hours

Specimen dimensions

Material	Specimen	Length l (mm)	Height b (mm)	Width w (mm)	Ligament (mm)	From notch to head (mm)	Notch base radius (mm)	Angle of notch (°)
Nominal dimensions		55.00	10.00	10.00	8.00	27.50	0.250	45°
Tolerances		55.60 / 54.40	10.075 / 9.925	10.110 / 9.890	8.075 / 7.925	27.92 / 27.08	0.275 / 0.225	47° / 43°
As-received								
	1A	54.98	10.03	9.99	8.018	27.53	0.255	45.69
	2A	54.98	10.02	9.99	7.989	27.44	0.250	45.81
	3A	54.97	10.03	9.99	7.988	27.46	0.250	46.04
	4A	54.97	10.02	9.98	7.991	27.44	0.250	45.76
	5A	54.99	10.02	10.00	7.986	27.44	0.250	45.83
	6A	55.01	10.03	10.03	7.991	27.46	0.250	45.75
	7A	55.02	10.04	9.99	7.999	27.49	0.250	45.93
	1B	54.98	10.02	10.00	8.008	27.39	0.255	45.68
	2B	54.94	10.02	10.00	7.967	27.67	0.250	45.98
	3B	54.97	10.03	10.00	7.963	27.46	0.250	45.69
	4B	54.94	10.02	10.00	7.979	27.48	0.250	45.59
	5B	54.95	10.01	10.00	7.936	27.53	0.255	45.97
	6B	54.95	10.00	9.99	7.956	27.50	0.255	46.11
	7B	54.96	10.03	9.97	7.973	27.51	0.260	45.73
	1C	54.99	10.04	10.01	8.032	27.31	0.250	45.80
	2C	54.97	10.02	10.00	8.000	27.32	0.255	45.48
	3C	54.98	10.03	10.01	7.958	27.63	0.250	45.56
	4C	54.98	10.04	9.99	7.999	27.42	0.260	45.97

Material	Specimen	Length l (mm)	Height b (mm)	Width w (mm)	Ligament (mm)	From notch to head (mm)	Notch base radius (mm)	Angle of notch (°)
Nominal dimensions		55.00	10.00	10.00	8.00	27.50	0.250	45°
Tolerances		55.60 / 54.40	10.075 / 9.925	10.110 / 9.890	8.075 / 7.925	27.92 / 27.08	0.275 / 0.225	47° / 43°
Aging, 5000 hours								
	1	54.98	10.02	9.99	8.039	27.02	0.244	44.21
	2	55.03	10.02	10.00	8.034	27.54	0.248	44.41
	3	55.00	10.01	10.01	8.016	27.73	0.246	44.15
	4	55.04	9.99	9.99	7.994	27.49	0.254	44.57
	5	55.04	10.02	9.98	8.026	27.76	0.251	43.66
	6	55.02	10.02	9.99	8.035	27.80	0.245	44.11
	7	55.04	10.02	10.01	8.032	27.27	0.250	44.93
	8	55.06	10.02	10.00	8.053	27.21	0.247	44.02
	9	55.01	10.02	10.01	8.063	27.24	0.253	43.71
	10	55.02	10.02	10.01	8.029	26.89	0.248	44.21
	11	54.99	10.01	10.00	8.031	27.84	0.252	44.33
	12	55.00	10.01	9.99	8.044	26.84	0.251	43.65
	13	55.00	10.01	10.01	8.033	27.38	0.246	44.57
	14	55.08	10.02	10.01	8.035	27.44	0.246	44.49
	15	55.08	10.01	9.97	8.065	27.38	0.248	44.73
	16	55.05	10.01	9.99	8.008	28.00	0.245	44.33
	17	55.13	10.00	10.00	7.991	26.95	0.246	44.71
	18	55.10	10.01	10.01	8.011	27.32	0.244	44.42

Test results

Specimen	T	KV_2	KV_{calc}	LE	FA	F_{gy}	F_m	F_u	F_a
	(˚C)	(J)	(J)	(mm)	(%)	(N)	(N)	(N)	(N)
	As-received								
1A	40.1	177.2	166.6	1.79	91.6	11013	16333	7600	6094
2A	21.9	183.4	171.6	1.87	100	11602	17412	-	-
4A	-120.6	103.0	101.0	1.35	29.0	13749	19403	16209	24
5A	-89.7	54.3	53.0	0.76	16.8	13557	18764	18764	642
7A	60.6	198.6	185.1	2.42	100	11853	17141	-	-
1B	-89.7	18.9	18.3	0.23	19.5	11548	14904	14904	1222
2B	-120.5	17.4	17.3	0.23	8.6	13193	15875	15875	628
3B	-10.1	74.4	70.0	0.96	48.9	11828	15991	15760	5417
4B	-30.5	77.0	75.1	0.96	36.3	12461	17306	17092	2949
5B	40.1	176.4	158.9	1.86	100	12030	16179	-	-
6B	-60.3	18.8	18.2	0.21	17.9	13471	15513	15513	1113
7B	-30.4	37.9	35.5	0.57	31.9	13135	15775	15775	4547
1C	-60.4	34.6	33.9	0.41	17.9	13000	17312	16899	29
2C	-10.2	65.5	62.1	0.92	43.9	12544	16120	16120	13670
3C	60.6	185.3	171.4	1.80	100	11817	16843	-	-
4C	21.9	160.3	149.4	1.70	84.0	12208	17372	11993	10380
	Aging, 5000 hours								
1	90.5	220.1	169.1	2.06	100	9962	15734	-	-
2	60.3	204.8	147.2	2.01	93.7	11300	16289	11171	9098
3	-0.1	53.1	51.5	0.73	43.0	12013	15461	15461	8664
4	0.2	68.0	66.0	0.98	32.4	12331	17108	17108	4908
5	-0.1	39.1	37.3	0.69	27.3	12814	14835	13623	6749
6	-55.2	19.9	19.0	0.30	10.9	13141	16002	16002	19
7	-20.0	26.5	25.2	0.41	25.4	12594	15149	15149	3637
8	90.6	218.1	165.5	2.02	100	9736	15693	-	-
9	19.8	55.7	53.7	0.86	40.2	11823	15508	14815	12768
10	40.0	182.5	115.6	1.58	77.6	11591	16188	14982	13547
11	19.8	81.8	80.0	1.20	59.9	12762	16498	16498	13396
12	-55.2	15.7	14.8	0.26	11.5	13685	15408	15408	12
13	40.1	105.6	102.3	1.39	67.1	12128	16205	15455	9715
14	0.2	39.3	38.0	0.66	30.1	12619	14808	14625	8114
15	-19.9	36.1	34.7	0.53	25.6	11049	14911	14170	2537
16	-20.2	37.6	36.6	0.64	26.3	12133	16393	16393	3120
17	-20.0	40.9	39.7	0.64	31.9	12496	16239	15834	4166
18	60.3	215.5	169.0	1.92	89.8	12239	16572	6506	4239

Project:	Niwel
Customer:	
Tester:	JL
File:	v7737-1a.chw

Specimen: 1A 4.12.2015 10:13:18

Material:	Base
State:	R
Size:	ChV_10*10
Construction:	Normal

Temperature [°C]:	40.1
E - pendulum [J]:	177.2
E - Load-Deflection [J]:	166.6
Ductile area [%]:	91.6
Lateral expansion [mm]:	1.79

Dose [10^19n/cm²,E>1MeV]: 0.0

	d[mm]	F[N]
Yield point:	0.40	11013
Maximum:	4.60	16333
Brittle start:	11.04	7600
Brittle end:	11.11	6094
Contact point:	2.68	4.3

Comment:

Charpy32 Version: 1.0.17 27.09.2012

Measured angle: -119.9225

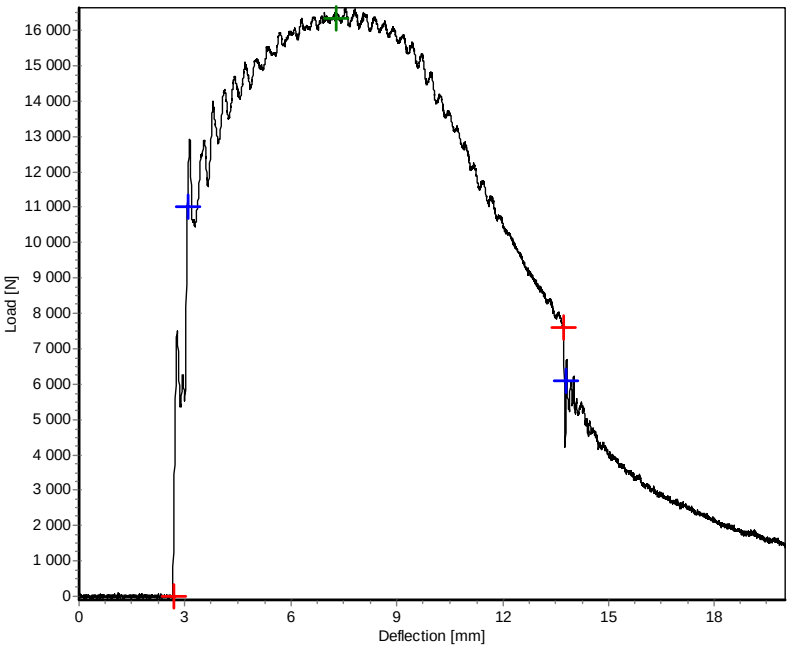

Hammer:		Load:	
PSW300 EN	(SN: 1588)	EG&G Model 5113 (Gain: 250, Volt: +5/-5)	
Mass:	20.263 kg	Cal. const: 12319 N/V	Calibrated: 22.9.2015
Length:	771 mm		
Zero energy:	0.7 J	Energy:	
vp:	5.43 m/s	Heidenhain ND-281	
E0:	299 J	Impact angle: 80.8524 units	Calibrated: 22.9.2015

Figure 1 Specimen 1A, as-received

Project:	Niwel
Customer:	
Tester:	JL
File:	v7769-2a.chw

Specimen: 2A 14.12.2015 11:44:50

Material:	Base
State:	R
Size:	ChV_10*10
Construction:	Normal

Temperature [°C]:	21.9
E - pendulum [J]:	183.4
E - Load-Deflection [J]:	171.6
Ductile area [%]:	100.0
Lateral expansion [mm]:	1.87

Dose [10^19n/cm²,E>1MeV]: 0.0

	d[mm]	F[N]
Yield point:	0.34	11602
Maximum:	4.19	17412
Brittle start:		
Brittle end:		
Contact point:	2.52	17.7

Comment:

Charpy32 Version: 1.0.17 27.09.2012

Measured angle: -118.7237

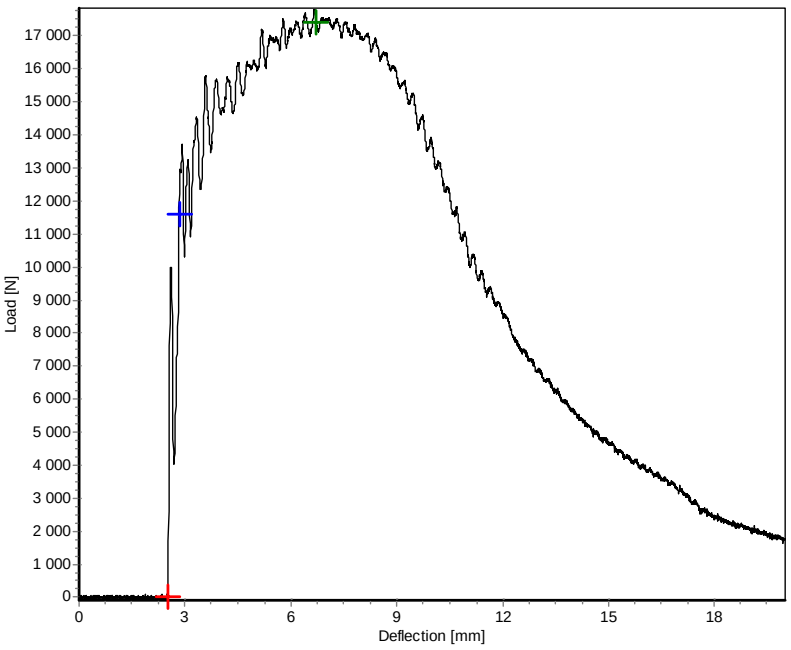

Hammer:		Load:	
PSW300 EN	(SN: 1588)	EG&G Model 5113 (Gain: 250, Volt: +5/-5)	
Mass:	20.263 kg	Cal. const: 12319 N/V	Calibrated: 22.9.2015
Length:	771 mm		
Zero energy:	0.7 J	Energy:	
vp:	5.43 m/s	Heidenhain ND-281	
E0:	299 J	Impact angle: 80.8544 units	Calibrated: 22.9.2015

Figure 2 Specimen 2A, as-received

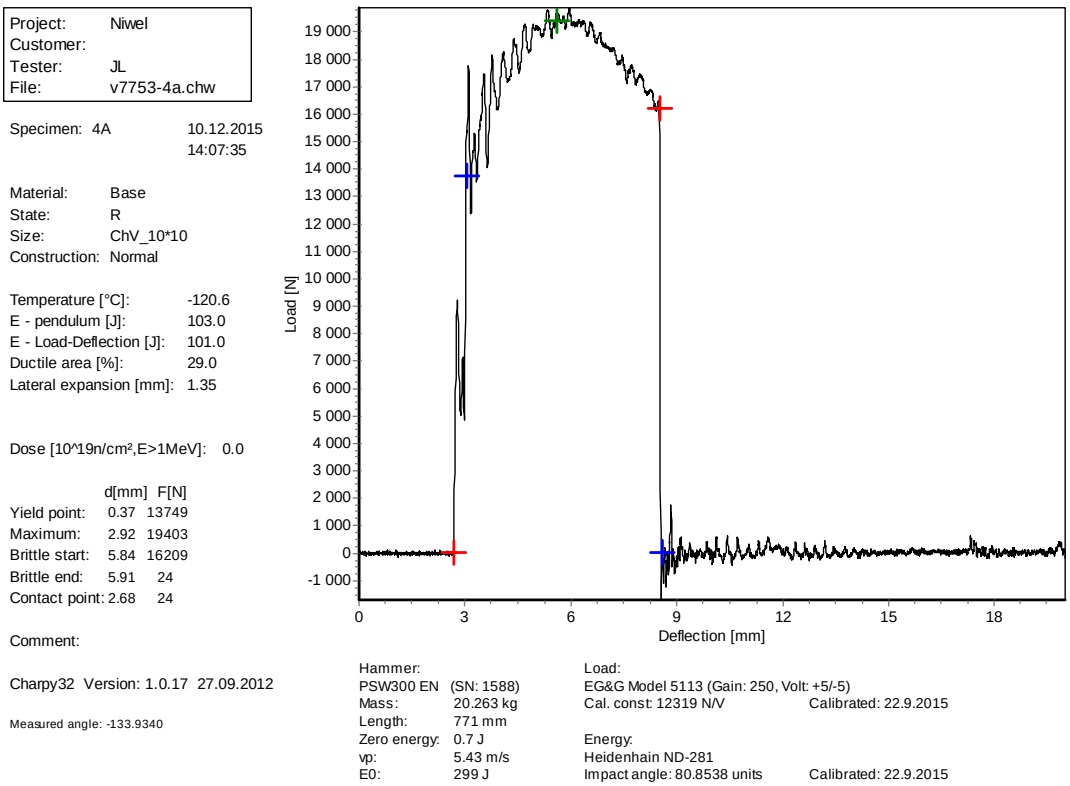

Figure 3 Specimen 4A, as-received

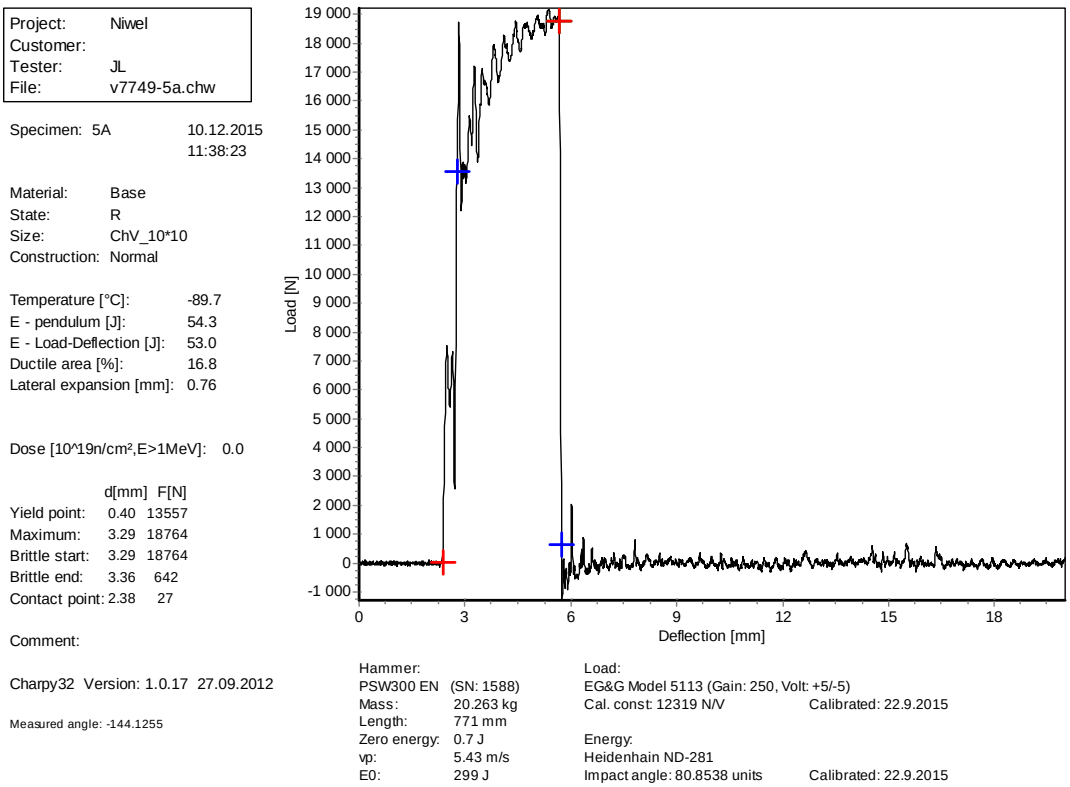

Figure 4 Specimen 5A, as-received

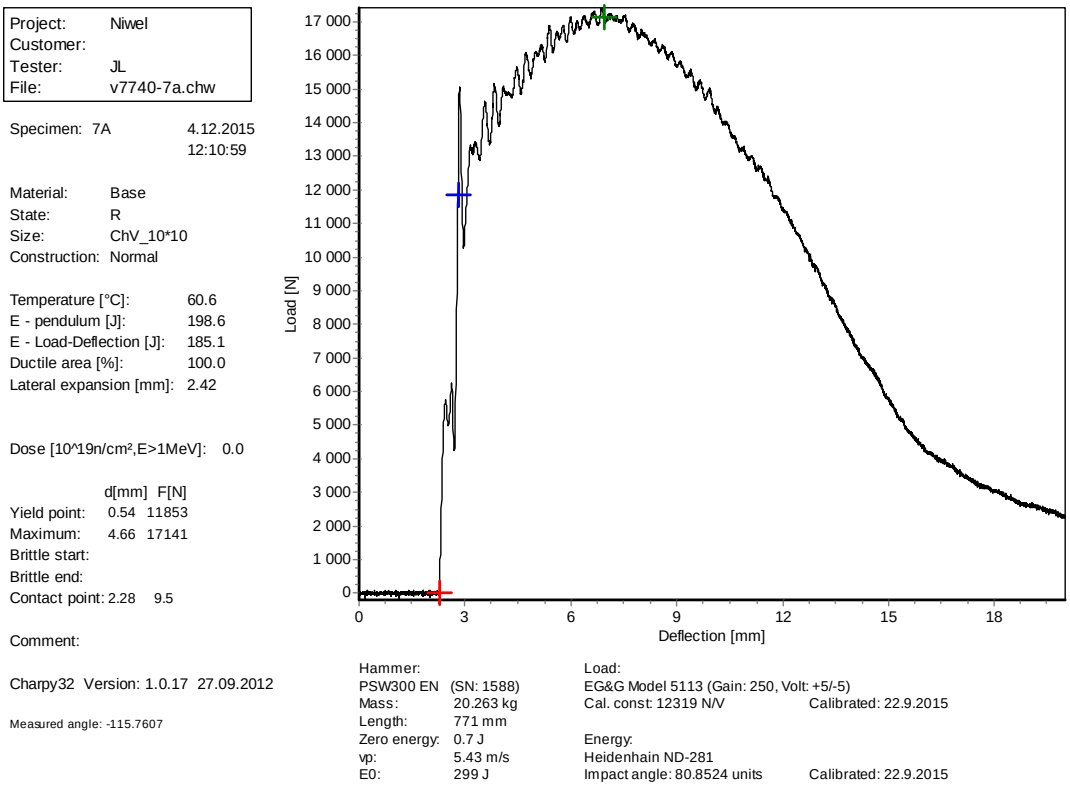

Figure 5 Specimen 7A, as-received

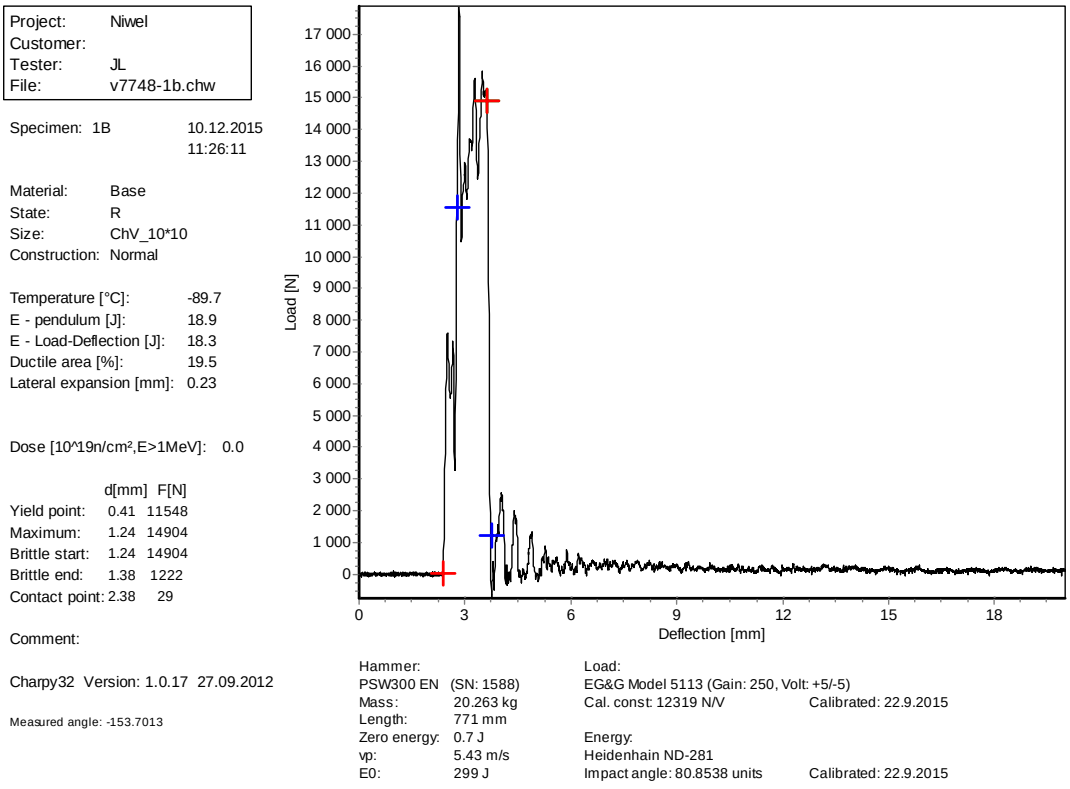

Figure 6 Specimen 1B, as-received

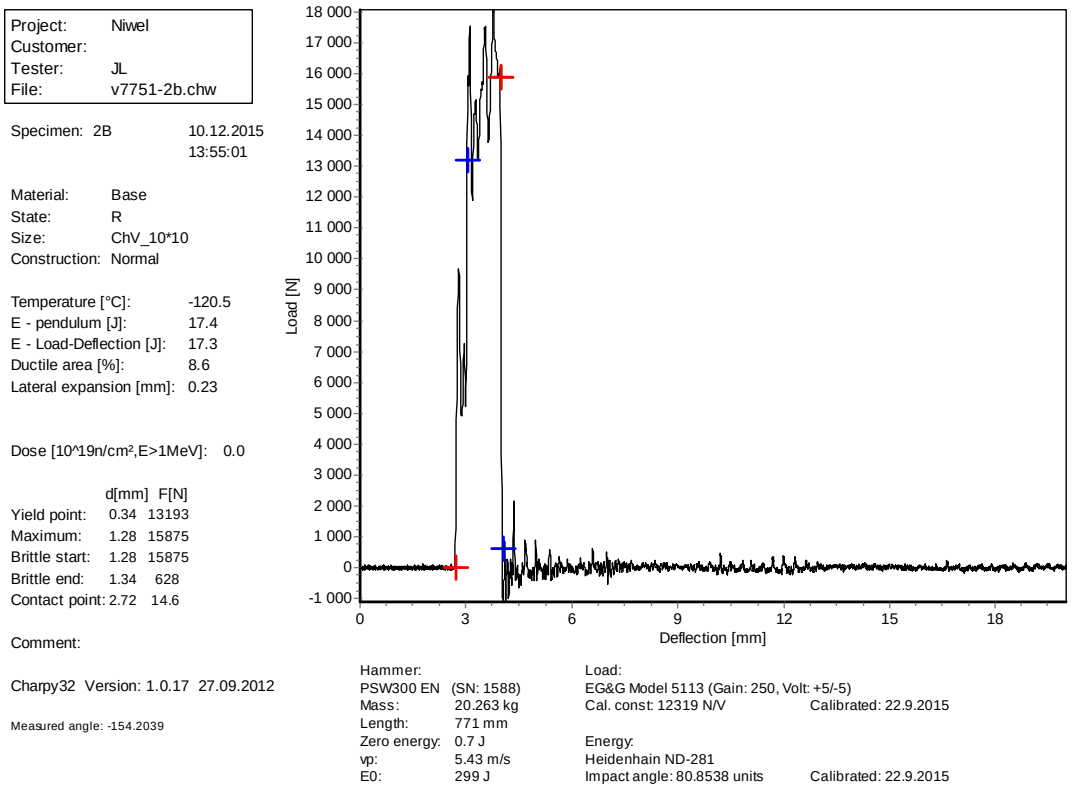

Figure 7 Specimen 2B, as-received

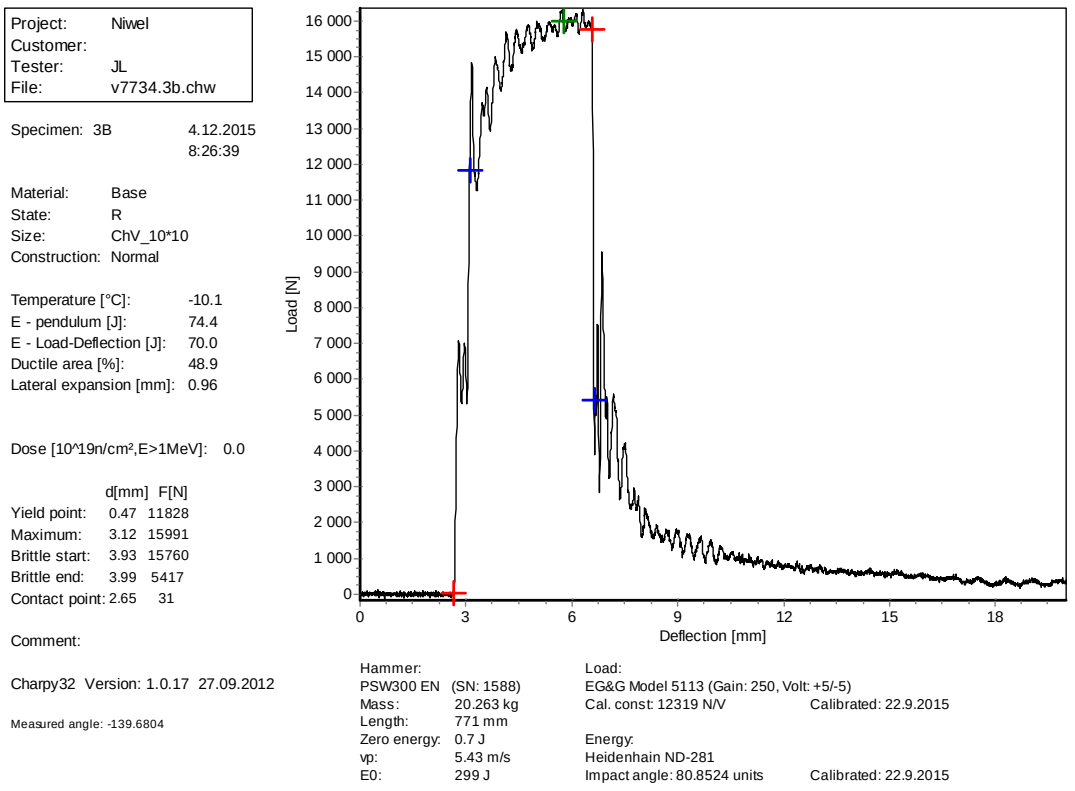

Figure 8 Specimen 3B, as-received

Project:	Niwel
Customer:	
Tester:	JL
File:	v7767-4b.chw

Specimen: 4B 14.12.2015 9:48:39

Material:	Base
State:	R
Size:	ChV_10*10
Construction:	Normal

Temperature [°C]:	-30.5
E - pendulum [J]:	77.0
E - Load-Deflection [J]:	75.1
Ductile area [%]:	36.3
Lateral expansion [mm]:	0.96

Dose [10^19n/cm²,E>1MeV]: 0.0

	d[mm]	F[N]
Yield point:	0.44	12461
Maximum:	3.56	17306
Brittle start:	4.46	17092
Brittle end:	4.60	2949
Contact point:	2.68	28

Comment:

Charpy32 Version: 1.0.17 27.09.2012

Measured angle: -139.1475

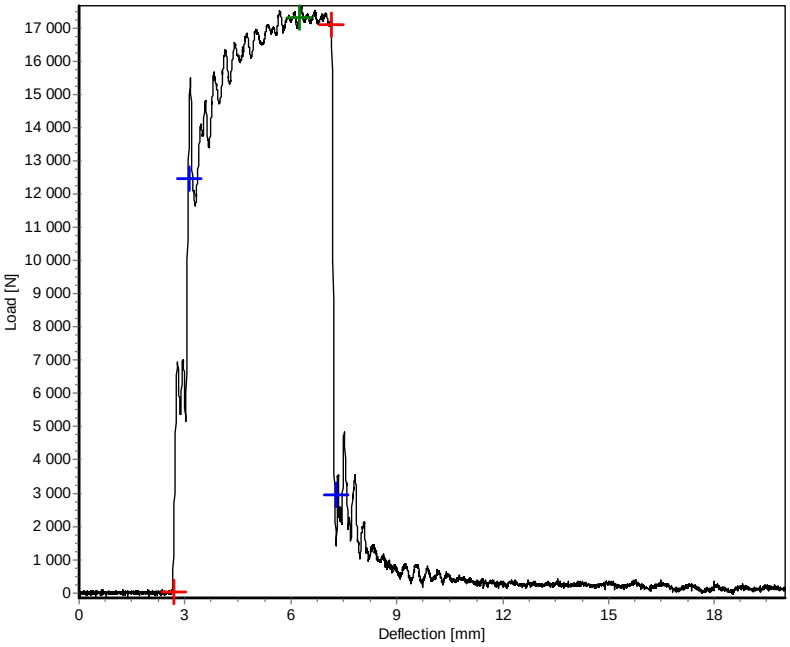

Hammer:		Load:	
PSW300 EN	(SN: 1588)	EG&G Model 5113 (Gain: 250, Volt: +5/-5)	
Mass:	20.263 kg	Cal. const: 12319 N/V	Calibrated: 22.9.2015
Length:	771 mm		
Zero energy:	0.7 J	Energy:	
vp:	5.43 m/s	Heidenhain ND-281	
E0:	299 J	Impact angle: 80.8544 units	Calibrated: 22.9.2015

Figure 9 Specimen 4B, as-received

Project:	Niwel
Customer:	
Tester:	JL
File:	v7738-5b.chw

Specimen: 5B 4.12.2015 10:26:13

Material:	Base
State:	R
Size:	ChV_10*10
Construction:	Normal

Temperature [°C]:	40.1
E - pendulum [J]:	176.4
E - Load-Deflection [J]:	158.9
Ductile area [%]:	100.0
Lateral expansion [mm]:	1.86

Dose [10^19n/cm²,E>1MeV]: 0.0

	d[mm]	F[N]
Yield point:	0.47	12030
Maximum:	3.72	16179
Brittle start:		
Brittle end:		
Contact point:	2.65	15.7

Comment:

Charpy32 Version: 1.0.17 27.09.2012

Measured angle: -120.0751

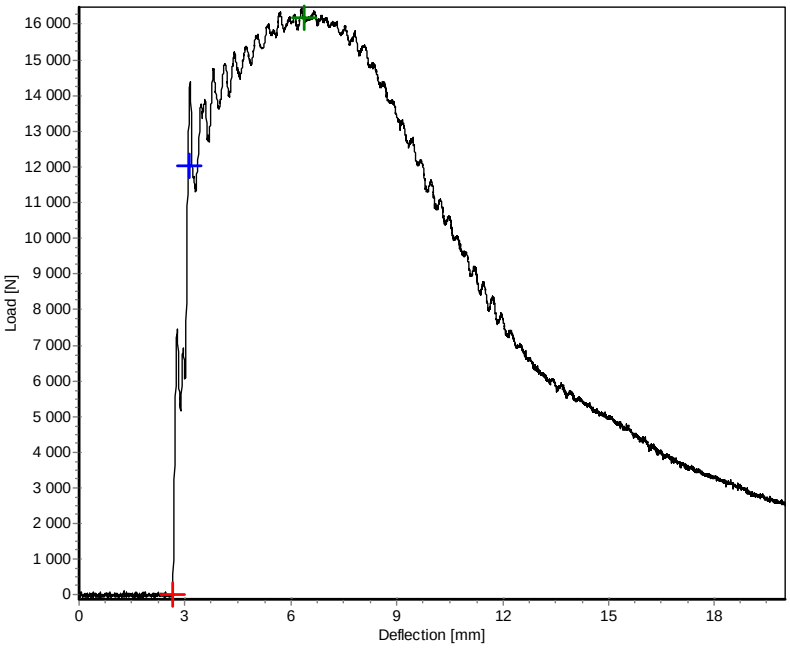

Hammer:		Load:	
PSW300 EN	(SN: 1588)	EG&G Model 5113 (Gain: 250, Volt: +5/-5)	
Mass:	20.263 kg	Cal. const: 12319 N/V	Calibrated: 22.9.2015
Length:	771 mm		
Zero energy:	0.7 J	Energy:	
vp:	5.43 m/s	Heidenhain ND-281	
E0:	299 J	Impact angle: 80.8524 units	Calibrated: 22.9.2015

Figure 10 Specimen 5B, as-received

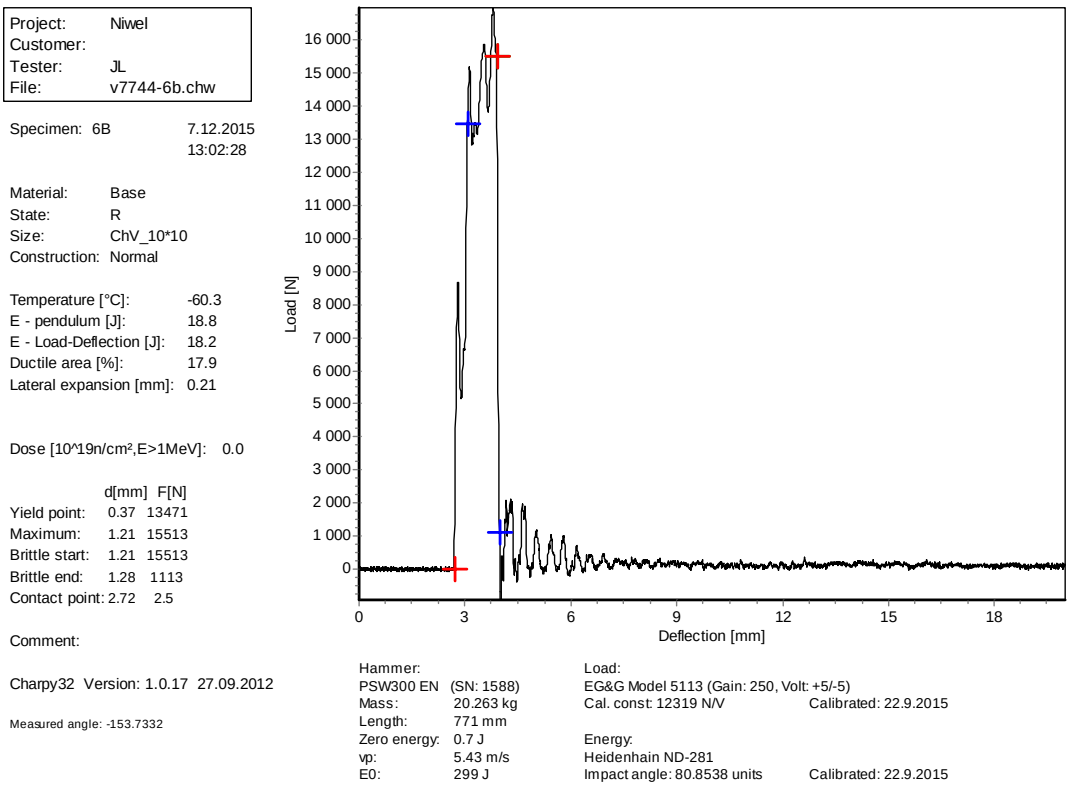

Figure 11 Specimen 6B, as-received

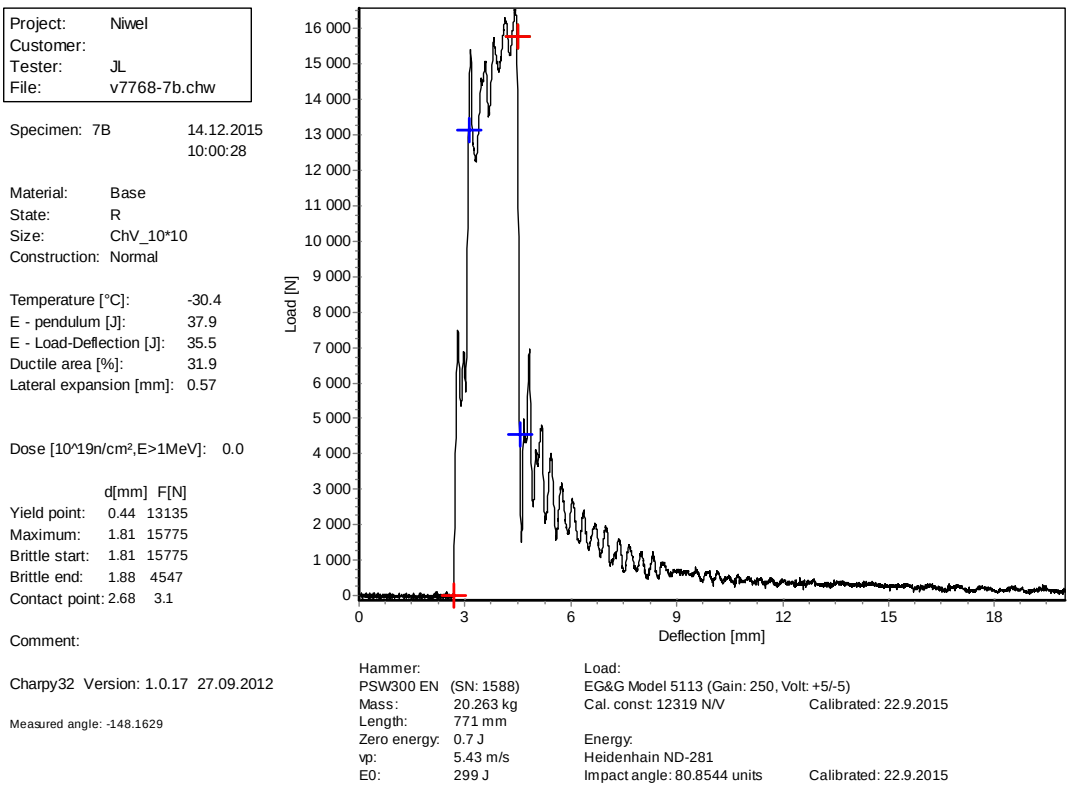

Figure 12 Specimen 7B, as-received

Project:	Niwel
Customer:	
Tester:	JL
File:	v7745-1c.chw

Specimen: 1C 7.12.2015 13:13:54

Material:	Base
State:	R
Size:	ChV_10*10
Construction:	Normal

Temperature [°C]:	-60.4
E - pendulum [J]:	34.6
E - Load-Deflection [J]:	33.9
Ductile area [%]:	17.9
Lateral expansion [mm]:	0.41

Dose [10^19n/cm²,E>1MeV]: 0.0

	d[mm]	F[N]
Yield point:	0.44	13000
Maximum:	2.18	17312
Brittle start:	2.28	16899
Brittle end:	2.38	29
Contact point:	2.68	29

Comment:

Charpy32 Version: 1.0.17 27.09.2012

Measured angle: -149.0351

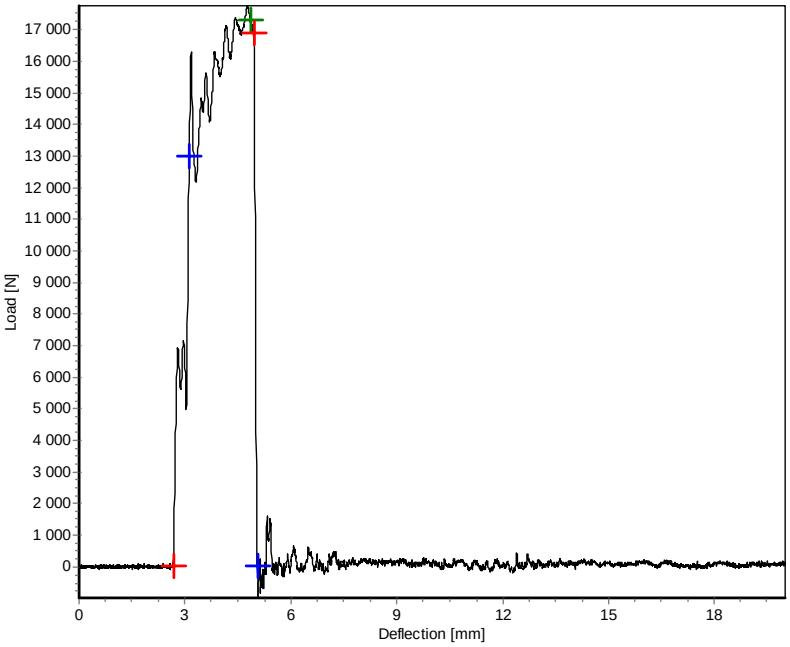

Hammer:		Load:	
PSW300 EN	(SN: 1588)	EG&G Model 5113 (Gain: 250, Volt: +5/-5)	
Mass:	20.263 kg	Cal. const: 12319 N/V	Calibrated: 22.9.2015
Length:	771 mm		
Zero energy:	0.7 J	Energy:	
vp:	5.43 m/s	Heidenhain ND-281	
E0:	299 J	Impact angle: 80.8538 units	Calibrated: 22.9.2015

Figure 13 Specimen 1C, as-received

Project:	Niwel
Customer:	
Tester:	JL
File:	v7735.2c.chw

Specimen: 2C 4.12.2015 8:38:24

Material:	Base
State:	R
Size:	ChV_10*10
Construction:	Normal

Temperature [°C]:	-10.2
E - pendulum [J]:	65.5
E - Load-Deflection [J]:	62.1
Ductile area [%]:	43.9
Lateral expansion [mm]:	0.92

Dose [10^19n/cm²,E>1MeV]: 0.0

	d[mm]	F[N]
Yield point:	0.44	12544
Maximum:	2.15	16120
Brittle start:	2.15	16120
Brittle end:	2.25	13670
Contact point:	2.68	30

Comment:

Charpy32 Version: 1.0.17 27.09.2012

Measured angle: -141.6028

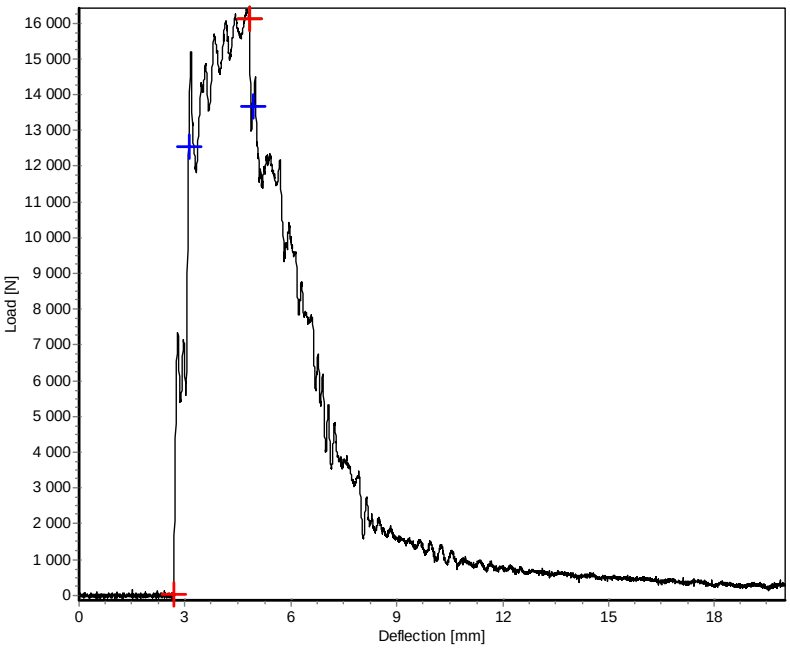

Hammer:		Load:	
PSW300 EN	(SN: 1588)	EG&G Model 5113 (Gain: 250, Volt: +5/-5)	
Mass:	20.263 kg	Cal. const: 12319 N/V	Calibrated: 22.9.2015
Length:	771 mm		
Zero energy:	0.7 J	Energy:	
vp:	5.43 m/s	Heidenhain ND-281	
E0:	299 J	Impact angle: 80.8524 units	Calibrated: 22.9.2015

Figure 14 Specimen 2C, as-received

Project:	Niwel
Customer:	
Tester:	JL
File:	v7741-3c.chw

Specimen: 3C 4.12.2015 12:28:56

Material:	Base
State:	R
Size:	ChV_10*10
Construction:	Normal

Temperature [°C]:	60.6
E - pendulum [J]:	185.3
E - Load-Deflection [J]:	171.4
Ductile area [%]:	100.0
Lateral expansion [mm]:	1.80

Dose [10^19n/cm²,E>1MeV]: 0.0

	d[mm]	F[N]
Yield point:	0.44	11817
Maximum:	4.26	16843
Brittle start:		
Brittle end:		
Contact point:	2.32	16.8

Comment:

Charpy32 Version: 1.0.17 27.09.2012

Measured angle: -118.3576

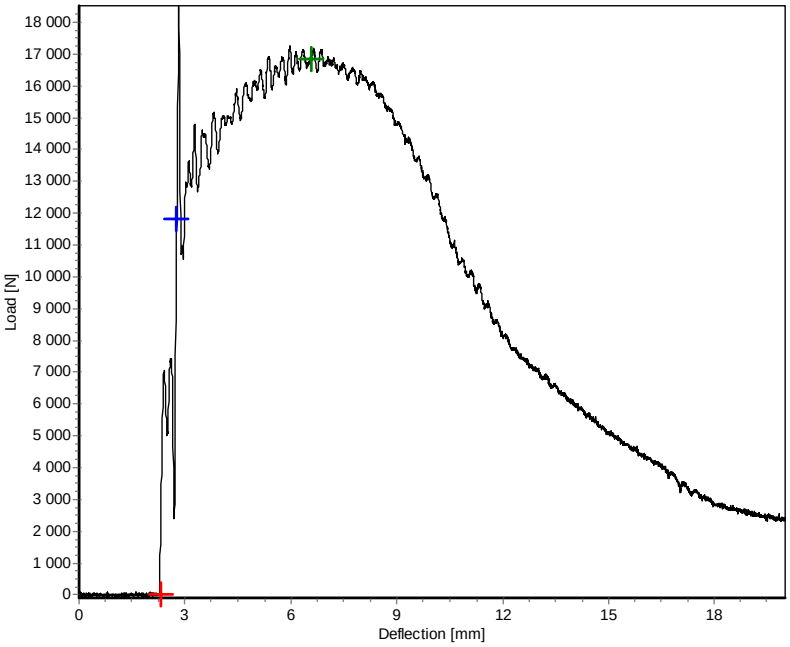

Hammer:		Load:	
PSW300 EN	(SN: 1588)	EG&G Model 5113 (Gain: 250, Volt: +5/-5)	
Mass:	20.263 kg	Cal. const: 12319 N/V	Calibrated: 22.9.2015
Length:	771 mm		
Zero energy:	0.7 J	Energy:	
vp:	5.43 m/s	Heidenhain ND-281	
E0:	299 J	Impact angle: 80.8524 units	Calibrated: 22.9.2015

Figure 15 Specimen 3C, as-received

Project:	Niwel
Customer:	
Tester:	JL
File:	v7770-4c.chw

Specimen: 4C 14.12.2015 11:52:43

Material:	Base
State:	R
Size:	ChV_10*10
Construction:	Normal

Temperature [°C]:	21.9
E - pendulum [J]:	160.3
E - Load-Deflection [J]:	149.4
Ductile area [%]:	82.2
Lateral expansion [mm]:	1.70

Dose [10^19n/cm²,E>1MeV]: 0.0

	d[mm]	F[N]
Yield point:	0.30	12208
Maximum:	4.16	17372
Brittle start:	8.22	11993
Brittle end:	8.29	10380
Contact point:	2.55	17.0

Comment:

Charpy32 Version: 1.0.17 27.09.2012

Measured angle: -123.1220

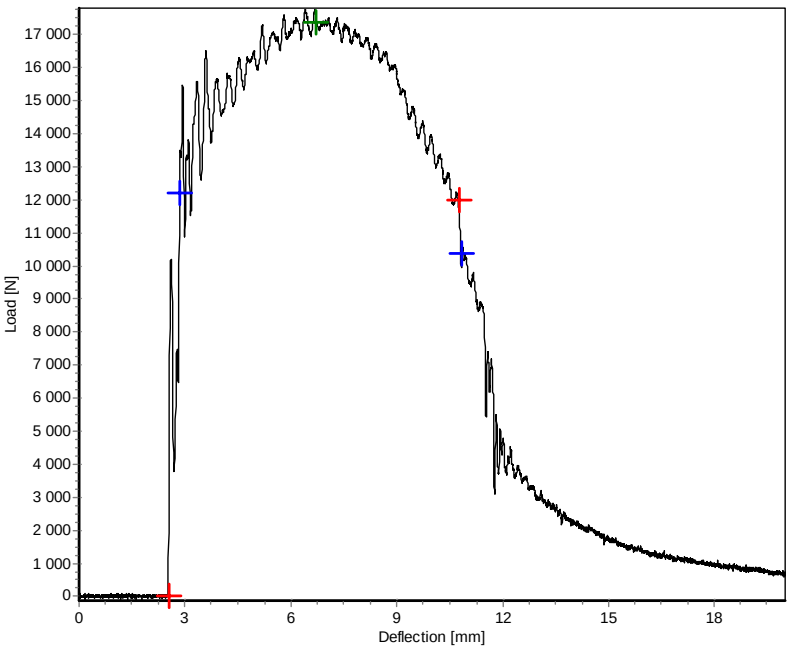

Hammer:		Load:	
PSW300 EN	(SN: 1588)	EG&G Model 5113 (Gain: 250, Volt: +5/-5)	
Mass:	20.263 kg	Cal. const: 12319 N/V	Calibrated: 22.9.2015
Length:	771 mm		
Zero energy:	0.7 J	Energy:	
vp:	5.43 m/s	Heidenhain ND-281	
E0:	299 J	Impact angle: 80.8544 units	Calibrated: 22.9.2015

Figure 16 Specimen 4C, as-received

Project:	NIWEL
Customer:	
Tester:	JL
File:	v7978-1.chw

Specimen: 1 26.7.2016 9:18:42

Material:	Base
State:	R
Size:	ChV_10*10
Construction:	Normal

Temperature [°C]:	90.5
E - pendulum [J]:	220.1
E - Load-Deflection [J]:	169.1
Ductile area [%]:	100.0
Lateral expansion [mm]:	2.06

Dose [10^19n/cm²,E>1MeV]: 0.0

	d[mm]	F[N]
Yield point:	0.40	9962
Maximum:	5.41	15734
Brittle start:		
Brittle end:		
Contact point:	2.66	28

Comment:

Charpy32 Version: 1.0.17 27.09.2012

Measured angle: -111.3431

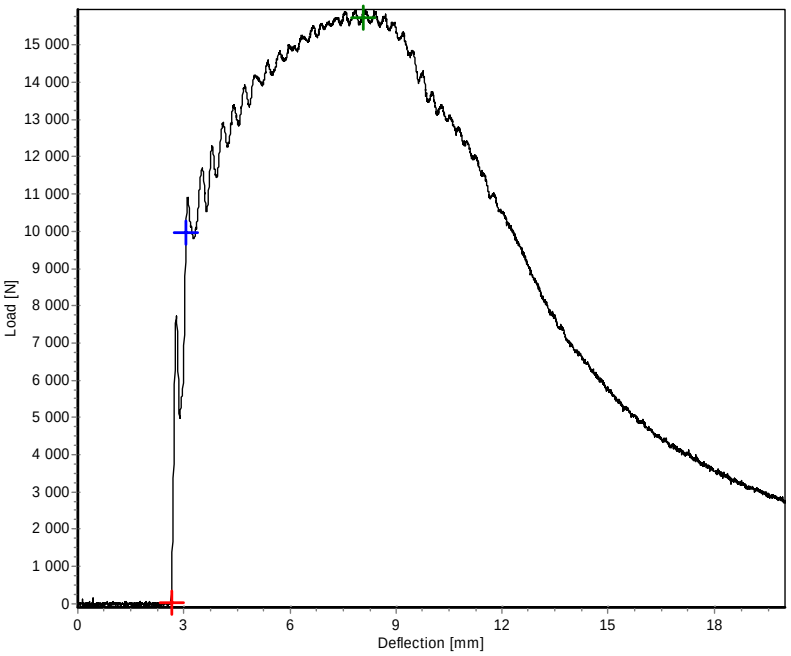

Hammer:		Load:	
PSW300 EN	(SN: 1588)	EG&G Model 5113 (Gain: 250, Volt: +5/-5)	
Mass:	20.263 kg	Cal. const: 12319 N/V	Calibrated: 22.9.2015
Length:	771 mm		
Zero energy:	0.7 J	Energy:	
vp:	5.43 m/s	Heidenhain ND-281	
E0:	299 J	Impact angle: 80.8522 units	Calibrated: 22.9.2015

Figure 17 Specimen 1, aging, 5000 hours

Project:	NIWEL
Customer:	
Tester:	JL
File:	v7970-2.chw

Specimen: 2 25.7.2016 9:37:55

Material:	Base
State:	R
Size:	ChV_10*10
Construction:	Normal

Temperature [°C]:	60.3
E - pendulum [J]:	204.8
E - Load-Deflection [J]:	147.2
Ductile area [%]:	93.7
Lateral expansion [mm]:	2.01

Dose [10^19n/cm²,E>1MeV]: 0.0

	d[mm]	F[N]
Yield point:	0.43	11300
Maximum:	4.25	16289
Brittle start:	7.67	11171
Brittle end:	7.67	9098
Contact point:	2.66	27

Comment:

Charpy32 Version: 1.0.17 27.09.2012

Measured angle: -114.5052

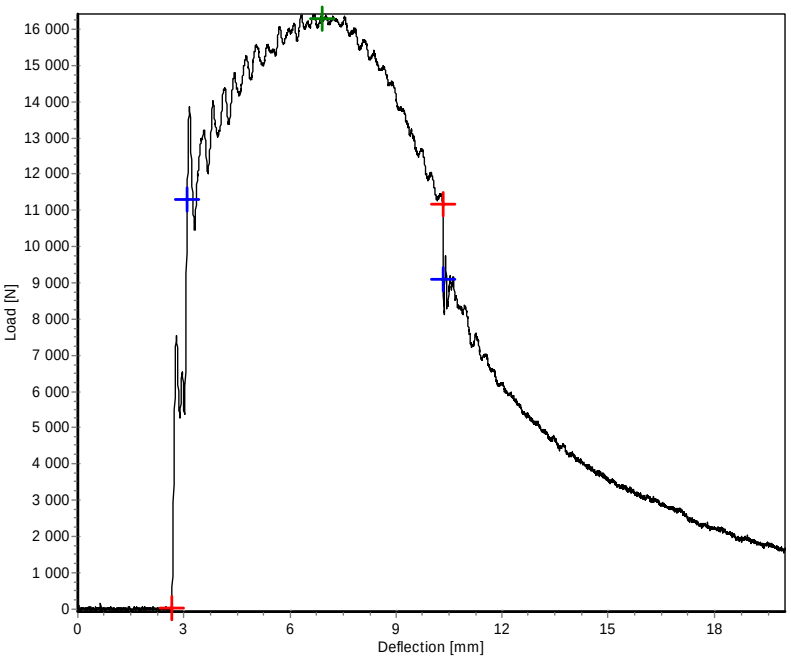

Hammer:		Load:	
PSW300 EN	(SN: 1588)	EG&G Model 5113 (Gain: 250, Volt: +5/-5)	
Mass:	20.263 kg	Cal. const: 12319 N/V	Calibrated: 22.9.2015
Length:	771 mm		
Zero energy:	0.7 J	Energy:	
vp:	5.43 m/s	Heidenhain ND-281	
E0:	299 J	Impact angle: 80.8534 units	Calibrated: 22.9.2015

Figure 18 Specimen 2, aging, 5000 hours

Project:	NIWEL
Customer:	
Tester:	JL
File:	v7982-3.chw

Specimen: 3 27.7.2016 8:36:51

Material:	Base
State:	R
Size:	ChV_10*10
Construction:	Normal

Temperature [°C]:	-0.1
E - pendulum [J]:	53.1
E - Load-Deflection [J]:	51.5
Ductile area [%]:	43.0
Lateral expansion [mm]:	0.73

Dose [10^19n/cm²,E>1MeV]: 0.0

	d[mm]	F[N]
Yield point:	0.33	12013
Maximum:	2.06	15461
Brittle start:	2.06	15461
Brittle end:	2.13	8664
Contact point:	2.69	27

Comment:

Charpy32 Version: 1.0.17 27.09.2012

Measured angle: -144.4109

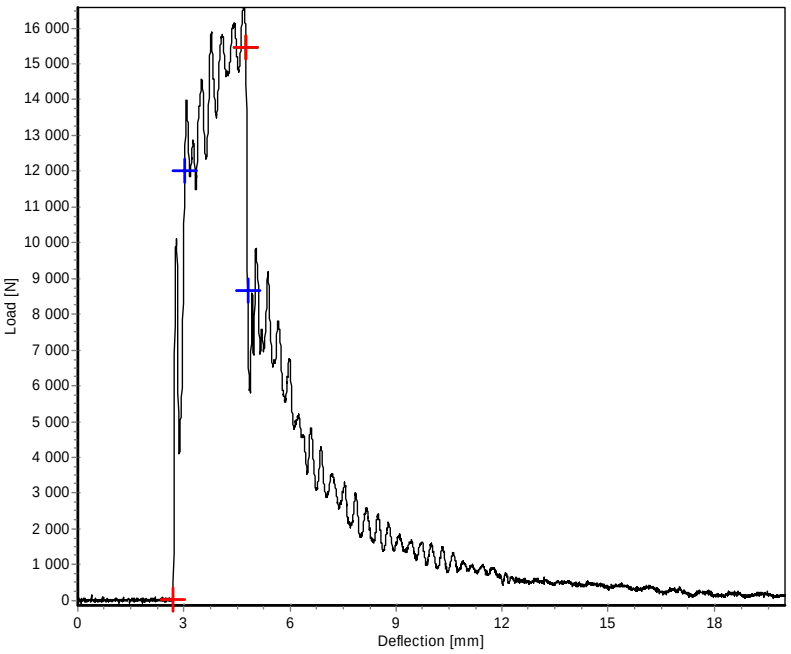

Hammer:		Load:	
PSW300 EN	(SN: 1588)	EG&G Model 5113 (Gain: 250, Volt: +5/-5)	
Mass:	20.263 kg	Cal. const: 12319 N/V	Calibrated: 22.9.2015
Length:	771 mm		
Zero energy:	0.7 J	Energy:	
vp:	5.43 m/s	Heidenhain ND-281	
E0:	299 J	Impact angle: 80.8524 units	Calibrated: 22.9.2015

Figure 19 Specimen 3, aging, 5000 hours

Project:	NIWEL
Customer:	
Tester:	JL
File:	v7990-4.chw

Specimen: 4 28.7.2016 9:37:20

Material:	Base
State:	R
Size:	ChV_10*10
Construction:	Normal

Temperature [°C]:	0.2
E - pendulum [J]:	68.0
E - Load-Deflection [J]:	66.0
Ductile area [%]:	32.4
Lateral expansion [mm]:	0.98

Dose [10^19n/cm²,E>1MeV]: 0.0

	d[mm]	F[N]
Yield point:	0.40	12331
Maximum:	3.99	17108
Brittle start:	3.99	17108
Brittle end:	4.05	4908
Contact point:	2.69	28

Comment:

Charpy32 Version: 1.0.17 27.09.2012

Measured angle: -141.0633

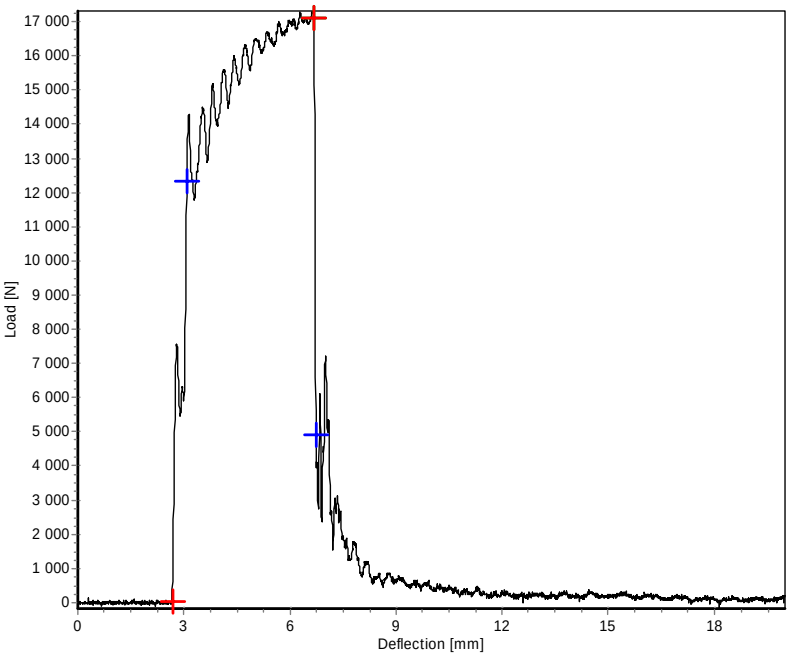

Hammer:		Load:	
PSW300 EN	(SN: 1588)	EG&G Model 5113 (Gain: 250, Volt: +5/-5)	
Mass:	20.263 kg	Cal. const: 12319 N/V	Calibrated: 22.9.2015
Length:	771 mm		
Zero energy:	0.7 J	Energy:	
vp:	5.43 m/s	Heidenhain ND-281	
E0:	299 J	Impact angle: 80.8530 units	Calibrated: 22.9.2015

Figure 20 Specimen 4, aging, 5000 hours

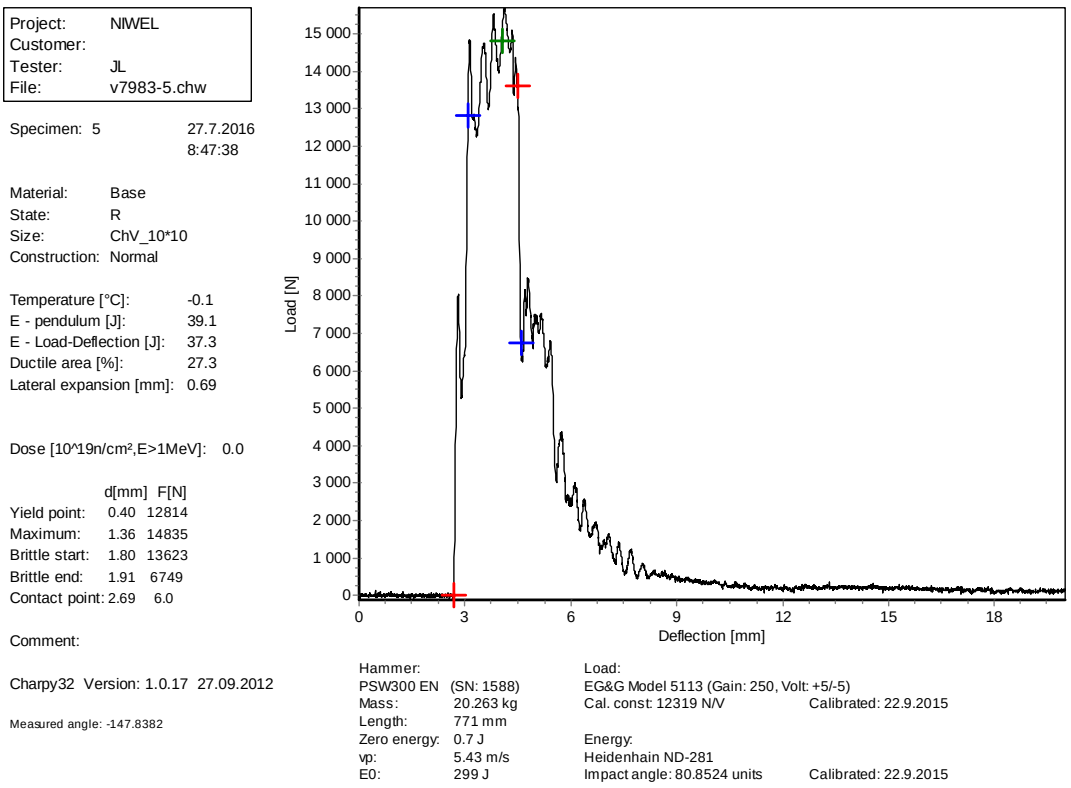

Figure 21 Specimen 5, aging, 5000 hours

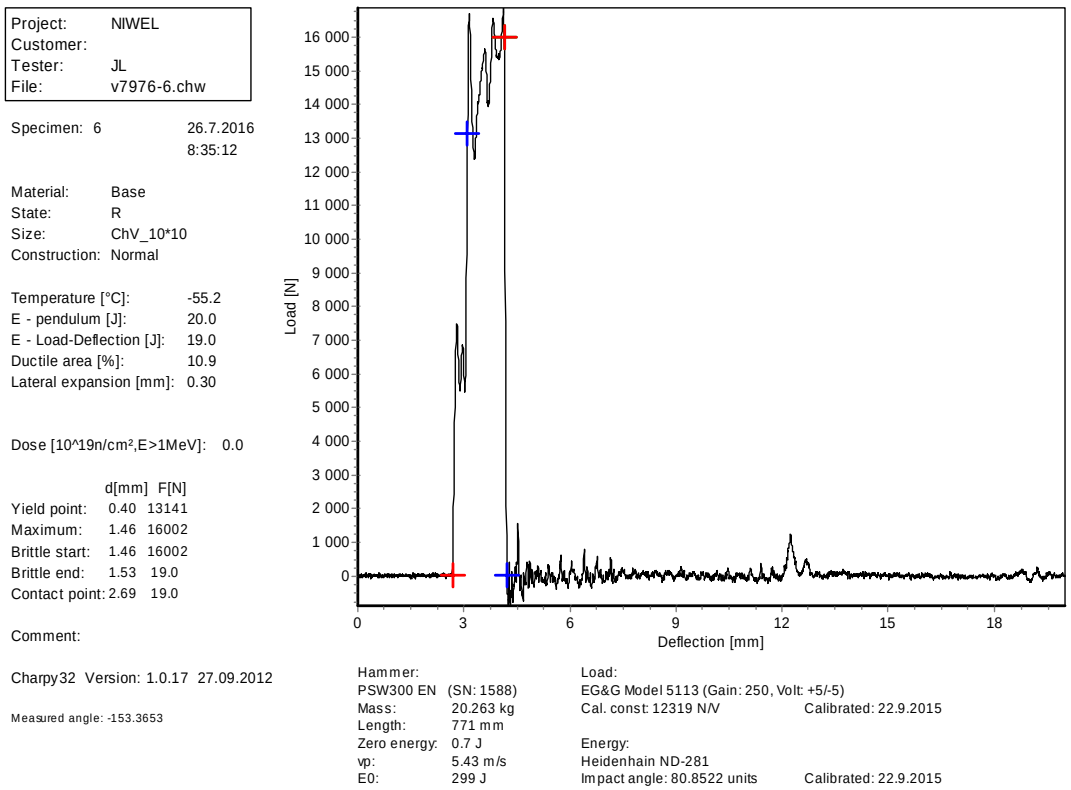

Figure 22 Specimen 6, aging, 5000 hours

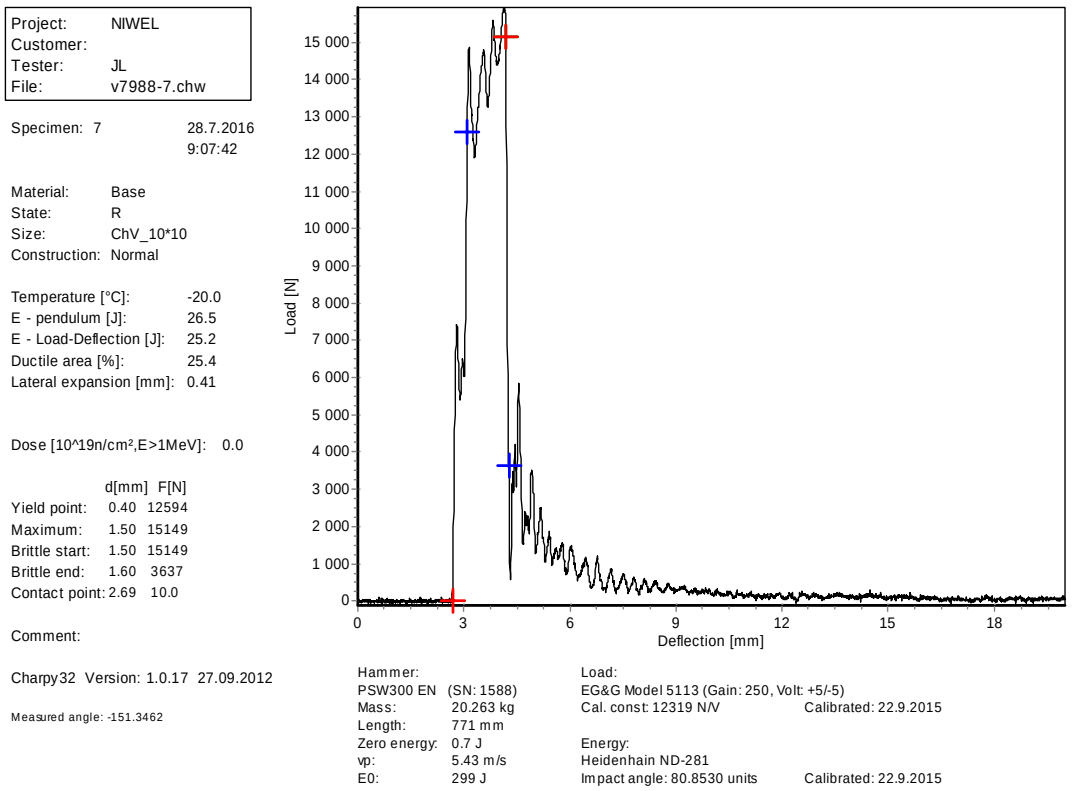

Figure 23 Specimen 7, aging, 5000 hours

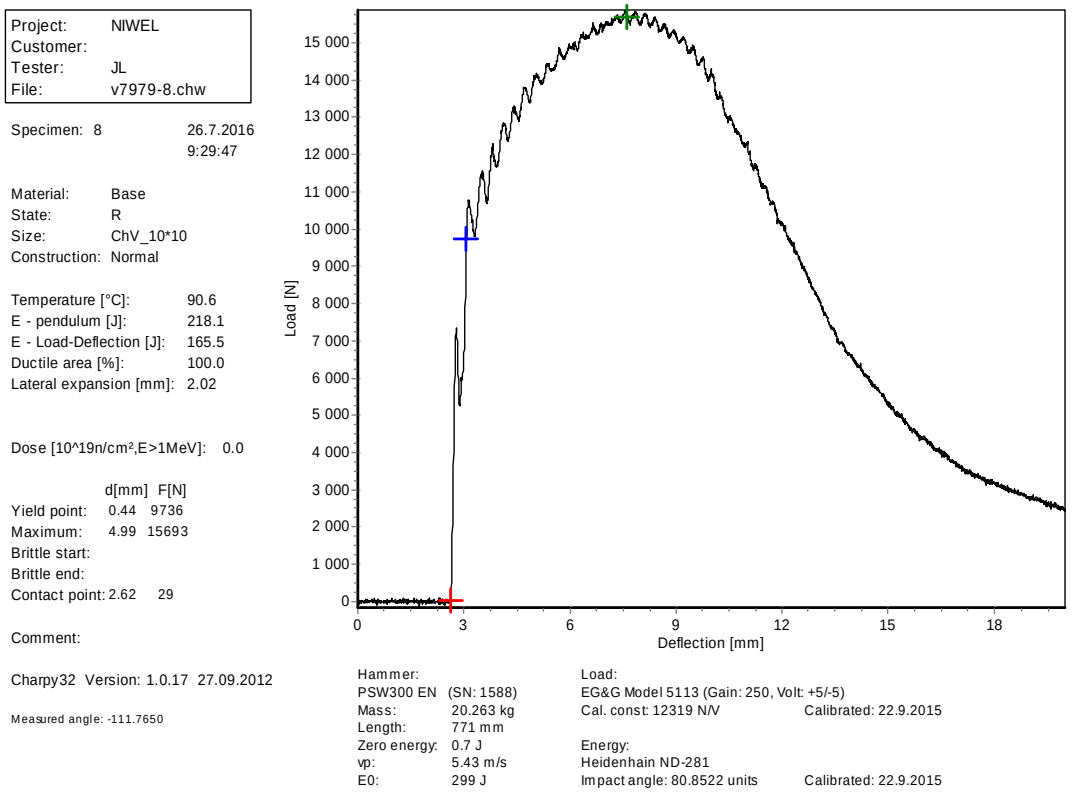

Figure 24 Specimen 8, aging, 5000 hours

Project:	NIWEL
Customer:	
Tester:	JL
File:	v7968-9.chw

Specimen: 9 25.7.2016 9:05:14

Material:	Base
State:	R
Size:	ChV_10*10
Construction:	Normal

Temperature [°C]:	19.8
E - pendulum [J]:	55.4
E - Load-Deflection [J]:	53.7
Ductile area [%]:	40.2
Lateral expansion [mm]:	0.86

Dose [10^19n/cm²,E>1MeV]: 0.0

	d[mm]	F[N]
Yield point:	0.40	11823
Maximum:	2.16	15508
Brittle start:	2.63	14815
Brittle end:	2.66	12768
Contact point:	2.69	10.0

Comment:

Charpy32 Version: 1.0.17 27.09.2012

Measured angle: -143.8687

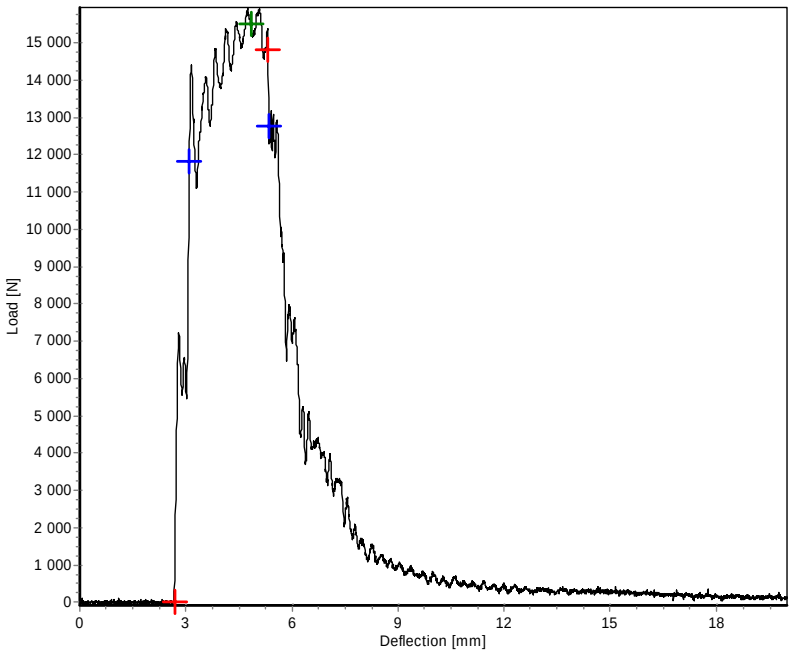

Hammer:		Load:	
PSW300 EN	(SN: 1588)	EG&G Model 5113 (Gain: 250, Volt: +5/-5)	
Mass:	20.263 kg	Cal. const: 12319 N/V	Calibrated: 22.9.2015
Length:	771 mm		
Zero energy:	0.7 J	Energy:	
vp:	5.43 m/s	Heidenhain ND-281	
E0:	299 J	Impact angle: 80.8534 units	Calibrated: 22.9.2015

Figure 25 Specimen 9, aging, 5000 hours

Project:	NIWEL
Customer:	
Tester:	JL
File:	v7984-10.chw

Specimen: 10 27.7.2016 9:09:14

Material:	Base
State:	R
Size:	ChV_10*10
Construction:	Normal

Temperature [°C]:	40.0
E - pendulum [J]:	182.5
E - Load-Deflection [J]:	115.6
Ductile area [%]:	77.6
Lateral expansion [mm]:	1.58

Dose [10^19n/cm²,E>1MeV]: 0.0

	d[mm]	F[N]
Yield point:	0.46	11591
Maximum:	3.72	16188
Brittle start:	5.18	14982
Brittle end:	5.25	13547
Contact point:	2.66	17.0

Comment:

Charpy32 Version: 1.0.17 27.09.2012

Measured angle: -118.9032

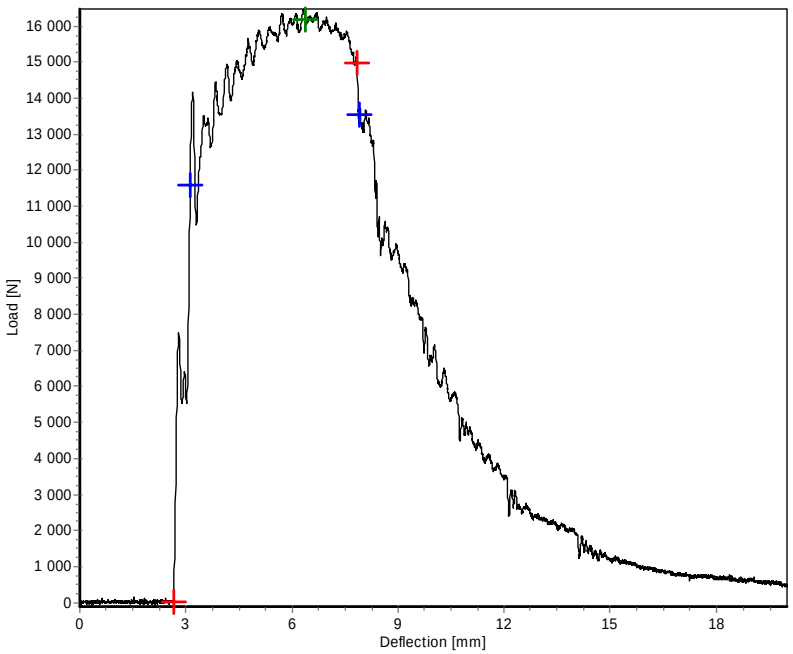

Hammer:		Load:	
PSW300 EN	(SN: 1588)	EG&G Model 5113 (Gain: 250, Volt: +5/-5)	
Mass:	20.263 kg	Cal. const: 12319 N/V	Calibrated: 22.9.2015
Length:	771 mm		
Zero energy:	0.7 J	Energy:	
vp:	5.43 m/s	Heidenhain ND-281	
E0:	299 J	Impact angle: 80.8524 units	Calibrated: 22.9.2015

Figure 26 Specimen 10, aging, 5000 hours

Project:	NIWEL
Customer:	
Tester:	JL
File:	v7969-11.chw

Specimen: 11 25.7.2016 9:16:13

Material:	Base
State:	R
Size:	ChV_10*10
Construction:	Normal

Temperature [°C]:	19.8
E - pendulum [J]:	81.8
E - Load-Deflection [J]:	80.0
Ductile area [%]:	59.9
Lateral expansion [mm]:	1.20

Dose [10^19n/cm²,E>1MeV]: 0.0

	d[mm]	F[N]
Yield point:	0.46	12762
Maximum:	3.45	16498
Brittle start:	3.45	16498
Brittle end:	3.52	13396
Contact point:	2.66	20.0

Comment:

Charpy32 Version: 1.0.17 27.09.2012

Measured angle: -138.1466

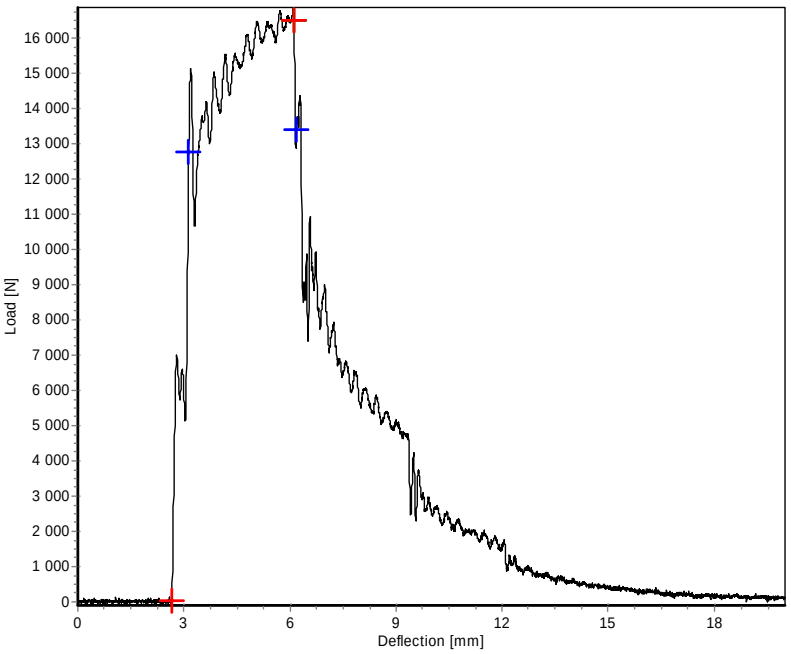

Hammer:		Load:	
PSW300 EN	(SN: 1588)	EG&G Model 5113 (Gain: 250, Volt: +5/-5)	
Mass:	20.263 kg	Cal. const: 12319 N/V	Calibrated: 22.9.2015
Length:	771 mm		
Zero energy:	0.7 J	Energy:	
vp:	5.43 m/s	Heidenhain ND-281	
E0:	299 J	Impact angle: 80.8534 units	Calibrated: 22.9.2015

Figure 27 Specimen 11, aging, 5000 hours

Project:	NIWEL
Customer:	
Tester:	JL
File:	v7977-12.chw

Specimen: 12 26.7.2016 8:46:10

Material:	Base
State:	R
Size:	ChV_10*10
Construction:	Normal

Temperature [°C]:	-55.2
E - pendulum [J]:	15.7
E - Load-Deflection [J]:	14.8
Ductile area [%]:	11.5
Lateral expansion [mm]:	0.26

Dose [10^19n/cm²,E>1MeV]: 0.0

	d[mm]	F[N]
Yield point:	0.43	13685
Maximum:	1.16	15408
Brittle start:	1.16	15408
Brittle end:	1.23	12.0
Contact point:	2.69	12.0

Comment:

Charpy32 Version: 1.0.17 27.09.2012

Measured angle: -154.7966

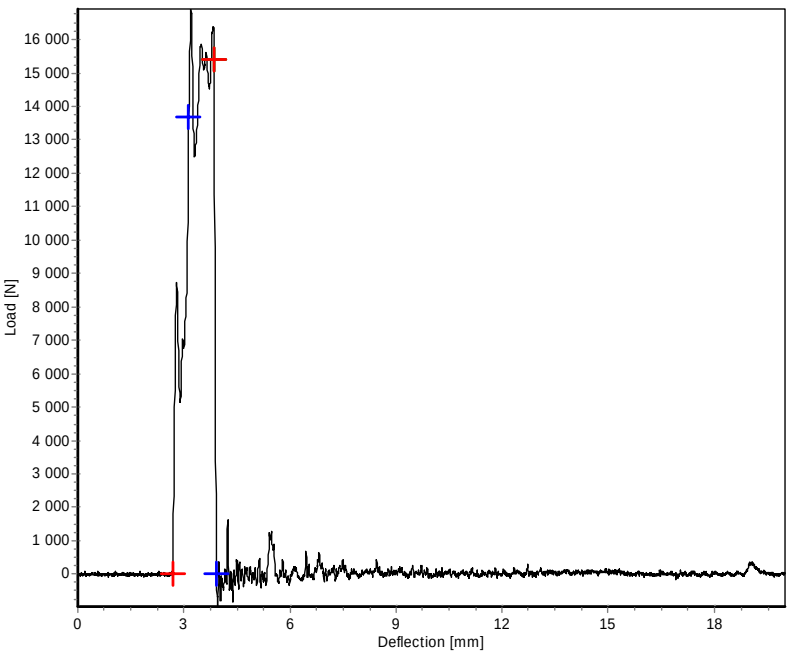

Hammer:		Load:	
PSW300 EN	(SN: 1588)	EG&G Model 5113 (Gain: 250, Volt: +5/-5)	
Mass:	20.263 kg	Cal. const: 12319 N/V	Calibrated: 22.9.2015
Length:	771 mm		
Zero energy:	0.7 J	Energy:	
vp:	5.43 m/s	Heidenhain ND-281	
E0:	299 J	Impact angle: 80.8522 units	Calibrated: 22.9.2015

Figure 28 Specimen 12, aging, 5000 hours

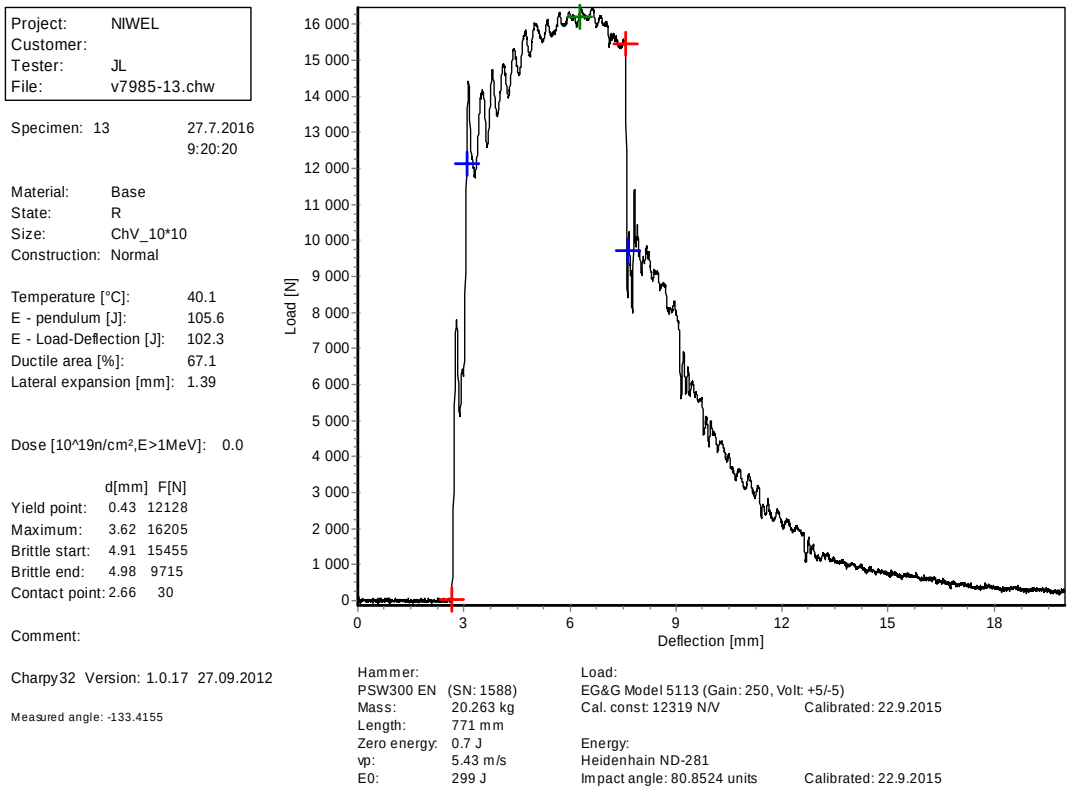

Figure 29 Specimen 13, aging, 5000 hours

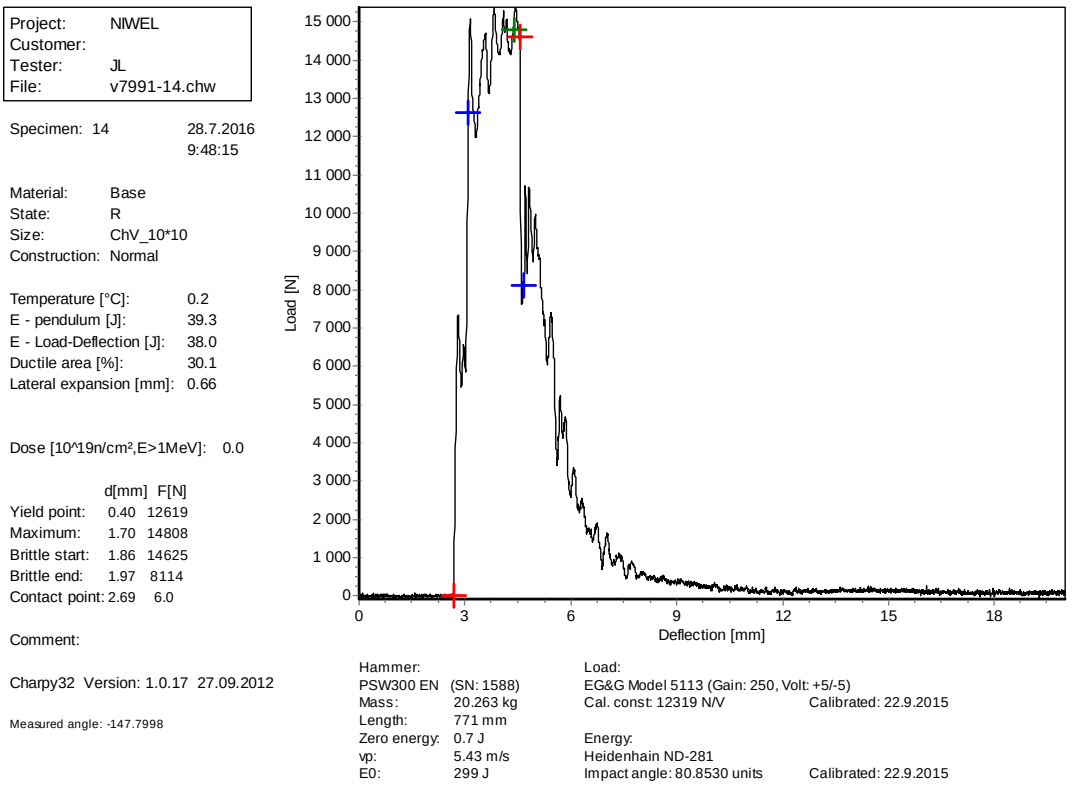

Figure 30 Specimen 14, aging, 5000 hours

Project:	NIWEL
Customer:	
Tester:	JL
File:	v7967-15.chw

Specimen: 15 25.7.2016 8:45:47

Material:	Base
State:	R
Size:	ChV_10*10
Construction:	Normal

Temperature [°C]:	-19.9
E - pendulum [J]:	36.1
E - Load-Deflection [J]:	34.7
Ductile area [%]:	25.6
Lateral expansion [mm]:	0.53

Dose [10^19n/cm²,E>1MeV]: 0.0

	d[mm]	F[N]
Yield point:	0.40	11049
Maximum:	1.77	14911
Brittle start:	2.26	14170
Brittle end:	2.41	2537
Contact point:	2.72	19.0

Comment:

Charpy32 Version: 1.0.17 27.09.2012

Measured angle: -148.6521

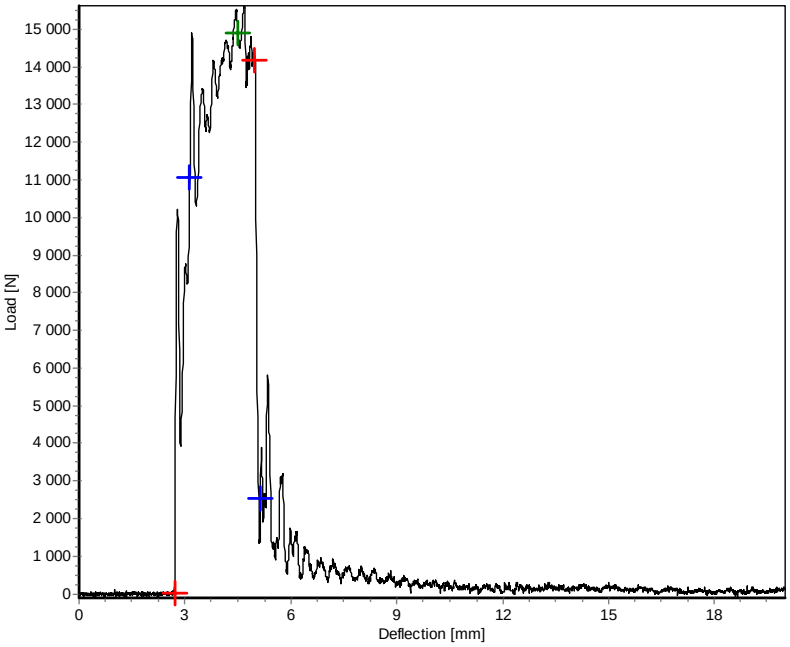

Hammer:		Load:	
PSW300 EN	(SN: 1588)	EG&G Model 5113 (Gain: 250, Volt: +5/-5)	
Mass:	20.263 kg	Cal. const: 12319 N/V	Calibrated: 22.9.2015
Length:	771 mm		
Zero energy:	0.7 J	Energy:	
vp:	5.43 m/s	Heidenhain ND-281	
E0:	299 J	Impact angle: 80.8534 units	Calibrated: 22.9.2015

Figure 31 Specimen 15, aging, 5000 hours

Project:	NIWEL
Customer:	
Tester:	JL
File:	v7966-16.chw

Specimen: 16 25.7.2016 8:34:50

Material:	Base
State:	R
Size:	ChV_10*10
Construction:	Normal

Temperature [°C]:	-20.2
E - pendulum [J]:	37.6
E - Load-Deflection [J]:	36.6
Ductile area [%]:	26.3
Lateral expansion [mm]:	0.64

Dose [10^19n/cm²,E>1MeV]: 0.0

	d[mm]	F[N]
Yield point:	0.43	12133
Maximum:	2.26	16393
Brittle start:	2.26	16393
Brittle end:	2.33	3120
Contact point:	2.69	16.0

Comment:

Charpy32 Version: 1.0.17 27.09.2012

Measured angle: -148.2488

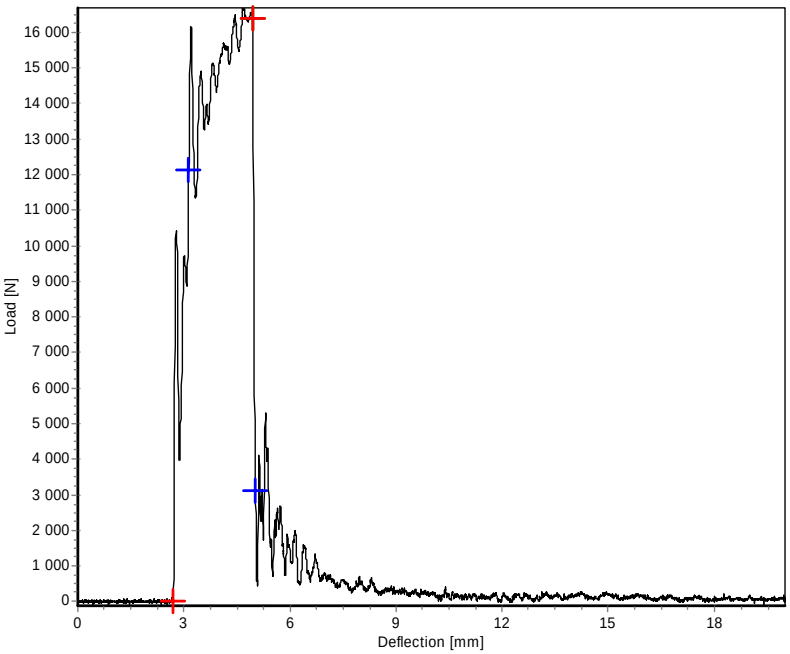

Hammer:		Load:	
PSW300 EN	(SN: 1588)	EG&G Model 5113 (Gain: 250, Volt: +5/-5)	
Mass:	20.263 kg	Cal. const: 12319 N/V	Calibrated: 22.9.2015
Length:	771 mm		
Zero energy:	0.7 J	Energy:	
vp:	5.43 m/s	Heidenhain ND-281	
E0:	299 J	Impact angle: 80.8534 units	Calibrated: 22.9.2015

Figure 32 Specimen 16, aging, 5000 hours

Project:	NIWEL
Customer:	
Tester:	JL
File:	v7989-17.chw

Specimen: 17 28.7.2016 9:18:41

Material:	Base
State:	R
Size:	ChV_10*10
Construction:	Normal

Temperature [°C]:	-20.0
E - pendulum [J]:	40.9
E - Load-Deflection [J]:	39.7
Ductile area [%]:	31.9
Lateral expansion [mm]:	0.64

Dose [10^19n/cm²,E>1MeV]: 0.0

	d[mm]	F[N]
Yield point:	0.33	12496
Maximum:	2.09	16239
Brittle start:	2.16	15834
Brittle end:	2.23	4166
Contact point:	2.69	18.0

Comment:

Charpy32 Version: 1.0.17 27.09.2012

Measured angle: -147.3875

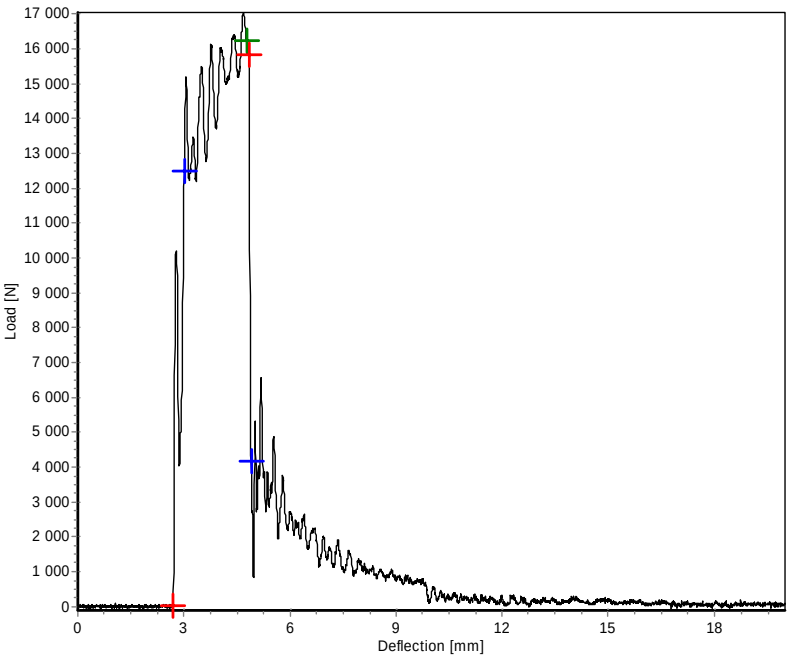

Hammer:		Load:	
PSW300 EN	(SN: 1588)	EG&G Model 5113 (Gain: 250, Volt: +5/-5)	
Mass:	20.263 kg	Cal. const: 12319 N/V	Calibrated: 22.9.2015
Length:	771 mm		
Zero energy:	0.7 J	Energy:	
vp:	5.43 m/s	Heidenhain ND-281	
E0:	299 J	Impact angle: 80.8530 units	Calibrated: 22.9.2015

Figure 33 Specimen 17, aging, 5000 hours

Project:	NIWEL
Customer:	
Tester:	JL
File:	v7972-18.chw

Specimen: 18 25.7.2016 9:57:58

Material:	Base
State:	R
Size:	ChV_10*10
Construction:	Normal

Temperature [°C]:	60.3
E - pendulum [J]:	215.5
E - Load-Deflection [J]:	169.0
Ductile area [%]:	89.8
Lateral expansion [mm]:	1.92

Dose [10^19n/cm²,E>1MeV]: 0.0

	d[mm]	F[N]
Yield point:	0.40	12239
Maximum:	4.49	16572
Brittle start:	11.80	6506
Brittle end:	11.87	4239
Contact point:	2.52	6.0

Comment:

Charpy32 Version: 1.0.17 27.09.2012

Measured angle: -112.3116

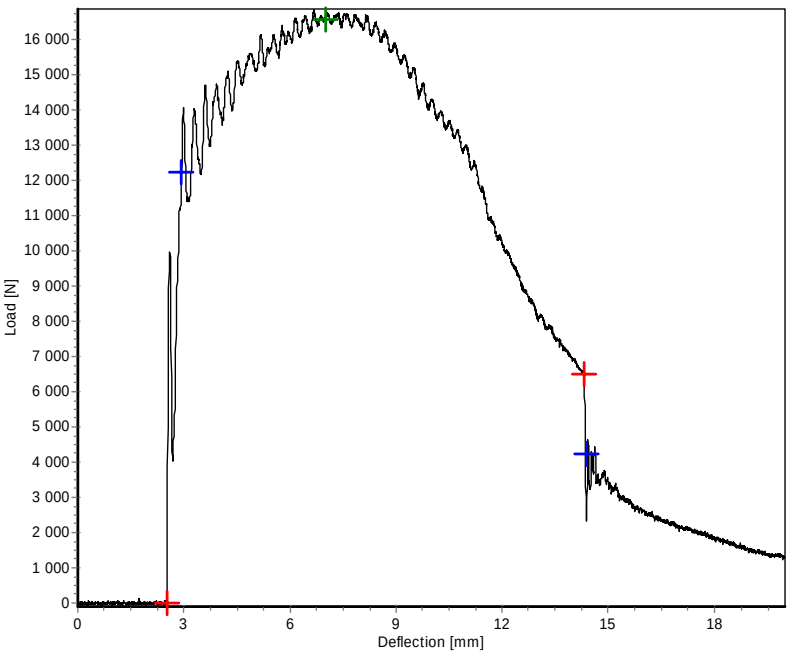

Hammer:		Load:	
PSW300 EN	(SN: 1588)	EG&G Model 5113 (Gain: 250, Volt: +5/-5)	
Mass:	20.263 kg	Cal. const: 12319 N/V	Calibrated: 22.9.2015
Length:	771 mm		
Zero energy:	0.7 J	Energy:	
vp:	5.43 m/s	Heidenhain ND-281	
E0:	299 J	Impact angle: 80.8534 units	Calibrated: 22.9.2015

Figure 34 Specimen 18, aging, 5000 hours

Figure 1 Specimen 1A, as-received

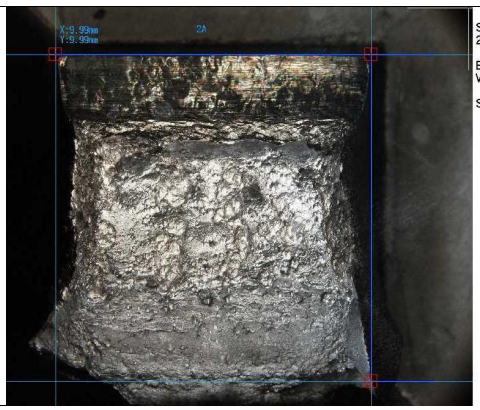

Figure 2 Specimen 2A, as-received

Figure 3 Specimen 4A, as-received

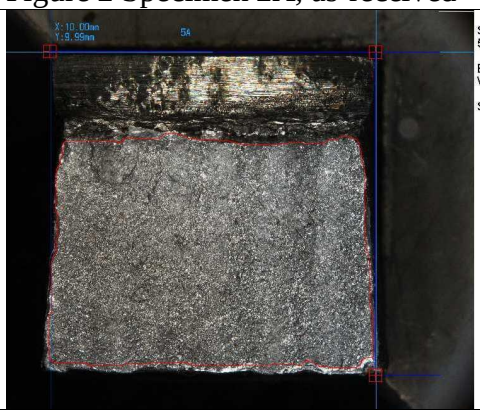

Figure 4 Specimen 5A, as-received

Figure 5 Specimen 7A, as-received

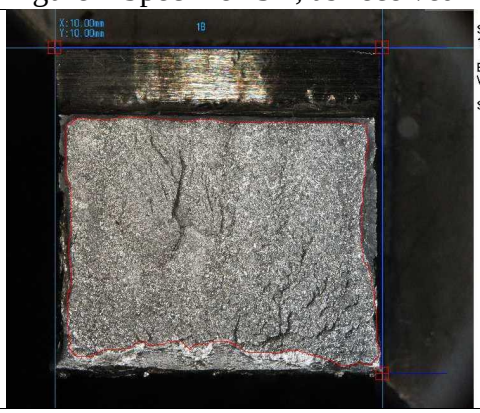

Figure 6 Specimen 1B, as-received

Figure 7 Specimen 2B, as-received

Figure 8 Specimen 3B, as-received

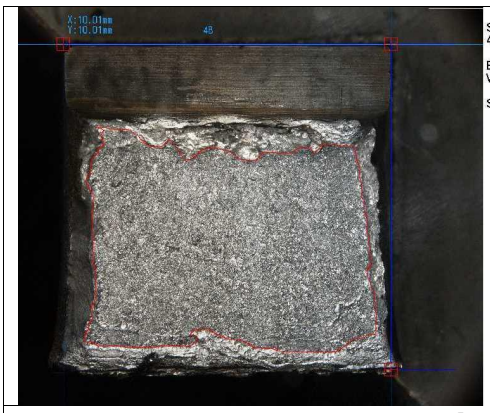

Figure 9 Specimen 4B, as-received

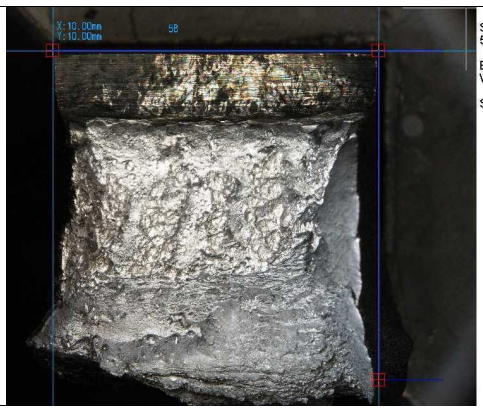

Figure 10 Specimen 5B, as-received

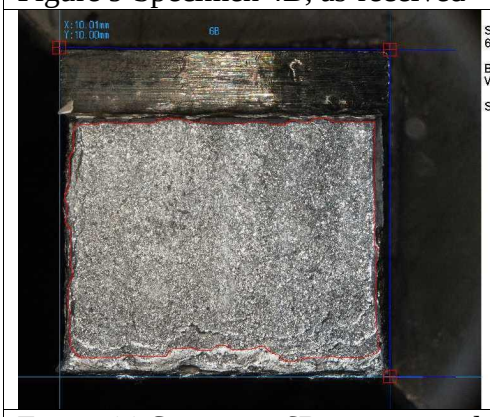

Figure 11 Specimen 6B, as-received

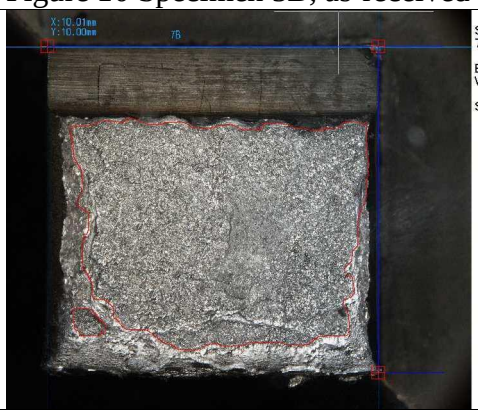

Figure 12 Specimen 7B, as-received

Figure 13 Specimen 1C, as-received

Figure 14 Specimen 2C, as-received

Figure 15 Specimen 3C, as-received

Figure 16 Specimen 4C, as-received

Figure 17 Specimen 1, aging, 5000 hours

Figure 18 Specimen 2, aging, 5000 hours

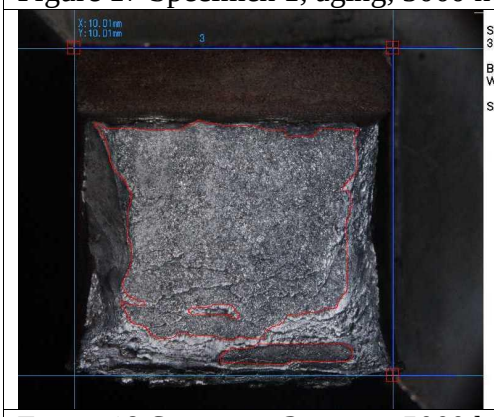

Figure 19 Specimen 3, aging, 5000 hours

Figure 20 Specimen 4, aging, 5000 hours

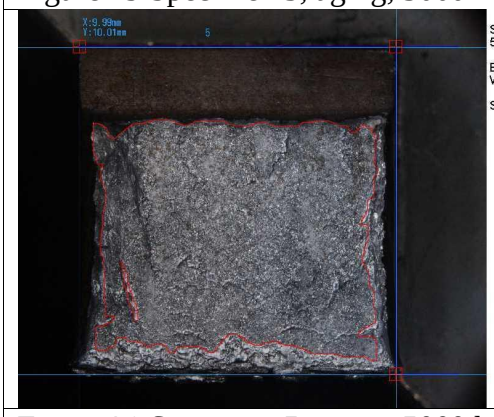

Figure 21 Specimen 5, aging, 5000 hours

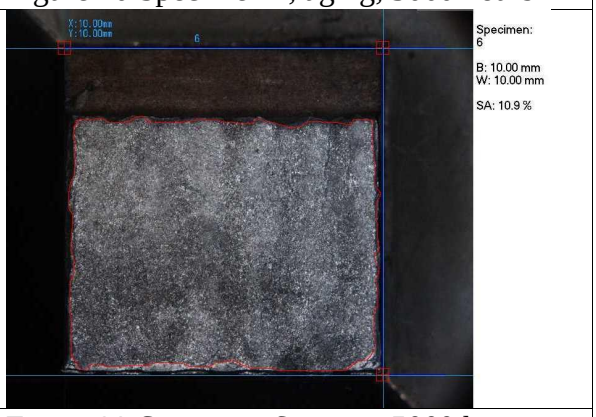

Figure 22 Specimen 6, aging, 5000 hours

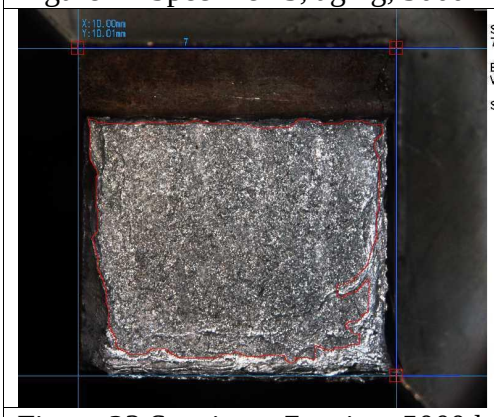

Figure 23 Specimen 7, aging, 5000 hours

Figure 24 Specimen 8, aging, 5000 hours

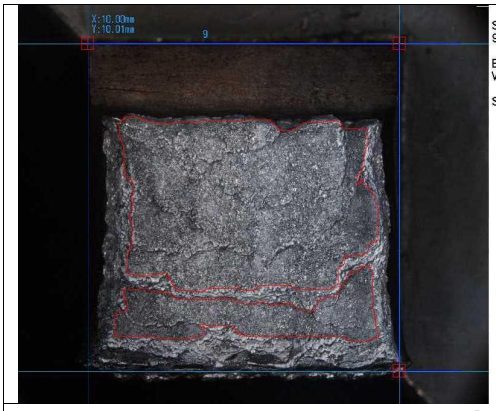

Figure 25 Specimen 9, aging, 5000 hours

Figure 26 Specimen 10, aging, 5000 hours

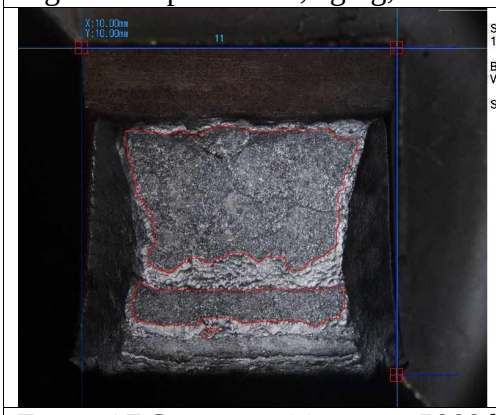

Figure 27 Specimen 11, aging, 5000 hours

Figure 28 Specimen 12, aging, 5000 hours

Figure 29 Specimen 13, aging, 5000 hours

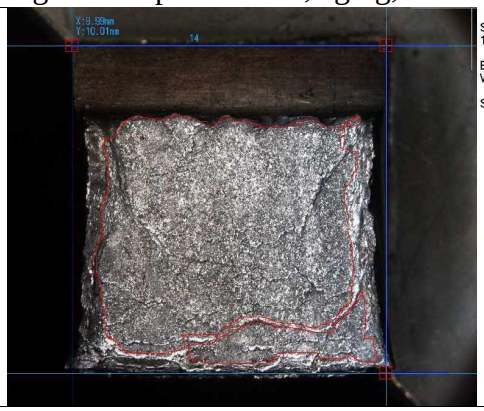

Figure 30 Specimen 14, aging, 5000 hours

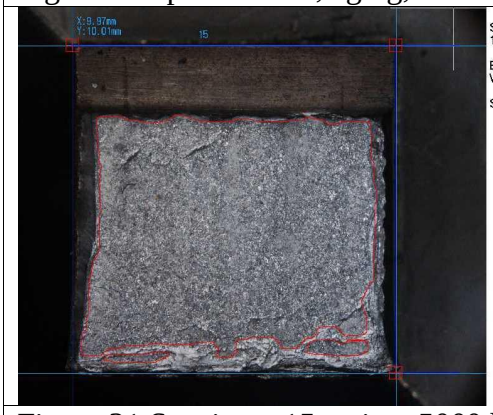

Figure 31 Specimen 15, aging, 5000 hours

Figure 32 Specimen 16, aging, 5000 hours

Figure 33 Specimen 17, aging, 5000 hours

Figure 34 Specimen 18, aging, 5000 hours

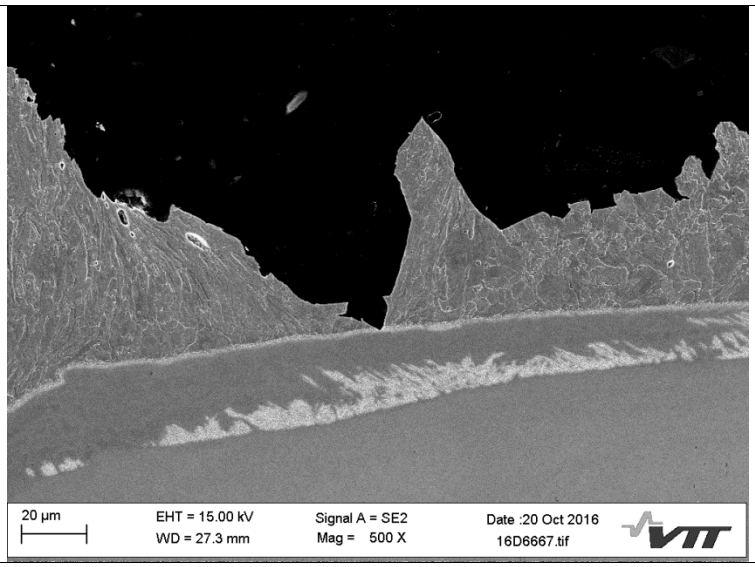

Figure 1 Specimen 2C, as-received, ductile and brittle fracture close to the V-notch root

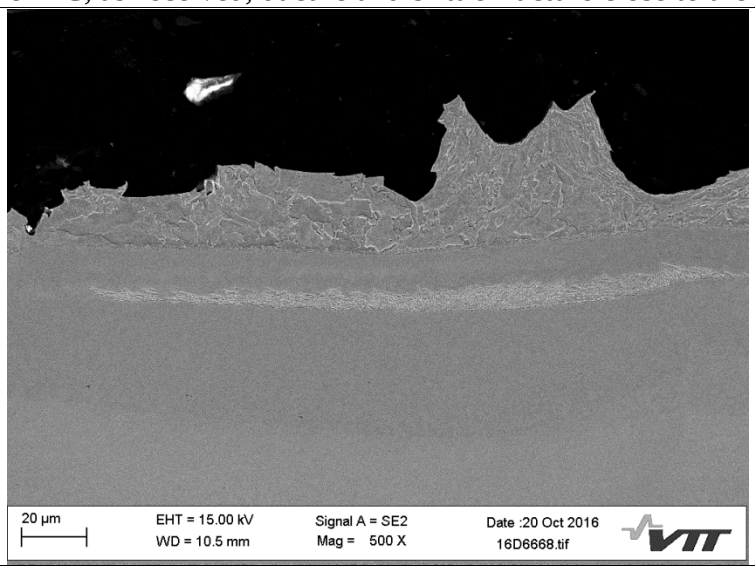

Figure 2 Specimen 2C, as-received, brittle fracture

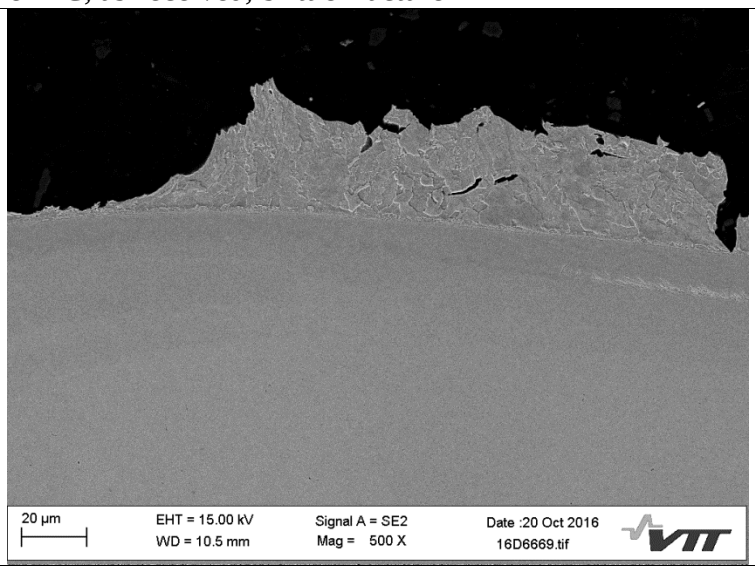

Figure 3 Specimen 2C, as-received, brittle fracture

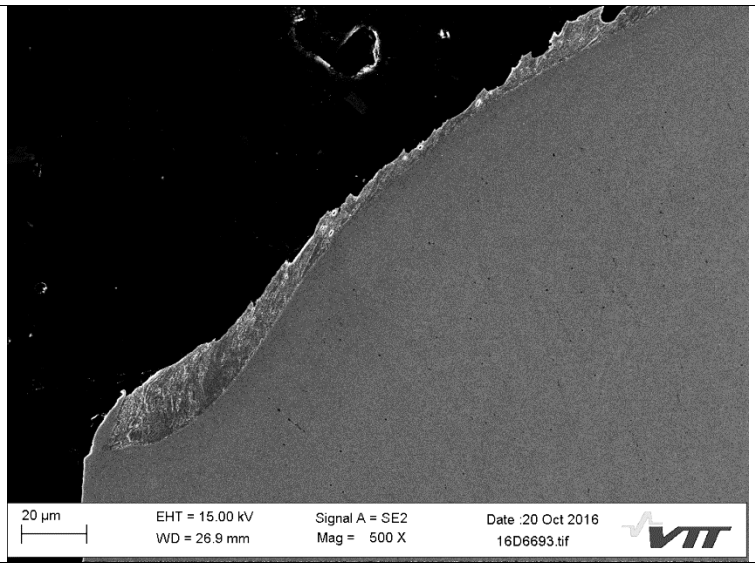

Figure 4 Specimen 4C, as-received, ductile fracture close to the V-notch

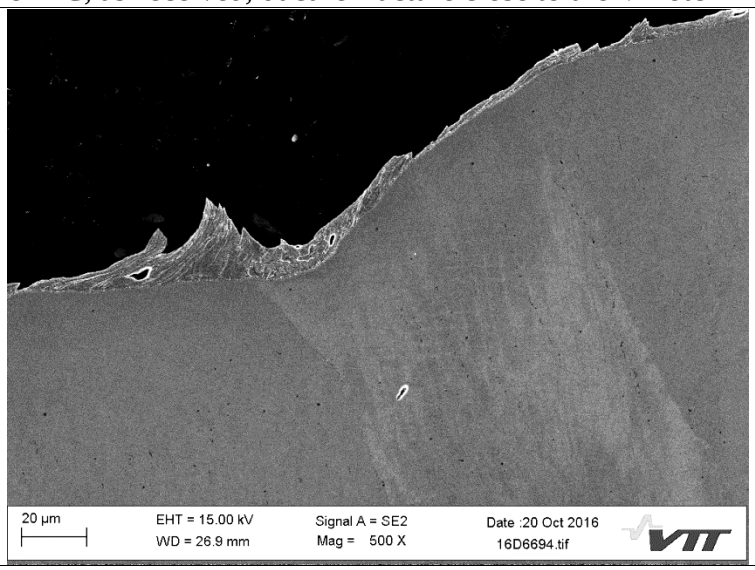

Figure 5 Specimen 4C, as-received, ductile fracture

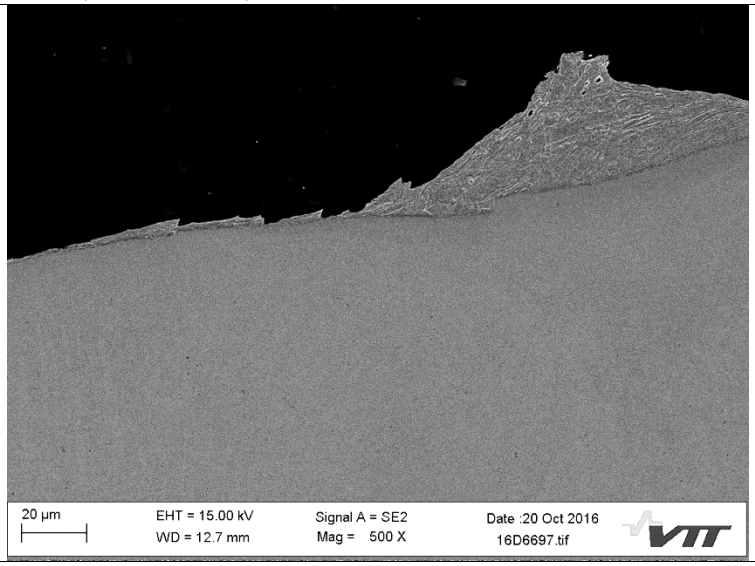

Figure 6 Specimen 4C, as-received, brittle fracture

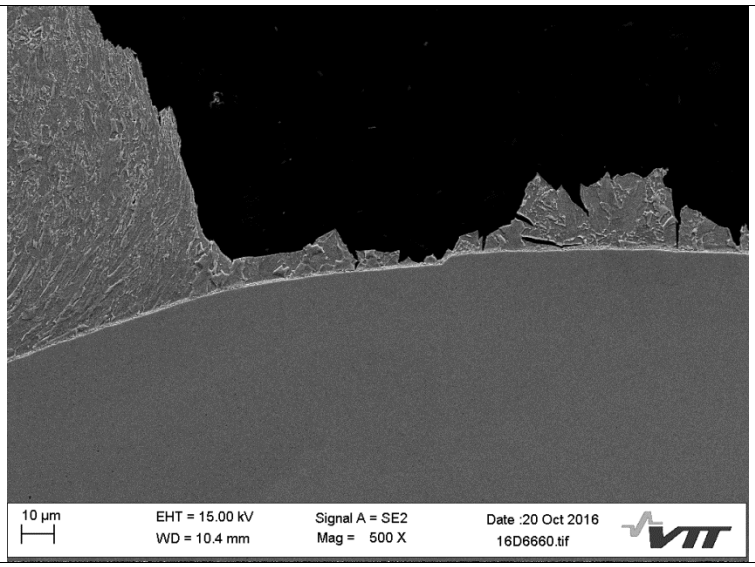

Figure 7 Specimen 6B, as-received, ductile and brittle fracture close to the V-notch root

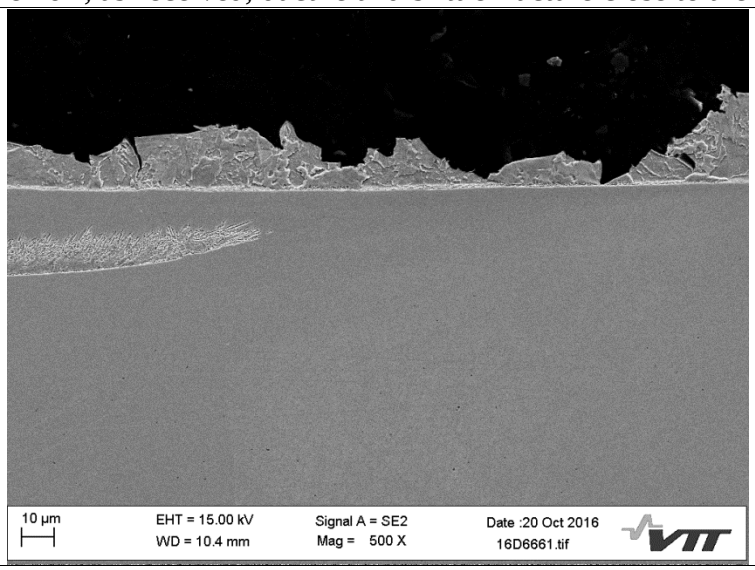

Figure 8 Specimen 6B, as-received, brittle fracture

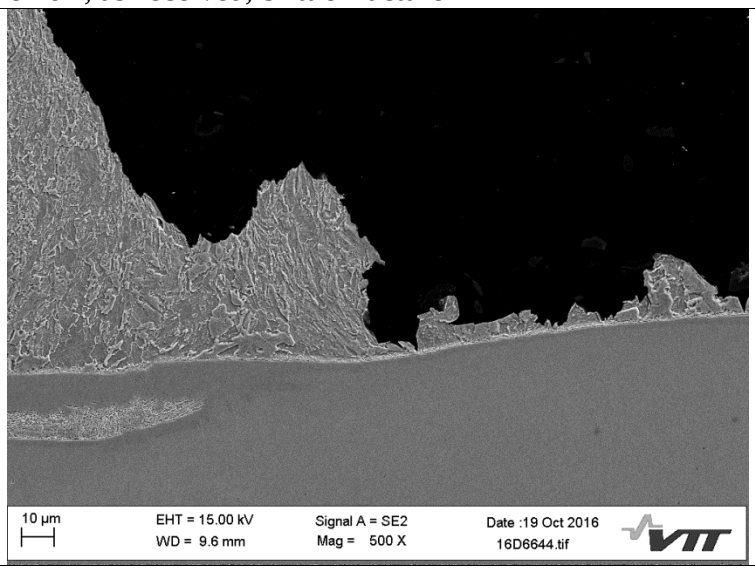

Figure 9 Specimen 12, aging, 5000 hours, brittle fracture close to the V-notch root

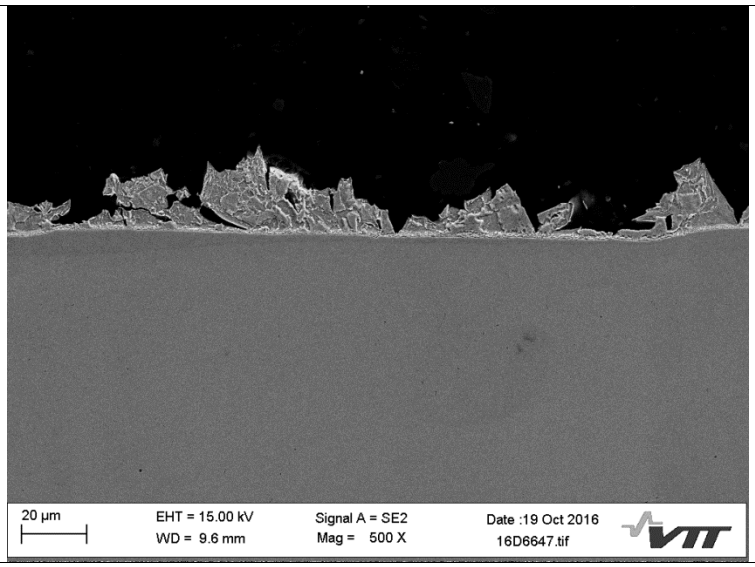

Figure 10 Specimen 12, aging, 5000 hours, brittle fracture

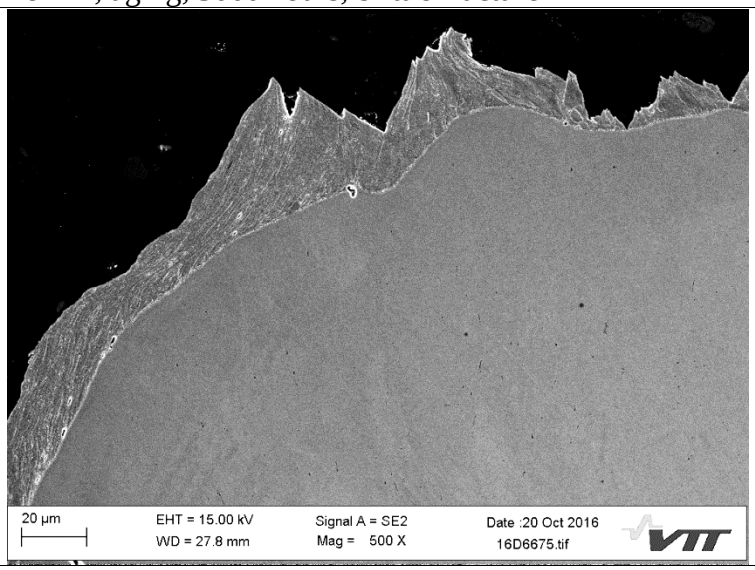

Figure 11 Specimen 17, aging, 5000 hours, ductile fracture close to the V-notch

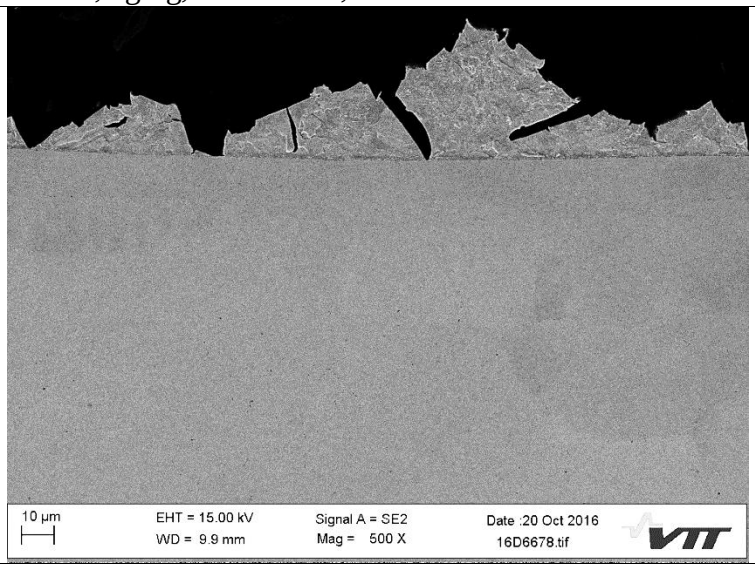

Figure 12 Specimen 17, aging, 5000 hours, brittle fracture

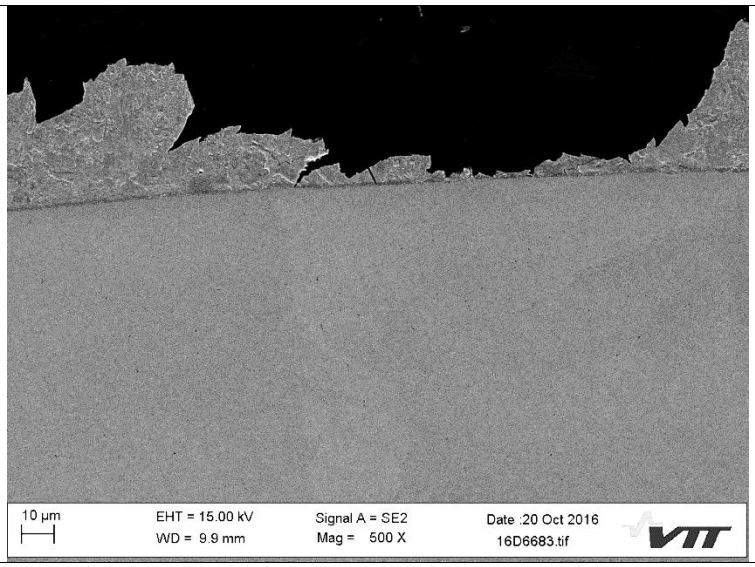

Figure 13 Specimen 17, aging, 5000 hours, brittle fracture

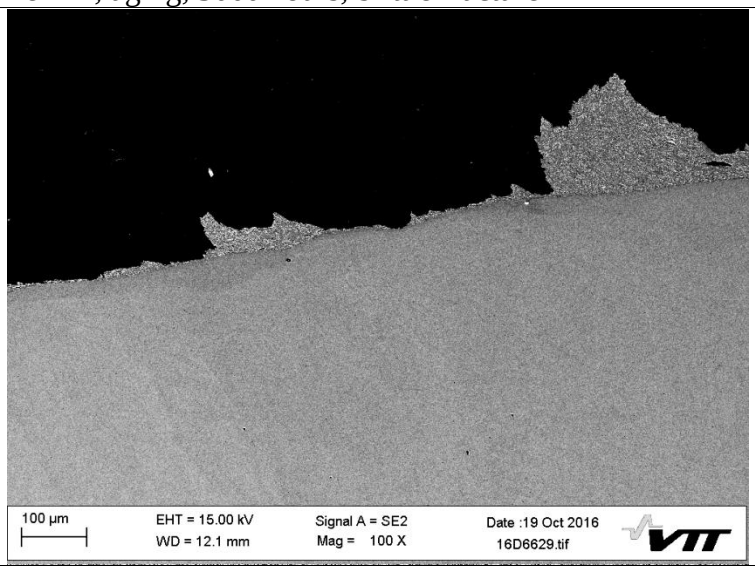

Figure 14 Specimen 18, aging, 5000 hours, ductile fracture

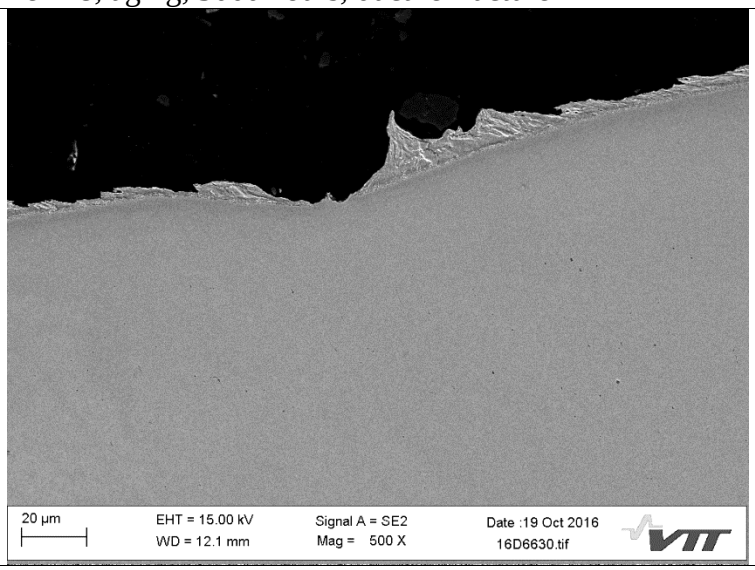

Figure 15 Specimen 18, aging, 5000 hours, ductile fracture